PHOTONICS

CMDITR Review of Undergraduate Research

Contributions from undergraduate research experiences within the
NSF Center on Materials and Devices for Information Technology Research

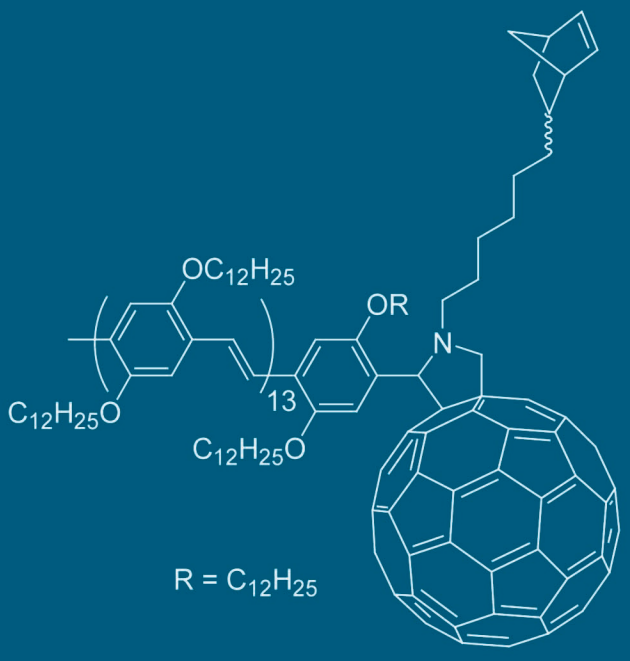

Volume 2, Number 1

The material is based upon work supported by the STC Program of the National Science Foundation No. DMR 0120967.

Printed in the United States at the University of Washington, Seattle, WA

Inquires should be addressed to:

Center on Materials and Devices for Information Technology Research
Educational Partnership Programs
University of Washington
Department of Chemistry
Box 351700
Seattle, WA 98195-1700

ehrdo@u.washington.edu
http://stc-mditr.org

Volume 2, Number 1

Welcome to the Second Edition of CMDITR Review of Undergraduate Research

This volume of the Reviews features extended abstracts of students who participated in the National Science Foundation (NSF) Center on Materials and Devices in Information Technology Research (CMDITR) Summer 2005 Research Experiences for Undergraduates (REU) program.

The REU experience often acts as a launching point or catalyst for entry by undergraduates into technical fields of study. The REU experience is symbiotic in nature as it supports not only the undergraduate participant who experiences research first-hand prior to committing to graduate study, but also the students mentors, be they faculty members, research scientists, post-doctoral fellows, or graduate students. While working with REU students graduate students and post-doctoral fellows learn teaching and mentoring skills needed to manage labs they will be responsible for in the future. Faculty members and other researchers, who share their expertise with these enthusiastic learners, also benefit as they reflect on the excitement upon which their careers have been built.

The CMDITR REU Summer Program placed undergraduate students from across the United States in CMDITR state-of-the-art research labs at the University of Washington, University of Arizona and Georgia Institute of Technology. The 2005 program expanded on the previous year's program with a doubling of the number of undergraduates to 32 participants. Several of these undergraduates in the 2005 program were part of a new, collaborative exchange program between Norfolk State University and Georgia Tech. All of these undergraduates worked on authentic interdisciplinary research contributing to advancements in information technology with researchers in the fields of chemistry, physics, optics, materials science and engineering. The REU Program emphasized the teamwork nature of scientific research and was supplemented by a collection of activities including ethics training and workshops in scientific communication.

The role of the Review is to offer a forum for participants involved in the CMDITR REU to share their research with their REU peers, future REU students, CMDITR graduates students and faculty members, and others interested in the work of CMDITR. The Review is also a forum that depicts the breadth and depth of CMDITR research.

To learn more about the CMDITR REU program and opportunities please visit http://stc-mditr.org/REU.

A special thanks to all the REU participants for their work, their mentors for their time and patience, and the REU program coordinators (Maggie Harden, Olanda Davidson Bryant, and Kristin Wustholz) for their efforts to make the program successful.

The extended abstracts included in the Review are presented in alphabetical order by the participant's last name.

Sara Selfe, Ph.D., Editor

TABLE OF CONTENTS

Synthesis of Dendrimer Building Blocks with Crosslinkable Moieties

Kathy L. Beckner
University of Kentucky

Dominic V. McGrath and David Sisk
McGrath Lab, Department of Chemistry
The University of Arizona

INTRODUCTION

Dendrimers have been employed in various applications primarily because of their ability to insulate materials and display functional groups.[1] Dendritic encapsulation of chromophores has been shown to enhance optical and electronic properties, while peripheral functional groups can be used for further reactivity.[2] Potential applications for dendrimers include organic light emitting devices, light harvesting and potentially drug delivery or gene therapy.[3] Dendritic cross-linking of peripheral functional groups can enhance dendrimer-based insulation,[4] create stable dendrimer films,[5] or generate dendritic nanocapsules.[6] In organic electronic devices, films are prepared by spin-casting, a process that requires the polymers to be soluble. However, in order to cast another layer over the previous one, the materials need to be insoluble after being deposited. Crosslinking has been shown to be a potential solution to this problem.[7]

The McGrath group has demonstrated that dendrimers with cinnamate moieties on their periphery can be photo-crosslinked to provide stable dendrimer films. Originally ethyl cinnamate esters were used to fabricate the photocrosslinkable dendrons. However the synthesis of these dendrons has proven difficult because of their insolubility at lower generations. The goal of this research is to replace the ethyl ester with a pentyl group in order to improve solubility. Increasing the solubility of these ester cinnamate dendrons in this way should allow the preparation of higher generation dendrons in greater quantities. Increasing the dendron's solubility by altering the ester in this fashion is also important for the spin casting process used in device fabrication.

Previously, an improved synthesis of 3,5-di-*tert*-butyl dendrons has been reported starting from 3,5-di-*tert*-butyl-4-hydroxytoluene (BHT).[8] In addition to the *tert*-butyl groups, these dendrons have a peripheral methoxy group on each ring. To increase the versatility of these dendrons, experiments were performed to vary the length and functionality of these peripheral alkoxy chains. For example, replacing the methoxy with an allyloxy. This particular end-group would allow for more versatility in the molecule, by making cross-linking a possibility. Dendrimers possessing this particular end-group has been shown to successfully cross-link in a ring closing metathesis reaction by the Zimmerman group.[9]

RESULTS AND DISCUSSION

In this project, several synthetic routes to prepare insulating and cross-linking dendrimers were explored. The synthesis of two types of dendrons were attempted: 3,5-di-*tert*-butyl dendrons and ester cinnamate dendrons. Two different methods were explored in the synthesis of 3,5-*tert*-butyl dendrons, while an effective synthetic route was established for ester cinnamate dendrons by employing a pentyl group.

The synthesis of the 3,5-di-*tert*-butyl dendrons was performed using previously published procedures (Scheme 1).[7] The original synthesis produced the 3,5-di-*tert*-butyl 4–methoxybenzyloxy terminated dendrons using a four step series of reactions that was performed without purification until the final product which was simply recrystallized. When the sequence was carried out with an allyl group however, it was not possible to isolate the product using similar methods. When the product could not be isolated by standard methods of purification, stepwise purification was attempted, however this proved unsuccessful.

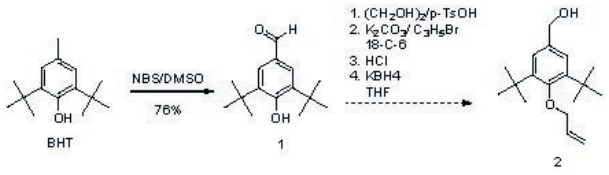

Scheme 1. Attempted synthetic route to 3,5-di-*tert*-butyl building blocks containing allyl ether end groups.

Subsequently a different approach was taken to try and produce **2** (Scheme 2). Instead of protecting the aldehyde, it was first reduced selectively to obtain benzyl alcohol **3**.

Attempts to alkylate the X residue proved fruitless. However, this methodology produced similar results in that the resulting product could not be isolated by standard purification methods.

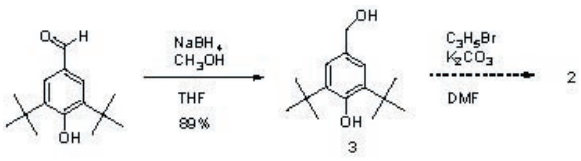

Scheme 2. Alternate route used in attempt to produce 3,5-di-*tert*-butyl terminated dendrons

Crosslinkable cinnamate dendrons were prepared with a pentyl ester similar to the ethyl ester previously reported (Scheme 3).[10]

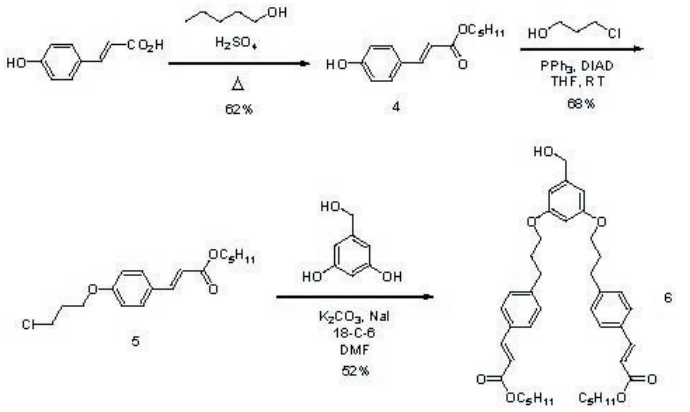

Scheme 3. Synthetic route used to produce [G-1]-cinnamate dendrons.

In the first step of the synthesis, which was taken from modified published procedures,[11] removal of the remaining pentanol used to produce **4** proved difficult and therefore was not an improvement over previous methodology. However, the solubility in the consecutive steps of the synthesis was greatly increased as a result of incorporation of the pentyl group. Compound **6** was found to be much more soluble than its ethyl ester counterpart. While the Mitsunobu reaction used to produce compound **5** still gave low yields, it was an improvement over the previous synthesis of ethyl ester cinnamate dendrons.

Compound **6** was then used to produce the [G2]-cinnamate dendron (**7**).

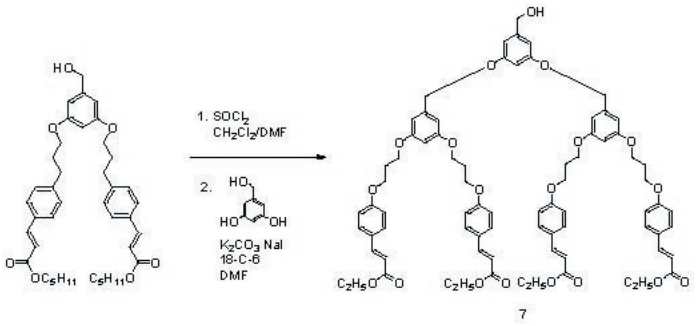

Scheme 4. Synthesis of [G-2]-cinnamate dendron.

CONCLUSIONS

In this project various synthetic routes were explored for generating both 3,5-di-*tert*-butyl terminal dendrons as well as crosslinkable cinnamate dendrons. It is possible that this reaction will work under less harsh conditions by using a weaker base. After an effective synthetic route is established for these dendrons, an entire class of BHT derived compounds may be synthesized with varying functionality. A synthetic route was developed to produce up to [G-2]-cinnamate dendrons with a pentyl group, which was found to be an improvement over the previous synthesis of ethyl ester cinnamate dendrons. In the future film studies will be performed on both polymers produced from these dendrons as well as the dendrons themselves to determine the effects of crosslinking.

REFERENCES

[1] Fréchet, J.M.J. *J. Polym. Sci. Part A: Polym Chem* **2003,** 41, 3713-3725.

[2] Grayson, S.M.; Frechet, J.M.J.; *Chem. Rev.* 101, 3819-3868.

[3] Grayson, S.M.; Fréchet, J.M.J. *Chem. Rev.* 101, 3819-3868.

[4] Guo, W.J.; Li, J.J.; Peng, X.; Wang, A. *J. Am. Chem. Soc.* **2003,** 12, 3901-3909.

[5] D'Ambruoso, G.D. Ph.D. Thesis, University of Arizona, 2004.

[6] Lencoff, N.G.; Spurlin, T.A.; Gewirth, A.A.; Zimmerman, S.C.; Beil, J.B.; Elmer, S.L.; Vandeveer, H.G. *J. Am. Chem. Soc.* **2004,** 126, 11420-11421.

[7] Zimmerman

[8] McGrath, D.V.; Shanahan, C.S. *J. Org. Chem.* **2005,** 70, 1054.

[9] Zimmerman, S.C.; Elmer, S.L. *J. Org. Chem.* **2004,** 69, 7363-7366.

[10] D'Ambruoso, G.D. Ph.D. Thesis, University of Arizona, 2004.

[11] Cernerd

ACKNOWLEDGEMENTS

-Dr. Dominic McGrath, Professor of Chemistry, University of Arizona

-McGrath Research Group

-Funding provided by the Center on Materials and Devices for Information Technology Research (CMDITR), an NSF Science and Technology Center No. DMR 0120967

Kathy Beckner will graduate from the University of Kentucky in Fall 2005 with a B.S. in chemistry. She would like to thank Dr. Dominic McGrath and the McGrath group for their support.

Contact Angle Measurements on Diamond Surfaces for a Study on Hydrophobic Forces

Ariel Bedford
Florida A&M University

Dr. Elisa Riedo, Lina Merchan
and Dr. Robert Szoszkiewicz
Riedo Lab, School Of Physics
Georgia Institute of Technology

INTRODUCTION

The hydrophobic force is the attractive force between hydrophobic surfaces in water solutions. It is usually measured at the nanoscale, and its origin and nature constitutes a major area of study presently. The entropy driven force that causes oil to separate from water is an example of the hydrophobic effect. Hydrophobic forces are crucial in many physical and biological phenomena such as protein folding. Currently, research dealing with these forces on surfaces that are hydrophobic and stable, such as diamond, is limited. The goal of this work was to study the hydrophobic behavior of diamond surfaces with different roughness and grain size and to relate this behavior to the range and magnitude of the hydrophobic forces generated by these surfaces. In particular we studied the relationship between hydrophobic force and surface characteristics such as static and dynamic contact angle, contact angle hysteresis, grain density and roughness.

THEORY

Static contact angle is the angle made by a tangent line between the gas and liquid phases of a water droplet on a surface. Decisive patterns of contact angle advancing and receding were used in order to view the hydrophobic character of the surfaces. When measuring the advancing contact angle of a surface, the contact angle steadily increases and peaks before having a steady decreasing period. This maximum contact angle is called advancing contact angle. The peak has to be seen in unison with a slight increase of the baseline length of the water droplet, and then a return to plateau-like recordings. On the other hand when measuring receding contact angles, the measurements were sensed to have slight decreases, a low point peak, and then steady increases, while having simultaneous baseline length measurements decreasing with the peaks, and having plateau-like recordings follow as well. The first duty in the research process consisted of taking static contact angle measurements of each surface. The second step was to then take advancing and receding contact angle measurements that were isolated into small intervals of time (usually 500 millisecond intervals over a 3 second period). The third task was to calculate any possible contact angle hysteresis on the surfaces, and the fourth assignment was to compare these results with previously recorded grain density and roughness data.

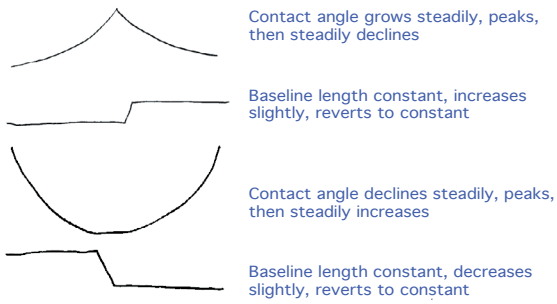

Advancing/receding contact angles vs. baseline lengths vs. time graph definitions

RESEARCH METHOD

Materials

Nine diamond surfaces were used in total throughout the work period. Five surfaces were nanocrystalline, had a thickness range of about 2-3μm, and had diamond grain in the scale of 100nm. The nanocrystalline surfaces were grown with varying concentrations of methane, which affected the grain size. The other four surfaces were two polycrystalline disks, having a thickness of around 180μm and totaling 11mm in diameter. Both sides of the polycrystalline surfaces were used for research; one side was deemed smoother due to being polished mechanically before being sent for this particular research use. The nanocystalline surfaces were signified from al25-al29, and the polycrystalline surfaces sd1u, sd1d, sd2u, and sd2d, respectively.

Procedure

Contact angle measurements were taken using a CAM 100 contact angle machine with a 50mm USB camera. For static contact angle measurements, the metal platform of the machine was adjusted in a manner so that a single water droplet could be lowered onto a sample surface. Producing a single water droplet for static contact angles and a continuous water flux for dynamic contact angles were manipulated using a water syringe suspended above the platform. The syringe was attached to an apparatus on the CAM that would allow for adjustment in height of the syringe

by a winding, spindle-like metal rod. Dynamic contact angle measurements were recorded by adjusting the metal platform so that the water syringe was nearly touching a sample surface. Therefore, the water flux could be better adjusted so that a droplet could grow or shrink for advancing contact angle and receding contact angle measurements, respectively. After taking an image of a single water droplet, camera frames and corresponding data were exported from the CAM software into Microsoft Excel software to plot graphs and chart pertinent data. The same format was followed for multiple images of a water droplet growing or shrinking on a sample surface.

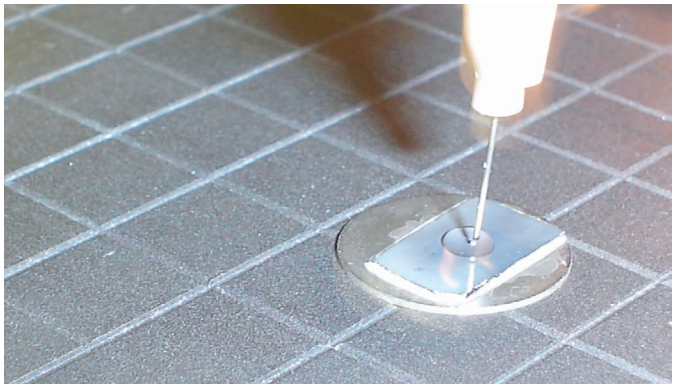

Water syringe placing water droplet on sample surface

ANALYSIS

Generally, advancing and receding contact angle graphs followed the definition described previously. The peaks for contact angles and plateaus for baseline length were observed accordingly. The average range of advancing contact angle measurements for all diamond surfaces was between 70°-89°; the range of advancing baseline lengths averaged between 3.8-5.2mm. The average standard error for advancing contact angles was around ± .394, and the average standard error for advancing baseline lengths was around ± .002. The average range between receding contact angle measurements for all diamond surfaces was between 22°-66°; the range of receding baseline lengths averaged between 4.4-4.28mm. The average standard error for receding contact angle measurements was around ± 2.95, and the average standard error for receding contact angle measurements was around ± .14. The range for static contact angle measurements for all diamond surfaces was between 71°-90°. The range of contact angle hysteresis for all diamond surfaces was quite large, between 8°-74°. The range of grain density for all diamond surfaces was between 7-15μm^{-2}; the range for roughness was between 5.2-41nm.

The grain density and roughness were inadvertently omitted for all the polycrystalline samples except one, surface sd1u, which had a roughness of sample recording of 5.2 nm sans a grain density recording.

Nanocrystalline Surfaces Comparison Chart

	al25	al26	al27	al28	al29	sd1u	sd1d	sd2u	sd2d
roughness of sample(nm)	34	41	28.5	31	28	5.2	N/A	N/A	N/A
grain density of sample(μm) $^{-2}$	7.3	7.5	7	10.6	15	N/A	N/A	N/A	N/A
static contact angles(°)	80	79.2	84	90	74.4	73.3	80.7	71	77
hysteresis of surfaces (°)	30	37	47	35	27	8	15	74	23
avg.adv. (°) contact angle	74	78	72	69	70	73	66	88	89
avg. rec. (°) contact angle	44	46	25	42	57	67	56	22	66

RESULTS/CONCLUSION

Surface sd1u, as shown above, had the lowest recorded measurement for roughness; it also had the lowest recorded measurement out of all the surfaces for contact angle hysteresis (8°). Generally, it was observed that the surfaces with high hysteresis seemed to have high roughness recordings. Surfaces with high roughness recordings also seemed to have high static contact angle measurements.

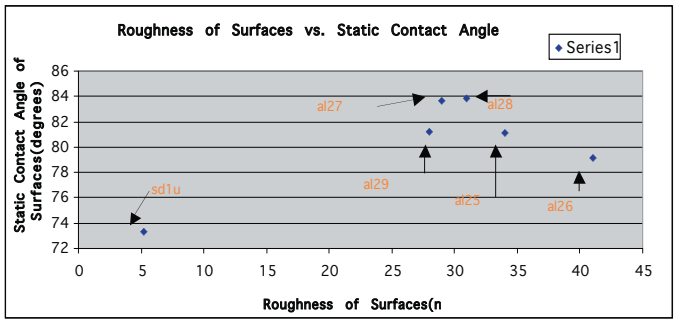

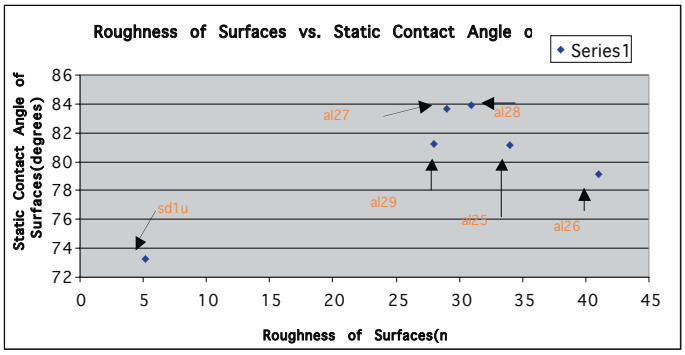

REFERENCES

[1] J. Israelachvili, Intermolecular & Surfaces Forces, Academic Press. 2nd Ed., 2003

ACKNOWLEDGEMENTS

Research support is gratefully acknowledged from the National Science Foundation Center on Materials and Devices for Information Technology Research (CMDITR), DMR-0120967.

Greetings, I am Ariel Bedford, chemical engineering student from Atlanta, Georgia. I attend Florida State University and hope to partake in more research in the nanotechnology sector.

Barium Titanate Doped Sol-Gel for Electro-Optic Devices

Deniz Civay
University of Washington

Nasser Peyghambarian, Robert Norwood, and Chris DeRose
Peyghambarian Lab, Optical Science Center
The University of Arizona

The goal of my research was to successfully dope $BaTiO_3$ nanocrystals into a sol-gel matrix, creating an electro-optic (EO) composite. After poling I determined the EO properties of the composite material. The resulting material exhibits an EO coefficient of 4pm/V however poling conditions are not yet optimized. The advantage of using sol-gel is that the composite material will be photopatternable.

RESEARCH METHODS

I began my research by reviewing relevant literature. The nanocrystals that have had some success in this field are $PbTiO_3$ and $BaTiO_3$. However $PbTiO_3$ and $BaTiO_3$ nanocrystals have not yet been doped into sol-gel. $BaTiO_3$ has a high EO coefficient but its high dielectric constant limits high speed and wide bandwidth operation. The low dielectric constant of sol-gel served to lower the overall dielectric constant of the composite improving the bandwidth of the material. I purchased some $BaTiO_3$ nanocrystals from Sigma-Aldrich and TPL, inc. in order to perform the experiments. The kind of testing that I performed on the $BaTiO_3$ nanocrystal composite films was to determine the EO coefficient and loss.

INTRODUCTION TO THEORY

I am investigating electro-optic nanocomposites because sol-gel is photopatternable. Doping sol-gel with an EO nanocrystal results in a photopatternable EO material. Barium titanate nanocrystals are being used because of the high EO coefficient of 150pm/V. Barium titanate nanocrystals are also easily accessible and cheap.

Some important material properties to consider are the scattering loss, dielectric constant and electro-optic coefficient. The scattering loss is a measure of how much energy is lost from a beam of light passing through a material due to inhomogeneities. See Figure 1 below for an illustration of this phenomenon.

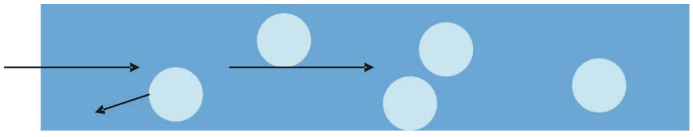

Figure 1. An illustration of scattering loss.

Another important material property is the dielectric constant. The dielectric constant limits operational bandwidth. Ideally the dielectric constant for optical and electrical waves should be matched. The third important material property to consider is the electro-optic coefficient. The electro-optic coefficient is a measure of how much the index of refraction changes with an applied electric field.

Before starting the experimental procedure I used the Maxwell-Garnet Theory to model the scatting loss and composite dielectric constant. The key variables in the Maxwell-Garnet Theory are the nanocrystal radius, the wavelength of the incoming light, the dielectric constant of the nanocrystal and sol-gel, the refractive index of the nanocrystal and sol-gel, and the volume fraction.

CALCULATIONS

The following equations are based on the Maxwell-Garnet Theory.

Equation 1:

$$C_{sca} = (8/3)*[(2*\pi*n_c*r)/(\lambda)]^4*\{[(n_c / n_m)^2-1]/[(n_c / n_m)^2+2]\}^2*\pi*r^2$$

Where:
n_m = index of refraction of the sol-gel = 1.5
n_p = index of refraction of the particle = 2.3
r = average particle radius = 20nm
λ = wavelength of light = 1550nm

C_{sca} = .389657701

Equation 2:

$$\alpha_{sca} = (3*\eta*C_{sca})/(4*\pi*r^3)$$

Where:

η = fill fraction of the spheres in the polymer host = 0-1

Equation 3:

$L_{3db} = 1/ \alpha_{sca}$

Where:

L_{3db} = propagation length for 1/e scattering loss

Equation 4:

$\alpha_{db} = [-10 \log (1/e)]/L_{3db}$

Where:

α_{db} = loss in db/cm

See Table 1 below for the α_{db} and L_{3db} values corresponding to a fill fraction from 0-1 in increments of .02.

n	L_{db} 1550 (cm)	αdb @ 1550 (db/cm)
0	0	0
0.02	0.42978	10.1051
0.04	0.21489	20.2102
0.06	0.14326	30.3152
0.08	0.10744	40.4203
0.1	0.08596	50.5254
0.12	0.07163	60.6305
0.14	0.06140	70.7355
0.16	0.05372	80.8406
0.18	0.04775	90.9457
0.2	0.04298	101.0508

Table 1. α_{db} and L_{db} values corresponding to a fill fraction from 0-.2.

Because the loss values calculated were too high to be useful, a graph of loss versus particle radius was created where three different fill fractions were used. See Figure 1 below.

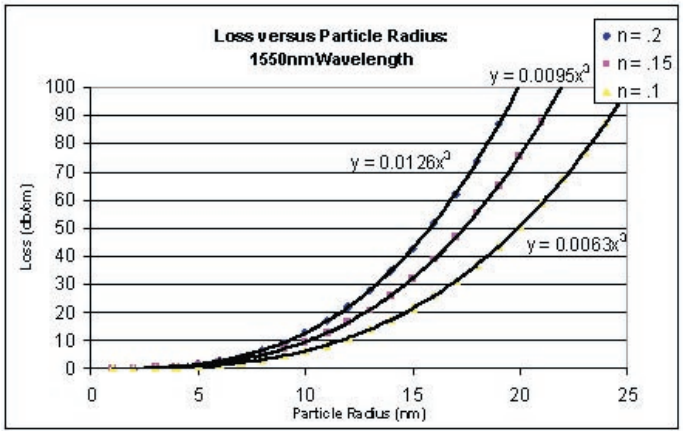

Figure 1. Loss versus particle radius for fill fractions of .2, .15, and .1.

Based on Figure 1 it can be determined that the loss is directly dependent on the fill fraction; the equation for n = .2 is exactly twice the equation for n = .1. A low fill fraction is ideal according to these graphs because it will minimize losses, however a low fill fraction will also reduce the electro-optic effect. A particle radius of 20nm with a fill fraction of .1 would have a loss of 50 dB/cm.

The next relationship analyzed the effect of a small change in refractive index between the matrix and the particle. This was accomplished by graphing the loss versus particle size for an n_m of 1.6, 1.7, 1.8, 1.9, and 2.0. This graph can be seen in Figure 2 below.

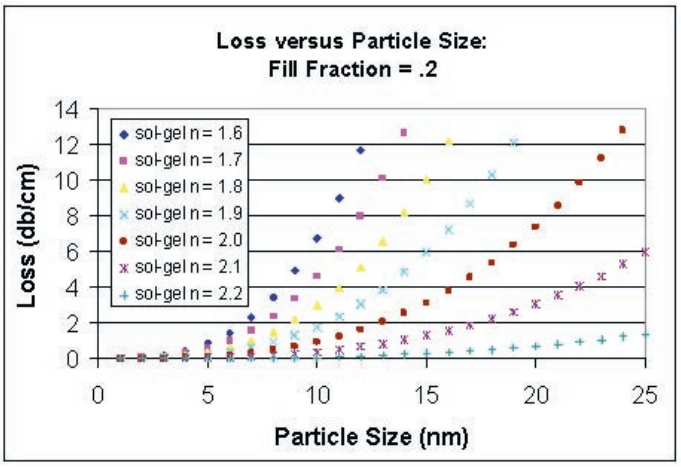

Figure 2. Loss versus particle size for various sol-gel indices of refraction.

By re-graphing one loss value from each line in Figure 2 versus the corresponding sol-gel index it can be determined that the relationship between the difference in refractive index and the loss is governed by the equation $y=172.23x^2-736.12x+790.82$, where x is the n_m. See Figure 3 for an illustration of this equation.

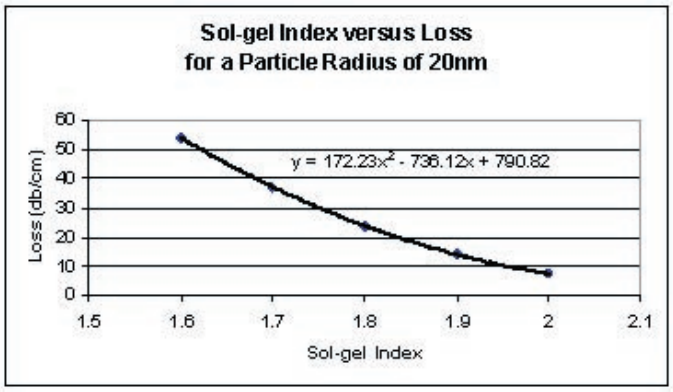

Figure 3. Sol-gel index versus loss.

Based on Figure 3 the index of the matrix needs to be greater than or equal to 1.9 in order to minimize loss. The index of the sol-gel currently being used is 1.5.

Equation 5*:*

$$k' = \frac{v_m * k'_m * [2/3 + k'_p/(3*k'_m)] + v_p * k'_p}{v_m * [2/3 + k'_p/(3*k'_m)] + v_d}$$

Where:

k' = composite dielectric constant

k'_m = dielectric constant of the matrix = 5

k'_p = dielectric constant of the particle = 1525

v_m = volume fraction of the matrix

v_p = volume fraction of the particle

The data for Figure 5 was obtained by varying the volume fraction of the particle from 0 to 1 and setting $v_m + v_p = 1$. According to Figure 4 the relative dielectric constant when the $v_p = .15$ is equal to 7.6.

SUMMARY

- The α_{db} for a fill fraction of .15 with the current assumptions is 75.8 db/cm (useful for Fabry-Perot devices but not waveguides)
- If the sol-gel index was increased to 1.9 the loss would be reduced to 14.2 db/cm
- At a fill fraction of .15 the composite dielectric constant is 7.6
- 5 nm particle radius would result in 1.2 db/cm loss for a .15 fill fraction (useful for waveguide devices)
- The final result is photopatternable

EXPERIMENTAL PROCEDURE

- The corresponding amount of grams for 1 wt%, 5 wt% and 10 wt% barium titanate were measured using the table below.

Wt%	$BaTiO_3$ (g)
1	0.0397
2	0.0803
3	0.1217
4	0.1639
5	0.2070
6	0.2511
7	0.2961
8	0.3421
9	0.3890
10	0.4371
11	0.4862
12	0.5364
13	0.5878
14	0.6404
15	0.6942
16	0.7493
17	0.8057
18	0.8635
19	0.9227
20	0.9834

Table 2. The amount of grams of barium titanate needed for each corresponding weight percent.

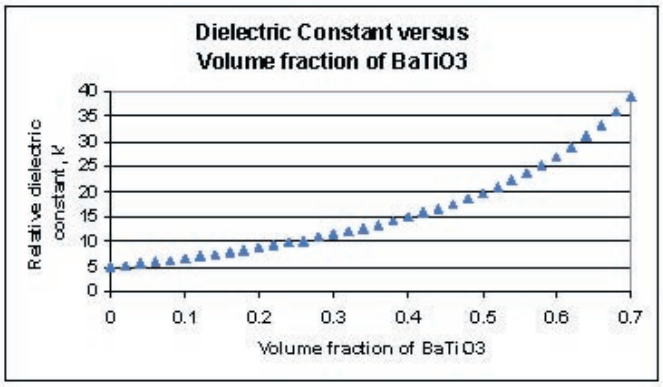

Figure 4. The dielectric constant versus the volume fraction of barium titanate.

- A ratio of 1:20, solute to solvent, was used for 1%. 1% $BaTiO_3$ was dissolved overnight in .8mL of water. A ratio of 1:5.5 was used for 5%: 5% $BaTiO_3$ was dissolved overnight in 1.15mL of isopropyl-alcohol. A ratio of 3.5:1 was used for 10%: 10% BaTiO3 was stirred overnight in 1.5mL of water.
  Note: All solutions appeared equally cloudy and white after stirring for one day.
- The 1% and 5% solutions then had a pre-mixed sol-gel added to it. The sol-gel added to the 10% solution had not yet been formed (the ingredients to form the sol-gel were added directly to the dissolved 10% barium titante). All samples were left to stir for 2 days.
- Each sol-gel solution was spun onto a half-etched ITO slide.
- The samples were then baked at 350 for 1hr.
  Note: The 10% slide looked the worst, then the 1%. The 5% made a decent quality slide. This difference is most likely due to the alcohol solvent and the fact that the sol-gel was added after it had been mixed.
- After making films containing 1%, 5% and 10% barium titanate an easy way to determine if the calculated loss agrees with the actual loss is to test the samples with a spectrophotometer. By using a spectrophotometer the actual loss will be recorded for various wavelengths. The data can then be compared to Figure 5.

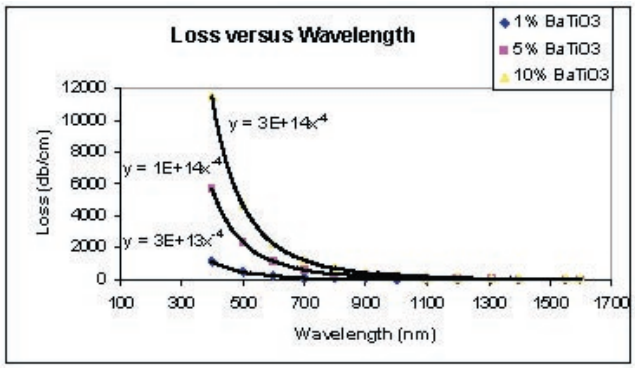

Figure 5. Loss versus wavelength for three different fill fractions.

RESULTS

The absorptivity versus the wavelength for 1 wt%, 5 wt% and 10 wt% of barium titanate was determined using a spectrophotometer. The theoretical and the experimental data do not appear to have any correlation other than a general shape; the trendlines from Figure 5 do not fit Figure 6.

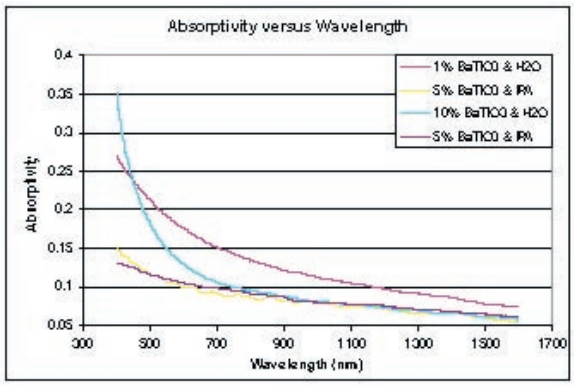

Figure 6. Absorptivity versus wavelength for three different fill fractions.

A possible explanation for the discrepancy between Figure 5 and Figure 6 is film quality. Because the spectrophotometer only analyzes a small portion of the sample and the 10 wt% was of poor quality, it is possible that the section analyzed did not contain any of the $BaTiO_3$/sol-gel. It is also possible that the barium titanate/water solution was not homogeneous.

Because the 5 wt% sample turned out the best I decided to do the simple reflection test on it to determine the electro-optic coefficient. There wais some electro-optic activity; however the numbers were very low. A common problem was the gold electrode peeling off of the sample. In the case where an R_{33} of 38.2 was achieved the gold was damaged. See Table 3 below.

BaTiO3 (g)	Solvent (mL)	Voltage (V)	Held for (min)	Temperature (°C)	R_{33}
0.22	1.15	200.00	3.00	150.00	1.40
0.22	1.15	200.00	3.00	160.00	OL
0.22	1.15	200.00	4.00	150.00	4.00
0.22	1.15	150.00	4.00	160.00	2.00
0.22	1.15	100.00	5.00	150.00	38.2*
0.22	1.15	100.00	3.00	150.00	0.20

Table 3. 5 wt% $BaTiO_3$ in IPA. *Irregular modulation curve.

WORK IN PROGRESS

- I have recalculated the amount of $BaTiO_3$ according to volume percent rather than weight percent to see if that is a more accurate description of the fill fraction.
- Rather than using IPA or water as the solvent I am now using a mild acid, .1N HCl, which the barium titanate is somewhat miscible in: However after one day in the refrigerator the solution separated.
- We now have two new solutions that have been spun and baked and are almost ready to be tested. One solution contains .21g of barium titanate and .4mL of HCl. The $BaTiO_3$ was added to the amount of HCl required for making the sol-gel. The second solution contained .43g of barium titanate mixed into 1.5mL of HCl, and then added to the sol-gel. The first solution is the only one that looks testable.
- In order to prevent the gold from peeling I am soft baking the film and then corona poling it at 150 degrees Celsius for 2 hours with 4kV applied. The gold will be sputtered after poling is complete.

ACKNOWLEDGEMENTS

Research support is gratefully acknowledged from the National Science Foundation Center on Materials and Devices for Information Technology Research (CMDITR), DMR-0120967.

Deniz Civay will be graduating from the University of Washington in December with a BS in materials science engineering. She then plans to pursue her PhD.

Synthesis of Norbornene Monomer of PPV-C_{60} Dyads (TDC-I-056)

Taína D. Cleveland
Georgia Institute of Technology

Dr. Jian-Yang Cho (JD) and Dr. Seth Marder
School of Chemistry & Biochemistry
Georgia Institute of Technology

INTRODUCTION

As the need for a renewable, clean energy source is expanding, a promising technology based on organic or polymeric materials may offer a lightweight, flexible, cost-effective renewable solar energy solution.[1] Conducting polymers like PPV (poly(1,4-phenylenevinylene)) functioning as donors and C_{60} derivatives as acceptors have been widely used for photovoltaic cell applications. However, composite films made by mixing PPV and C_{60} usually leads to phase separation because C_{60} tends to form crys tals which makes the donor and acceptor molecules incompatible in composite films. It results in poor homogeneity and low optical quality of the films leading to inefficient intramolecular and intermolecular energy or electron transfer in solar cells.

OBJECTIVE OF THE RESEARCH PLAN

The objective of this investigation is to synthesize polymeric materials where donors and acceptors are covalently linked to polymer backbone, which presumably can avoid phase separation problems. In addition, these polymeric materials can be dissolved in common organic solvents, "wet" methods such as spin coating can be used for device fabrication.

Most PPVs have wide molecular weight distribution, making them less applicable to control morphology in the solid. A synthetic procedure for the preparation of PPV reported by Kretzschmann and Meier[2] is adopted in this research plan because the synthesized PPV shows low polydispersity index (PDI).

RESEARCH METHODS

The research plan will be approached through organic syntheses followed by characterization of organic products in each step. The first step of the synthesis follows a Williamson ether synthesis. The second step involves formylation of an aromatic compound. The third step is a condensation reaction to form an imine. The fourth step is a poly-condensation reaction where potassium tert-butoxide is used. The fifth step is to regenerate the aldehyde through the hydrolysis of imine. The sixth step is the reduction of the aldehyde to a primary alcohol. The seventh step combines PPV, C60 and a polymerizable norbornene moiety to yield a norbornene-containing PPV-C60 dyads. The eighth step follows Williamson ether synthesis. A proposed synthetic scheme is shown in Figure 1.

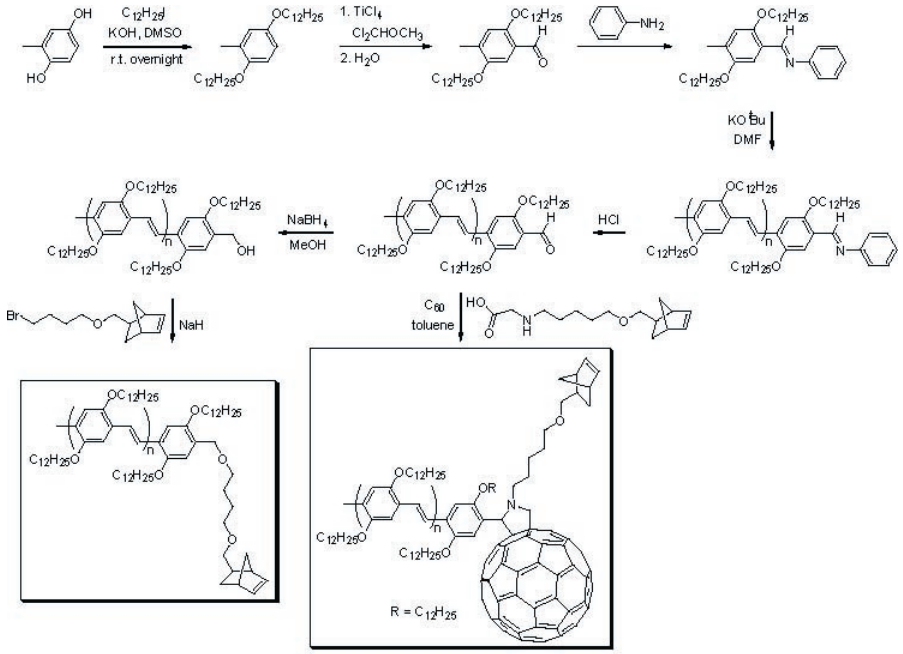

Figure 1. Proposed synthetic scheme for preparation of ROMP monomers.

SYNTHESIS

Synthesis of 1,4-bis(dodecyloxy)-2-methyl-benzene (TDC-I-001).

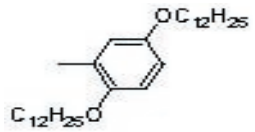

A mixture of 1-iodoundecane (101.0g, 0.34 mol), 2-methylbenzene-1,4-diol (10.47 g, 0.08 mol), and potassium hydroxide grinded pellets (37.88 g, 0.67 mol) in 200 mL of DMSO was stirred at room temperature for 1 day. The reaction mixture was poured into H2O and extracted with methylene chloride. The organic layer was washed with water (3 X 300 mL) and dried over magnesium sulfate. Excess of solvent was remove under reduce pressure. The crude product was recrystillized from hot ethanol to give white solid. A second crop was further purified using charcoal to eliminate undesired brown color (38.64 g, 99.48%). 1H NMR (300MHz, CDCl3 δ): 6.60-6.72 (m, 3H), 3.87 (t, J = 6.3 Hz, 2H), 3.86 (t, J = 6.6 Hz, 2H), 2.18 (s, 3H), 1.67-1.80 (m, 4H), 1.20-1.46 (m, 39H), 0.86 (t, J = 6.8 Hz, 6H).

Synthesis of 2,5-bis dodecyloxy-4-methyl-benzaldehyde (TDC-I-020).

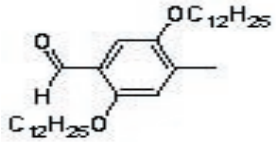

A Schlenk tube was charged with 1,4-bis-dodecyloxy-2-methyl-benzene (TDC-I-001, JYC-VI-044, JYC-VI-0046) (36.66 g, 79.5 mmol). The Schlenk tube was evacuated and refilled with N_2. Under a nitrogen counterflow, add 50 mL of dry CH_2Cl_2. The reaction mixture was allowed to cool down to 0°C in an ice bath. Titanium tetrachloride (17.4 mL, 0.15 mol) was added dropwise using a syringe. α,α- dichloromethyl methyl ether (98%) (7.1 mL, 0.027 mol) was added dropwise via a syringe. Hydrogen chloride gas was generated and neutralized with 10% solution of NaOH. The reaction was stirred at 0°C for an hour. The reaction mixture was poured into ice and H_2O. The aqueous layer was adjusted to pH~7. The organic layer was extracted with dichloromethane and dried over magnesium sulfate. Excess of solvent was removed under reduce pressure. The crude product was recrystallized from hot hexanes to give light brown solid (33.83 g, 87.0%). Proton NMR indicates the presence of isomer mixture of 3,6-bis-dodecyloxy-2-methylbenzaldehyde and 2,5-bis-dodecyloxy-4-methyl-benzaldehyde in 9:1 ratio. The crude product was purified by repeated column chromatography (three times) (silica gel, hexanes:dichloromethane = 7:3) to give pale yellow solid (21.17 g, 54.4%). 2,5-bis-dodecyloxy-4-methyl-benzaldehyde. 1H NMR (300 MHz, $CDCl_3$ δ): 10.39 (s, 1H), 7.20 (s, 1H), 6.77 (s, 1H), 4.01 (t, J = 6.3 Hz, 2H), 3.94 (t, J = 6.3 Hz, 2H), 2.25 (s, 3H), 1.71-1.83 (m, 4H), 1.24-1.57 (m, 36H), 0.86 (t, J = 6.6 Hz, 6H). HRMS-EI (m/z): M^+ calcd for $C_{32}H_{56}O_3$, 488.42295; found, 488.42373.

Synthesis of (E)-N-(2,5-bis(dodecyloxy)-4-methyl benzylidene)aniline (TDC-I-026).

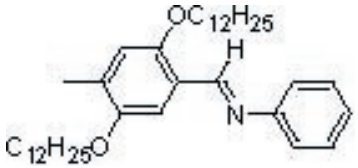

A mixture of 2,5-bis-dodecyloxy-4-methyl-benzaldehyde (TDC-I-020) (15.73 g, 0.03 mol), freshly distilled aniline (2.92 mL, 0.032mol), 250 mL of ethanol, and 40 mL of benzene. A Dean-Stark and condenser were used to remove water generated in the reaction and shift the reaction to completion. The reaction mixture was refluxed at 95°C for 2 days. Excess solvent were remove under reduce pressure. The crude product was recrystallized from hot hexanes and charcoal was added to discolor the solution. The crude product was off-white solid (16.08 g, 88.6%). ^{1}H NMR (300 MHz, C_6D_6, δ): 9.31 (s, 1H), 8.15 (s, 1H), 7.34-7.35 (m, 2H), 7.15-7.21 (m, 2H), 6.97-7.01 (m, 1H), 6.68 (s, 1H), 3.78 (t, J = 6.6 Hz, 2H), 3.70 (t, J = 6.3 Hz, 2H), 2.35 (s, 3H), 1.57-1.66 (m, 4H), 1.20-1.40 (m, 36H), 0.92 (t, J = 6.6 Hz, 6H). ^{13}C{^{1}H} NMR (75 MHz, C_6D_6, δ): 156.24, 153.93, 152.22, 132.41, 129.41, 128.32, 127.99, 127.67, 125.63, 123.93, 121.42, 116.08, 109.27, 69.43, 68.38, 32.31, 30.10, 30.03, 29.99, 29.80, 29.77, 29.74, 29.66, 26.45, 23.09, 17.19, 14.35.

Synthesis of PPV (TDC-I-042).

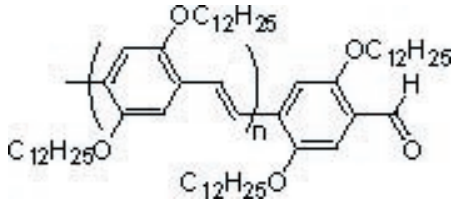

A Schlenk tube was charged with (E)-N-(2,5-bis(dodecyloxy)-4-methylbenzylidene)aniline (TDC-I-026) (4.5 g, 7.9 mmol). The Schlenk tube was evacuated and refilled with nitrogen. Under counterfolw of nitrogen 50 mL of dry DMF were added, and potassium tert-butoxide (1.79 g, 16 mmol). The reaction mixture was refluxed at 90°C for 3 days. The reaction mixture was monitored through UV-VIS. The reaction mixture was treated with HCl to neutralize the potassium tert-butoxide. An orange solid was recovered and it was washed with water, ethanol and acetone. The crude product was fluorescence. Proton NMR indicates that

the reaction had not reached completion, because of the presence of imine in the region of 9.3 ppm. Excess of HCl was added to mixture of crude product and methanol, to complete the hydrolysis of imine to an aldehyde. The polymeric product was again collected by vacuum filtration, washed with water, ethanol, and acetone, and dried under vacuum to give an orange solid (3.42 g). Based on proton NMR integration indicates n equals to 13 which is consistent to the reported value in literature (n = 13).

Synthesis of Norbornene monomer of PPV-C_{60} dyads (TDC-I-056).

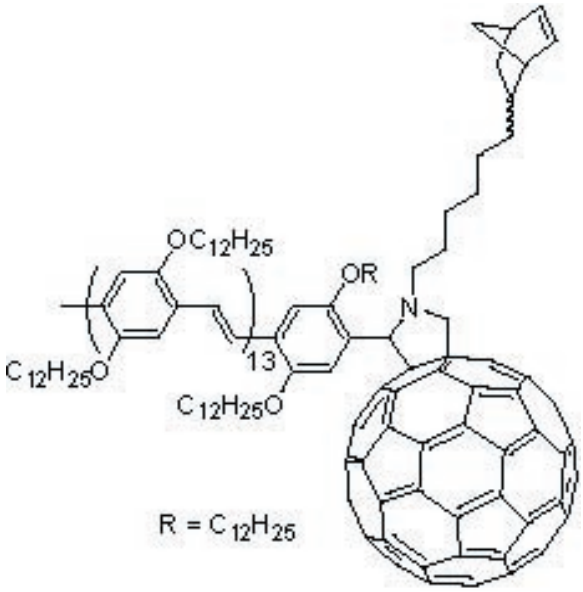

A Schlenk round bottom flask (500 mL) was charged with PPV (0.71 g, 0.1 mmol), (6-bicyclo[2.2.1]hept-5-en-2-yl-hexylamino)-acetic acid (51 mg, 0.2 mmol), C_{60} (72.4 mg, 0.1 mmol), and dry toluene (100 mL). The reaction mixture was refluxed at 120 °C overnight. Excess of solvent was remove under reduced pressure. Methanol was added reaction mixture and a dark brown solid was collected by vacuum filtration. ^{1}H NMR spectrum of the dark brown solid shows the disappearance of aldehyde resonance. The dark brown solid did not show fluorescence properties.

ACKNOWLEDGEMENTS

Research support is gratefully acknowledged from the National Science Foundation Center on Materials and Devices for Information Technology Research (CMDITR), DMR-0120967.

Development of Efficient Two-Photon Radical Initiators and Low Shrinkage Materials

Amanda Cooper
Georgia Institute of Technology

Takashi Okada and Seth Marder
Marder Lab, School of Chemistry and Biochemistry
Georgia Institute of Technology

INTRODUCTION

The development of highly efficient two-photon induced radical initiators and the development of low shrinkage polymers for use in 3-D microfabrication are two areas of current interest in the field of photonics. An efficient form of two-photon radical initiators that has been developed involves a dye unit that is connected by a bridge to an initiator (Structure A). We propose that this molecule can be made more efficient by introducing electron donating groups to the dye unit thereby making the unit more electron rich (Structure B). By creating a more electron rich dye unit, the overall difference between the LUMO of the excited dye and the initiator is increased. An increase in the difference leads to a greater rate of electron transfer.

Efficient low shrinkage materials for 3-D microfabrication need to exhibit two characteristics: a minimal loss in volume during cross-linked polymerization and good solubility in organic solvents of the non-cross linked material. Currently in the area of low shrinkage materials, units that polymerize by chain polymerization have been found to lose around 1-5% volume mass in the polymerization reaction. This loss of volume mass, we believe, can be reduced to nearly 0% by using a ring opening reaction as opposed to a chain linking reaction. This can be achieved by attaching an epoxide or oxetane group, which can then be initiated to cross-link (Structure C). To maximize the solubility in organic solvents, it has been proposed to use single molecules that are capable of cross linkage as opposed to polymers. This minimizes the additional interactions at sites on the molecule that are not related to the cross linkage.

EXPERIMENTAL FOR TWO PHOTON RADICAL INITIATOR

1) 2,5-bis(chloromethyl)-1,4-dimethoxybenzene

1, 4-dimethoxybenzene (27.6g, 0.20 mol), paroformaldehyde (18.1g, 0.60 mol), acetic acid (330 mL) and HCl (600 mL) were combined and stirred for five minutes. The reaction was then sonicated for one hour. The resulting solid was filtrated and washed several times with water. The crude product was recrystallized with acetone and methylene chloride. The pure product was dried to yield a white solid (13.5g, 28.7%).

2) tetraethyl-1,5-bismethoxyl-p-xylene phosphonate

2,5-bis(chloromethyl)-1,4-dimethoxybenzene (13.5g, 0.057 mol) and triethylphosphite (115 mL,) were combined and refluxed overnight. The reaction was cooled to room temperature. An equal amount of hexane was added and the mixture was stirred for 25 minutes. The product was filtrated and washed several times with hexane. The product was dried and a white solid was collected (22.9g, 90.8%).

3) diethyl 4-{(E)-2-[4-(dibutylamino)phenyl]ethenyl} -2,5-dimethoxybenzylphosphonate

Tetraethyl-1,5-bismethoxyl-*p*-xylene phosphonate (15.6g, 0.035mol) and 4-N,N-dibutylaminobenzaldehyde (6.00g, 0.039mol, 91%pure) were added together in anhydrous THF (300mL). The reaction mixture was cooled to 0°C. After one hour, tBuOK(1M, 23.4mL) was added. The reaction ran overnight. The reaction was quenched with water (121mL) and the

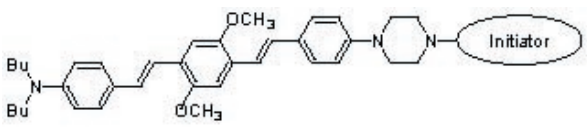

Structure A

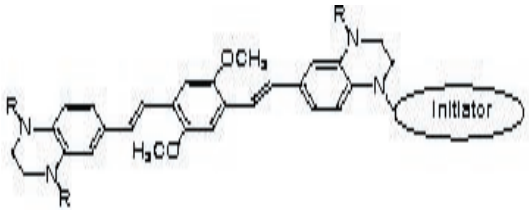

Structure B

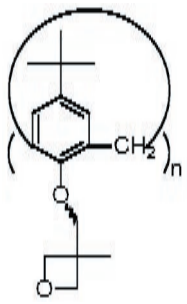

Structure C

product was extracted three times with EtOAc and then washed three times with water. The organic layer was dried. The solid product was purified by column chromatography using EtOAc as the eluent. The purified product was dried and a bright yellow solid was collected (7.15g, 50.0%).

4) 4-piperazinobenzaldehyde

Piperazine (20.8g, 0.242mol) was added to a solution of K2CO3 (11,3g, 0.082mol) in 30mL DMSO. The reaction set to reflux under nitrogen. Once the reflux temperature was reached, 4-fluorobenzaldehyde (8.5mL) in DMSO (10mL) was added. The reaction was refluxed overnight. Water was added (1150mL) and the solid product was filtered (9.02g, 58.9%).

5) 4-N-t-butoxycarbonyl-N'-(p-formylphenyl)piperazine

4-piperazinobenzaldehyde (9.02g, 0.047mol) was dissolved in anhydrous DCM (112mL) under nitrogen. The solution was cooled to 0°C. After 20 minutes, triethylamine (6.6mL, 0.047mol) and di-t-butyldicarbonate (10.8mL, 0.047mol) was added. The reaction was allowed to warm to room temperature and left overnight. The reaction mixture was washed three times with water and dried. No product was obtained.

6) N-(4-{(E)-2-{4-[4-(1-t-butoxycarbonyl)piperazin-1-yl]phenyl}ethenyl}-({[2,5-dimethoxyphenyl]ethenyl}phenyl)-N,N-dibutylamine

Diethyl 4-{(E)-2-[4-(dibutylamino)phenyl]ethenyl}-2,5-dimethoxybenzylphosphonate (7.15g, 0.014mol) and 4-N-t-butoxycarbonyl-N'-(*p*-formylphenyl)piperazine (4.01g, 0.014mol) were added together in anhydrous THF (160mL). The mixture was cooled to 0°C. After 20 minutes, tBuoK (1M, 14.5mL) was added. The reaction was run overnight. The reaction was quenched with water (130mL). The product was then extracted with EtOAc and washed several times with water. The organic layer was dried. A column was run to purify the product using hexane:EtOAc (5:1) as an eluent. The purified product was dried and a bright yellow solid was collected (6.07g, 66.4%)

7) 4-N,N-(2,5-dimethoxy-4-{(E)-2-[4-piperazin-1-ylphenyl]ethenyl}ethenyl)aniline

N-(4-{(E)-2-{4-[4-(1-t-butoxycarbonyl)piperazin-1-yl]phenyl}ethenyl}-({[2,5-dimethoxyphenyl]ethenyl}phenyl)-N,N-dibutylamine (6.07g, 0.0093mol) was dissolved in THF (200mL). HCl (2M, 60mL) was then added and the reaction was heated to reflux. After four hours, the reaction was allowed to cool to room temperature and left overnight. NaOH (2M, 65.6mL) was then added. The product was extracted with ether:DCM (8:2) and then dried. Product was found to contain very few impurities, but will be further purified before yield is determined.

EXPERIMENTAL FOR LOW SHRINKAGE OLIGOMER

1) p-t-butyl-calix[8]arene

Paraformaldehyde (17.5g, 0.55mol), *p*-t-butylphenol (50.0g, 0.33mol), and NaOH (10M, 1mL) were added together in xylene (300mL). The reaction was heated to reflux. The reaction was left overnight and refrigerated for several hours, but no product formed.

2) (1-bromo)butyl-(2-[3-oxetane])propyl ether

1,4 dibromobutane (78.7mL, 0.58mol), 3-methyl-3-oxetane methanol (20.0g, 0.20mol), NaOH (23.5g, 0.60mol), and TBAB (1.26g, 0.020mol) were added together in hexane (200mL) and water (100mL). The reaction was heated to reflux and left overnight. The product was extracted with hexane and washed with water. The organic layer was dried, leaving a pale brown liquid. The liquid was distilled using a full vacuum twice, but the product could not be purified.

3) octakis(t-butyl)-octakis[2-(3-oxetane)propyloxy] butoxycalix[8]arene

P-t-butyl-calix[8]arene (0.500g, 0.00061mol), K2CO3 (1.34g, .0098mol), and KI (0.563g, .0033mol) were added together in anhydrous DMF (15mL). The reaction was heated to 100°C. (1-bromo)butyl-(2-[3-oxetane])propyl ether (2.60g, 0.0098mol) in anhydrous DMF (10mL) was added dropwise. The reaction was left overnight. No product formed.

CONCLUSIONS AND OUTLOOK

The synthesis of the donor portion of the two photon radical initiator is nearly complete. The final crude product will be purified through recrystallization and the yield will be determined. The pure product will then attached to an acceptor molecule consisting of a fluoro-substituted triphenyl sulfur compound. The resulting molecule will then be tested for its ability as a two photon radical initiator using UV-vis spectrometry. We believe that the molecule will absorb at a high peak wavelength, which will indicate a large amount of energy dissipated upon irradiation.

The synthesis of the oligomer did not present any yield in any of the steps. For the first synthesis, a possible explanation is that the reaction is an equilibrium reaction with water as a by-product. In order to drive the reaction to completion, water must be removed. This was not done the first time, so the synthesis will be repeated using a Dean-Stark trap to remove water from the reaction mixture. The purification of the second synthesis will be reattempted, and the temperature during the vacuum distillation will be monitored more closely. After the first two products have been obtained, the third experiment will be reattempted

using different reaction conditions, specifically a different base. Once the final oligomer has been synthesized, it will be tested for volume shrinkage during crosslinking. The irradiated film will then be treated with organic solvent and the solubility of the oligomer will be tested.

Future research will focus on the synthesis of other potential efficient two photon radical initiators and low shrinkage materials. The results of the efficiencies of the products will be tested and compared to one another. Once we obtain an efficient radical initiator and low volume shrinkage material, the products will be synthesized on a large scale and distributed to various research groups to be used for experiments in other fields of photonics.

ACKNOWLEDGEMENTS

Research support is gratefully acknowledged from the National Science Foundation Center on Materials and Devices for Information Technology Research (CMDITR), DMR-0120967.

Synthesis of Nonlinear Optical-Active Materials

Dan Daranciang
Washington University in St. Louis

Donald Responte and Werner Kaminsky
Department of Chemistry
University of Washington

INTRODUCTION

Since the first observation of second harmonic generation (SHG) in 1961 by Franken, multiple nonlinear optical materials have been characterized and studied. Franken irradiated quartz with 694 nm light, and to his surprise, he detected emitted photons at 347 nm, half the original wavelength and therefore twice the energy of the incoming photons. This singular observation, the result of a second order phenomenon involving the absorption of two photons, spawned a new classification of materials: nonlinear optical (NLO) materials. NLO materials promise to have great utility in developing tomorrow's technology. Taken together, the sheer quantity and variety of NLO effects that have been observed allow us to harness the properties of light in exciting and unexpected ways. Photonics-based technology sees use today in everything from pulse measurement devices to fiber optics.

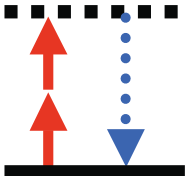

Figure 1. Schematic of SHG. Two photons of wavelength λ (red) are absorbed to reach a "virtual" excited state. A single photon at λ/2 (blue) is emitted.

While many such materials have been discovered (two examples are $KTiO_4$ and KDP, potassium dihydrogen phosphate), a great deal of work remains. For one, though the "classic" examples of NLO materials have certainly been proven SHG active, experimentation we have performed shows that other compounds can have even larger SHG efficiencies. In addition, the current example of chromophores has recently attracted much experimental interest, but these compounds are difficult to synthesize, involve lengthy reaction sequences, and afford increasingly smaller percent yields at each step.

We proposed this summer to synthesize and characterize by X-ray diffraction and SHG emission experiments a certain class of materials, *i*-butyl-*N*-phenyl thiocarbamates. Through this work, we hypothesized that we could lay out a basis for the simple, rational synthesis and design of NLO active materials, which demonstrated significant activity compared to the compounds currently in wide use.

METHODS

The key characteristic of all NLO active materials is seen in their packed lattice geometry. In order to exhibit second-, third-, or *n*th-order optical effects, the unit cell of the material must be *non-centrosymmetric*. Otherwise, upon excitation of the material, dipole-dipole vibrations occur in equal magnitude but opposite direction, and therefore cancel each other out. Another consideration in our design was how to ensure that our products, in addition to being NLO active, could potentially have photonics applications. We decided to use aromatic functional groups in our products. Aromatic rings contain regions of high π-electron density, which would give our compounds the ability to readily transfer charge.

With this in mind, we chose to study the reaction of aryl isothiocyanates with (*S*)-2-butanol. (*S*)-2-butanol is a relatively low molecular weight chiral ligand with only one possible nucleophilic reaction, and therefore its product with a substituted aryl isothiocyanate is easily predictable. Since it is chiral, the product would have a chiral carbon center, and we were therefore assured that the unit cell of the product could not have a center of symmetry.

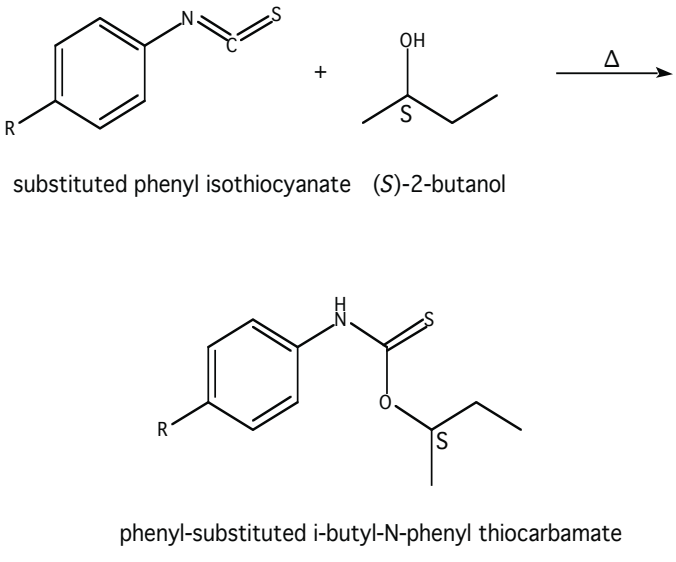

Figure 2. The reaction of aryl isothiocyanates with (*S*)-2-butanol. When R = EWG, the isothiocyanate undergoes electrophilic attack at the cumulene carbon, affording the phenyl-substituted *i*-butyl-*N*-phenyl thiocarbamate. The geometry at the indicated carbon on the butanol is preserved.

Aryl isothiocyanates were selected because of their molecular features. The aromatic ring provides a high number of mobile electrons, which was key for potential nonlinear optical applications. Unlike thiocyanates (the –S=C=N linkage), *iso*thiocyanates feature a –R=S linkage, which builds out selected hydrogen bonds, structures molecular packing, and enhances crystal growth. In addition, the sulfur atom scatters well, allowing absolute X-ray structure determinations (XRD). The crystalline nature of these products made for easy characterization by XRD.

To study the feasibility of using this reaction to obtain crystals, racemic 2-butanol was used to test the reaction with a variety of aryl isothiocyanates, many of which had an electron-withdrawing group (EWG) at the *para* position: phenyl isothiocyanate, 4-fluorophenyl isothiocyanate, 4-chlorophenyl isothiocyanate, 4-bromophenyl isothiocyanate, 4-nitrophenyl isothiocyanate, and 3-chlorophenyl isothiocyanate. We then performed a second reaction with the costlier (*S*)-2-butanol to obtain the non-centrosymmetric structure.

The reaction involved mixing or dissolving the isothiocyanate in 2-butanol with the aid of vortexing. The reaction mixture was heated in a sand bath at about 110° C for 3 h, then allowed to cool to room temperature. Crystals were grown by slow evaporation of the solvent.

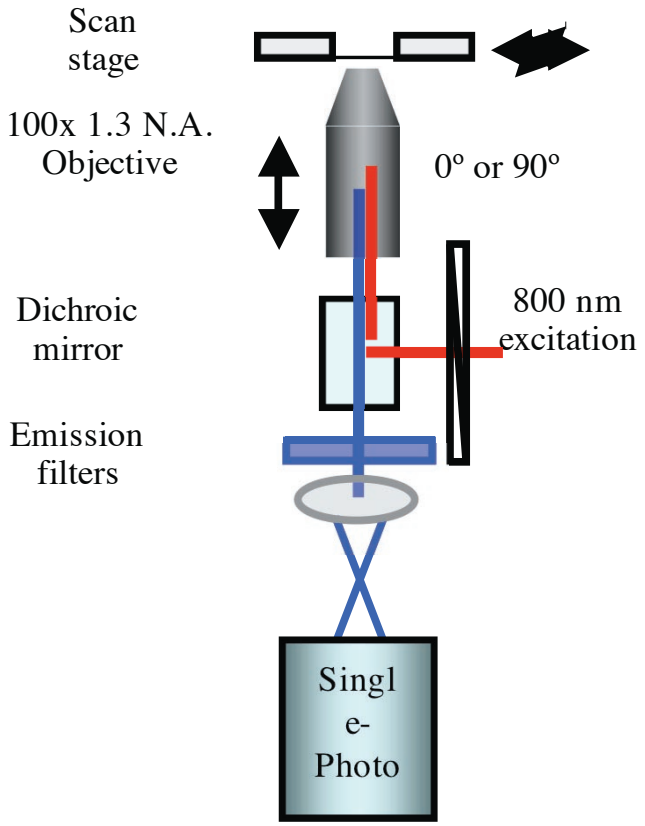

Figure 3. SHG microscope diagram. Light of 800 nm wavelength is pulsed onto the sample (P = 1 or 2 mW) and the number of emitted 400 nm photons is recorded by the single-photon photomultiplier tube.

In order to "get an idea" of our compounds' NLO activity, we decided to subject powder forms of our compounds to an SHG activity test using a SHG microscope (Figure 3), with two standards: KAP and KDP.

Using a powder form was a step we took to minimize the orientation dependence of SHG in crystals. It was also easier to obtain a powder than to grow crystals of acceptable size and purity for other studies. The scan area was (20 μm)^2 with a step size of 1 μm, and we measured the average SHG counts (emitted photons of half the wavelength of the incoming photons) over each area, omitting areas that did not achieve significant SHG activity. These averages were compared to give rough relative activity determinations.

RESULTS

We succeeded in synthesizing and characterizing two target compounds: *i*-butyl-*N*-(4-nitrophenyl) thiocarbamate (Fig. 4) and *i*-butyl-*N*-(4-chlorophenyl) thiocarbamate (Fig. 5). Crystalline products were obtained for the other reactions we attempted (in particular, the 4-bromophenyl isothiocyanate, 4-fluorophenyl isothiocyanate, and 3-chlorophenyl isothiocyanate with (*S*)-2-butanol), but unfortunately, due to time constraints, these were not characterized. The quality of the XRD structures was excellent in most cases. As expected, the products were chiral, which the space groups confirmed.

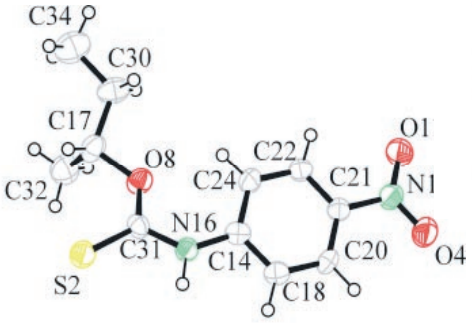

Figure 4. *i*-butyl-*N*-(4-nitrophenyl) thiocarbamate XRD structure. Space group: P 21.

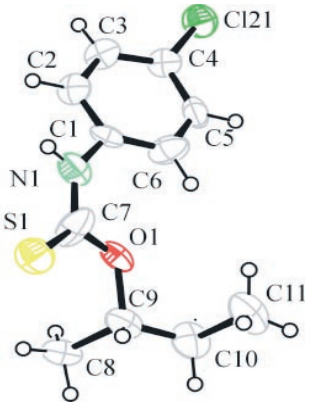

Figure 5. *i*-butyl-*N*-(4-chlorophenyl) thiocarbamate XRD structure. Space group: P 21.

When we attempted to form *i*-butyl-*N*-phenyl thiocarbamate, we were surprised to obtain a previously unseen product (according to searches of the Cambridge Structural Database and SciFinder) containing seven phenyl rings (Fig. 7).

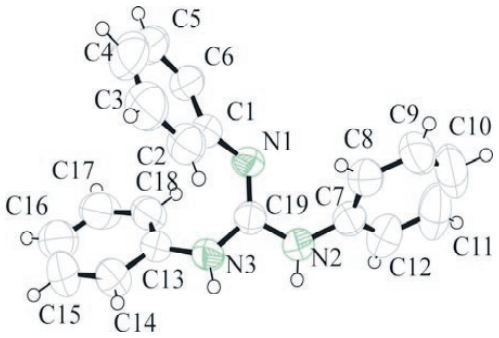

Figure 7. $Ph_7N_7C_3H_2$•PhNCS•C_6H_6 XRD structure. Space group: P 21/c.

It is heavily conjugated and also chiral, and therefore predicted to have nonlinear optical activity. However, its crystals were not large enough to perform SHG studies on. In addition, attempts to replicate this synthesis have met with failure, giving the less complex three-ringed compound: triphenylguanidine (Fig. 8).

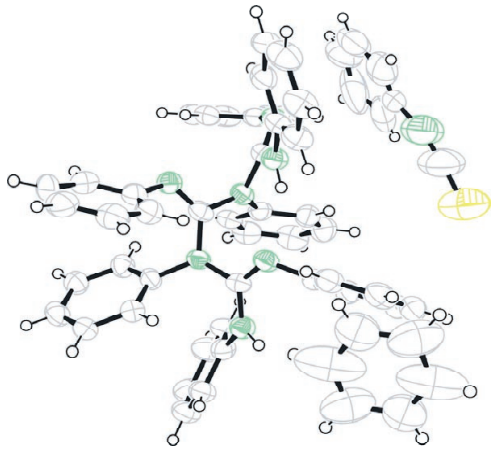

Figure 8. Triphenylguanidine XRD structure. Space group: P na 21.

We were not discouraged by the failure to obtain the predicted product. On the contrary, due to this unexpected discovery, we were able to characterize triphenylguanidine by SHG, and it gave counts four times as large as KDP and six times as large as KAP, two far better-known NLO materials. We believe that prolonged heating caused an overreaction—the thiocarbamate was probably formed, but went on to react with other phenyl isothiocyanate units.

Raster images of the powder forms of the crystals revealed unmistakable inhomogeneities in the crystals, which limited our ability to find a meaningful average. Therefore, our reported averages only consider those areas where high SHG intensity was observed. Despite this limitation, we did obtain average SHG counts of KAP, KDP, triphenylguanidine, and 4-chlorophenyl isothiocyanate powder samples in the method described previously. KAP and KDP were our two standards, and 4-chlorophenyl isothiocyanate was a negative control. As previously stated, triphenylguanidine was highly active relative to our standards.

CONCLUSIONS

Triphenylguanidine shows high SHG activity relative to KDP and KAP, but further characterization of the thiocarbamates is needed. There is still much work to do toward developing a strong theoretical understanding of what gives rise to the SHG activity of these compounds. We have already attempted to react other chiral nucleophilic ligands with the aryl isothiocyanates, such as methylbenzylamine and *l*-menthol, and some of these crystal products currently await characterization. Many optical properties of this family of compounds remain unexplored.

As a whole, the research lays out a basis for the rational design of NLO active materials. The understanding to be gleaned from this series of experiments should shed additional light on this fascinating problem.

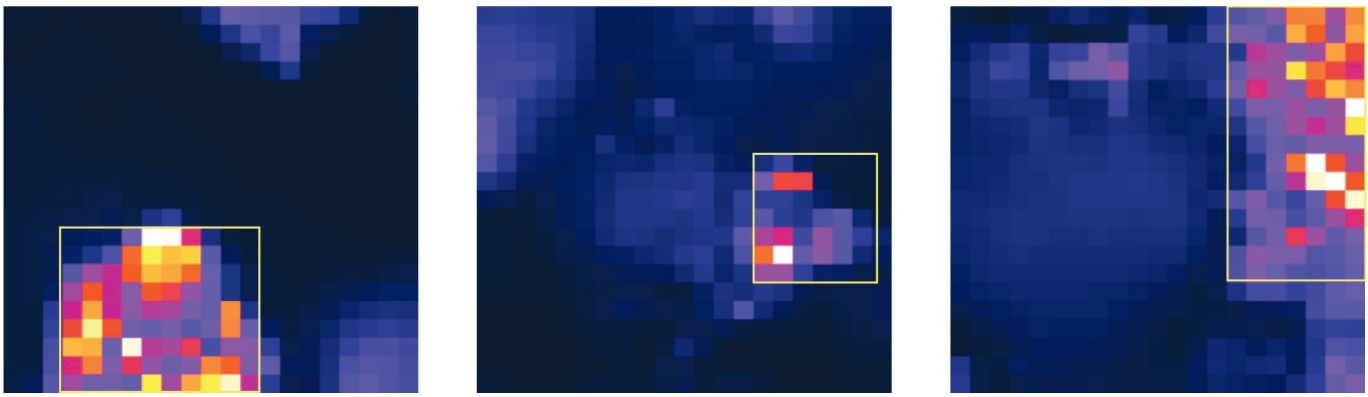

Figure 9. From left to right, (20 μm)^2 raster images of KAP, KDP, and triphenylguanidine powder with a step size of 1 μm (P = 2 mW). Even at this small scan size, observed SHG intensity is not constant. The boxed yellow area in each image is the area where the averages in Fig. 10 are taken from.

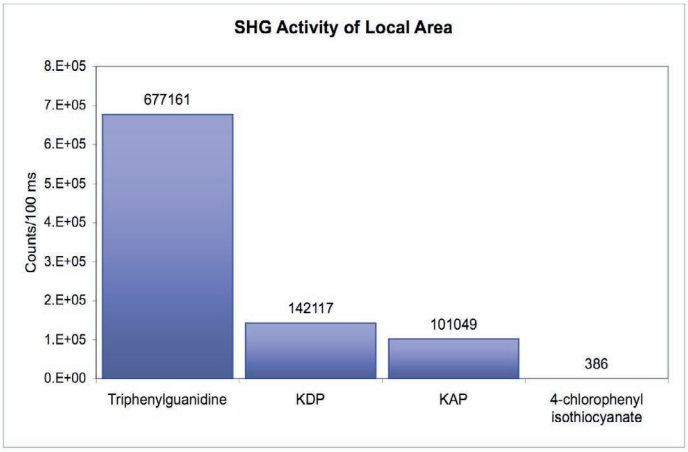

Figure 10. Average SHG counts/100 ms for powder samples over the boxed areas in Fig. 9.

REFERENCES

1. Bauman, R. *J. Eng. Chem. Data* 1966, *11,* 274-276.

2. Kaminsky, W.; Fitzmaurice, A.; Glazer, A. *J. Phys. D.: Appl. Phys.* 1998, *31,* 767-775.

3. Smith, P. *The Organic Chemistry of Open-Chain Nitrogen Compounds;* W. A.Benjamin: New York, 1965; pp 234-247.

ACKNOWLEDGEMENTS

The authors wish to thank all the members of the 2005 Hooked on Photonics REU program at the University of Washington, and are especially indebted to Bart Kahr for lab space and guidance, the NSF for funding, the MDITR-STC, Kristin Wustholz, and Sara Selfe.

Dan Daranciang, a senior at Washington University in St. Louis, is completing a double major in chemistry and Germanic languages and literatures. He hopes to be accepted to graduate school in the fall.

Behavioral Properties of Colloidal Crystals at and Around Thermally Induced Defect Sites

Mallory Davidson
University of Washington

Ashlee St. John and Dr. L. Andrew Lyon
Lyon Lab, School of Chemistry and Biochemistry
Georgia Institute of Technology

Soft sphere interactions are described for PNIPAm (Poly-N-isopropylAcrylamide) micro gel particle assemblies doped with gold nanoparticles as a laser hits a small region of the crystal. The gold nanoparticles will act as a local heater excited by the laser and will introduce a defect into the assembly. The thermoresponsivity of the microgel particles will be utilized to study the behavioral properties the system. Observation of the assembly as it melts to form a defect at a particular spot and how the microgel particles will reorder themselves after the heat is removed will be analyzed. This will be done for a more fundamental knowledge of colloidal crystals with soft sphere interactions. In addition, it will provide a better understanding of the kinetics and thermodynamics of the crystallization process.

INTRODUCTION

There is a lot of known information on hard sphere interactions with crystal assemblies, but not a lot about soft sphere interaction systems.[1] Colloidal crystals with soft interactions will be researched for fundamental understanding of the kinetics and thermodynamics of the crystallization process. With the information provided through this research the knowledge gained can be applied for later scientific applications of optic and sensing devices. Namely thermoresponsivity of the particles will be utilized to study the behavioral properties of the system. The particles deswell as the temperature increases to the lower critical solution temperature of the polymer; allowing the system to act more as a fluid.[2]

EXPERIMENT

Assemblies of PNIPAm (Poly-N-isopropylAcrylamide) microgels doped with gold nanoparticles will have a defect induced by positioning a frequency doubled Nd: YAG (Yttrium Aluminum Garnet, λ=532nm) laser at a small section of the crystal. As the laser hits a section of the crystalline the gold nanoparticles will absorb the photons from the laser because of their high extinction coefficient. The energy gained will be released in the form of heat. This released heat will warm up the crystal, and one can observe what happens to that part of the crystal as the defect is induced. Also one can observe the crystal as it cools down after the laser is removed to see how the defect reorders into a crystal.

Differential interference contrast microscopy was used to look at the microgel particles. Afterwards the images attained were analyzed using IDL software. IDL was used to obtain particle trajectories of the images.

RESULTS AND DISCUSSIONS

Gold Incorporation

In order to induce a defect the crystal assemblies needed to be doped with gold nanoparticles. UV VIS Spectrophotometry was run to determine how many gold nanoparticles were needed in the assemblies. Enough gold nanoparticles were needed to absorb photons from the laser, but not too many nanoparticles so that there were no perturbed phase behaviors. At the first noticeable peak of 520nm (this is where gold particles of this size absorb) from the UV VIS read out determined how much gold was put into the sample. It was found to be 500μL. See figure 1.

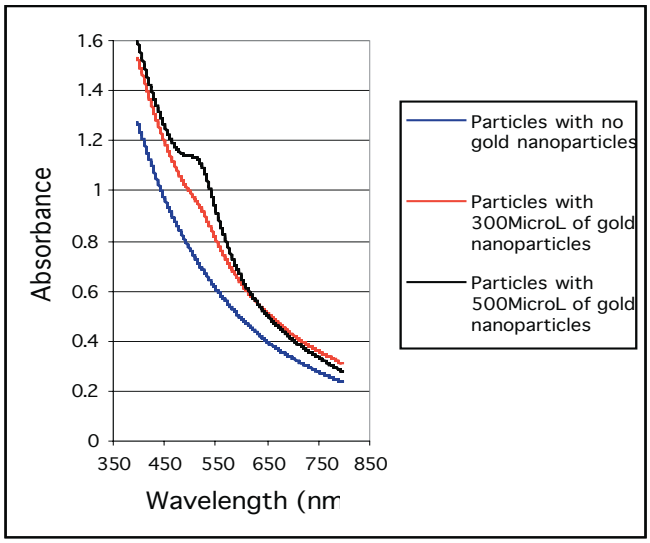

Figure 1. Determination of the amount of gold nanoparticles needed to dope the crystalline assemblies.

In addition, comparisons of the assemblies with gold nanoparticles were observed under heat cycling between 35°C and room temperature to ensure no aggregation occurred. See Figure 2. This was done in a series of ten temperature cycling. If they were to aggregate then the spectra would look different shifting closer to a wavelength around 560nm. It was found that the slopes all had similar trends having a distinct point at 520nm where the gold is visible. Thus no aggregation was observed.

Phase Behavior

Another test for these particles was done to ensure that there was no perturbing of the phase behavior trend between the two crystalline assemblies. It was observed that the assemblies doped with gold nanoparticles tended to start off in a glassy phase until they were heated. Yet the two assemblies followed the same trend of melting at the same temperature.

Inducing the Defect

After ensuring the assemblies were relatively the same the assemblies with the gold nanoparticles were tested with the microscope and laser. The assembly was maintained at a set temperature using an objective heater and temperature stage, and then the laser was introduced to heat up a particular area of the sample. In addition, laser intensity was used to vary the amount of energy added to the system. The energy ranged from barely exciting a particular spot to melting a certain area of the assembly. It was seen that as the melting temperature was approached it took less intensity from the laser to melt or excite the sample. The opposite was also observed that when the sample was far away from the melting temperature it took more energy from the laser to excite the sample.

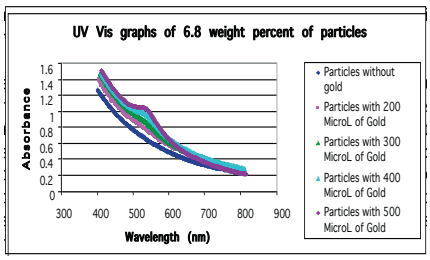

Figure 2. Annealing process of a microgel showing no aggregation after 10 heat cycles between 35°C and room temperature.

CONCLUSIONS AND RECOMMENDATIONS

It was shown that a defect could be introduced from the YAG laser. For defect and trajectory images see Figure 3. However analysis of the crystal assemblies proved to be inconclusive because as the sample would be heated up the crystal would be excited out of phase in the microscope image and the software that traces the particles could not produce accurate images of the particles of the microgel that were out of phase. This out of phase transition occurred in the viewing of the microscope image that the camera took. So clear crystalline trajectories of the defect were hard to obtain. In the future it is suggested to use the most crystalline sample so that clean trajectory images can be obtained. In addition, one could take longer movies so that the an observation of both the melting and recrystalliation process could be made. In this experiment one could only look at fluid to crystalline transition with the camera that was used.

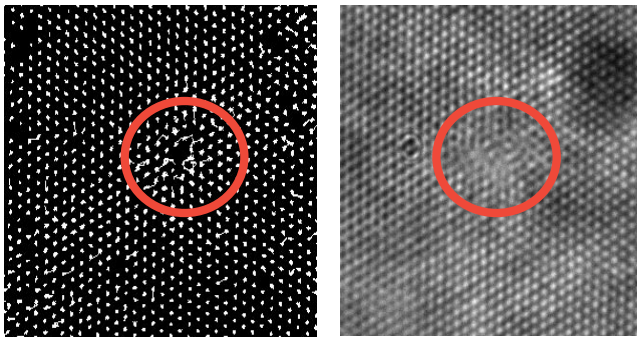

Figure 3. Left is trajectory of a microgel assembly obtained from IDL. Right is image obtained from the camera on the microscope. Circled areas are the locations of the laser and the induce defect in the sample.

ACKNOWLEDGEMENTS

MDITR NSF

REFERENCES

1. Torquato, S,; Truskett, T.M., Debenedetti, P.G. Is random close packing of spheres well defined? Phys. Rev. Lett. 2000, 84, 2064.
2. WU, J.; Zhou, B.; Hu, Z. Phase behavior of thermally responsive microgel colloids. Phys. Rev. Lett. 2003, 90, 048304

Mallory Davidson is currently studying chemical engineering at the University of Washington. Upon graduation in June 2006 she plans to get a full time job either doing marketing or consulting for engineering companies. However, graduate school is a considered a future option

Optical Properties of Metal Nanoparticle Composites

Krystle L. Dzienis
Pennsylvania State University

Wojtek Haske and Dr. Joe Perry
Perry Labs, Department of Chemistry and Biochemistry
Georgia Tech

Metal nanoparticle films and composites were investigated to study their electronic and optical properties in hopes to develop procedures for their use in electronic and photonic devices. Much emphasis was placed on studying the digestive ripening process under argon flow and studying the behavior of nanoparticles in a polymer matrix forming a nanocomposite thin film.

INTRODUCTION

There is a strong interest in metal nanoparticles and their composite films because of their potential use in advanced materials with interesting electronic and optical properties[1]. In order to utilize these composites in future device applications, the ability to manipulate the size, arrangement, and morphology of metal nanoparticles has to be achieved[2]. In order to better understand and use them in these devices, nanoparticles should be monodispersed and highly soluble.

Metal nanoparticles absorb electromagnetic waves by inducing oscillation of electrons, so called plasmons, which result in the enhancement of the electric field in the vicinity of the particles. This phenomenon can contribute to enhancements of nonlinear optical properties of molecules close to the nanoparticle surface. Metal nanoparticles will be modified with two-photon chromophores to investigate changes in optical properties of the chromophores.

EXPERIMENTAL

Synthesis

Gold (Au) and silver (Ag) nanoparticles have been synthesized using a one phase method. Either hydrogen tetrachloroaurate or silver nitrate is reduced by sodium borohydride in the presence of thiol ligands in an ethanol solution. Thiol ligands used in this study include octane thiol (OT) and dodecane thiol (DT).

Digestive Ripening

Metal nanoparticles were dissolved in a toluene solution with excess thiol ligands[2]. The solution was then refluxed for approximately three hours in an argon atmosphere.

Solution Preparation

Small amounts of silver 3:1 (OT:DT) (silver nanoparticles coated with a ratio of 3 to 1, octane thiol to dodecane thiol, ligands) or gold (DT) (gold nanoparticles with dodecane thiol ligands) nanoparticles were dissolved in various solvents to study the effect of solvent on the nanoparticle's UV-vis absorption peak. Solvents used to prepare these solutions included dichlorobenzene, dichloromethane, toluene and cyclohexane.

Film Preparation

All of the films investigated were prepared on glass substrates. The nanocomposite films consisting of Au or Ag nanoparticles mixed with various polymers (PS = polystyrene, PMMA = poly (methyl methacrilate), PVK = poly (vinyl carbozole)), were spin cast at 1000rpm for 2 minutes using a toluene based solution.

RESULTS

Digestive Ripening

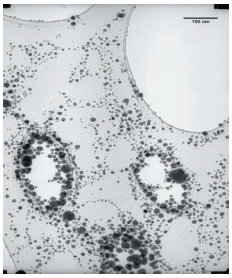

Figure (a) – Au before

Figure (b) – Au after

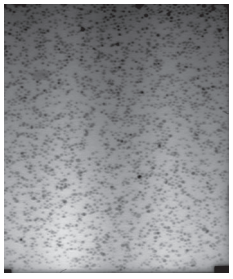

Figure (c) – Ag before

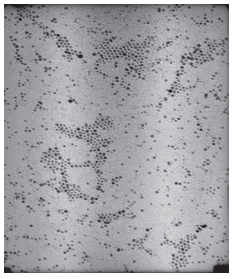

Figure (d) – Ag after

Transmission electron microscopy has been used to investigate the effects of digestive ripening. *Figure (a)* and *(b)* shows Au nanoparticles before and after digestive ripening, respectively. Before digestive ripening, the average size of the particles was 7.1±5nm, which is a much larger size range compared to 4.9±0.8nm for particles after digestive ripening. *Figure (c)* and *(d)* shows Ag 3:1 (OT:DT) nanoparticles before and after digestive ripening, respectively. Before digestive ripening the particles were 4.6±1.5nm in size. After digestive ripening the particles were slightly smaller and more uniform with an average size of 4.0±1.2nm.

Absorption spectra in the UV-visible range were measured on Au (DT) nanoparticles before and after digestive ripening, in a toluene solution. Before digestive ripening the spectrum shows a broader absorption peak with a higher baseline (*Graph a)* than the solution after digestive ripening.

Ag nanoparticles were not soluble after digestive ripening and an absorption spectrum in solution could not be measured.

Nanoparticle Solutions

An investigation of solvent effects was conducted on Au (DT) and Ag 3:1 (OT:DT) nanoparticles.

UV-vis spectroscopy was performed on the various solutions (*Graph b* and *c)*. The absorption spectra of Ag nanoparticles were similar in all solvents investigated. Au nanoparticles had two distinct sets of absorption spectra, with particles in toluene and cyclohexane showing slightly narrower plasmon bands than particles in dichlorobenzene and dichloromethane.

Thin Film Composites

Ag 3:1 (OT:DT) nanoparticles were combined with various polymers to cast nanocomposite films. Before casting the films the solutions were filtered using a 0.2μm filter.

A red shift of surface plasmon resonance is seen showing a maximum absorption peak around 500nm (*Graph d*) compared to silver nanoparticles in solutions, which show a maximum absorption peak around 420nm. Since polystyrene showed the largest red shift and was the most readily available, it was used for all of the subsequent nanocomposite film preparations.

A similar red shift of surface plasmon resonance with respect to solution measurements was also seen for Au (DT) nanoparticles in polystyrene (*Graph e)* (filtered with .1μm filter).

The maximum of the absorption spectrum was shifted from 500nm in solution to 545nm in polystyrene films. Films with higher weight ratios of nanoparticles exhibited larger red shifts of the plasmon band (570nm).

An investigation of ligand effect on nanocomposite films was also conducted. Thin films of Ag 3:1 (OT:DT) nanoparticles (filtered with 0.45μm filters) and Ag 1:1 (OT:DT) nanoparticles (fil-

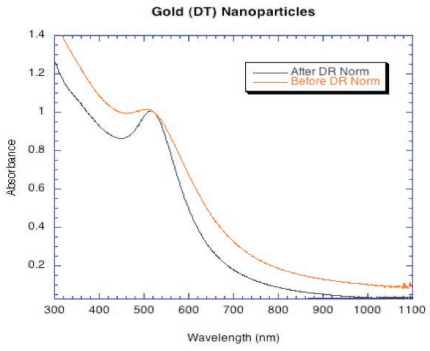

Graph (a) - UV-vis of Au nanoparticle

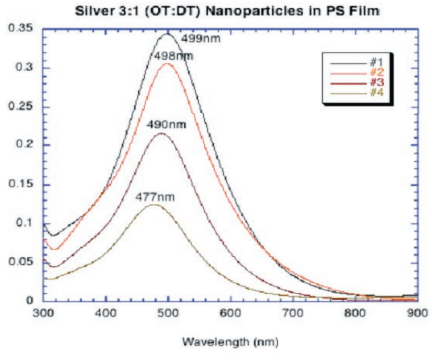

Graph (b) - Absorption spectra of Ag 3:1 (OT:DT) nanoparticles in solution

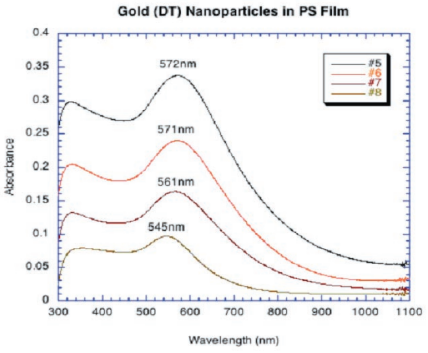

Graph (c) - Absorption spectra of Au (DT) nanoparticles in solution

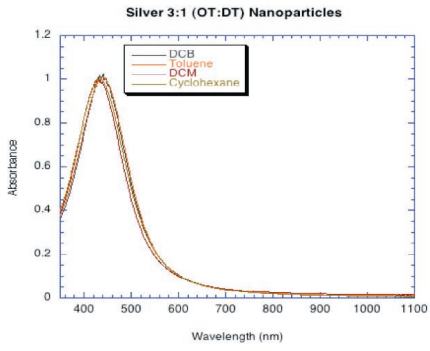

Graph (d) – Absorption spectra of Ag 3:1 (OT:DT) nanoparticle films

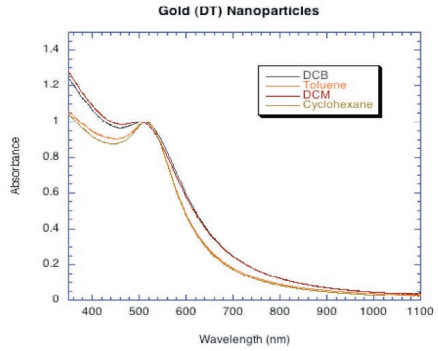

Graph (e) – Absorption spectra of Au (DT) nanoparticles in polystyrene films. The Au nanoparticle amount was decreased by ½ in every film (top to bottom).

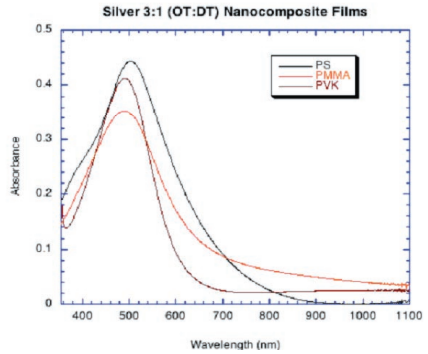

Graph (f) - Absorption spectra of Ag 3:1 (OT:DT) nanoparticle films in polystyrene. The weight ratio of nanoparticles was decreased by ½ for every sample from sample 1 to sample 4.

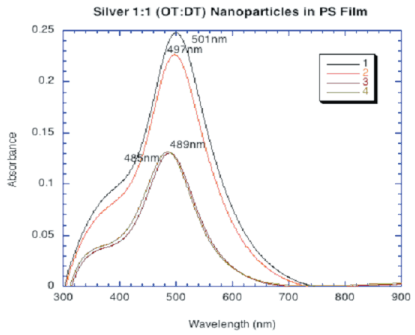

Graph (g) - Absorption spectra of Ag 1:1 (OT:DT) nanoparticle films in polystyrene. The weight ratio of nanoparticles was decreased by ½ for every sample from sample 1 to sample 4.

tered with 0.2μm filters) in polystyrene were prepared with various weight ratios, (*Graph f* and *g* nanoparticle ratios decreased by ½ for each solution).

In both cases a blue shift in the absorption peak was observed when the nanoparticle concentration was lowered. The Ag 1:1 spectrum also shows a shoulder around 400nm.

CONCLUSION

Completing the digestive ripening process under an argon flow shows many improvements to the Au nanoparticles. These improvements include a more uniform size and better solubility of the Au nanoparticles. The effect of digestive ripening on Ag 3:1 (OT:DT) nanoparticles was not as beneficial. After digestive ripening, the Ag nanoparticles were no longer soluble and only a slight change in their size range was seen.

For Au (DT) and Ag 3:1 (OT:DT) in various solvents, no major shifts in the surface plasmon band was seen.

When particles are placed in a polymer matrix a red shift of surface plasmon resonance occurs. When Ag 3:1 (OT:DT) nanoparticles were placed in various polymers, there were differences in the size and shape of the absorption spectra. These differences might be due to the different arrangements the nanoparticles have in the different polymers, and the possibility of aggregates forming could have varied depending on the polymer structure. Additionally, the local environment around the nanoparticles in different instances could affect the plasmon resonance. A blue shift occurs when the concentration of nanoparticles to polymer is lowered, which might be due to interactions between nanoparticles. Additional investigations are needed to provide further insight into these findings. Investigation of the digestive ripening of Ag nanoparticles in various solvents will be conducted to see if control of the size distribution of the nanoparticles can be obtained. Also, X-ray diffraction studies of the nanocomposite films will be performed to investigate the arrangement of nanoparticles in the polystyrene matrix.

ACKNOWLEDGEMENTS

STC-MDITR, Summer 2005 REU – "Hooked on Photonics," NSF, COPE, Georgia Institute of Technology, Dr. Joe Perry, Wojtek Haske, Perry Research Group

REFERENCES

[1] T. Shimizu, T. Teranishi, S. Hasegawa, M. Miyake, J. Phys. Chem. B 2003, 107, 2719-2724.

[2] X.M. Lin, C.M. Sorensen, K.J. Klabunde, Journal of Nanoparticle Research 2: 157-164, 2000.

Krystle Dzienis is currently studying Materials Science and Engineering, specializing in polymers at the Pennsylvania State University. She is planning on continuing her education in the field of Materials Science by going on to graduate school upon completing her undergraduate degree in May 2007.

Electro-Optic Properties of Hybrid Sol-Gel Materials in Fabry-Perot Modulators

Brenda Eby
University of Idaho

Haiyong Gan, Hongxi Zhang and Mahmoud Fallahi
Fallahi Lab, Optical Science Center
University of Arizona

INTRODUCTION

The electro-optic (EO) effect occurs when an electric field is applied across a material that has an optical electromagnetic wave traveling through it. The applied electric field causes changes in the indices of refraction in the material that result in modulations in the light wave passing through the material. This modulation phenomenon is useful as it can be used in high-speed data transfer and optical communication applications.[1] As a result, materials exhibiting desirable electro-optic properties are currently in high demand. This research examined the electro-optic properties of hybrid sol-gel materials in Fabry-Perot Modulator devices.

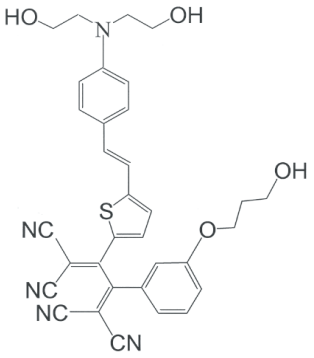

Figure 1. TCBD Chromophore Structure[4]

MATERIAL

EO polymers exhibit anisotropic properties because of their uniaxial character. Hybrid sol-gels are a unique type of EO polymer, which combine the rigid matrix stability of Si/SiO2 with the polarizability of organic chromophore molecules.[2] Hybrid sol-gels are attractive as EO polymers because they are low cost, easy to process materials with low loss.[3]There are two ways to achieve this meshing of inorganic and organic compounds. The first is through doping (guest host) which introduces the chromophores to the sol-gel media with no physical linkage. This method has lead to such problems as phase separation, high loss, and poor thermal stability. The second method, side-chain, links the chromophores covalently to the silica backbone. This reduces the problems demonstrated in the first method and has shown promise in thermal and temporal stability. The chromophore, TCBD (3-[5-(2-{4-[bis-(2-hydroxy-ethyl)-amino]-phenyl}-vinyl)- thiophen -2 -yl] -2 ,5 –dicyano -4 -[3 -(3-hydroxy -propoxy) -phenyl] –hexa -2 ,4-diene-dinitrile), is shown in Figure 1. Chromophore material was provided by the University of Washington and processing of hybrid sol-gel material was done using methods previously established.[4]

DEVICE

Fabry-Perot Etalons, Figure 2, are symmetric structures with the EO polymer sandwiched between two layers each of which contain a glass substrate, a transparent conductive electrode and a highly reflective (>99%) Distributed Bragg Reflective (DBR) mirror.

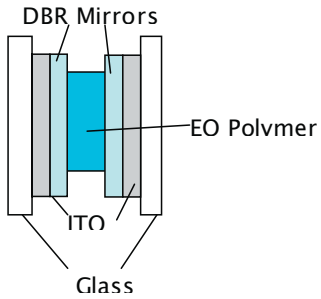

Figure 2. Fabry-Perot Etalon Schematic

Fabry-Perot Etalons are commonly used in data transmission and have applications as modulators, tunable filters, and optical switches. As light passes through the device a resonance due to internal reflection occurs inside the EO polymer cavity between the highly reflective DBR mirrors. Interference between these two surface results in only specific wavelengths of light being transmitted. Successive reflections will cancel each other out because of destructive interference except at the wavelengths were the light waves are in phase. The equation that describes the phase shift because of the DBR mirror difference between successive reflections is:

$$\delta = \left(\frac{2\pi}{\lambda}\right) 2nl\cos\theta$$

Equation 1

Where λ is the wavelength of the incident wave, l is the thickness of the film, n is the refractive index of the EO polymer, and θ is the internal incident angle of the light going through the device. The waves in phase are reinforced through constructive interference, resulting in strong narrow transmission bands that vary depending upon the multiple factors shown in Equation (1). They include film thickness, change in refractive index due to EO effect, and surface roughness. In general transmission will occur whenever the phase shift satisfies the following equation:

$$\delta = 2m\pi$$

Equation 2. where m = any integer

A typical wavelength versus transmission spectra illustrating this is shown in Figure 3.

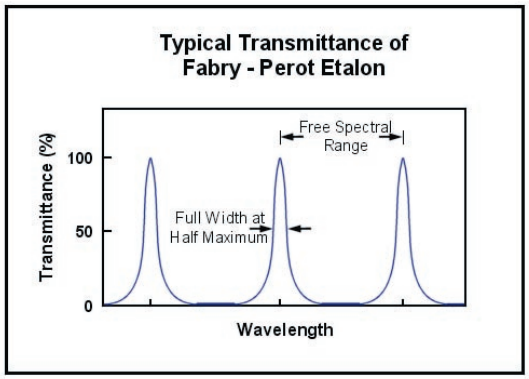

Figure 3. Typical Transmittance Spectra for Fabry Perot Etalon
Adapted from Lambda Research Optics Inc.

When voltage is applied to the material a shift in the resonance wavelength occurs and correlates to the change in refractive index (Δn) due to the electro-optic effect and the change in thickness (Δl) due to a change in the piezo (mechanical) forces acting upon the material.

DEVICE ASSEMBLY / POLING

Indium tin oxide, a transparent conductive material acts as the electrode in the device and is the first layer deposited onto the glass substrate. Then the DBR layer is coated on top followed by the TCBD sol-gel. The TCBD sol-gel is prepared and spin coated at varying speeds to set the thickness of the EO polymer film. After baking, this layered material is corona poled above the glass transition temperature at a high voltage. Poling is done to orient the chromophore molecules and force non-centro-symmetry in the film. The combination of temperatures above the glass transition temperature, which causes the Si/SiO_2 sol gel matrix to relax, and the application of a high electric field causes the highly polarizable chromophore molecules to rotate and orient themselves with the electric field. After poling another glass slide with ITO and DBR is placed on top of the EO polymer and electrical wires are connected to each ITO layer. The layers are then clamped and epoxy is applied to seal the device.

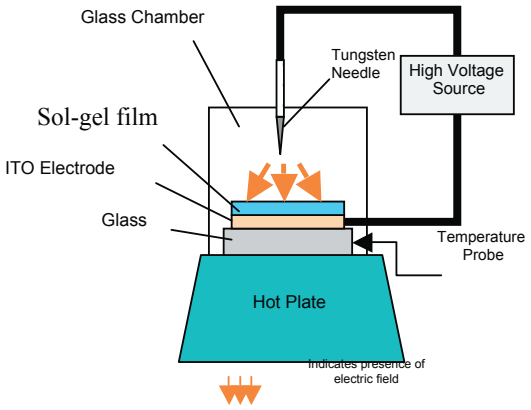

Figure 4. Corona Poling Apparatus

METHODS

The resonance wavelength and the shift in that wavelength are measured by using a broadband source which outputs through a fiber collimator into the Fabry-Perot Etalon. Light that is transmitted from the cavity is focused onto a single mode fiber detector which leads to a optical spectrum analyzer (OSA). The OSA measures the wavelength while the applied voltage is varied letting the wavelength shift be directly observed.

By switching the broadband source to a narrowband, tunable laser the extinction ratio and dynamic modulation of the sample can be measured. The laser propagates through a collimator, continues through the device cavity and finally the transmitted light is focused onto the fiber detector. The dynamic modulation can be observed by switching the DC voltage source to AC by inserting a function generator and changing to a photo detector which inputs into a digital oscilloscope. See Figures 5, 6, and 7 below for testing schematics.

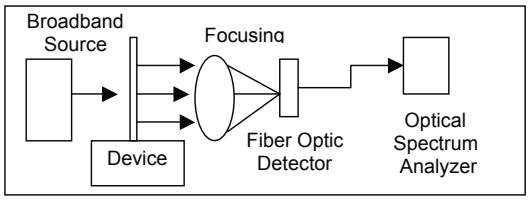

Figure 5. Shift Measurement Schematic

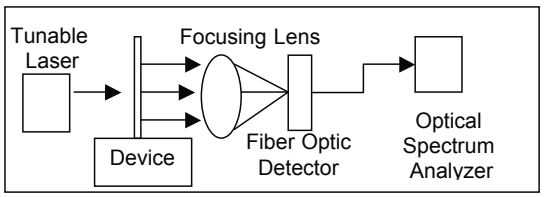

Figure 6. Extinction Measurement Schematic

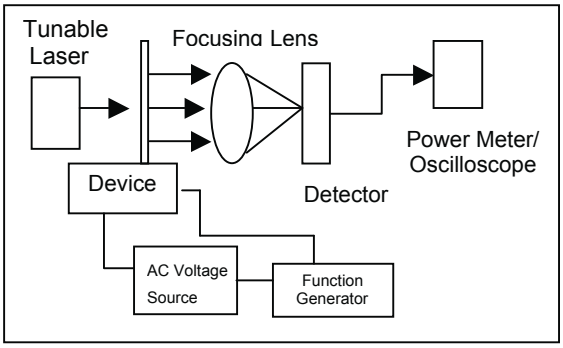

Figure 7. Dynamic Modulation Measurement Schematic

Additional measurements with a surface profiler were done to analysis the roughness of the individual layers of the Fabry-Perot Etalon device. Each surface was scanned in sequence with preceding material layers in place. For example, the third layer, DBR, was scanned with ITO and glass layers below it.

RESULTS / DISCUSSION

By varying the voltage over a range of 60 V, the shifts in Figure 8 were observed. After normalizing the shift wavelengths, the average shift was calculated.

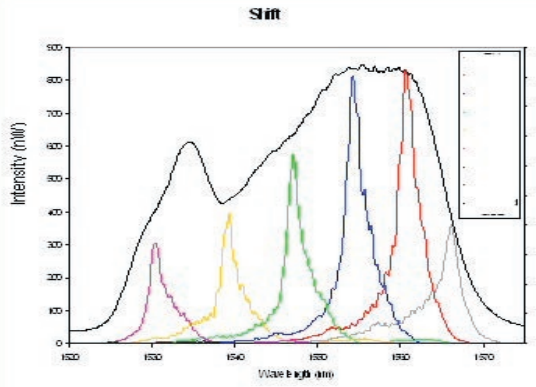

Figure 9. Shift Measurement Results

Extinction measurements also show promising results with an extinction ratio measured at 5 Volts. The extinction ratio is the log ratio of the intensity at 0 volts compared to the intensity at an applied voltage.

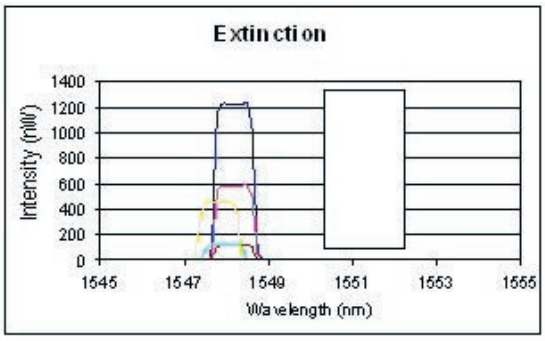

Figure10: Extinction Results TCBD Sol-gel

Surface analysis of the sample was shown to be a major factor in the performance of the device. Scans of the different device levels are shown along with the average standard deviation values. See **Figures 11, 12.**

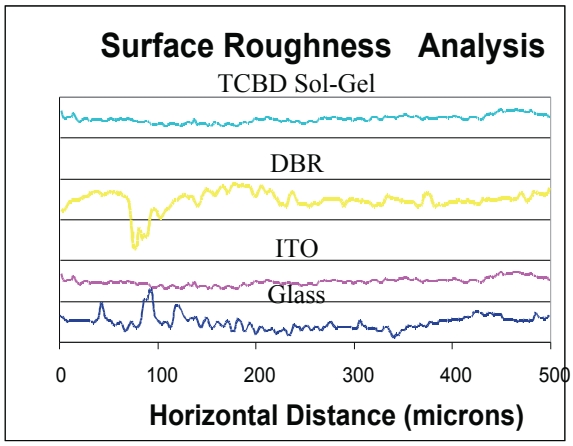

Figure 8: Surface Scans

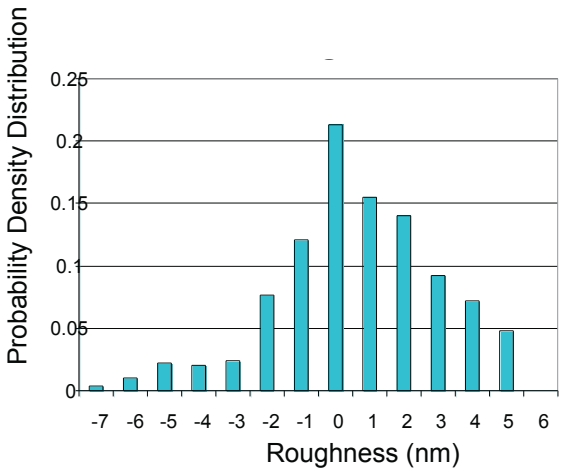

Figure 12. Probability Density Distribution for TCBD Sol-Gel

The average standard deviation shown below is the value obtained from averaging the distribution of each surface scan. Six or more scans for each surface were recorded. The DBR mirror is the roughest surface in the device. This has implications in the device performance as the roughness can be directly tied to the performance of the device.

Surface	Average Standard Deviation
TCBD Sol-Gel	3.02 nm
DBR Mirror	5.36 nm
ITO	1.36 nm
Glass	2.31 nm

Table 1. Indication of Roughness from Surface Scanning of Materials

CONCLUSIONS

Fabry-Perot modulators with electro-optic hybrid sol-gel were successfully fabricated and tested. The samples examined demonstrate promising results with measured wavelength shifts and extinction ratios. This indicates low drive voltage requirement. Additionally dynamic modulation showed a rapid response with low loss. Results indicate that the hybrid sol-gel Fabry-Perot Modulators are promising devices for many optical applications.

FUTURE WORK

Research in the future will examine avenues in which to increase the performance of the EO polymer Fabry-Perot Etalon devices. Plans to replace the ITO with ZnO are being examined. Improving surface consistency and material homogeneity also are avenues to pursue in the near future to increase device performance.

REFERENCES

1. A. Yariv, *Optical electronics in Modern Communications*, 5th ed. Oxford University, New York. (1997)
2. H.Goudket, M. Canva, and Y. Levy, Journal of Applied Phsics. 90, 6044 (2001)
3. S. Najafi, T. Touam, R. Sara, M. Andrews and M. Fardad, Journal of Lightwave Technology. 16, 1640 (2000)
4. H. Zhang, D. Lu, Nu.Peyghambarian, M. Fallahi, J. Lou, B. Chen and A.K.Y. Jen, Optics Letters 30 (2): 117-119 JAN 15 (2005)

ACKNOWLEDGEMENTS

National Science Foundation
University of Arizona
College of Optical Sciences

Funding for this research provided by the Center on Materials and Devices for Information Technology Research (CMDITR), an NSF Science and Technology Center No. DMR 0120967

Quantized Hamilton Dynamics Applied to Condensed Phase Spin-Relaxation

Stephen T. Edwards
Harvey Mudd College

Oleg Prezhdo
Department of Chemistry, University of Washington

INTRODUCTION

Chemistry has a myriad of quantum effects. However, to treat all of chemistry with quantum mechanics would be nearly impossible. Many quantum systems have no closed form solution, and numerical techniques are often prohibitively computationally expensive. Classical mechanics offers numerically simple solutions, but cannot reproduce quantum results, such as tunneling or zero-point energy. As an approximation to the Heisenberg representation of quantum mechanics, quantized Hamilton dynamics offers a method of treating these systems that maintains both quantum effects and the relative simplicity of classical mechanics.[1]

Quantum two-state systems are frequently encountered in chemistry and physics, for instance a spin-½ particle or the polarization of light. The behavior of these systems become very complex when interaction with their environment is considered.2 The spin-boson system simulates the coupling of a two-state spin system to an environment of harmonic oscillators. This system has been well studied,[2,3] so it is a good system to compare new solution methods to, such as quantized Hamilton dynamics.

QUANTIZED HAMILTON DYNAMICS

The time evolution of quantum expectation values is given by Ehrenfest's theorem, or the Heisenberg representation (eq 1).

$$\frac{d}{dt}\langle A\rangle = \frac{i}{\hbar}\langle [H, A]\rangle \tag{1}$$

When treated with Ehrenfest's theorem, quadratic potentials, such as the harmonic oscillator, yield equations of motion that look exactly classical. However, more complicated potentials will generate an infinite hierarchy of equations of increasing order; the time evolution of $\langle q\rangle$ will depend on $\langle q^2\rangle$, and the evolution of $\langle q^2\rangle$ will depend on $\langle q^3\rangle$, etc. A novel method, by Prezhdo et. al.[1] in quantized Hamilton dynamics (QHD), ends the infinite hierarchy at a given order. Using an approximation borrowed from many-body theory expectation values of high order operators are broken down into products of lower order operators. For example a third order operator is decomposed as,

$$\langle ABC\rangle \approx \langle A\rangle\langle BC\rangle + \langle B\rangle\langle AC\rangle + \langle C\rangle\langle AB\rangle - 2\langle A\rangle\langle B\rangle\langle C\rangle \tag{2}$$

Using second order equations, QHD can reproduce important quantum effects such as zero-point energy and tunneling. These effects are preserved while reducing the complexity of a quantum problem to one that is nearly as simple than classical mechanics.

THE SPIN-BOSON MODEL

The Spin-Boson model consists of a single two-state spin system coupled bilinearly to a bath of harmonic oscillators through the vibrational coordinate. The model has applications to condensed phase nonadiabatic electron transfer, low temperature proton transfer, and macroscopic quantum coherence in SQUIDS.[3] The system is described by the Hamiltonian

$$H = \hbar\Omega\sigma_x + \hbar\varepsilon\sigma_z + \sum_j \Big(\frac{p_j^2}{2\mu_j} + \frac{1}{2}\mu_j\omega_j^2 q_j^2 - \frac{g_j}{2}(\sigma_z q_j + q_j\sigma_z)\Big) \tag{3}$$

where σx and σz are Pauli matrices. The term is related to tunneling probability; 2ħε is the energy gap between the two spin states; and p_j, q_j, ω_j, μ_j, and g_j are respectively the momentum, coordinate, frequency, reduced mass, and coupling strength of the jth bath oscillator.

This system has been analyzed and solved in many ways, including use of the non-interacting blip approximation[2] and with Makarov and Makri's numerical path integrals.[3] The quantized Hamilton dynamics scheme is applied to this system so that its results can be compared with exact solutions as well as providing an alternate solution to this problem. Additionally, this is the first application of QHD to model the condensed-phase with a bath of harmonic oscillators.

To obtain the dynamics of the system, equations of motion were generated to second order with eq 1. A third order term appeared in the equations of motion for $\langle\sigma_x q_j\rangle$ and was decomposed using eq 2 as follows:

$$\begin{aligned}\sum_k g_k\langle\sigma_x q_j q_k\rangle &\approx (\langle\sigma_x q_j\rangle - 2\langle\sigma_x\rangle\langle q_j\rangle)\sum_k g_k\langle q_k\rangle + \langle\sigma_x\rangle\sum_k g_k\langle q_j q_k\rangle + \langle q_j\rangle\sum_k g_k\langle\sigma_x q_k\rangle \\ &\approx (\langle\sigma_x q_j\rangle - \langle\sigma_x\rangle\langle q_j\rangle)\sum_k g_k\langle q_k\rangle + g_j\langle\sigma_x\rangle(\langle q_j^2\rangle - \langle q_j\rangle^2) + \langle q_j\rangle\sum_k g_k\langle\sigma_x q_k\rangle\end{aligned} \tag{4}$$

where the last step in eq 4 makes the approximation that $\langle q_j q_k\rangle = \langle q_j\rangle\langle q_k\rangle$ for $j \neq k$, that is, bath oscillators are uncoupled. Similar decomposition and approximations are applied to third order terms in the time derivatives for

$\langle\sigma_x p_j\rangle$, $\langle\sigma_y q_j\rangle$, and $\langle\sigma_y p_j\rangle$.

For simplicity $\hbar$ was set to unity. The set of first order equations for the spin system are

$$\frac{d}{dt}\langle\sigma_z\rangle = 2\Omega\langle\sigma_y\rangle \quad (5)$$

$$\frac{d}{dt}\langle\sigma_x\rangle = -2\varepsilon\langle\sigma_y\rangle + 2\sum_j g_j\langle\sigma_y q_j\rangle \quad (6)$$

$$\frac{d}{dt}\langle\sigma_y\rangle = -2\Omega\langle\sigma_z\rangle + 2\varepsilon\langle\sigma_x\rangle - 2\sum_j g_j\langle\sigma_x q_j\rangle \quad (7)$$

The bath terms evolve as

$$\frac{d}{dt}\langle q_j\rangle = \frac{\langle p_j\rangle}{\mu_j} \quad (8)$$

$$\frac{d}{dt}\langle p_j\rangle = -\mu_j\omega_j^2\langle q_j\rangle + g_j\langle\sigma_z\rangle \quad (9)$$

$$\frac{d}{dt}\langle q_j^2\rangle = \frac{2}{\mu_j}\langle p_j q_j\rangle_s \quad (10)$$

$$\frac{d}{dt}\langle p_j q_j\rangle_s = \frac{\langle p_j^2\rangle}{\mu_j} - \mu_j\omega_j^2\langle q_j^2\rangle + g_j\langle\sigma_z q_j\rangle \quad (11)$$

$$\frac{d}{dt}\langle p_j q_j\rangle_s = \frac{\langle p_j^2\rangle}{\mu_j} - \mu_j\omega_j^2\langle q_j^2\rangle + g_j\langle\sigma_z q_j\rangle \quad (12)$$

The first order spin terms depend on second order terms that mix spin and bath degrees of freedom.

$$\frac{d}{dt}\langle\sigma_z q_j\rangle = 2\Omega\langle\sigma_y q_j\rangle + \frac{1}{\mu_j}\langle\sigma_z p_j\rangle \quad (13)$$

$$\frac{d}{dt}\langle\sigma_z p_j\rangle = 2\Omega\langle\sigma_y p_j\rangle - \mu_j\omega_j^2\langle\sigma_z q_j\rangle + g_j \quad (14)$$

$$\begin{aligned}\frac{d}{dt}\langle\sigma_x q_j\rangle &= -2\varepsilon\langle\sigma_y q_j\rangle + \frac{1}{\mu_j}\langle\sigma_x p_j\rangle \\ &+2g_j\langle\sigma_y\rangle(\langle q_j^2\rangle - \langle q_j\rangle^2) \\ &+2\langle q_j\rangle\sum_k g_k\langle\sigma_y q_k\rangle \\ &+2(\langle\sigma_y q_j\rangle - \langle\sigma_y\rangle\langle q_j\rangle)\sum_k g_k\langle q_k\rangle\end{aligned} \quad (15)$$

$$\begin{aligned}\frac{d}{dt}\langle\sigma_x p_j\rangle &= -2\varepsilon\langle\sigma_y p_j\rangle - \mu_j\omega_j^2\langle\sigma_x q_j\rangle \\ &+2(\langle\sigma_y p_j\rangle - \langle\sigma_y\rangle\langle p_j\rangle)\sum_k g_k\langle q_k\rangle \\ &+2\langle p_j\rangle\sum_k g_k\langle\sigma_y q_k\rangle \\ &+2g_j\langle\sigma_y\rangle(\langle p_j q_j\rangle_s - \langle p_j\rangle\langle q_j\rangle)\end{aligned} \quad (16)$$

$$\begin{aligned}\frac{d}{dt}\langle\sigma_y q_j\rangle &= -2\Omega\langle\sigma_z q_j\rangle + 2\varepsilon\langle\sigma_x q_j\rangle + \frac{1}{\mu_j}\langle\sigma_y p_j\rangle \\ &-2g_j\langle\sigma_x\rangle(\langle q_j^2\rangle - \langle q_j\rangle^2) \\ &-2\langle q_j\rangle\sum_k g_k\langle\sigma_x q_k\rangle \\ &-2(\langle\sigma_x q_j\rangle - \langle\sigma_x\rangle\langle q_j\rangle)\sum_k g_k\langle q_k\rangle\end{aligned} \quad (17)$$

$$\begin{aligned}\frac{d}{dt}\langle\sigma_y p_j\rangle &= -2\Omega\langle\sigma_z p_j\rangle + 2\varepsilon\langle\sigma_x p_j\rangle - \mu_j\omega_j^2\langle\sigma_y q_j\rangle \\ &-2(\langle\sigma_x p_j\rangle - \langle\sigma_x\rangle\langle p_j\rangle)\sum_k g_k\langle q_k\rangle \\ &-2\langle p_j\rangle\sum_k g_k\langle\sigma_x q_k\rangle \\ &-2\langle\sigma_x\rangle(\langle p_j q_j\rangle_s - \langle p_j\rangle\langle q_j\rangle)\end{aligned} \quad (18)$$

There are eleven equations (2 first order, 6 mixed terms, and 3 second order) for every bath oscillator and three for the spin terms that are required to describe motion of the system.

ANALYSIS OF DYNAMICS

It has been demonstrated that the spin-boson system can evolve with many different patterns ranging from coherent oscillations, to incoherent relaxation and complete localization depending on various parameters.[3] The particular case studied with QHD is the asymmetric system, $\varepsilon > \Omega > 0$ and watching a system, starting with $\langle\sigma_x(0)\rangle = 1$, relax. The resulting equations of the spin-boson system were then numerically integrating using a 4th-order Runge-Kutta algorithm. The initial conditions for the bath oscillators give minimal bath energy and uncertainty: $\langle p_j^2\rangle = \frac{\omega_j\mu_j}{2}$ and $\langle q_j^2\rangle = \frac{1}{2\mu_j\omega_j}$. The other terms are all set initially to zero.

BATHS OF SINGLE OSCILLATORS

For the gas phase (no bath oscillators), the system can be solved analytically, and $\langle\sigma_z\rangle$ oscillates sinusoidally in time with frequency.

$$\omega_0 = 2\varepsilon\sqrt{1 + \frac{\Omega^2}{\varepsilon^2}} \quad (19)$$

This behavior changes when adding a single bath oscillator. If a bath oscillator is added with an oscillation frequency not close to the natural frequency of the spin system a new oscillation, less than ω_0, is added to the behavior of $\langle\sigma_z\rangle$. The closer ω_j is to ω_0 the stronger the amplitude and the lower the frequency of the added oscillation. This single oscillator response is shown in the time-domain of $\langle\sigma_z\rangle$ in Figure 1 and the frequency domain in Figure 2.

Adding single bath oscillators at frequencies, that are not close to the spin system's natural frequency, cause relatively simple behavior in the system. This behavior of $\langle\sigma_z\rangle$ coupled to a single bath oscillator off of ω_0 can be described as energy pass-

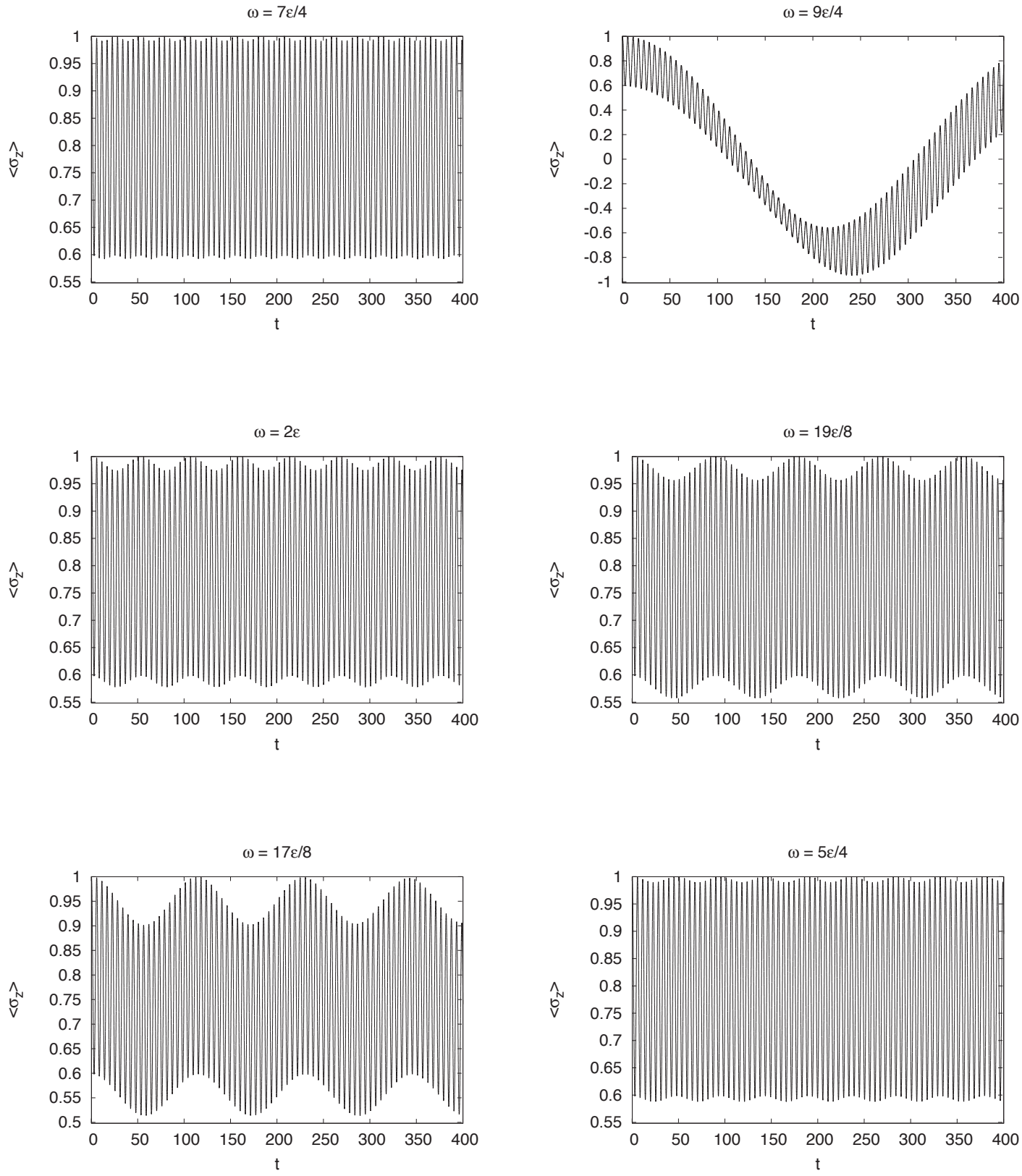

Figure 1. Asymmetric Systems Coupled to Single Oscillators of frequency ω. In these simulations ε = 2Ω = 0.5. Coupling constant g = 0.02. The fast oscillation has a frequency of $\omega_0 \approx \frac{9\varepsilon}{4}$, while the slower oscillation is dependent on ω of the bath oscillator.

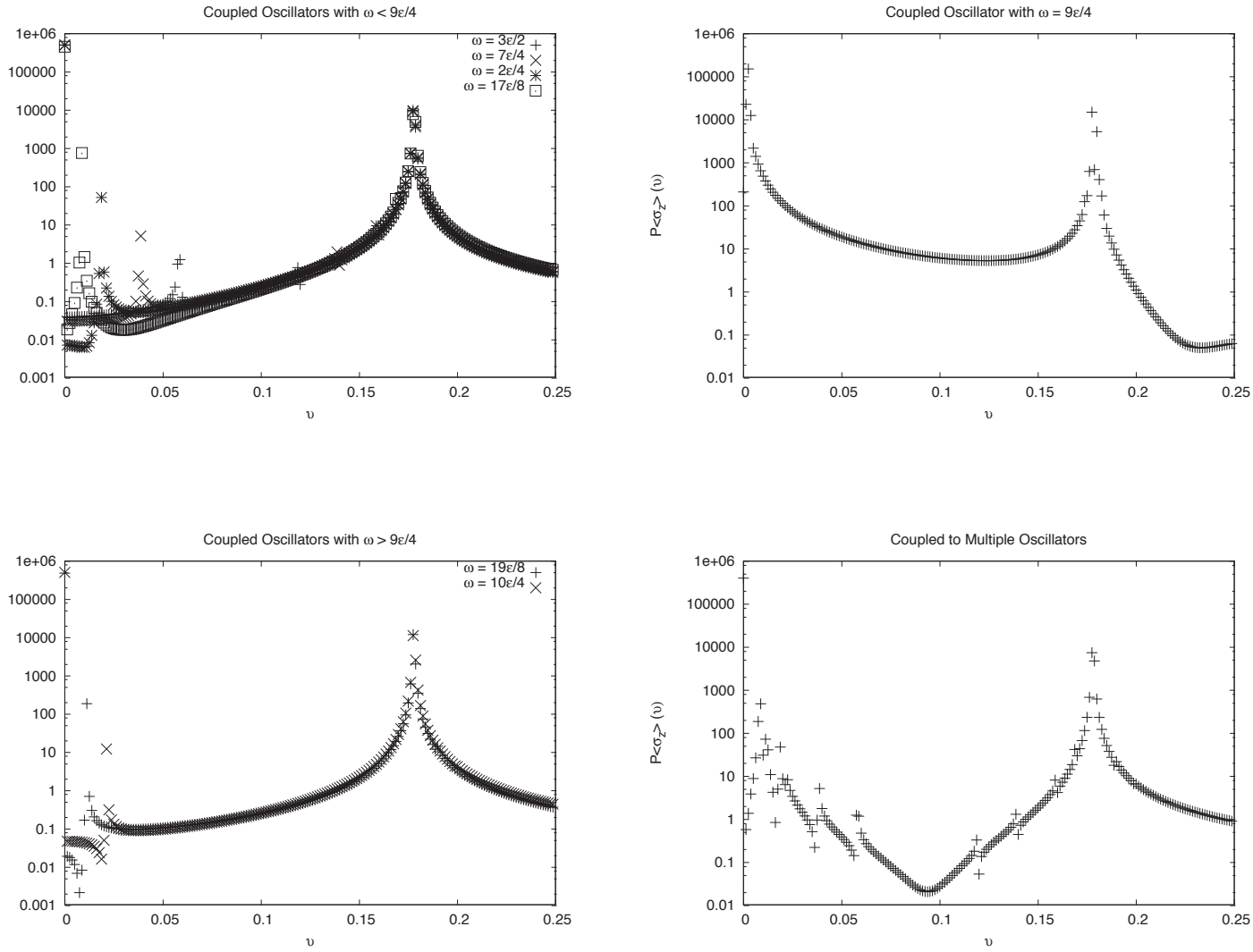

Figure 2. Power Spectra of Asymmetric Systems Coupled to Single Oscillators, using the same conditions as Figure 1. The power spectra of the asymmetric systems show two major oscillations. A high frequency oscillation, dependent on Ω and ε and the slower oscillation is dependent on ω. For an oscillator where ω is the natural frequency of the spin system more complicated behavior occurs.

ing from the spin system into the harmonic oscillator and then returning into the spin system. The lower frequency oscillation is the flow of energy back and forth from spin to boson.

However, for single oscillators where ω_j is on ω_0 cause more complicated behavior. In Figure 2 the oscillator at $\omega_j = \frac{9\varepsilon}{4} \approx \omega_o$ shows gives a responses over a range of frequencies and of greater magnitude. This behavior needs to be studied more in depth.

LARGER BATHS

A more realistic condensed phase involves many bath oscillators. The last plot in Figure 2 shows the power spectrum of multiple bath oscillators, coupled to the spin system, with all the shown frequencies except for $\omega = \frac{9\varepsilon}{4}$. The power spectrum is more complex than a simple sum of the single oscillator power spectra – most notably by the dip in the spectra just below frequencies of $\nu = 0.1$.

Coupling many bath oscillators also changes the behavior of $\langle\sigma_z\rangle$ in the time domain into a more physical result. Finally, is the case with many oscillators. Figure 3 shows the case where the spin system is coupled to 25 oscillators, spaced evenly between $\frac{3\varepsilon}{2}$ and $\frac{5\varepsilon}{2}$. The behavior of this system is obviously more complex than just the addition of a new oscillation, as evident in the power spectra of $\langle\sigma_z\rangle$ (Figure 3). It decays to a lower energy state over time and the spin stays in a low energy state until the numerical solution eventually grows unstable. Figure 3 greatly resembles the same system that is presented in Makri's solution,[3] although a more careful comparison still needs to be made.

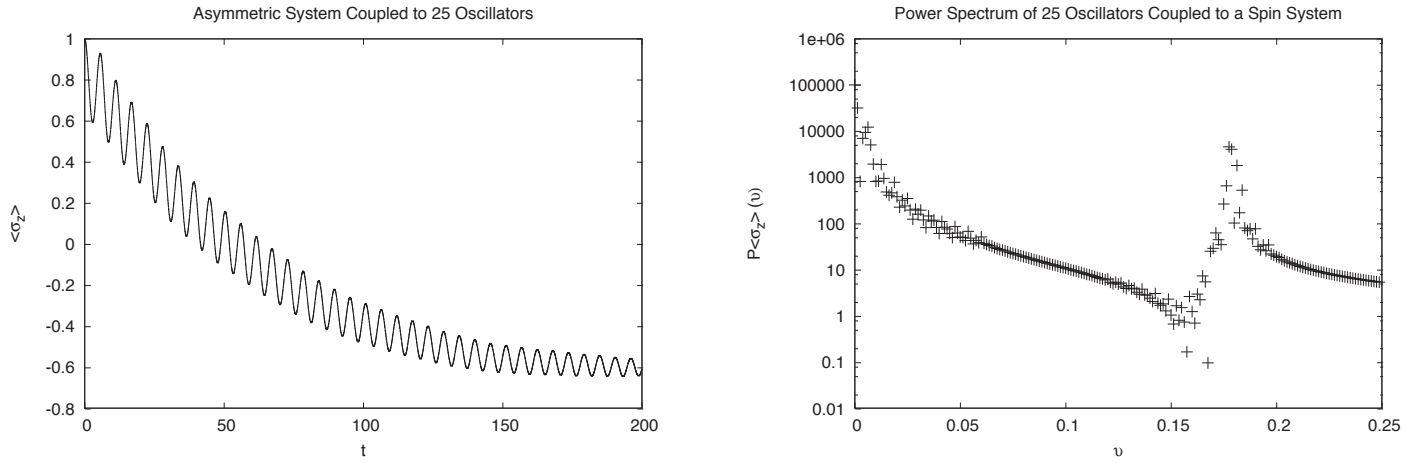

Figure 3. An Asymmetric System Coupled to 25 Oscillators. The frequencies of the bath oscillators, ω, are evenly spaced between 3" $\frac{3\varepsilon}{2}$ to $\frac{5\varepsilon}{2}$. Using the same Ω, ε, and coupling as Figs. 1 and 2, the spin system decays in the presence of more oscillators.

CONCLUSION

The model here has proven to be non-trivial with interesting behavior. The approximations made in QHD seem to give reasonably physical results while suitably simplifying the dynamics. However, there is still much to explore and verify with this model. The frequency of the new spinoscillation induced by coupling to a harmonic oscillator should be determined as a function of ω_j and perhaps g_j. Also, the frequency response from adding oscillators near ω_0 should be determined.

In addition to frequency responses, the difference between treating the system as closed with a finite set of oscillators at discrete frequencies or as an open system, like a Langevin equation, where the bath has continuous spectral density should be addressed. There could be a way to incorporate the QHD approximation into a Langevin-type formalism, making use of the tools of statistical mechanics.

In all, the QHD spin-boson model successfully gives a physical solution for the asymmetric system. The decay of spin is qualitatively the same as the data presented by Makri.[3] There are still many more aspects of this model to explore, such as symmetric systems, and asymmetric systems with $\Omega > \varepsilon$ as well as deciphering the response of these systems to various baths with different spectral densities.

REFERENCES

1O. V. Prezhdo and Y. V. Pereverzev, J. Chem. Phys. 113, 6557 (2000).

2A. J. Leggett et al., Rev. Mod. Phys. 59, 1 (1987).

3N. Makri, J. Math. Phys. 36, 2430 (1995).

ACKNOWLEDGEMENTS

Research support is gratefully acknowledged from the National Science Foundation Center on Materials and Devices for Information Technology Research (CMDITR), DMR-0120967.

Investigating New Cladding and Core Materials for Hybrid Electro-optic Modulators

Parissa Fathalipour
University of Arizona

Robert A. Norwood, Chris DeRose and Amir Fardad
Norwood Lab, Optical Science Center
University of Arizona

INTRODUCTION

Detailed knowledge of the optical properties of materials that are used for electro-optic devices will help lead to the design and formulation of improved waveguide cladding materials. This in turn will also lead to the improvement in design and performance of various optical devices which use these optical waveguide materials.

OBJECTIVE AND MOTIVATION

The purpose of this research is to investigate and characterize a variety of electro-optic materials, sol gels, and nanoparticle doped sol-gel thin films by use of a prism coupler. Detailed measurements of the dependence of the refractive index on wavelength and polarization were taken, as well as measurements of the uniformity of the refractive index over the area of the prepared film. The data collected gave more insight into the make-up and structure of thin films being used in waveguides, provided better input data for modeling and simulations, assisted in the development of improved devices, and may eventually lead to new or improved cladding materials. In particular, the observation large birefringence in some of our standard sol-gel materials provides a potential explanation for the anomalously high losses that have been observed in these materials.

APPROACH

Optical characterization of thin films can be easily and accurately done by use of a prism coupler, specifically a Metricon Model 2010 prism coupler. The prism coupler is able to make its highly accurate measurements (±.0001) by directing a laser of a specific wavelength to a prism of a high refractive index, which is coupled with a sample with a pressure ranging from 20psi to about 40psi. The prism, sample, and photo detector are mounted on a stage which rotate and varies the angle at which the laser enters the prism thuss allowing the waveguide modes of the film to be found. When three or more modes are found the prism coupler is able to calculate the index of refraction and thickness of the substrate film; it also is able to give the standard deviation of the measurements of the thickness and index. The measurements were taken at four different wavelengths 632.8nm, 830nm, 1300nm, and 1550nm to ensure thorough results. The sample films involved were formulated and fabricated using a technique called spin coating which is commonly used in the semiconductor industry. The films to be investigated were initially of known materials such as silicon dioxide on a silicon wafer, hydrogen based sol-gels, and fluorinated sol-gels. For all samples the TE index and thickness was to be found at each wavelength as well as the TM index and thickness also at each wavelength. The TE index is the refractive index for waveguide modes polarized parallel to the surface of the film, while TM modes are polarized normal to the surface of the film.

Experience was used to set a standard as to what was an acceptable standard of deviation for the measurements, with the requirement that the error in the index of refraction was to be no greater than 0.002% and that in the thickness had to be less than 1.0%. The initial measurements were taken of the silicon dioxide on a silicon wafer. The TE index, TM index, and thickness were found, and the measurements were repeated until standard deviations were within the acceptable standard range. The data was then analyzed and fit using a plotting program called Axum. The data was to be fitted to the Cauchy dispersion formula given in Equation (1) given below:

$$n(\lambda) = A + \frac{B}{\lambda^2} + \frac{C}{\lambda^4} \quad (1)$$

which is generally applicable to materials far from any significant absorption bands. Using this equation coefficient A, B, and C were calculated and then expected values were found and compared to the measured values. With these values the dispersion curves were made, which give the index of refraction vs. wavelength. This was repeated also for the TM data. In order to get an understanding of the birefringence of the sample the index difference had to be found, TE index minus TM index. This was also graphed versus wavelength and gave us our birefringence graph. Once the measured data was accurate and concurred with the previous data the focus was moved to three hydrogen based films Sample 6 spin speed of 500r/30s, Sample 7 1500r/30s, and Sample 8 3000r/30s, which were supplied by Chris DeRose. The same procedure was followed as with the silicon dioxide. One

difficulty that was found with these samples was to attain a good coupling point. The higher spin speed proved to be the most difficult, but after multiple runs accurate data was found. The research then became more detailed by investigating the cladding and core films wavelength dependent refractive index and the effects of TE and TM polarization. These were the fluorinated sol-gel samples provided by Amir Fardad. The same steps were taken and as before these samples proved to be more challenging because of their nonuniformities and rough surfaces. Coupling spots were hard to find because the surface of the samples were nonuniform and also the silicon wafers used were much thinner than with the previous samples. This resulted in the need to adjust measurement pressure, which had to be lowered and varied and the samples had to be moved to multiple locations until accurate data could be collected. All plots were then analyzed to find characteristics of the films such as high or low dispersion and birefringence.

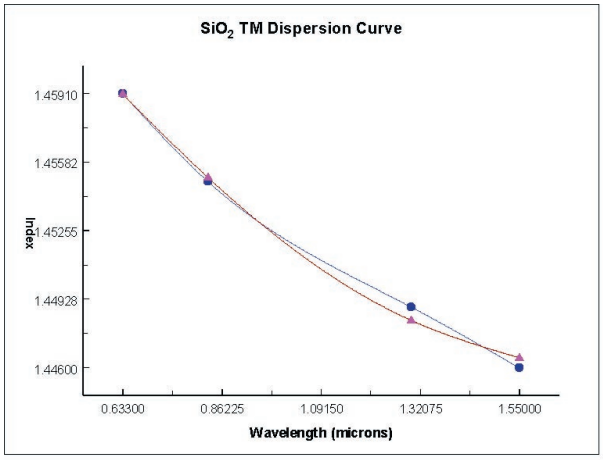

Figure 1. TE dispersion curve of SiO_2 film

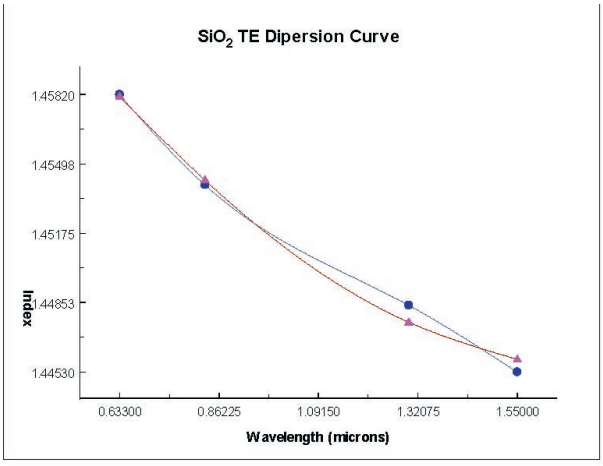

Figure 2. TM dispersion curve of SiO_2 film

RESULTS

The results of this research became most interesting when the hydrogen based sol-gels were analyzed. All other samples acted as they should, demonstrating little birefringence and low dispersion. As can be seen from Figures 1 and 2 the dispersion for SiO_2 is low. These figures also show the general shape of the curves this should not vary much from sample to sample. Also seen below is Figure 3, which shows the low birefringence of the silicon dioxide film.

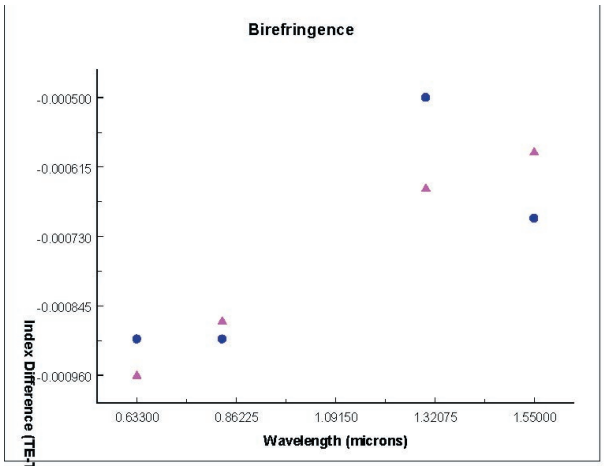

Figure 3. Birefringence of SiO_2 film

The data below is for the fluorinated core sol-gel film, which also exhibits low dispersion and birefringence. The only main difference is that the index of refraction is much lower than the SiO_2 and the hydrogen based film and this is due to the substitution of hydrogen with fluorine, which reduces the molecular polarizability of the sol-gel. Figure 4 shows the TE dispersion curve and Figure 5 shows the birefringence.

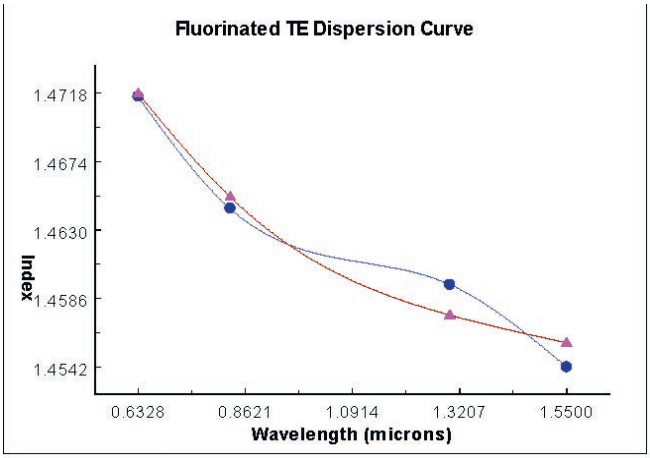

Figure 4. Fluorinated TE dispersion curve

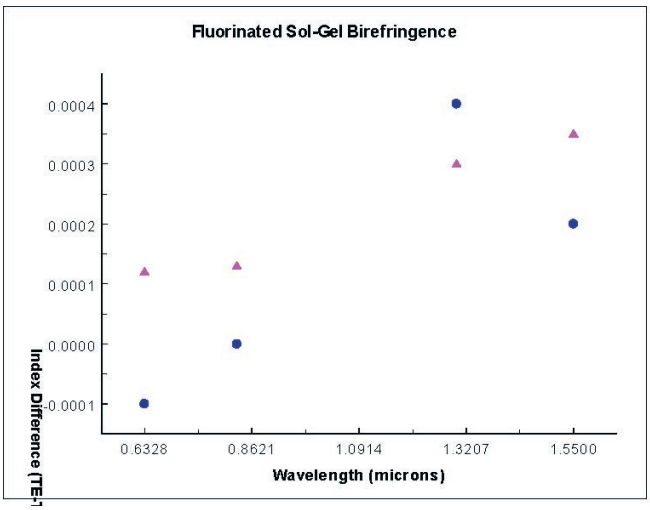

Figure 5. Fluorinated sol-gel birefringence

When the hydrogen based sol-gels were analyzed the plots show a low amount of dispersion in both TE and TM direction. The data shown is for the spin speed of 1500/30 rps, which demonstrates the low dispersion that all the hydrogen based sol-gels exhibit as seen in Figure 6.

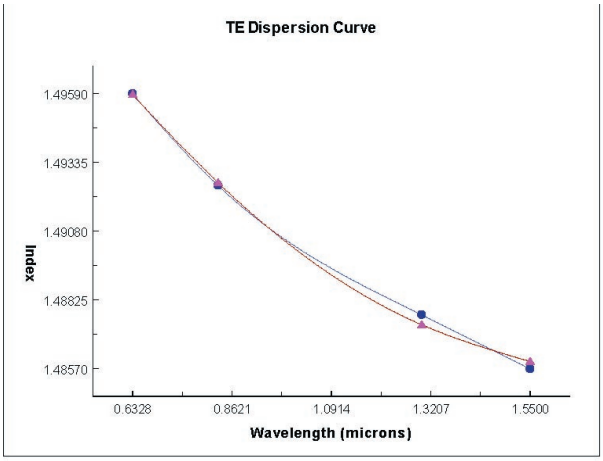

Figure 6. TE dispersion curve

However, the birefringence for these samples was exceptionally high compared to the SiO_2 and fluorinated samples. Looking at the scale it can be seen that the magnitude of the birefringence for the hydrogen based sol-gel is ten times larger than that of the SiO2 and fluorinated films that is why it is such an interesting result. This high birefringence that these samples exhibited is demonstrated in Figure 7. High birefringence can lead to local variations in the refractive index that can subsequently result in scattering. It is hypothesized that the high birefringence of the hydrogen-based sol-gels could be a major contributor to the anomalously high waveguide loss that has been observed in these films.

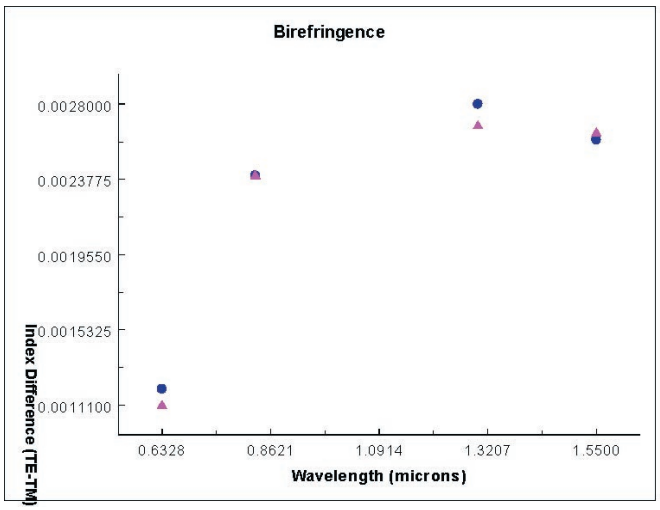

Figure 7. Birefringence of Hydrogen based film

CONCLUSIONS

The hydrogen based sol-gel samples had the largest birefringence this finding is important because it means that there is a large change in index depending if its TE or TM. The large difference means that the sol-gel is polarization dependent, which could have a large impact in optical systems. The large birefringence also means that there is potentially birefringence induced waveguide loss in the hydrogen-based sol-gels. The loss is due to the microdomain scattering that happens within the waveguides.

FUTURE WORK

In future research poled and un-poled films will also be looked at, the main focus will be on poled films and how the index of refraction varies across the film, as poling nonuniformities can lead to significant problems in fabricating high performance devices. Nanoparticle doped sol-gels will also be investigated in future research. The data will then be used to investigate new or improved cladding materials for a target core material. A key goal of this next phase will be to develop a cladding material with a refractive index much closer to that of the electro-optic polymer material, which has a refractive index of approximately 1.62 at 1550mn. Two potential approaches are considered. One is high index nanoparticle doping of sol-gels; silicon nanoparticles with indices of 3.5 have been obtained and will be dispersed in photopatternable sol-gels that have been previously developed. The dependence of the refractive index on nanoparticle loading will be studied, assuming that good dispersions can be made. Another approach is to investigate the use of selective photobleaching of the electro-optic polymer layer to alter the refractive index, therefore allowing it to be a cladding layer for itself.

ACKNOWLEDGEMENTS

Dr. Robert Norwood
Chris DeRose
Amir Fardad
University of Arizona
College of Optical Sciences

Funding for this research provided by the Center on Materials and Devices for Information Technology Research (CMDITR), an NSF Science and Technology Center No. DMR 0120967

Parissa would like to thank Dr. Norwood for giving me an opportunity to gain invaluable experience this summer.

Synthesis of TPD-Based Compounds for Use in Modification of ITO Surfaces and Metal Nanoparticles

Aaron D. Finke
University of Arizona

Michal Malicki and Seth R. Marder
Marder Lab
Georgia Institute of Technology

INTRODUCTION

Metal oxides, in particular the transparent semiconductor indium tin oxide (ITO), have been shown to be effective charge transport materials in organic photovoltaic cells. However, the relative ease in which ITO surfaces can lose their charge transfer properties, thus creating "dead spots" on their surfaces, has raised questions recently about the relative efficiency of these metal oxides to transfer charge.

The surface of ITO is highly reactive in ambient conditions, making the surface problematic for practical use. Upon contact with water, ITO hydrolyses to form surface metal hydroxyl groups and, in many cases, complete hydrolysis of the surface metal to form metal hydroxides, which dissociate form the surface and are physiosorbed onto the metal surface. In conditions where oxygen is absent (such as those used in vapor deposition), oxygen deficiencies can form on the surface, leading to positive charge formation on the surface. Physiosorbed metal hydroxides are especially poor at transferring charge, are insoluble in most solvents, and bind tightly to ITO. Their presence can result in reduced device efficiency and lifetime, as a result of thermal breakdown that can occur due to charge buildup on the surface[1].

Chemisorption (chemical bonding) of molecules onto ITO surface defects which can facilitate charge transfer has been shown to be an effective solution to this problem. Several moieties have been shown to aid in charge transfer when chemically bonded to ITO: recently, ferrocenedicarboxylic acid and 3-thiopheneacetic acid have both been shown to greatly aid in hole transfer across the ITO surface in OLEDs. A recent question has been asked in light of these results: will directly binding the hole transport layer commonly used in OLEDs, a class of bis(triaryl) amines called TPD [2,3], aid in hole transport as well? Furthermore, it has been shown that while carboxylic acid moieties bind well to surface defects on ITO, phosphonic acid moieties bind even more tightly, and therefore are of interest. Synthesis of TPD with an alkyl phosphonic acid functionality would be used to test the effects of direct attachment of the hole-transport layer via a strong binding functionality.

TPD may also have other applications in the functionalization of nanoparticles. Gold nanoparticles exhibit surface plasmon resonance, which is thought of as collective oscillations of surface electrons. The induced oscillating electric field in close proximity to the surface of the nanoparticle shows much higher amplitude than the amplitude of the electric field of the incoming light. TPD compounds show two-photon absorption in roughly the same region as the surface plasmon resonance. Therefore, attaching TPD to a gold nanoparticle via a thiol may increase the rate of two-photon absorption of TPD [4,5].

Therefore, the synthesis of a TPD-based compound which can allow for a variety of different functionalities to be synthesized will be important in showing the effects of TPD in various systems. Synthesis of TPD with a phenolic functionality can give TPD such versatility and should allow for several different TPD-based compounds to be made from a single source compound.

METHOD

The proposed synthetic scheme for phenol-functionalized TPD is shown in Figure 1, which is partly based on previous fuctionalized syntheses[6] . The major route for synthesis involves multiple steps utilizing Buchwald-Hartwig palladium-catalyzed aminations [7]. A *tert*-butyldiphenylsilyl (TBDPS) group is used as a protecting group for a phenol to be revealed after the coupling reactions; this is necessary as the acidic phenol hydrogens are incompatible with the reaction conditions of Buchwald-Hartwig amination. This phenol can be used as a starting material for a variety of different reactions, allowing for several different functionalities to be attached easily onto it.

RESULTS AND DISCUSSION

Synthesis of TPD was performed in good yield for all reactions, except for one step. The amination of 4-bromo-4'-iodobiphenyl with phenyl-m-tolyl amine was attempted several times with two different conditions. Initially, the amination was attempted through copper(I)-catalyzed Ullmann condensations. However, the reaction never went to completion, even after several days of heating. After workup, the product was isolated in 16% yield. Another pathway was chosen, through palladium-catalyzed amination. While the reaction progressed much more quickly (~24h), these conditions aminate both aryl bromides and

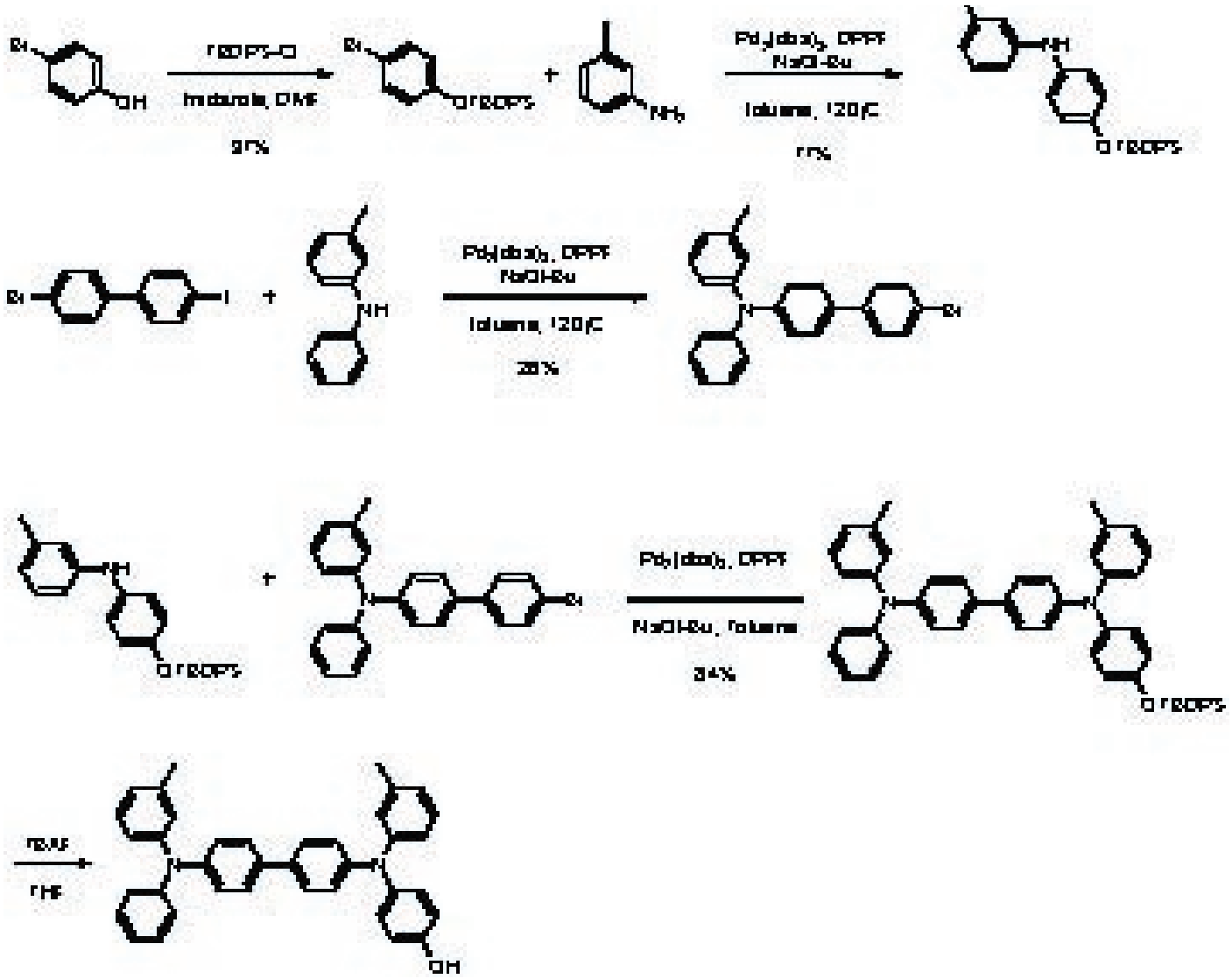

Figure 1. Synthesis of TPD with one phenol group.

iodides, thus making diamination a major byproduct of the reaction. With these conditions, the product was isolated in 26% yield.

The TPD phenol was isolated and, as it is a compound not previously described in literature, it will need to be fully characterized before proceeding with alkylation, using NMR, MS, and elemental analysis.

EXPERIMENTAL

Synthesis of 4-bromo-(*tert*-butyldiphenylsilyl) oxybenzene

To a 500 mL round-bottom flask was added 4-bromophenol (10.0 g, 0.057 mol), imidazole (4.77 g, 0.07 mol), and DMF (50 mL). *Tert*-butylchlorodiphenylsilane (19.0g, 0.069 mol) was added with to the mixture while stirring. The reaction was stirred at room temperature under nitrogen atmosphere overnight. A white precipitate formed over this time. The reaction was added to 50 mL CH_2Cl_2 to dissolve the precipitate, then poured into 50 mL water. The mixture was extracted with CH_2Cl_2 three times, the extracts of which were combined and washed with water four times (50 mL each) and brine three times (50 mL each), then dried over anhydrous $MgSO_4$. The solvent was removed under reduced pressure. Column chromatography in 4:1 hexanes:CH_2Cl_2 gave a colorless oil which crystallized to form a white solid overnight (24.1g, 97% yield). ^{1}H NMR (500 MHz, , CD_2Cl_2, ∂): 7.70 (dd, 4H), 7.45 (tt, 2H), 7.38 (t, 4H), 7.19 (dt, 2H), 6.65 (dt, 2H), 1.05 (s, 9H).

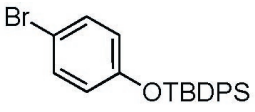

Synthesis of 4-bromo-4'-iodobiphenyl

To an oven-dried 500 mL round-bottom flask was added 4-bromobiphenyl (44.6 g, 0.191 mol), KIO_4 (22.0 g, 0.095 mol), and iodine (24.6 g, 0.097 mol). Acetic acid (132 mL, 2.30 mol) was added to the flask, followed by water (11 mL) and concentrated sulfuric acid (5.6 mL). The reaction was heated with stirring at 70 °C overnight. The reaction mixture was cooled to room temperature and water (250 mL) was added to the flask. The mixture was filtered and washed with water to give a pinkish-white solid. The precipitate was recrystallized in toluene to give colorless, needle-like crystals (64.9 g, 94% yield). ^{1}H NMR (500 MHz, CD_2Cl_2, ∂): 7.78 (d, J = 5.4 Hz, 2H), 7.58 (d, J = 5.4 Hz, 2H), 7.45 (d, J = 5.4 Hz, 2H), 7.32 (d, J = 5.4 Hz, 2H).

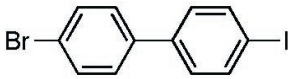

Synthesis of 4-(tert-butyldiphenylsilyl)oxyphenyl m-tolyl amine.

An oven-dried 250 mL three-neck flask was sealed with septa and was purged with nitrogen gas for ten minutes. 100 mL anhydrous toluene was added to the flask. Tris(dibenzylideneace tone)dipalladium (0) ($Pd_2(dba)_3$) (0.169 g, 0.184 mmol) and diphenylphosphinoferrocene (DPPF) (0.212 g, 0.382 mmol) was added to the flask and the mixture was stirred for ten minutes. 4-bromo-(*tert*-butyldiphenylsilyl)oxybenzene (6.06 g, 0.0147 mol), m-toluidine (2.0 mL, 0.0184 mol) and sodium *tert*-butoxide (1.71 g, 0.0184 mol) were added to the flask. A reflux condenser was added to the flask and the reaction was heated to reflux under nitrogen atmosphere for ~36 h. Upon completion of the reaction as monitored by TLC, the solvent was evaporated under reduced pressure and the resulting brown oil was dissolved in 100 mL dichloromethane and washed with water three times, dried over $MgSO_4$ and the solvent evaporated. Column chromatography in 7:3 hexanes:dichloromethane gave a yellow, viscous oil (4.50g, 70% yield). ^{1}H NMR (300 MHz, $CDCl_3$, ∂): 7.71 (m, 4H), 7.39 (m, 6H), 7.08 (m, 1H), 6.86 (d, 2H), 6.70 (m, 5H), 2.24 (s, 3H), 1.12 (s, 9H).

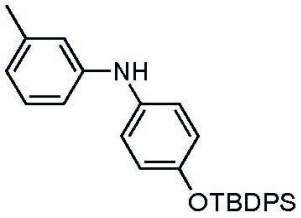

Ullmann condensation of (4'-Bromo-biphenyl-4-yl)-phenyl-m-tolyl-amine.

An oven-dried 250 mL round-bottom flask was purged with nitrogen gas for ten minutes. 70 mL anhydrous toluene was added to the flask via syringe. The following reagents were added to the flask in order: phenyl m-tolyl amine (7.66 g, 0.0418 mol), 4-bromo-4'-iodobiphenyl (14.3 g, 0.0402 mol), 1,10-phenanthroline (0.290 g, 1.61 mmol), CuCl (0.161 g, 1.62 mmol), and KOH (17.7 g, 0.316 mol). A Dean-Stark trap and reflux condenser were attached to the flask and the reaction was heated to reflux for one week. The reaction was taken off heat and the toluene evaporated under reduced pressure. The resulting black sludge was dissolved in 500 mL dichloromethane and washed with water three times, dried over anhydrous $MgSO_4$ and the solvent evaporated. Column chromatography in 9:1 hexanes:dichloromethane gave a white solid (3.5 g). The solid was recrystallized in ethanol to give white crystals (2.77 g, 16% yield). ^{1}H NMR: 7.52 (dt, 2H), 7.41 (m, 4H), 7.24 (m, 2H), 7.11 (m, 5 H), 7.02 (t, 1H), 6.90 (m, 3H), 2.24 (s, 3H).

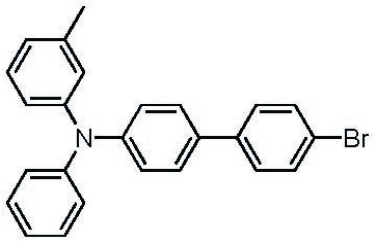

Buchwald-Hartwig amination of (4'-bromo-biphenyl-4-yl)-phenyl-m-tolyl-amine.

To an oven-dried large Schlenk tube there was added $Pd_2(dba)_3$ (0.626 g, 0.884 mmol), DPPF (0.889 g, 1.60 mmol), sodium *tert*-butoxide (4.22 g, 44.0 mmol), and 4-bromo-4'-iodobiphenyl (14.9 g, 42.0 mmol). The tube was sealed with a septum and evacuated under vacuum for ten minutes, then purged with argon gas for ten minutes. Phenyl-*m*-tolylamine (6.41g, 34.9 mmol) was added via syringe and anhydrous toluene (70 mL) was added via cannula. The mixture was heated with stirring to 100°C for 24h. The solvent was evaporated under reduced pressure, and the resulting oil was dissolved in 50 mL dichloromethane, which was filtered through silica to give a red oil. Column chromatography on SiO_2 using 9:1 hexanes:dichloromethane as eluent gave a white solid (4.50 g). The solid was recrystallized in ethanol to give colorless, needle-like crystals (3.79g, 26% yield). ^{1}H NMR (300 MHz, CD_2Cl_2, ∂): 7.52 (dt, 2H), 7.41 (m, 4H), 7.24 (m, 2H), 7.11 (m, 5 H), 7.02 (t, 1H), 6.90 (m, 3H), 2.24 (s, 3H).

Synthesis of N4'-[4-(tert-Butyl-diphenyl-silanyloxy)-phenyl]-N4-phenyl-N4,N4'-di-m-tolyl-biphenyl-4,4'-diamine.

To an oven-dried Schlenk tube there was added (4'-Bromo-biphenyl-4-yl)-phenyl-*m*-tolyl-amine (2.02 g, 4.86 mmol), 4-(*tert*-butyldiphenylsilyl)oxyphenyl m-tolyl amine (2.50 g, 5.70 mmol),

$Pd_2(dba)_3$ (88.6 mg, 0.0968 mmol), DPPF (110 mg, 0.198 mmol), and sodium *tert*-butoxide (0.584 g, 6.08 mmol). The tube was sealed with a septum, evacuated under vacuum for ten minutes and purged with argon gas for ten minutes. Anhydrous toluene (20 mL) was added via cannula. The mixture was heated with stirring to 100°C for 24h. Toluene was evaporated under reduced pressure, and the resulting brown oil was dissolved in 20 mL dichloromethane, then filtered through silica gel, and the solvent evaporated. Column chromatography on SiO_2 using 4:1 hexanes: toluene as eluent gave a glassy, yellow solid (3.16g, 84 % yield). ^{1}H NMR (300 MHz, CD_2Cl_2, ∂): 7.79 (d, 4H), 7.42 (m, 10H), 7.28 (t, 2H), 7.12 (m, 6H), 7.01 (m, 4H), 6.90 (m, 9H), 2.28 (s, 3H), 2.26 (s, 3H), 1.17 (s, 9H).

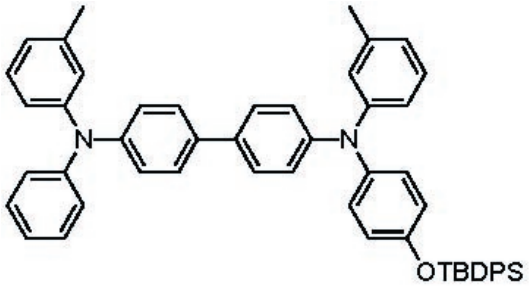

REFERENCES

(1) Brumbach, M. Doctoral Thesis; University of Arizona: Tucson, 2003.

(2) Okumoto, K.; Wayaku, K.; Noda, T.; Kageyama, H.; Shirota, Y. *Synthetic Mealst* **2000**, *111*, 473-476.

(3) Shirota, Y.; Okumoto, K.; Inada, H. *Synthetic Mealst* **2000**, *111*, 387-391.

(4) Stellacci, F.; Bauer, C. A.; Meyer-Friedrichsen, T.; Wendeleers, W.; Marder, S. R.; Perry, J. W. *J. Am. Chem. Soc.* **2003**, *125*, 328-329.

(5) Wendeleers, W.; Stellacci, F.; Meyer-Friedrichsen, T.; Mangel, T.; Bauer, C. A.; Pond, S. J. K.; Marder, S. R.; Perry, J. W. *J. Phys. Chem. B* **2002**, *106*, 6853-6863.

(6) Hreha, R. D.; Zhang, Y. D.; Domercq, B.; Larribeau, N.; Haddock, J. N.; Kippelen, B.; Marder, S. R. *Synthesis-Stuttgart* **2002**, 1201-1212.

(7) Hartwig, J. F. *Angew. Chem. Int. Ed.* **1998**, *37*, 2046-2067.

ACKNOWLEDGEMENTS

Research support is gratefully acknowledged from the National Science Foundation Center on Materials and Devices for Information Technology Research (CMDITR), DMR-0120967.

Aaron Finke is a senior majoring in chemistry at the University of Arizona. He will graduate in May 2006 and plans on attending graduate school in organic or inorganic chemistry.

Optimizing Hybrid Waveguides

Andrew Gardner
Highline Community College

Kjersti Kleven and Scott Dunham
Department of Electrical Engineering
University of Washington

This paper outlines research into how much the propagation constant of hybrid waveguides changes when the index of refraction of the cladding layer is altered. Various indexes of the cladding layer, heights of the silicon block, widths of the silicon blocks, and spaces between the two silicon blocks were modeled to find optimal dimensions to produce the maximum change in the propagation constant.

INTRODUCTION

Waveguides have been used in optical modulators for more than ten years. Recently, the concept of hybrid waveguides has been a focus of research. Hybrid waveguide can perform the same function as traditional waveguides, although they designed and operate much differently.

Waveguides act much like wires for light. While electric wires conduct or guide electricity, waveguides propagate or guide light. Traditional waveguides do this by guiding the light inside a high index material surrounded by lower index cladding layer. However, hybrid waveguides are unique in that they actually guide the light in a low index region between two blocks of high index material.[1]

Light propagates through a waveguide the as a mode. Modes are a spatial distribution of optical energy or an electromagnetic wave that is a solution of Maxwell's wave equations. Two important types of modes for this application are guided modes and substrate radiation modes. The substrate radiation mode is an unguided mode which means the wave will disperse into the substrate layers. A guided mode is a wave that experiences total internal refraction and remains well confined within the waveguide. There can also be more that one guided mode inside a waveguide.

For every mode of a waveguide, there is an associated propagation constant. The propagation constant describes how fast the wave moves along the waveguide. The triangle in Fig. 1 shows a vector relationship between how fast the wave moves through the material and the propagation constant, beta(β). Theta(θ) is the actual angle of wave movement inside the waveguide. The planar waveguide in Fig. 1 demonstrates how a waveguide can have two modes. Notice that both modes experience total internal refraction, but they bounce off the surfaces at different angles. This shows why the two modes are different. Since the waves travel at the same speed inside the material but at different angles, they travel along the X axis at different speeds. The same principle applies to all guided waves in a waveguide.

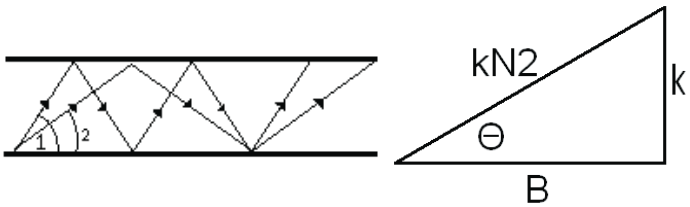

Figure 1. Right: The propagation constant vector relationship. Left: A waveguide with two guided modes.

The power flow diagram of a 2-D cross-section of a waveguide (see Fig. 2) shows how light waves propagate through a 3-D waveguide. The red area indicates where the majority of the light is concentrated. Fig. 2 demonstrates the difference between a hybrid waveguide and a traditional waveguide. In the hybrid waveguide the mode is much more confined in the narrow low index region rather than in the high index blocks. This happens because of a large discontinuity in the transverse E-field at the high-index material–cladding interface.[2]

Another advantage of a hybrid waveguide is that the modes of the waveguide depend more on the index of refraction (index) of the cladding layer than traditional waveguides because the light propagates through the cladding material. If an active material is used for the cladding layer, the index of this material could be changed, which would affect the propagation of the mode. Recent advances in electro-optic (EO) polymers allow them to experience a very large change in their index of refraction when an electric field is applied across them.[3] This effect can be used with hybrid waveguides to change the propagation constant of the modes of a hybrid waveguide enough to allow the waveguides to be reduced in size for modulator applications and still remain effective. For an example, in a Mach-Zehnder modulator a traditional waveguide arm would have to be about 2cm in length while a hybrid waveguide arm would only have to be .5 to 1mm in length to be equally effective.

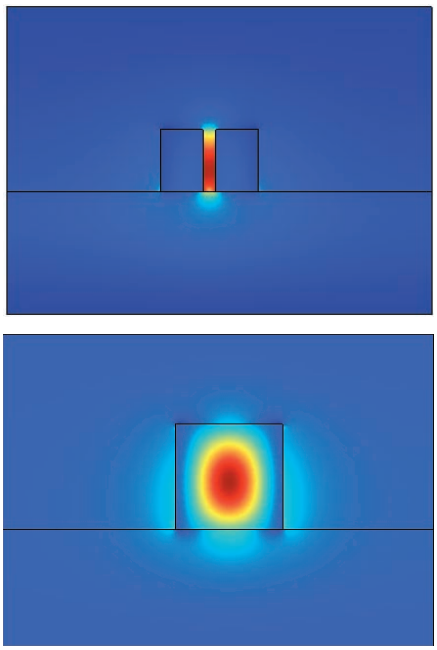

Figure 2. Top: A power flow diagram of a hybrid waveguide's guided mode. Bottom: Power flow diagram of a traditional waveguide guided mode.

The goal for this summer's research is to discover how changing the dimensions of hybrid waveguides will affect the waveguide's propagation constant and also what dimensions will produce the greatest change in the propagation constant due to a constant change in the index of refraction without allowing light to form a guided mode in the silicon blocks.

To accomplish this task, a modeling program called FEMLAB 3 was used for simulation of the structures. The dimensions that can be changed are: the index of the cladding layer, the height and width of the blocks, and the space between the two blocks (space).

RESULTS

An EO polymer's ability to alter the index of refraction can be modeled by a simple equation: [3]

$$-\Delta n = \frac{n^3 r_3 V}{2d} \quad (1)$$

Where n is the original index of refraction, r_{33} is an electro-optic coefficient, V is voltage applied, and d is the distance between electrodes. Using appropriate values, the typical Δn is around -.002 to -.003. In this paper all shifts of index of refraction of the cladding layer will be -.002, and will be referred to as "the shift", and "the change" or "change" will refer to how much the propagation constant changes due to a -.002 change in the index of refraction of the cladding layer. All the graphs will show the absolute change of the propagation constant. Also note that the graphed data is derived from finding the difference of two propagation constants; one when the index of the cladding layer is unshifted or without an applied voltage (for example 1.202), the other is when the index of the cladding layer is shifted due an applied voltage (for example 1.200).

Index of Refraction

Looking at the effect the shift has on the propagation constant when the base index of refraction of the cladding layer is varied, it is found that over the range of 1 to 1.5 the changes is relatively constant. With dimensions of height 200nm, width 180nm and space 50nm, the change only varies by $6m^{-1}$ over an index change of 0.03, as illustrated in Fig. 3. A larger range of indexes was sampled and similar results were found.

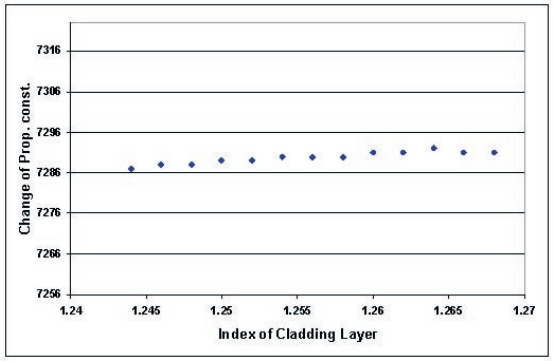

Figure 3. The amount the propagation constant changes with a -.002 change of the index of the cladding layer. Data observed at height: 200nm, width: 180nm, and space: 50nm.

It is important to note that the larger the index of cladding layer will result in a larger change in the index of refraction, according to Eq. (1). This was not taken in to account in the above analysis.

Height of the Silicon Blocks

Adjusting the height of the silicon blocks has a much different effect than changing the index of the cladding. To determine the maximum change in propagation constant, a range of heights from 200nm to 390nm were sampled with a width of 200nm, a space of 50nm, and a index of the cladding layer of 1.002 (see Fig. 4). A maximum change was found at 370nm. However, with silicon blocks this tall, a second guided mode exists within the blocks themselves. The shorter the silicon blocks are, the more the undesired guided mode becomes a substrate radiation mode.

The question then becomes, when does the guided mode in the silicon blocks become primarily a substrate radiation mode (see Fig. 5)? It seems that a useful range for heights will be between 160nm to 270nm depending on the width of the silicon blocks. In this range the power going through the substrate will be around half as much as the power going through the space. It should also be noted that since the range of effective heights is far

away from the height that has the maximum change, variations of the height will cause a noticeable difference in the propagation constant and also how much it changes due to the shift, as shown in Fig. 6.

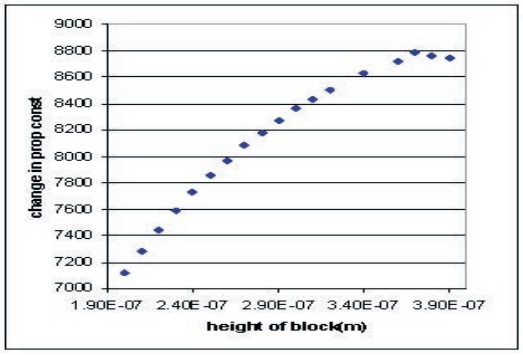

Figure 4. The amount the propagation constant changes due to a -.002 change of the index of the cladding layer. Data observed at width: 200nm, space: 50nm, and index of cladding: 1 to 1.002

Width of Silicon Blocks

When the width of the silicon blocks was model at various dimensions, the results were more pleasing than when the height was varied. Adjusting the width can produce a maximum change while the second undesired mode is remains unguided. This is convenient because variations in the width due to manufacturing process will not alter the change significantly (see Fig. 7). However, there is not a universal ideal width. The ideal width depends on the height, space, and the index of the cladding layer, but it was observed that the range of ideal widths is between 170nm to 250nm and it is always 10 to 40nm less than the height of the silicon blocks.

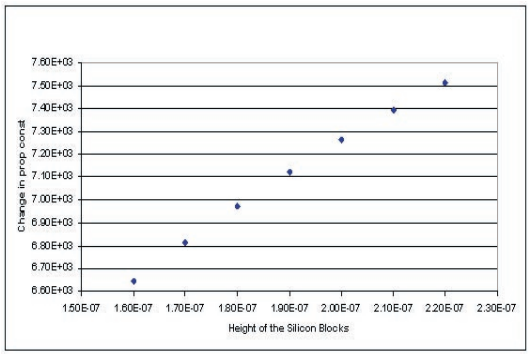

Figure 6. The amount the propagation constant changes due to a -.002 change of the index of the cladding layer over an appropriate range. Data observed at width: 180nm, space: 50nm, and index of refraction: 1.2 to 1.202

It is possible to get a second guided mode within a hybrid waveguide by increasing the width of the silicon blocks, but the blocks would have to be much wider than where the optimal dimensions illustrated in Fig. 7. Also if the blocks are not tall enough to have a guided mode increasing the width will have little affect on how well guided the second, undesired mode will be.

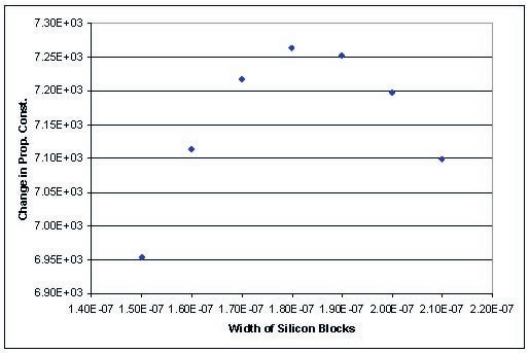

Figure 7. The amount the propagation constant changes due to a -.002 change of the index of the cladding layer. Data observed at height: 200nm, space: 50nm, and index of refraction: 1.2 to 1.202

Space between the Silicon Blocks

Looking at what happens when the space between the two silicon blocks is the varied, a maximum change can be observed, as shown in Fig. 8. Unlike height and width, the ideal space is at a currently hard to manufacture dimensions (typically around 50nm). At currently manufacturable dimensions the change decreases near linearly as space increases (see Fig. 8).

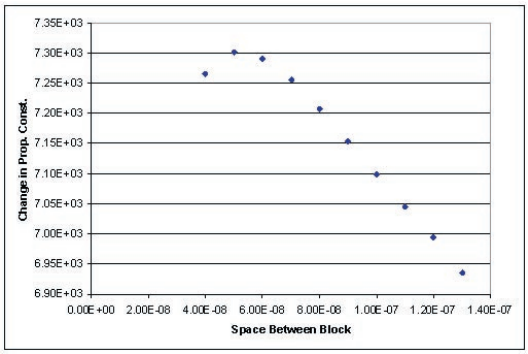

Figure 8. The amount the propagation constant changes due to a -.002 change of the index of the cladding layer. Data observed at height: 210nm, width: 200nm, and index of refraction: 1 to 1.002

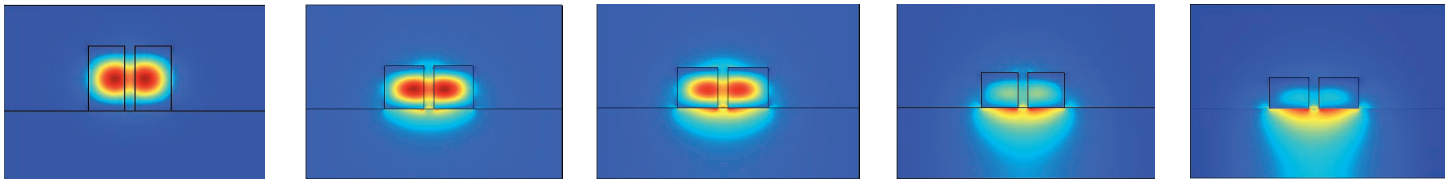

Figure 5. This shows how decreasing the height (370 nm, 250 nm, 230 nm, 200 nm, 170 nm) can direct the light in to the substrate.

At closer spaces the second undesired guided mode becomes more guided, and less power flows though the space. Wider spaces will result in a less guided undesired mode for the modeling index of refraction and dimensions of the silicon blocks.

CONCLUSIONS

As the index of refraction of the cladding layer increases, the change in propagation constant due to a 0.002 decrease in the index of the cladding remains largely constant.

When the height is increased, a maximum change of propagation constant is observed due to a constant change in the index of refraction. However, as the silicon blocks get taller a second guided mode is also formed.

A greater silicon width also results in a maximum in the change in propagation constant with a constant variation of the index of the cladding. Again, wider silicon blocks more strongly support a second, undesired guided mode.

When the space between the two silicon blocks is increased, the change in propagation constant experiences a maximum at currently difficult to manufacture dimensions.

There is a tradeoff between how strongly guided the undesired mode is and how much the propagation constant can change. The larger the propagation constant change, the more strongly guided a mode is within the silicon blocks.

REFERENCES

1. Qianfan Xu, Vilson R. Almeida, Roberto R. Panepucci, and Micheal Lipson. Opt. Lett. Vol. 29, No. 14, July 15, 2004

2. Vilson R. Almeida, QianFan Xu, Carlos A. Barrios, and Michal Lipson. Opt. Lett. Vol. 29, No. 11, June 1, 2004.

3. G. L. Lee and P. K. L. Yu. Journal of Lightwave Technology, vol 21, no. 9 Sept 2003.

ACKNOWLEDGEMENTS

Prof. Scott Dunham, Kjersti Kleven, (mentor), University of Washington Electrical Engineering Dept., Hooked on Photonics program, National Science Foundation, STC-MDITR

Andrew Gardner recently earned an AS in Engineering from Highline Community College and is currently in the Electrical Engineering Department at the University of Washington. He intends to graduate with a BSEE in spring 2007.

Synthesis and Analysis of Thiol-Stabilized Nanoparticles

Eddie Howell
Norfolk State University

Joe Perry and Wojtek Haske
Perry Lab, School of Chemistry and Biochemistry
Georgia Institute of Technology

Dr. Carl Bonner
Center for Materials Research
Norfolk State University

INTRODUCTION

Metal nanoparticles have gained much interest in the scientific community in recent years due to the unique optical and electronic properties that these particles possess. Potential applications for metal nanoparticles include biological imaging, three-dimensional microfabrication, and optical data storage.[1]

The primary obstacle scientists are currently trying to overcome is identifying ways to manipulate the size, shape, and distributions of these nanoparticles. A characteristic of all metal nanoparticles is that delocalized electrons exhibit collective oscillations in an electric field. These collective oscillations are commonly referred to as plasmons. The particles can absorb energy from electromagnetic waves when the frequency is in resonance with the plasmons. Large local electric fields are present near the nanoparticle surface. This effect is called near-field enhancement of the electric field. It has been shown in some cases that this near field enhancement can enhance the nonlinear optical properties of molecules near the surface of the nanoparticle.

The first four weeks of this research project were spent at Norfolk State University working with Dr. Carl Bonner to find suitable methods and reagents for synthesizing the silver nanoparticles. During the following five weeks in Dr. Perry's research lab at Georgia Tech the research project has involved the synthesis of silver nanoparticles with different thiol ligands on their surface. Polymer nanocomposite films were prepared using these nanoparticles and their optical properties were investigated

METHODS

Synthesis of Silver Nanoparticles

A single-phase method was used for synthesizing the silver nanoparticles which involves reducing silver ions with sodium borohydride in the presence of thiol ligands (see Fig. 1 for the ligands used). The process begins with making a solution of silver nitrate dissolved in ethanol. The desired amounts of thiol ligands were then added to the solution. The ratio or type of ligands for each batch was varied, but the silver to total thiol ratio was held constant at 3:1 for all batches. The solution was then placed in an ice bath and stirred for 15 minutes. A solution of sodium borohydride dissolved in ethanol was then added dropwise to the silver nitrate solution and allowed to reflux for another 15 minutes. The resulting solution was then placed in a freezer and allowed to sit overnight, causing the thiol-coated nanoparticles to precipitate out of the suspension and settle to the bottom of the flask. The nanoparticles were then filtered and washed sequentially with ethanol, distilled water, and acetone to remove any excess sodium borohydride. The particles were dried in a vacuum oven at room temperature overnight.

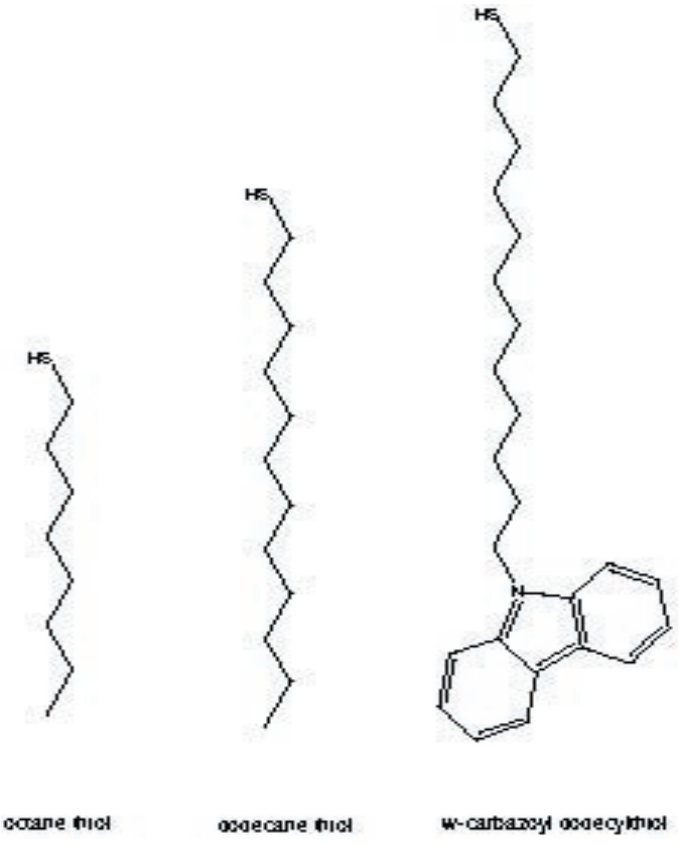

Figure 1. Thiol ligands used to coat the silver nanoparticles.

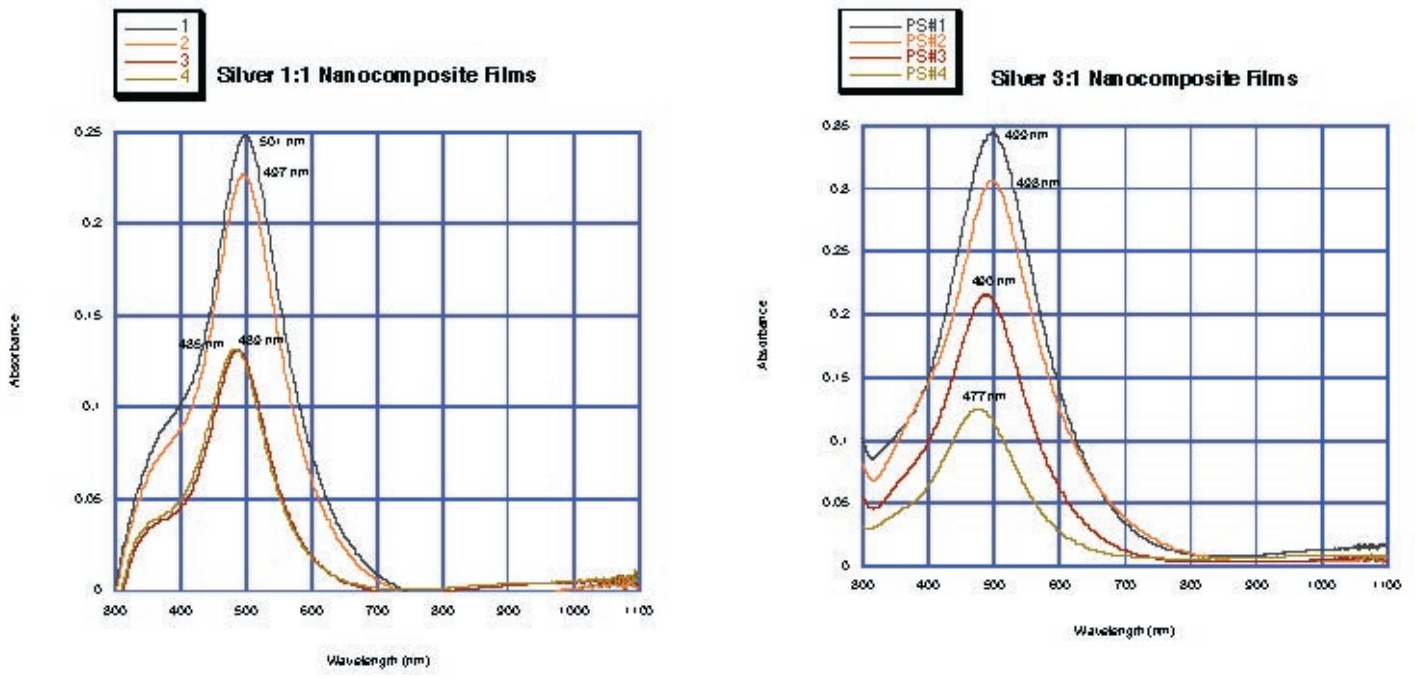

(**a**) (**b**)

Figure 2. Absorption spectra of silver nanoparticles in polystyrene thin films. The particles were coated with octanethiol to dodecanethiol ratios of (**a**) 1:1 and (**b**) 3:1

Nanocomposite Films

The silver nanoparticles were dissolved in a polystyrene matrix and made into thin films to study their optical properties. The first method used to make these films was spin coating. The nanoparticles and polystyrene were first dissolved in a solvent such as toluene and placed in a small vial. A small amount of solution was then drawn from the vial with a syringe. A glass substrate was placed onto the spin coater and the solution was filtered and dispensed onto the substrate evenly. The substrate was allowed to spin for two minutes at 1000 rpm. UV-vis absorption spectra were measured for these films with varying ligand ratios and nanoparticle concentrations. Films made in this manner, however, were too thin to be used for x-ray diffraction studies, so a different method, (solvent-evaporation method), was employed. The glass substrates also had to be modified with an adhesion promoter to keep the polymer from peeling off of the glass slides.

Three drops of the adhesion promoter solution were put onto the slide and the slide was then rotated at 3000 rpm for 3 seconds on the spin coater. The slide was then heated at 90°C on a hot plate for 30 seconds. This process was repeated 3 times. Initially, to make the nanocomposite films, a microscope slide was covered with the nanoparticle/polymer solution and placed in an evaporation chamber overnight to allow the solvent to slowly evaporate. The films obtained were thick enough for x-ray diffraction measurements, but the particles were not very well dispersed throughout the film. This was likely due to the particles aggregating overnight as the solvent evaporated.

To try and prevent the aggregation of particles the solutions were filtered in the same way but the films were prepared at a higher temperature. The temperature had to be lower than the boiling point of the solvent to keep the film from bubbling, so a solvent with a high boiling point was used (dichlorobenzene). The modified slides were placed on a hot plate and first heated to 120°C. The nanocomposite solution was then filtered onto the slides and allowed to sit for 1 hour.

RESULTS

Absorption spectra were obtained for the nanocomposite films made by spin coating (Fig. 2). The nanoparticles were synthesized with octanethiol to dodecanethiol ligand ratios of 1:1 and 3:1. The concentration of nanoparticles for each successive film in each graph was decreased by one-half. The absorption spectra for the 1:1 films exhibit a shoulder at about 400 nm, which as of now cannot be fully explained. The absorption peaks of the 1:1 films are narrower than those of the 3:1 films, which may correlate with a change in the shape and distribution of silver nanoparticles within the polymer matrix. A blue shift in the position of the plasmon resonance band is observed when the concentration of nanoparticles in the film decreases.

CONCLUSIONS

Changing the thiol ligands bonded to the silver nanoparticles has shown to alter the optical properties of the nanocomposites. This is likely due to the fact that different ligands or different ligand ratios in the case of mixed coatings, can affect the interaction between nanoparticles or between the nanoparticles and the polymer, and the arrangement in the solid matrices. For weak binding, as the concentration of nanoparticles decreases, the space between individual particles increases, and the interactions between them could become weaker. More studies are needed to determine why this causes a blue shift in the absorption peaks.

FUTURE WORK

In the future, properties of chromophore thiol-coated metal nanoparticles will be investigated to determine how different ligands affect nonlinear optical properties of the nanoparticle-chromophore system. By using solvent evaporation methods, the films can be made with a thickness that is sufficient for use in x-ray diffraction studies. X-ray diffraction will be used to further study the spatial arrangements of the silver nanoparticles in polymer matrices.

ACKNOWLEDGEMENTS

Dr. Joe Perry, Faculty Advisor, Georgia Institute of Technology
Wojtek Haske, Graduate Student, Georgia Institute of Technology
Perry Group, Georgia Institute of Technology
Dr. Carl Bonner, Faculty Advisor, Norfolk State University
Center for Materials Research, Norfolk State University

REFERENCES

1. Stellacci, F.; et al. *J. Am. Chem. Soc*. **2003**, *125*, 328

Quinoxaline-Containing Polyfluorenes: Enhanced Blue Electroluminescence by Addition of a Hole Blocking Layer

Kelli A. Irvin
Montana State University

Jessica M. Hancock and Samson A. Jenekhe
Deptartments of Chemical and Chemical Engineering
University of Washington

INTRODUCTION

The commercial market today is saturated with products using flat panel displays from cell phones to computer screens and personal data organizers to billboards. Currently, liquid crystal displays (LCDs) dominate the market with high resolution and affordability[1]. The only challenger to this domination may perhaps be the organic light-emitting diode (OLED). OLEDs show promise to consume less energy, lower costs due to ease of manufacturing of conjugated polymers, and be brighter than LCDs. In addition, conjugated polymers have properties such as ease of processing using spin casting, low drive voltages due to the excellent charge mobility, and novel properties such as flexibility.[2] OLEDs don't have the need for backlighting and the overall product would have a slimmer profile due to the nanoscale thickness of the layers used in processing. [3]

Conjugated polymers were first recorded to be electroluminescent in the 1990s by J.H. Burroughes, *et al.,* using poly(*p*-phenylene vinylene), or PPV. [4] Since their initial discovery, great advancements have been made included tunable color, stable color across a voltage range, and more efficient devices using multiple layers.

Challenges that need to be overcome for OLEDs include display lifetimes and stable true blue color. Poly(9,9'-dioctyl-fluorenes), or PFO, has been widely researched as an emissive layer yielding stable blue color.[5] PFO is a p-type material that transport holes and blocks electrons with high mobility throughout the delocalized conjugated chain. Although PFO is capable of efficiently transporting holes, it lacks the ability to efficiently transport electrons and block holes. Copolymerization with an n-type material shows promise to enhance the electron transport properties of the polymer while maintaining the blue emission. Therefore, more research is needed to find a material that exhibits stable blue color and has the ability to be a bifunctional emissive layer.

BACKGROUND

Previously, Kulkarni, *et al*.[6], completed work using six molar ratios of the copolymer 2,3-bis-(p-phenylene)quinoxaline-containing poly(9,9'-dioctyl-fluorenes) (QXF) (Figure 1a) as the emissive layer in OLEDs to obtain stable blue electroluminescence. The motivation for incorporating the quinoxaline moiety was to improve the electron transport of commercially produced PFO. Copolymerizing a p-type and n-type material could eventually lead to the realization of a material capable of efficient electron and hole transport. The configuration of the devices incorporated poly(*N*-carbazole) (PVK) to enhance the injection of holes into the device. The work outlined in the proceeding sections introduced a hole blocking layer into the architecture of the device in an effort to enhance brightness and efficiency. Ultimately, the true ability of QXF as an emitter will be shown or the realization of QXF as a bifunctional material will be demonstrated.

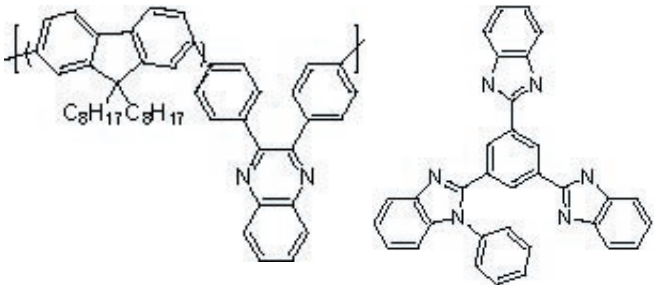

Figure 1. Chemical structures of (left) QXF and (right) TPBI**.**

Fabrication and Characterization of LEDs

Three configurations of devices were fabricated using three selected molar ratios based on the quinoxaline content as the emissive layer. The three molar ratios will be noted as QXF2, QXF5, and QXF15 (Figure 1a). All devices were fabricated with the same anode and cathode using indium-tin oxide (ITO) and LiF/Al, respectively. Poly(ethylenedioxythiophene) doped with poly(styrenesulfonate) (PEDOT) was spin cast for improved injection of holes. The first device as shown in Figure 2a was a single layer LED with the copolymer QXF as the emissive layer. PVK was incorporated into the architecture of the second configuration (Figure 2b). The third device (Figure 2c) included both the PVK layer and incorporated 1,3,5-tris(*N*-phenylbenzimidizole-2-yl)benzene (TPBI) (see Figure1b) as a hole blocking layer. The three architectures based on QXF as the emissive layer were ITO/PEDOT/QXF/LiF/Al (Diode I), ITO/PEDOT/PVK/QXF/LiF/Al (Diode II), and ITO/PEDOT/PVK/QXF/TPBI/LiF/Al (Diode III).

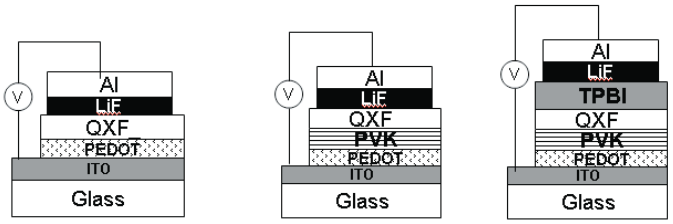

Figure 2. Device Configurations of (top left) ITO/PEDOT/QXF/LiF/Al (Diode I), (top right) ITO/PEDOT/PVK/QXF/LiF/Al (Diode II), and (bottom) ITO/PEDOT/PVK/QXF/TPBI/LiF/Al (Diode III).

Glass coated with indium-tin oxide (ITO) was used as the substrate and anode. The ITO glass was cleaned by a process of twenty minute cycles of sonication in deionized (DI) water, a 50:50 by volume mixture of DI water and isopropyl alcohol, toluene, DI water, and acetone, respectively. The substrate was dried overnight under vacuum. PEDOT was spin cast from a filtered 1:3 dispersion of PEDOT and DI water. The PEDOT layer was spin cast onto the ITO to achieve on average a thickness of 55 nm. The PEDOT layer was heat treated at 180°C for ~15 minutes under vacuum. Where applicable, a 10-15 nm layer of PVK was cast onto the PEDOT layer and dried four hours at 50°C under vacuum. The copolymer [QXF(2,5,15)] was cast subsequently from a filtered 1% weight solution in toluene to achieve a 50-60 nm layer and was dried overnight under vacuum at 50°C. When applicable, a 20-25 nm layer of TPBI was deposited via thermal evaporation at pressures of less than 3 x 10^{-6} torr and a deposition rate of 0.2-0.3 nm/s.. The electrodes were also deposited using thermal evaporation. 2 nm of LiF was evaporated followed by 145-150 nm of Al deposited without breaking vacuum at pressures <2 x 10^{-6} torr. The resulting diodes exhibited an area of 0.2 cm^2.

Characterization of the devices was performed directly after the deposition of the electrodes to obtain maximum results. Luminance-current-voltage (L-I-V) characteristics were measured simultaneously using an optometer with a luminance sensor head to detect photons and a semiconductor parameter analyzer used to measure current density as a function of voltage.

RESULTS AND DISCUSSION

Synthesis and Characterization

The synthesis and characterization of the varying molar ratios of the QXF copolymer were completed by Kulkarni, *et al.*, and is discussed in detail in that work. [6]

Photophysical Properties

Dilute solutions (10^{-7} M) in toluene were used to investigate the optical absorption and photoluminescent (PL) emission spectra of each molar ratio. Thin film data was collected from 50 nm thin films cast from 1% wt solutions in toluene. A Lambda 900 UV/Vis/Near-IR spectrophotometer was used to record the absorption spectrum. The PL emission was obtained using a Photon Technology International spectrofluorimeter with an excitation wavelength of 380 nm for all devices. Table 1 shows all results for absorption and PL emission spectra.

polymer	λ_{max} [a] sol'n (nm)	λ_{max} [b] sol'n (nm)	λ_{max} [a] thin film (nm)	λ_{max} [b] thin film (nm)
QXF2	385	415	383	438
QXF5	382	415	382	437
QXF15	377	415	381	428

[a] The absorption maximum in toluene solution or in a thin film.
[b] The PL emission maximum in toluene solution or in a thin film.

Table 1. Photophysical Properties

Photophysical properties were measured in solid state and a solution state. The solution state environment afforded a study of a single polymer chain. Conversely, the thin film state allows insight into the how the polymer chains interact with one another. Therefore, the thin film, or solid state, expresses the properties of a system of polymer chains and how their interactions effect emission and absorption of wavelengths of light.

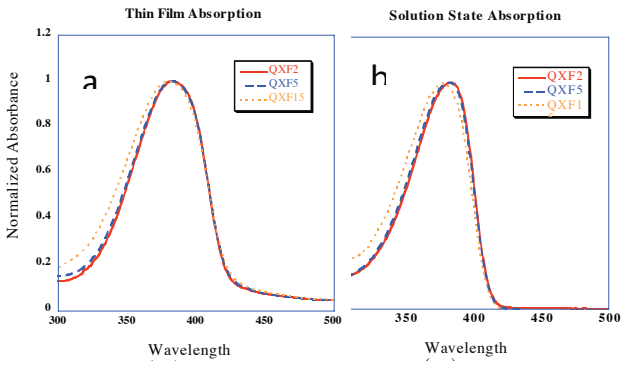

Figure 3. Absorption Spectra of QXF2, QXF5, and QXF15 in (a) thin film and (b) solution state.

The absorption spectra of both the thin film and solution state are shown in Figure 3a and 3b. The absorption spectra show the absorption of energy as electrons are promoted to various vibronic levels within the excited state and allows for the study of the ground state of the material. The QXF2, QXF5, and QXF15 copolymers showed maximum absorbance wavelengths of 385, 382, and 377 nm respectively in solution state. As the molar ratio of quinoxaline increased, a blue shift of 8 nm was observed in the solution state absorption spectra. Likewise, the thin film exhibited a slight shift of 2 nm in the maximum absorption peaks of QXF15 (381 nm) to QXF5 (383 nm). It is understood that increased conjugation length leads to red shifted absorption. Therefore, the higher energy absorption band of the QXF15 relative to QXF2 is indicative of decreasing conjugation length due

to the increasing quinoxaline content. The quinoxaline content interrupts the conjugation along the carbon backbone of the polymer by introducing kinks and bends which disturb the delocalized electron cloud.

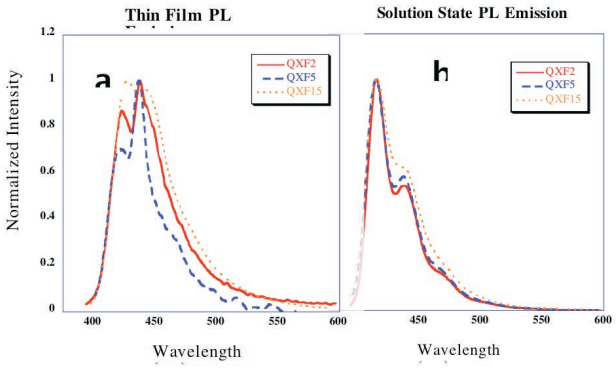

Figure 4. Photoluminescent Emission Spectra of QXF2, QXF5, and QXF15 in (a) thin film and (b) solution.

The PL emission spectra for both thin film and solution state are shown in Figure 4 with maximum emission at 383 nm (QXF2) and 438 nm (QXF2), respectively. The PL emission is a snapshot excited state of the copolymer and emission is a result of the relaxation of excited electrons from the lowest vibration level of the excited state to the ground state. The solution state PL emission spectrum (Figure 4b) is red shifted ~34 nm from the solution state absorption spectrum, and the thin film PL spectrum (Figure 4a) is red shifted ~50 from the thin film absorption spectrum. The thin film PL emission spectra shows a ~15 nm red shift relative to the solution state emission. The red shift in the PL spectra suggests increasing conjugation length as a result of interchain interactions between neighboring polymer and increased delocalization of electrons that resulted in a lower energy emission.

Electroluminescent Properties

Table 2 shows the electroluminescent properties of Diodes I, II, and III (Figure 2) based on QXF2, QXF5, and QXF15 as the emissive layers. The results for the single layer (Diode I) devices will not be shown graphically or in tabular form. The electronic structures for Diodes I, II, and II are shown in Figure 5. The values are of the electron affinity (EA) and ionization potential (IP) of each material. The electronic structures of each diode show the extent of barrier to charge injection between adjacent layers and demonstrate the ease of charge mobility through the diode. QXF has a low-lying IP of 5.8 eV relative to vacuum level (0 eV). The addition of PEDOT as a hole injection layer between the anode and the emissive layer minimized the barrier to hole injection, but a significant difference of 0.6 eV still existed between the IPs of PEDOT and QXF. PVK has an ionization potential of 5.8 eV that approaches ohmic contact between the IP of QXF and the IP of PVK implying that no barrier for the injection of holes into the emissive layer exists. Diode I was fabricated to insure that Diode II was demonstrating enhanced device performance for all molar ratios due to the minimization of the barrier to charge injection. Kulkarni, *et al*., completed the cyclic voltammetry of the copolymer and found no significant differences in the ionization potential and electron affinity of the copolymer relative to PFO.[6] However, it was expected that the addition of the n-type quinoxaline moiety would improve the electron transport properties of the materials leading to a higher electron affinity. TPBI has a low- lying ionization potential at 6.7 eV that blocks holes and aides in confining charge recombination to the emissive layer. Therefore, the addition of the TPBI hole blocking layer could improve performance and efficiency of the devices by minimizing quenching of the charges at the interfaces.

	L_{max} (cd/m²)	$J_{L\,max}$ (mA/cm²)	V[a] (V)	V_{on} (V)	λ_{max}^{EL} (nm)	EQE[b] %	LE[c] (cd/A)	$L_{@\,LE}$ (cd/m²)	CIE 1931
PVK Device									
QXF2	305	170	11	~5	422	0.81	0.20	235	(0.16, 0.04)
QXF5	1180	470	15	~5	421	0.33	0.25	1180	(0.16, 0.04)
QXF15	176	221	11	~6	421	0.34	0.092	110	(0.16, 0.05)
TPBI Device									
QXF2	1620	185	13	~5	424	1.52	0.91	1530	(0.19, 0.09)
QXF5	1510	265	12	~5	437	1.77	0.71	115	(0.16, 0.05)
QXF15	425	137	13	~6	424	0.81	0.40	165	(0.15, 0.08)
PFO	700	170	8	~4	421	3.2	0.91	108	(0.16, 0.11)

[a] Drive Voltage, [b] External Quantum Efficiency is defined as the ratio of the number of photons emitted per number of electrons injected
[c] Luminous Efficiency is a calculation made by dividing the maximum luminance (L_{max}) but the current density at the $L_{max.}$

Table 2. Electroluminescent Characteristics

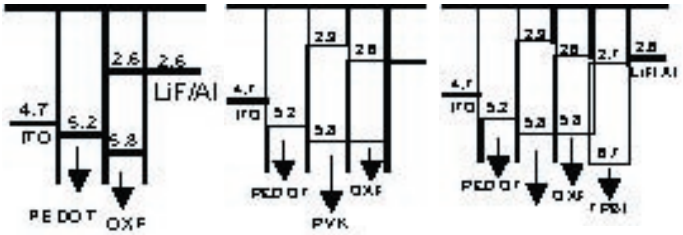

Figure 5. Electronic Structures of (a) Diode I, (b) Diode II, and (c) Diode III.

The EL spectra of Diode II and Diode II of each molar ratio are shown in Figure 6. No significant shifts in the peaks or line shape were found for any diodes or molar ratios over the applied voltage range. All diodes were blue emitting with an average CIE of ~(0.16, 0.04), which is similar to the true blue color emitted from the PFO homopolymer. On average, a blue shift of ~15 nm was shown for the EL emission relative to the thin film PL emission.

The current density-voltage and luminance-voltage graphs of Diodes II and III are shown for each molar ratio in Figures 7 and 8, respectively. The turn-on voltages for the QXF2 and QXF5 were ~5 V for all device configurations, while the QXF15 had consistently higher turn-on voltages of ~6 V. The quinoxaline moiety improves electron injection, but the higher turn-on voltages for QXF15 suggest that the improved electron injection lead to a charge imbalance.

Maximum luminances for Diode I were 230, 160, and 24 cd/m^2 with luminous efficiencies (LE) of 0.05, 0.03, and 0.01 cd/A for QXF2, QXF5, and QXF15, respectively. The EQE values were very low at 0.19, 0.14, and 0.032% for QXF2, QXF5, and QXF15. The low brightnesses and efficiencies for the device were expected due to the large barrier to hole injection of 0.6 V between the PEDOT and QXF layers. Highest brightness for Diode II was exhibited by QXF5 with a luminance of 1180 cd/m^2, LE of 0.25 cd/A, and EQE of 0.33%. For Diode III, the QXF2 copolymer exhibited the highest brightness, relative to QXF5 and QXF15, of 1623 cd/m^2 with a LE of 0.91 cd/A and EQE of 1.52%.

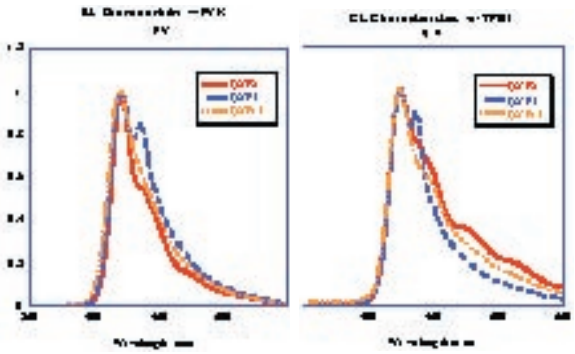

Figure 6. EL Spectra of QXF2, QXF5, and QXF15 for (a) Diode II and (b) Diode III.

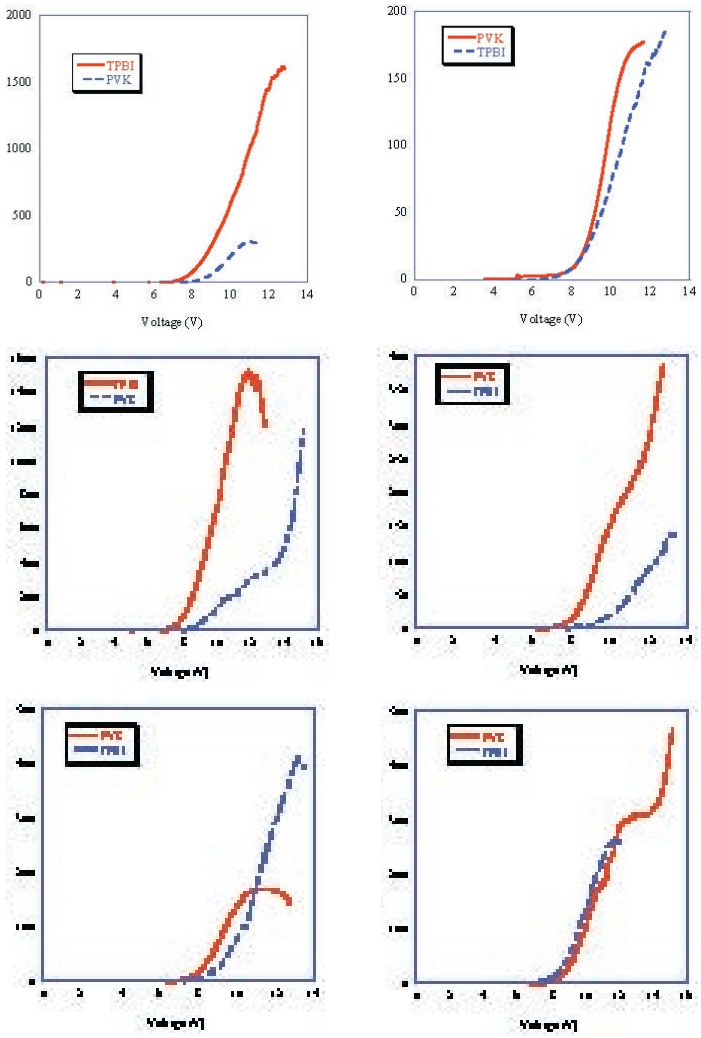

Figure 7. (left column) Luminance-Voltage Characteristics of (top) QXF2, (middle) QXF5, and (bottom) QXF15. Red is Diode III, Blue is Diode II unless otherwise noted.

Figure 8. (right column) Current Density-Voltage Characteristics of (top) QXF2, (middle) QXF5, and (bottom) QXF15. Red is Diode II, Blue is Diode III.

The addition of the TPBI hole blocking layer in Diode III for all molar ratios improved luminance and efficiency. For QXF2, Diode II had a maximum luminance of 310 cd/m^2, LE of 0.20 cd/A, and EQE of 0.81%. The addition of the TPBI layer in Diode III for QXF2 showed a brightness of 1620 cd/m^2, LE of 0.91 cd/A, and EQE of 1.52%. The brightness improved by a factor of 5 and the EQE showed an increase of 0.7% in Diode III relative to Diode II for QXF2. Similar improvements between Diode II and Diode III were shown for QXF5 and QXF15. These improvements in luminance, LE, and EQE between Diode II and Diode III for all molar ratios are due to the low lying IP of TPBI which aides in the containment of charge recombination to the emissive layer.

All molar ratios exhibited an increase in efficiency and brightness when TPBI was added to the device architecture. However,

QXF2 and QXF5 displayed higher brightnesses for all diodes than QXF15. The increased quinoxaline content in QXF15 lead to an imbalance in charge injection that resulted in poor device results for all diodes relative to the results for QXF5 and QXF2. Kulkarni *et al*. observed a similar trend for molar ratios up to 50 mol % quinoxaline (QXF50).[6]

For the Diode III architecture, QXF2 demonstrated a higher brightness of 1620 cd/m^2 than the same device based on QXF5 (L_{max} of 1510 cd/m^2). However, the EQE value for Diode III based on QXF5 was 1.77% which is higher than the EQE of the same diode based on QXF2 (1.52%). For Diode II, a similar trend of higher brightness and lower EQE for QXF5 relative to QXF2 was exhibited. Therefore, better balance in charge injection cannot be conclusively attributed to either QXF2 or QXF5.

A device with configuration of Diode III was constructed based on the homopolymer PFO as the emissive layer. A peak brightness of only 700 cd/m^2 was shown for this diode. The brightness of 700 cd/m^2 is significantly lower than peak brightness achieve for similar diodes based on QXF2 and QXF5. QXF2 and QXF5 demonstrated peak brighnesses >1510cd/m^2. The addition of the n-type material improved brightness relative to PFO and this improvement can be attributed to better electron transport in the QXF2 and QXF5 copolymers.

CONCLUSIONS

QXF2 and QXF5 show promise as copolymers capable of stable blue electroluminescence over a wide voltage range. Diode III for QXF2 and QXF5 exhibited improved brightness from a similar diode using PFO as the emissive layer. The improvement in brightness suggests less quenching of luminance at the interface for devices based on a copolymer of n-type and p-type materials compared to a device using a p-type material as the emissive layer. The incorporation of TPBI as a hole blocking layer into a device with PVK as a hole injection layer exhibited enhanced brightness and efficiency when compared to a device without the TPBI layer. The power of n-type and p-type materials compolymerized as an emissive layer with the incorporation of a hole blocking layer into a device was demonstrated.

REFERENCES

1. Kelly, S.M.; Flat Panel Displays. In *Flat Panel Displays: Advanced Organic Materials*; Connor, J.A.; RSC Materials Monographs Series; R. Soc. Chem: Cambridge, UK 2000; pp 5-7.
2. Friend, R.; Burroughes, J.; Shimoda, T.; Polymer diodes. Physics World 1999, pp. 35-36.
3. Howard, Webster E. Better Displays with Organic Films. *Scientific American*, Jan 12, 2004, pp 1-4.
4. Burroughes, J.H., et al. Light-emitting diodes based on conjugated polymers. *Nature* **1990**, *347*, 539-541.
5. Leclerc, M. Polyfluorenes: Twenty Year of Progress. Journal of Polymer Science: Part A: Polymer Chemistry 2001, Vol 39, 2867-2873.
6. Kulkarni, A.P.; Zhu, Y.; Jenekhe, S.A. Quinoxaline-Containing Polyfluorenes: Synthesis, Photophysics, and Stable Blue E Electroluminescence. *Macromolecules* **2005**, *38*, 1553-1563.

ACKNOWLEDGEMENTS

Prof. Jenekhe, Jessica Hancock (mentor), Deptartments of Chemistry and of Chemical Engineering at the University of Washington, Hooked on Photonics program, National Science Foundation, STC-MDITR

Kelli Irvin is currently studying chemical engineering at Montana State University. She will be transferring to the University of Washington in Winter of 2006 to complete her degree. Kelli intends to obtain an engineering position in industry upon graduation.

Synthesis of Dendron-Functionalized Chromophores: An Approach to Supramolecular Assembly for Electro-optic Applications

Zerubba Levi
Gonzaga University

Sei-Hum Jang and Alex Jen
Department of Materials Science and Engineering
University of Washington

INTRODUCTION

Organic nonlinear optical (NLO) chromophores present a number of applications in optical communication systems and storage devices. Basic research efforts are aimed at pushing the bandwidths of optical networks to 80, 100 and even 160 GHz with the use of novel organic chromophores. The application of organic electronics to commercial devices demands the thermal, chemical, and photo-stability of the materials. Balancing the optical transparency while maximizing the nonlinear response and ensuring accentric geometry of the chromophores in bulk materials is also of critical importance.

Recent work in the synthesis of NLO materials has extensively used dendrimers to reduce dipole-dipole interactions between chromophores through the site-isolation effect. As a result, much higher poling efficiencies, temporal alignment stabilities and nonlinear responses have been observed. In this project a series of NLO chromophores were synthesized with the careful selection of monolithic and binary dendron structures to produce pre-aligned systems with the capacity for supramolecular assembly upon electric field poling.

Benzene and hexafluorobenzene (HFB) are known to cocrystalize in a face-to-face manner through several noncovalent associative interactions such as electrostatic quadrupolar interactions (see Figure 1).[1]

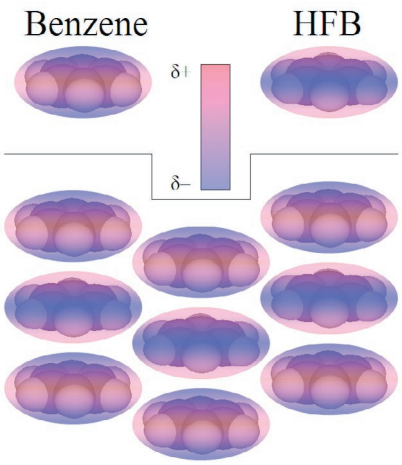

Figure 1. Stacking arrangement of Benzene/HFB complex.

Recent efforts in the Jen group have provided solid state evidence that arene-fluoroarene dendrons can produce supramolecular structures. The results provided by the Jen group illustrate chromophores capable of the arene-fluoroarene (Ar-Ar^F) interactions produced enhanced r_{33} coefficients, T_g values, and thermal stabilities relative to those chromophores that could only exhibit Ar-Ar or Ar^F-Ar^F interactions. This suggests the Ar-Ar^F interactions between monolithic dendrons ameliorate the poling process through π-π attractive forces that counteract the dipole-dipole forces among the chromophores. Despite the significant improvements of the r_{33} coefficients of these systems over other materials, work still needs to be made to improve the thermal properties of the materials.

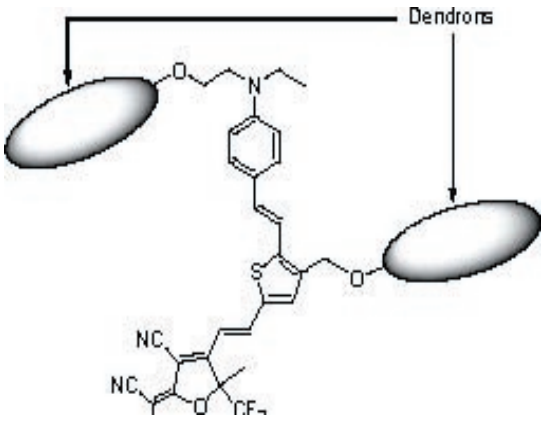

Figure 2. Chromophore functionalized with dendrons

Studies using *ab initio* calculations performed with the DFT method indicate the cohesive energy of heterodimers (E_c) increases as the electron density of the π-donating system increases (see Table 1).

Heterodimer	E_c (kcal/mol)
Benzene/HFB	4-6
Anthracene/HFB	7.7
Pyrene/HFB	8.3
Triphenylene/HFB	8.6

Table 1. Cohesive Energies (E_C) for Heterodimers [2,3]

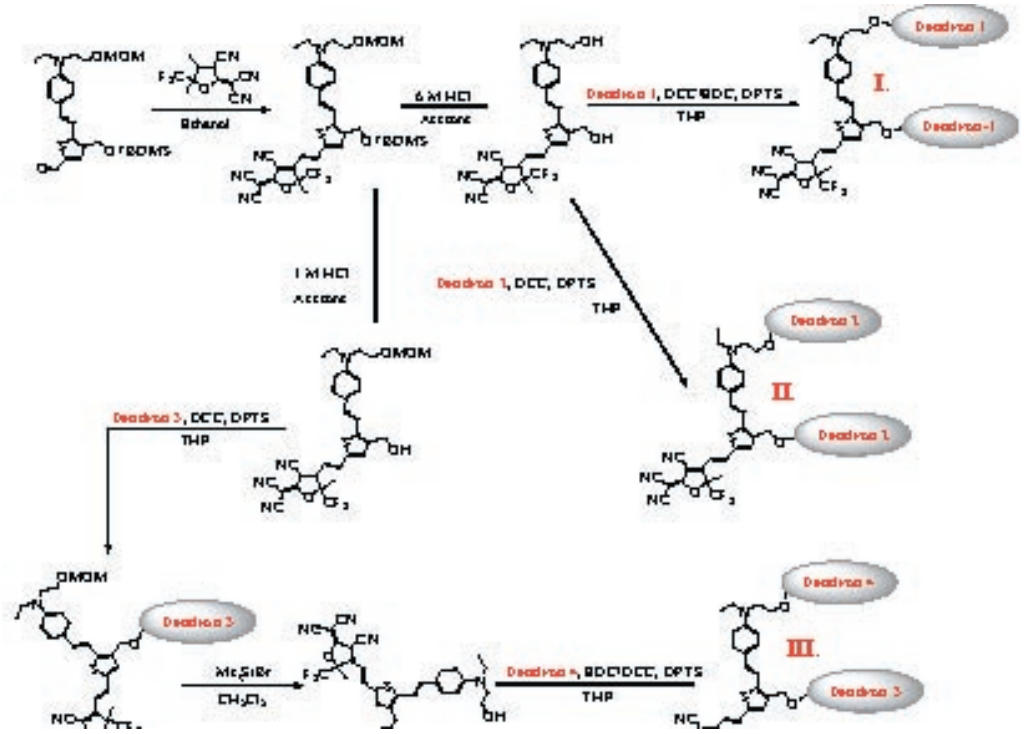

Therefore, a monolithic anthracene-based dendron was synthesized and covalently attached to a chromophore. It was hypothesized that replacement of a phenyl group with an anthracenyl group would lead to an increased cohesive energy between the dendrons (An-Ar^F) thereby strengthening the self-aligning properties of the chromophore. Furthermore, it was expected that the increase in noncovalent attraction between dendrons would result in a higher T_g and an increased thermal stability upon electric field poling.

While previous work has only been concerned with monolithic dendrons, it is important to inquire about the nature of binary dendron systems. The potential for noncovalent, electrostatic quadrupole-quadrupole interactions between dendrons still exists, but it is unclear whether the binary dendron systems offer any energetic or geometric advantages for supramolecular assembly. With this uncertainty present binary dendrons were also synthesized with arene/fluoroarene moieties.

EXPERIMENTAL

Synthesis of Dendron-Functionalized Chromophores

The reaction scheme above illustrates an important synthetic simplification of the binary dendron systems (dendrons 1 and 2) relative to the monolithic dendron systems (dendrons 3 and 4).

Material[a]	T_g (°C)[b]	λ_{max} in soln. (nm)[c]	λ_{max} in thin film (nm)	Poling Field (MV/cm)	r_{33} (pm/V)[d]
1	57	671	719	0.75	52
2	76	655	689	0.75	51
3	75	667	703	1	108
4	153	678	771	---	---
I.	122	670	720	0.75	95
II.	76	660	700	0.73	102
III.	122	670	720	0.75	51

a. Materials 1-4 synthesized previously by Jen Group
b. Measured by DSC (10 °C/min in N_2)
c. Solution in 1,4-dioxane
d. E-O coefficient measured by simple reflection at the wavelength of 1300 nm

Table 2. Results and Comparisons

The binary dendron system requires a single deprotection step followed by a single catalytic esterification. Employing monolithic dendrons necessitate two separate deprotection reactions and two esterifications. Furthermore, r_{33} measurements (see Table 2 below) illustrate the binary dendron systems offer significant improvements in EO activity while maintaining the thermal properties of the monolithic dendron systems.

Chromophore I. displays 100 % stability in the EO activity after 24 hours at $75_{o}C$; similar temporal stability is absent in materials 1-4.

CONCLUSIONS

In summary, a series of monolithic and binary dendrons were synthesized, and covalently attached to highly efficient NLO chromophores. The primary motivation of this work is fine tuning the strengths of arene-fluoroarene interactions between dendrons to produce pre-aligned supramolecular self-assembly to improve material stability and poling efficiencies. Anthracene was incorporated into the dendrons in an effort to increase the noncovalent, arene-fluoroarene interactions between dendrons. While the presence of anthracene increased the thermal stability of the materials, it is unclear for now whether the replacement of the phenyl ring with anthracene leads to stable pre-alignment or improved poling efficiency. However, the binary dendron systems show significantly improved EO activities relative to previous monolithic dendron systems studied. The basis for this improvement will be further studied. Full characterization of structures and material properties are ongoing.

REFERENCES

1. Patrick, C. R.; Prosser, G. S. *Nature* **1960**, *187*, 1021.
2. Collings, J. C.; Roscoe, K. P.; Robins, E. G.; Batsanov, A. S.; Stimson, L. M.; Howard, J. A.; Clark, S. J.; Marder, T. B. *New J. Chem*. **2002**, *26*, 1740-1746.
3. Castellano, R. K.; Diederich, F.; Meyer, E. A. *Angew. Chem. Int. Ed*. **2003**, *42*, 1210-1250.

ACKNOWLEDGEMENTS

Many thanks are given to Tae-Dong Kim, and Zhengwei Shi for helpful discussions and important synthetic intermediates, Steve Hau for sample poling and r_{33} measurements, and the NSF STC-MDITR 2005 Summer REU Program for funding.

Zerubba Levi will be graduating from Gonzaga University in the spring of 2006 with a B.S. in Chemistry. Following graduation he intends to pursue a Ph.D. degree in Organic Chemistry.

Building an Optical Oximeter to Measure the Oxygen Content of Blood Non-invasively

JoAnn Lin
University of Washington

Dr. Antao Chen
Applied Physics Laboratory
University of Washington

INTRODUCTION

Light of certain wavelengths is able to penetrate deeply into the skin and may be absorbed or reflected by the blood. The particular wavelength of light and the color of the blood determine whether the light is reflected or absorbed (Ma et al., 1999). The hemoglobin in red blood cells changes color when bound to oxygen, causing oxygenated blood to appear bright red. The red color is visible because oxygenated blood reflects red light and absorbs other wavelengths. Deoxygenated blood appears dark red because deoxyhemoglobin does not reflect much red light. Deoxyhemoglobin and oxyhemoglobin have significant differences in absorption of light in the near infrared region (approximately 700 nm-900 nm, figure 1).

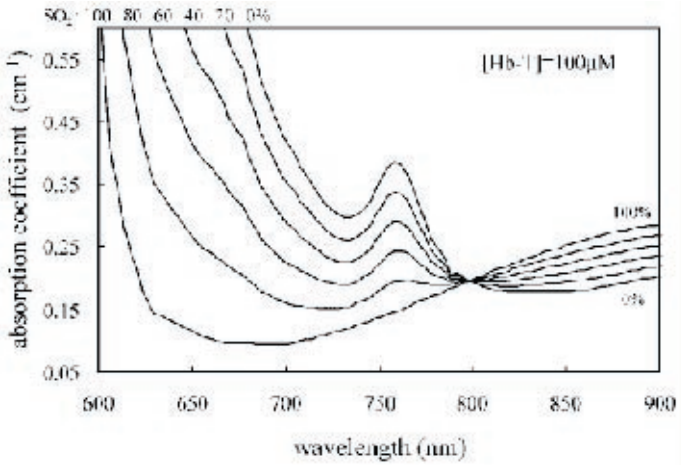

Figure 1. Taken from p. 373 of "Near-infrared spiroximetry: noninvasive measurements of venous saturation in piglets and human subjects" (Franceschini et al., 2002). Near-infrared absorption spectra of 100 μM hemoglobin concentration for different values of oxygen saturation (SO_2) in the range of 0-100%. The curve for 0% saturation corresponds with deoxyhemoglobin. The curve for 100% saturation corresponds with oxyhemoglobin.

Light entering the tissue is scattered in many different directions. A detector placed at a given location collects photons that have on average traveled through the tissue along a banana-shaped path. The depth of light penetration can be controlled by the choosing the distance between the light source and the detector. If the detector and source are placed close together, the photons collected have on average penetrated a shallower depth of tissue compared to photons collected from a more distant source.

An optical oximeter uses near infrared spectroscopy to measure the level of oxygen in the blood. One application of optical oximetry is the detection of hemorrhages in the brain. Blood that is not circulating will appear darker due to lower oxygen concentrations. The oximeter uses low intensity laser light for measurement and is non-invasive.

The Oximeter

An optical oximeter was built to measure the oxygen content of blood, with the goal of focusing on measuring the oxygenation of blood in the brain. The oximeter consists of a probe that is placed over the skin on the head, circuits to process signal information, and a computerized system to record data. The components were tested separately to ensure they worked as expected.

Wavelengths of 635 nm (red light) and 800 nm (near infrared light) are produced by laser diodes which are configured to oscillate in brightness and are flashed on the skin. Only one wavelength is flashed at a time. The light penetrates the skin and blood vessels, and some of the light is reflected from the blood. The reflected light is collected by a photomultiplier tube (PMT) which converts the light signal into an electrical signal.

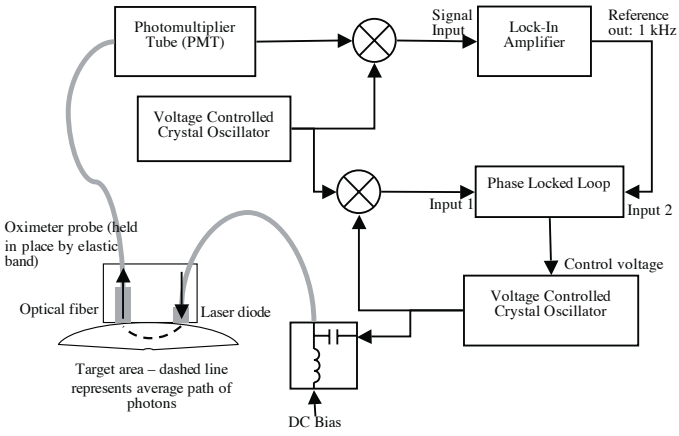

Figure 2. Diagram of one channel of the oximeter. 45 mA is used for the DC bias. Circles represent the frequency mixers.

A 1/8" diameter optical fiber collects and directs light to the PMT. Voltage controlled crystal oscillators (VCXO) are used to provide the AC signal and a laser current supply is used to provide the DC power. The laser diode is powered to its lasing threshold, so that the AC signal appears as a change in intensity. Changes in the oxygenation levels of the blood are expected to correspond with changes in the signal amplitude. A phase locked loop (PLL) locks the phase between the VCXO signals which prevents drift in the frequency. Frequency mixers output the difference between two input frequencies (figure 2).

The laser light is intensity modulated to allow the measurement of intensity as well as phase shift. From this information the absorption and scattering may be determined (Hueber et al., 2001). Typically frequencies around 100 MHz or higher have been used in other oximeters (Franceschini et al., 2002; Ma et al., 1999). The modulation for the oximeter was chosen to be 54 MHz because the laser diodes had higher intensities at this frequency than at the other frequency choice of 100 MHz (figure 4). The setup in figure 3 was used to test the frequency range available.

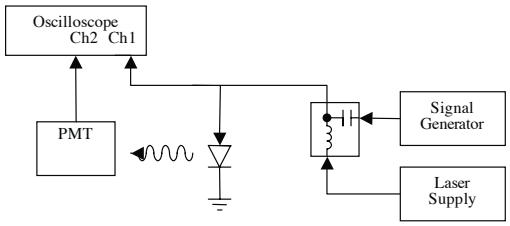

Figure 3. Setup for the test of the laser diode and PMT signal. The oscilloscope (Tektronix model TDS 3054) is set to acquire at 64 averages.

EXPERIMENT

A white phantom was used to simulate biological tissue in preliminary testing (figure 5). A 1/4" hole in the phantom allows a cylinder of black plastic or red plastic to be inserted. The black plastic is expected to absorb light and the red plastic is expected to reflect red light. The red laser diode was used in the test. The signal was collected through a BNC board using the NI-DAQ system with LabView 6.0. The oximeter was tested with a source-detector separation of 1 cm (figure 6) and 2 cm (figure 7).

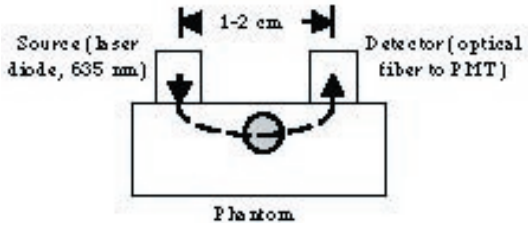

Figure 5. Phantom test for the oximeter. The phantom is placed so the hole is equidistant from the centers of the source and detector. The dashed line represents the average path traveled by photons collected by the detector.

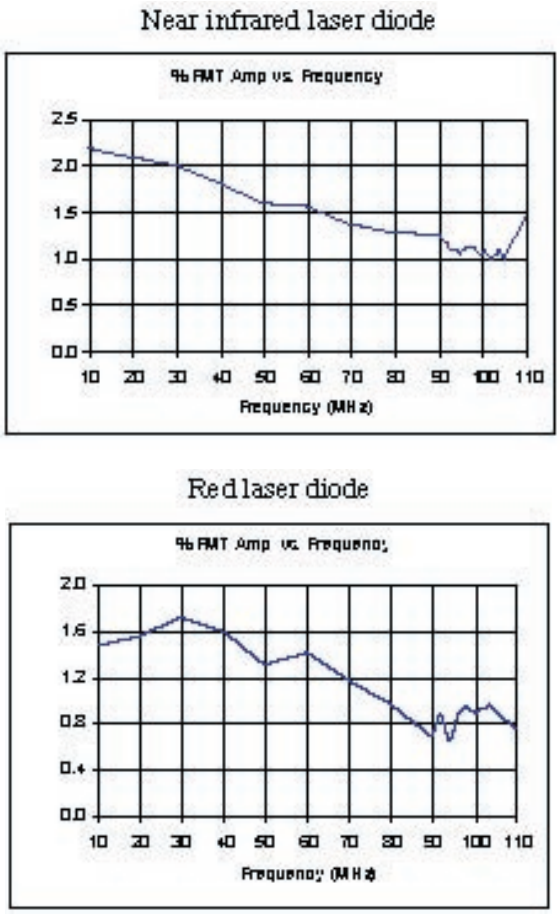

Figure 4. Frequency range test for the red and near infrared laser diodes. The amplitude of the signal from the PMT is greater around 50 MHz than at 100 MHz. In the oximeter, the light collected will be a small fraction of the light emitted by the laser diode sources, so it is important that the laser diodes emit at as high an intensity as practical.

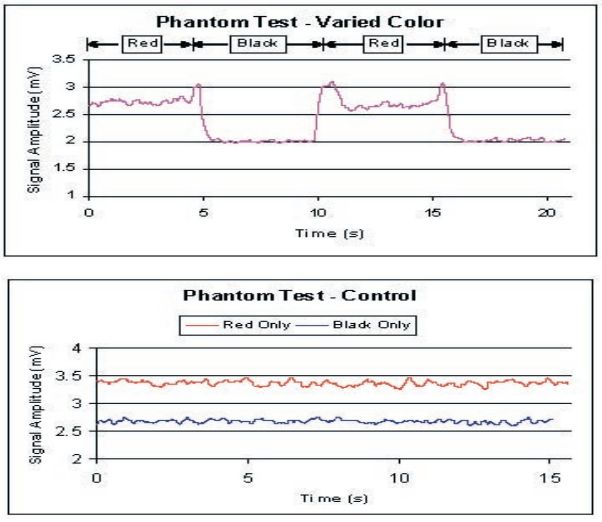

Figure 6. Oximeter tested using the red laser source (635 nm) with 1 cm between the source and detector. Left: Signal amplitude when the red and black plastic are alternated. Right: Signal amplitude with only the red or black plastic in the phantom. The amplitude for the red plastic is larger relative to the amplitude for the black plastic. Differences in the red/black values between tests are most likely due to irregularities in the testing procedure (e.g. phantom was not well secured).

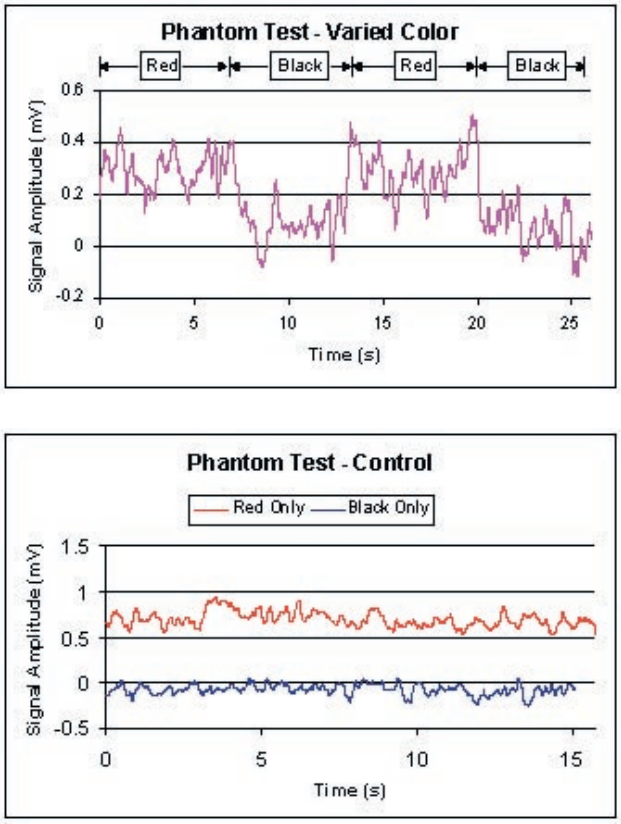

Figure 7. Oximeter tested using the red laser source (635 nm) with 2 cm between the source and detector. Left: Red and black plastic are alternated. Right: Only the red or black plastic in the phantom. The amplitude for the red plastic is larger relative to the amplitude for the black plastic. Differences in the red/black values between tests are most likely due to irregularities in the testing procedure. At 2 cm separation, the light collected by the PMT is more scattered and has lower intensity than at 1 cm. The noise in the signal is significant at 2 cm separation.

FUTURE WORK

One channel of the oximeter was successfully built. Testing is ongoing, and will include the phantom test with the near infrared laser diode and a greater variation of source-detector separation. The spacing of the optical fiber and laser diode on the oximeter probe will be adjusted according to the values for maximum and optimum source-detector separation.

Future work includes building another channel for the second laser diode and reducing noise in the signal. The oximeter must also be made more compact for practical use. In the future the oximeter may be tested on live subjects (pending approval).

REFERENCES

1. Franceschini, M.A., et. al. *J. Appl. Physiol.* **2002**, *92*, 372-384.
2. Hueber, D.M., et. al. *Phys. Med. Biol.* **2001**, *46*, 41-62.
3. Ma, H.Y., et. al. *Proc. SPIE* **1999**, *3597*, 642-9.

ACKNOWLEDGEMENTS

This research funded by the National Science Foundation STC-MDITR and Research Experiences for Undergraduates program. Dr. Antao Chen of the Applied Physics Laboratory at the University of Washington mentored the research.

JoAnn Lin plans to continue research work and is currently pursuing a bachelor's degree in Bioengineering at the University of Washington.

Moisture Uptake of Thin Polymer Films

Ephriam Lucas
Georgia Institute of Technology

Dr. Sue-Ann Bidstrup Allen and Dr. Paul Kohl
Georgia Institute of Technology

Ate He
Fort Valley State University

Thin films are layers of either conductive or non-conductive films that are added to the top surface of wafers. These films may be used to form interconnects between devices or insulators between interconnects layers. A variety of materials can be deposited on a wafer. Three main categories of thin films materials are conductors, insulators, and semiconductors. In this research a polymer "insulator" is used as the thin film. This polymer film is used and tested to see how much moisture it absorbs under different circumstances. These films can later be used to coat microchips for computer, cell phones etc.

A slide of quartz crystal with a gold electrode on each side is used in this project. After coating the quartz with a thin polymer film on one side, the quartz crystal is attached in a sealed glass cell. The cell is connected to nitrogen to test the moisture absorption. The nitrogen enters into the cell in two forms: wet nitrogen and dry nitrogen. The nitrogen that has been condensed with water is called wet nitrogen, and the direct nitrogen flow is dry nitrogen. While using dry nitrogen, the relative humidity is zero, which means that there is no water at all in the cell. When a voltage is applied to the quartz, it vibrates and the frequency is proportional to the mass of the film. Once the mass of the film is changed by moisture uptake, the frequency reflects that change. The more moisture the film absorbs the heavier the film will be causing the frequency to be lower. The theory behind this is the higher the condenser temperature, the higher the moisture content inside the cell, which increasing the relative humidity. The higher the relative humidity, the more moisture the polymer film will uptake, which increases the mass of the thin polymer film.

There has not been much progress in this research as of yet due to inaccurate data. The data recorded show that there was a 2.5% increase in weight when changing from dry nitrogen to wet nitrogen and a 2.21% decrease in weight when changing back from wet to dry. This tells us that all the moisture is not being reabsorbs. We believe the frequency values are inaccurate due to the fact that the nitrogen flow is not constant. The nitrogen flow rate constantly fluctuates when changing from wet to dry and dry back to wet. A way to stabilize the nitrogen flow at a slow steady rate is needed before this research can be continued.

ACKNOWLEDGEMENTS

Research support is gratefully acknowledged from the National Science Foundation Center on Materials and Devices for Information Technology Research (CMDITR), DMR-0120967.

Toward Molecular Resolution c-AFM with Carbon Nanotube Tips: Development of Carbon Nanotube Growth Techniques

Austin McLeod
Northern Arizona University

Neal R. Armstrong, Paul Lee and Ken Nebesny
Armstrong Lab, Department of Chemistry
The University of Arizona

Carbon nanotube tips (CNTs) will be formed for use in nanometer scale imaging in atomic force microscopy. Optimized versions of these tips promise to provide for very high-resolution imaging, minimization of sample damage due to the weak interactions anticipated between the tip and soft materials (organic thin films), and the prospect for measuring electrical properties of organic thin film, owing to the electrically conductive nature of the CNT.

OBJECTIVES / THESIS

AFM nanometer-scale imaging is hindered by standard AFM tips because they have poor aspect ratios, which can cause sample damage during the investigation of the surfaces of organic films. AFM tips modified with carbon nanotubes (CNTs) should help greatly to increase the resolution, owing to the small diameter of the CNT and excellent aspect ratios. The Dai group at Stanford University has developed a process to grow carbon nanotubes on silicon wafer tips in mass quantities.[1] Our approach is to grow nanotubes in carpet like fashion and pick them up using the method of dielectrophoresis developed by Hyung Woo Lee.[2] Ultimately, we anticipate growing carbon nanotubes directly onto individual AFM tips.

Most carbon nanotubes are about 10-50 nm in diameter and between 100 – 1000 nm long, some have been grown to about 2 mm in length, but that length will not be necessary for our work. Carbon nanotubes are typically grown from a catalytic nanoparticle surface (the iron particle), which becomes the nucleation site of the nanotube's growth and a carbon source, which becomes the structure of the nanotube. Nanotubes with a 10:1 aspect ratio would be preferred, meaning about 100-200 nm long and 10-20 nm in diameter.

RESEARCH METHODS / RESULTS

Carbon nanotubes are typically grown via chemical vapor deposition at low pressures, using catalytic nanoparticles to initiate tube growth and location of the tube. Usually, carbon nanotubes attach very tightly to the nanoparticles, making separation difficult. Carbon nanotubes can also be attached directly to conventional AFM tips. A group from the Korea Advanced Institute of Science and Technology has developed a technique to attach the nanotubes directly to the AFM tip.[2] Our first attempts will be to grow carbon nanotubes on silicon nitride surfaces because that is what AFM tips are made from, growing nanotubes directly onto the AFM tip at the correct orientation might be difficult, so a benchmark experiment was preformed.

In our first experiment we tried to grow carbon nanotubes on a silicon nitride wafer using a ferric nitrate, $Fe(NO_3)_3 \cdot 9H_2O$, solution to coat the silicon surface with iron particles. Chemical vapor deposition (CVD) was utilized to grow the SWNT in a quartz tube using acetylene as the carbon source and ultra-high purity (UHP) nitrogen gas as the carrier gas. AFM was used to characterize the silicon nitride surface. AFM showed that the ferric nitrate iron source yielded, what looked like, "megatubes" (Figure 1).

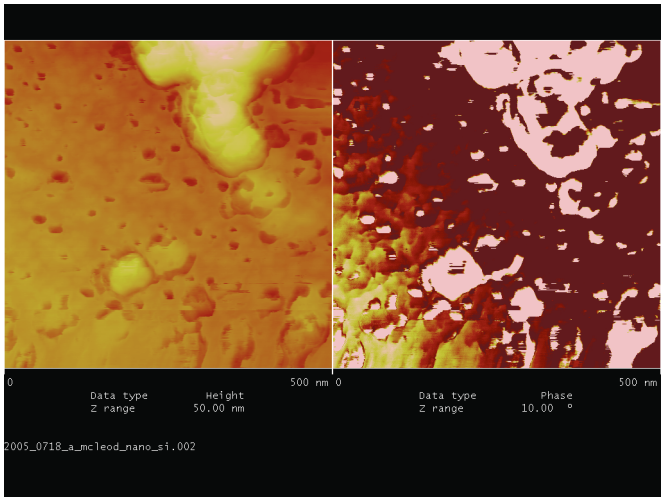

Figure 1. AFM image of CVD with Ferric Nitrate Catalyst source

The next technique involved using an iron source that was already on the nanometer scale. Ferrosound EMG 1111 nanoparticles made by Ferrotec, Inc were cleaned and separated in ethanol,

and they were spun-coated on the surface of the silicon nitride. AFM images show the nanoparticles had an even distribution across the surface (Figure 2). The carbon nanotubes grown on these surfaces were very difficult to image with AFM because some soot was forming on the surface.

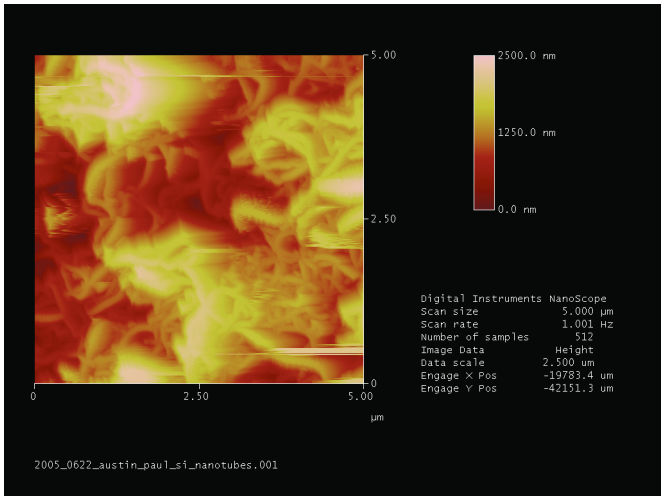

Figure 2. Iron nanoparticles on silicon nitride surface

The last technique utilized ferrocene as the iron source, and xylenes as the carbon source.[3] The CVD was preformed in a reducing atmosphere of hydrogen gas, and in the presence of a carrier gas, argon. The wafers were cleaned in "piranha" for 30 minutes (4:1 ratio of sulfuric acid and 30% hydrogen peroxide), rinsed with nanopure water, and dried with compressed nitrogen gas before they were placed inside the quartz tube. The wafers were placed in the quartz tube using a measuring tape into the "hot zone." The "hot zone" from prior experiments was determined to be in the middle of the furnace, the hottest part of the center of the furnace. (Figure 3).

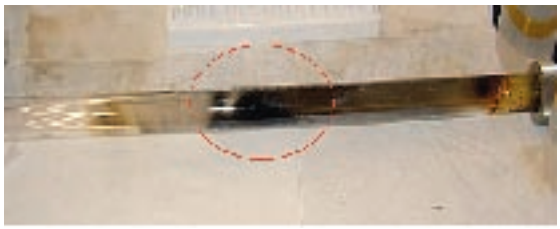

Figure 3. The "hot zone" is circled in red in figure 3 and indicated by the blackened nanotubes area.

Field Emission Scanning Electron Microscopy (FESEM) characterized the silicon nitride wafers with the carbon nanotubes. FESEM was used to characterize the surface because the resolution is much higher compared to standard SEM. In Figure 4, the carbon nanotubes is of excellent aspect ratio (about 10 length to 1 diameter). This SWNT is about 20 nm in diameter and about 200 nm long.

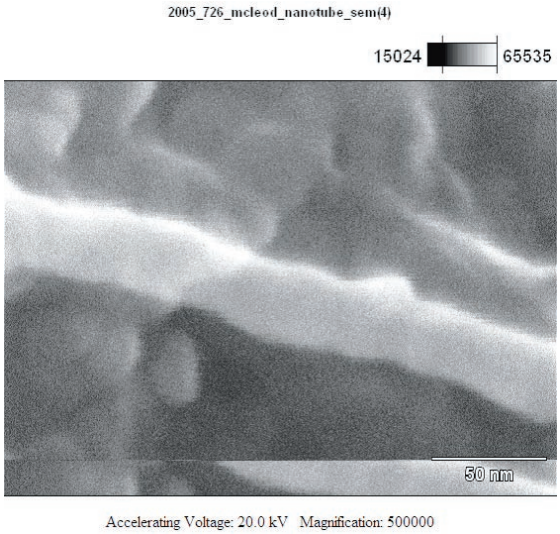

Figure 4: FESEM image of a carbon nanotube

In Figure 5, the nanotubes shown in the FESEM image show bright spots, which are believed to be iron particles, the nucleation site of the nanotubes. These nanotubes appear to be about 20 nm in diameter and about 200 nm between each bright spot. Recent findings show that CNTs grow for a certain amount of time (length) before they start to close up, but before they close up another iron particle inserts itself and keeps the tube open, and that particle becomes the spot for the next CNT to grow from.[4]

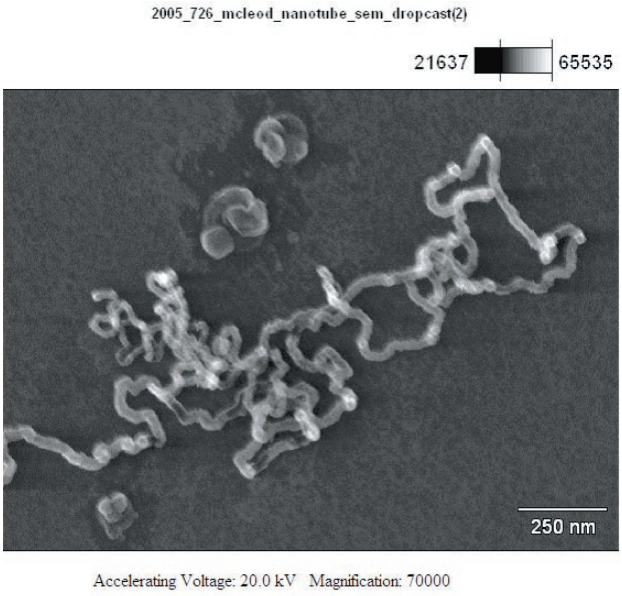

Figure 5: FESEM image of a carbon nanotube

Electron Dispersion X-ray Spectroscopy (EDX or EDS) was performed on one of these bright spots (Figure 5), but since these are on silicon substrate, the silicon signal is much too high to see if there is indeed iron within the nanotubes (Figure 6).

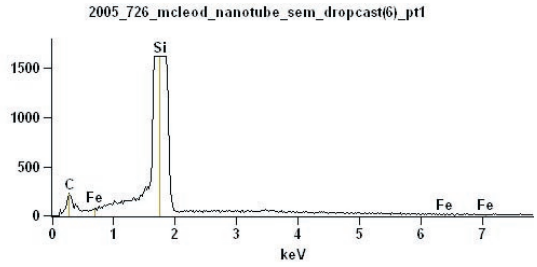

Figure 6. EDX of Substrate

FUTURE WORK

An experiment to perform, would be to grow the nanotubes on gold foil, and then perform EDX on the gold foil to see if a carbon and iron peak show up on the gold because the gold peak is shifted over from the silicon peak.

Carbon nanotubes can be grown in carpet like fashion as seen by Maldonado et al. (Figure 7). Dielectrophoresis can be preformed on the nanotubes to attach them directly to the AFM tip (Figure 8).[2] Although, it might be possible to grow a carbon nanotube directly onto an AFM tip, the alignment of the tip and the carbon nanotube is crucial to obtaining an excellent AFM image see figure 9.[5] Therefore growing "nanotube carpets" followed by dielectric attachment of the nanotube enables more control of the alignment of the AFM tip with respect to the CNT. Future work needs to be done to attach the CNTs to the AFM tip.[5]

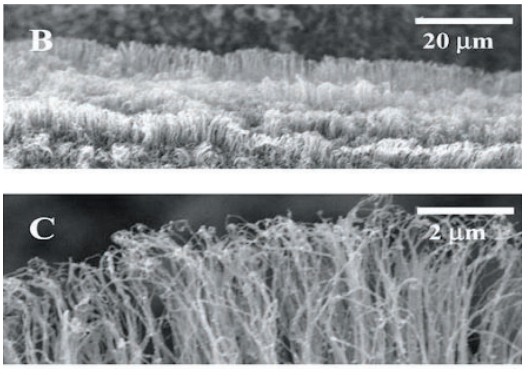

Maldonado et al. J. Phys. Chem. B 2004.

Figure 7: "Nanotube Carpets"

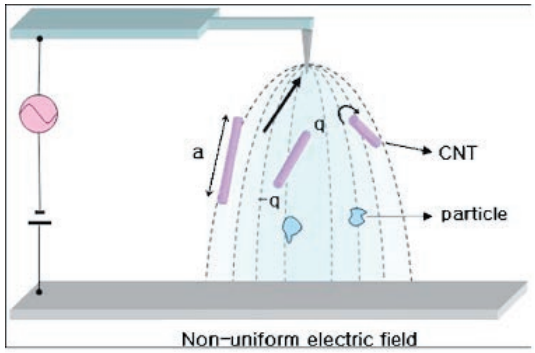

Hyung Woo Lee et al. Rev. Sci. Inst. 2005

Figure 8: Dielectric Attachment of CNT to AFM tip

Figure 9: AFM tip with CNT attached

CONCLUSIONS

When carbon nanotubes can be attached, repeatedly, to AFM tips, they will become very important for performing conductive atomic force microscopy (c-AFM) measurements and increasing the resolution of the AFM image. In addition to decreasing the aspect ratio of AFM tips using CNT they also have interesting properties that also can affect surface measurements. Carbon nanotubes are almost entirely composed of carbon, and carbon will have much lower Van der Waals interaction with the organic thin film surface, which means that the surface damage will be minimized. Most AFM tips are made of silicon, and these types of AFM tips do cause sample damage to soft materials. AFM tips can also be made of gold, platinum, or boron doped diamond tips. These conductive tips can cause sample damage, but these carbon nanotube tips will enable scientists to perform c-AFM experiments to soft samples without sample damage.

REFERENCES

[1] Erhan Yenilmez, Qian Wang, Robert J. Chen, Dunwei Wang, and Hongjie Dai. *Wafer scale production of carbon nanotube scanning probe tips for atomic force microscopy.* Applied Physics Letters, **2002**, 80, 2225-2227.

[2] Hyung Woo Lee, Soo Hyun Kim, and Yoon Keun Kwak, Chang Soo Han. *Nanoscale fabrication of a single multiwalled carbon nanotubes attached atomic force microscope tip using an electric field*. Review of Scientific Instruments, **2005**, 76, 046108-1.

[3] Stephen Maldonado and Keith J. Stevenson *. *Influence of Ni-*

trogen Doping on Oxygen Reduction Electrocatalysis at Carbon Nanofiber Electrodes. J. Phys. Chem. B **2005**, 109, 4707-4716.
[3] Stephen Maldonado and Keith J. Stevenson *. *Direct Preparation of Carbon Nanofiber Electrodes via Pyrolysis of Iron(II) Phthalocyanine: Electrocatalytic Aspects for Oxygen Reduction*. J. Phys. Chem. B **2004,** *108,* 11375-11383.
[4] Christian P. Deck, Kenneth Vecchio *. *Growth mechanism of vapor phase CVD-grown multi-walled carbon nanotubes*. Carbon 43, **2005**, 2608–2617.
[5] R. Schlaf* et al. Using carbon nanotubes catilevers in scanning probe metrology. ***In press***.

ACKNOWLEDGEMENTS

-**Dr. Neal R. Armstrong**, Professor of Chemistry and Optical Sciences, University of Arizona
-**Armstrong Research Group**
-**Dr. Ken Nebesny**, associate staff scientist, LESSA facility, University of Arizona
-**Paul Lee**, assistant staff scientist, LESSA Facility, University of Arizona
-**Clayton Shallcross**, Graduate Student, University of Arizona
-**Alex Veneman**, Graduate Student, University of Arizona
-**Margo Ellis** – FESEM operator
-**Dr. Timothy Vail**, Dept. of Chemistry, Northern Arizona University

Funding provided by the Center on Materials and Devices for Information Technology Research (CMDITR), an NSF Science and Technology Center No. DMR 0120967

I'd like to thank Dr. Neal R. Armstrong, and his group for mentoring me this summer at the University of Arizona.

Synthesis and Characterization of Extended Squaraine Compounds

Tehetena Mesganaw
Georgia Institute of Technology

Shijun Zheng and Seth Marder
Marder Lab, School of Chemistry and Biochemistry
Georgia Institute of Technology

INTRODUCTION

Organic dyes encompass a broad range of applications that are being investigated in the quest for new advancements in various technological areas. Squaraines are a novel class of organic dyes that have delocalized π-electron systems that absorb at long (near infrared) wavelengths. These extended squaraines with alkyl side chains can easily form good optical quality, thin films. These molecules are nonlinear optical materials and as such can potentially be used for optical switching applications. In a nonlinear optical material, when the light intensity shined on the material increases, the electron cloud distorts, and the refractive index changes. As a result, the way light propagates through the material changes. Therefore, squaraine compounds are on the rise and demands for these dyes will increase rapidly in years to come.

RESEARCH METHOD

Synthesis of (1)

The synthesis of **(1)** provides one of the building blocks for the final squaraine compound. Excess pyrrole was reacted with 11-bromomethyl-tricosane in the presence of NaH and DMF. The reaction was done under N_2 at 60 ºC and left for 3 days. The desired product **(1)** resulted in a yield of <50%. By ^{1}H NMR it was concluded that an elimination product (E2) formed because of the heat added to the reaction, and the fact that pyrrole anion is very basic also aided in the formation of the elimination product.

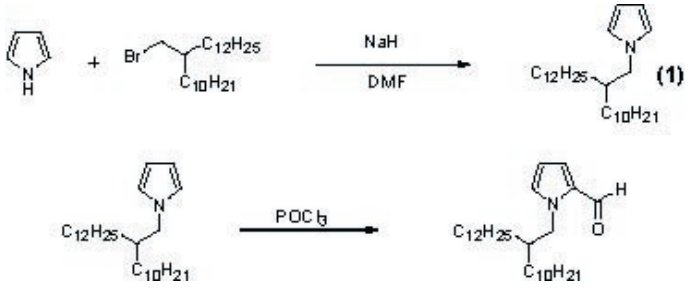

Scheme 1. The attempted synthesis of the pyrrole that will be used for squaraine resulted in a low yield of **(1)**.

Synthesis of (2)

1H-pyrrole-2-carbaldehyde was reacted with excess 11-bromomethyl-tricosane in NaH and DMF under N_2 to yield **(2)**.

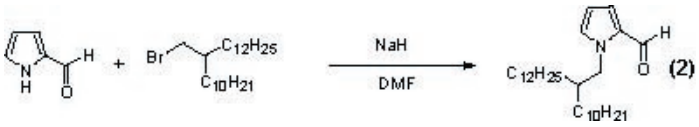

Scheme 2. A revised synthetic scheme to successfully isolate **(2)**.

Synthesis of (3)

1H-Pyrrole-2-carbaldehyde was reacted with 3-bromomethyl-heptane with excess of NaH and DMF under N_2. After 5 days at room temperature, the solution was washed with ice cold water and extracted with ethyl ether (×6). It was washed with deionized water (×4) and dried over magnesium sulfate. Column Chromatography, eluent hexanes in silica, was used for purification to give **(3)**, 1-(2-ethyl-hexyl)-1H-pyrrole-2-carbaldehyde.

Scheme 3. Synthesis of pyrrole **(3)** that will be used for the condensation with squaric acid.

Synthesis of (4)

Dibutyl-phenyl-amine was reacted with $POCl_3$, in a Vilsmeir formylation to give **(4)**[1]**.** 4-Dibutylamino-benzaldehyde, **(4)**, was reduced to an alcohol by sodium borohydride in ethanol. After 45 minutes at room temperature, the solution was concentrated and aqueous ammonium chloride was added. Fresh 100 mL of dichloromethane was added and the organic layer was extracted (×2), dried over magnesium sulfate and concentrated to give a yellow oil **(5)**.

(4-Dibutylamino-phenyl)-methanol was treated with triethyl phosphite in iodine at 0ºC and left overnight under N_2. Vacuum distillation was performed at 60 ºC and remaining liquid was purified by column chromatography, eluent 1:1 hexanes to ethyl acetate to give rise to **(6)**. By a Horner-Emmons condensation, compound **(6)** (4-Dibutylamino-benzyl)-phosphonic acid diethyl ester in dry THF was reacted with 3,4-Dibutoxy-thiophene-2-carbaldehyde in a solution of potassium *tert*-butoxide in dry THF under N_2. After an hour, the concentrated solution was purified by column chromatography, eluent 10:1 hexanes to ethyl acetate in silica to give the compound **(7)**.

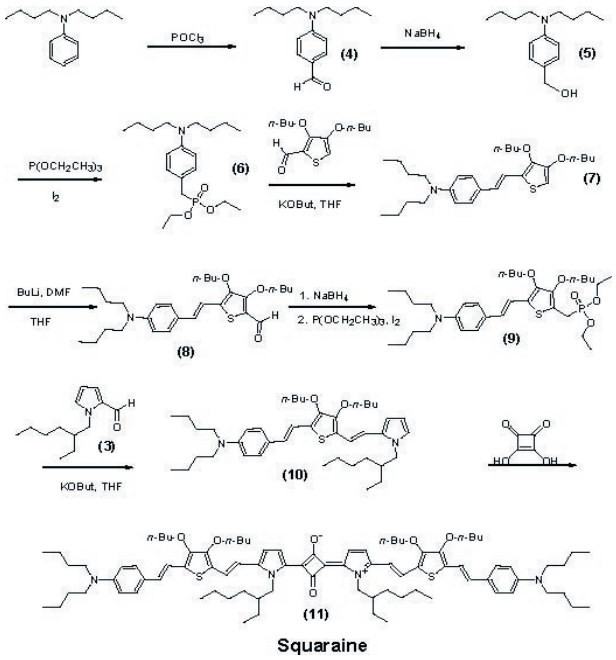

Scheme 4. Synthesis of the desired product, squaraine **(11)** using **(3)**.

Dibutyl-{4-[2-(3,4-dibutoxy-thiophen-2-yl)-vinyl]-phenyl}-amine, **(7)** was then treated with butyl lithium in dry THF at 0 ºC, after two hours DMF was added and left overnight all under N_2. The red solution was washed with water and extracted with ethyl acetate (3×). The organic phase is collected and dried over magnesium sulfate. The concentrated solution was purified by column chromatography, eluent 10:1 hexanes to ethyl acetate in silica to give **(8)**. 3,4-dibutoxy-5-[2-(4-dibutylamino-phenyl)-vinyl]-thiophene-2-carbaldehyde, **(8),** was reduced by sodium borohydride in ethanol, similar to the procedure for compound **(5)**, which was then reacted with tri-ethyl phosphate in iodine at 0 ºC and left overnight under N_2. Vacuum distillation was performed on the solution for two hours and purified by column chromatography, eluent 4:1 hexanes to ethyl acetate to yield **(9)**.

Compound **(3)**, 1-(2-ethyl-hexyl)-1H-pyrrole-2-carbaldehyde was reacted with {3,4-Dibutoxy-5-[2-(4-dibutylamino-phenyl)-vinyl]-thiophen-2-ylmethyl}-phosphonic acid diethyl ester, compound **(9)**, in dry THF and a solution of potassium *tert*-butoxide in dry THF by a Horner-Emmons Condensation, under N_2, for an hour and a half. The concentrated oil was purified by column chromatography, eluent 10:1 hexanes to ethyl acetate in silica to give rise to compound **(10)**. Dibutyl-{4-[2-(3,4-dibutoxy-5-{2-[1-(2-ethyl-hexyl)-1H-pyrrol-2-yl]-vinyl}-thiophen-2-yl)-vinyl]-phenyl}-amine, **(10)** is treated with squaric acid to give the desired compound **(11)** Squaraine.

CONCLUSION

After several failed reactions, it was determined that an alkylated pyrrole carbaldehyde can be synthesized in high yield. Many of these reactions caused side products which required careful purification techniques that took longer than expected. Therefore, the desired product squaraine is one reaction away from completion. After pure squaraine is obtained, tests will be performed on the organic dye to determine its efficacy in producing optical quality, thin films.

REFERENCES

M.J. Plater, T. Jackson. *Tetrahedron 59 (2003)*. pages 4673-4685 (page 4679).

ACKNOWLEDGEMENTS

Research support is gratefully acknowledged from the National Science Foundation Center on Materials and Devices for Information Technology Research (CMDITR), DMR-0120967.

Tehetena Mesganaw is currently attending the Georgia Institute of Technology and majoring in Chemistry. After graduation im Fall 2006, she plans to attend graduate school and obtain her Ph.D in Organic Chemistry. From there, she plans to do research on the AIDS epidemic.

Enhanced Heat Dissipation Substrates for Organic Semiconductor Devices

Aaron Montgomery
University of Virginia

Dr. Samuel Graham
Georgia Institute of Technology

Ashante Allen, Erik Sunden and Adam Christensen

`Many electronic devices are susceptible to overheating which can result in failures of the device. This can be exemplified through electronic chips located inside a computer. To address these failures, much research has been performed to develop thermal management solutions for microelectronic devices. These solutions have generally been geared towards Si-based microelectronics and have achieved cooling capabilities of 100 W/cm^2 or greater. While such power densities are not expected in organic semiconductors, these devices have unique thermal management challenges arising from their inherent low thermal conductivity (results in high thermal resistance), the use of thermally resistive substrates for flexible electronics, and the need to have transparent materials for photon transfer. Thus, new concepts for both active and passive thermal management of organic semiconductor devices (OSD) must be explored.

In this work, I will primarily concentrate on developing new schemes for the removal of thermal energy through both active and passive mechanisms by "thermally connecting" the OSD to high thermal conductivity substrates. The thermal connection will be based on carbon nanotubes (CNTs) which will act as a thermal interface material (TIM) with superior properties to conventional TIMs. These CNTs possess a very high thermal conductivity (900-10,000w/mk). I will investigate the use of multilayer catalysts to produce highly aligned CNTs on metal substrates and the creation of actively cooled PMMA and Si (gold coated) substrates using various bonding techniques. There is a severe lack of attention on the thermal characterization and heat dissipation in OSD. Much of what I do here will be new and provide much needed contributions to the challenges of thermal management in OSDs. In addition, with overheating of chips stalls the advancement of better electronic devices.

The multilayer catalysts deposition onto metal substrates has proven successful in producing some CNT growth (Figure 1). Some parameters that contribute to this growth are the type of catalyst deposited onto the metal, the maximum temperature during the procedure, and the length that the sample is exposed to the gases. By changing these parameters I am hoping to produce a recipe that will generate better quality CNT growth with fewer defects. Also, success was achieved at bonding Si (gold coated) to Si and PMMA to PMMA. Using a furnace, Si bonding can be accomplished at 460 degrees Celsius for 5 minutes and is used to for creating microfluidic channels for active cooling. Concerning polymers, a hydraulic press successfully bonded PMMA with a carbon nanofiber interlayer at 250 degrees Fahrenheit while maintaining 400lbs of force for 5 minutes (Figure 2). This laminated structure was used to create a flexible heat spreader in polymer substrates for improve heat dissipation. Future work will involve finding a feasible bonding method for PET which is more commonly used for flexible organic semiconductors and to continue to produce CNT growth onto metal substrates with the least amount of defects.

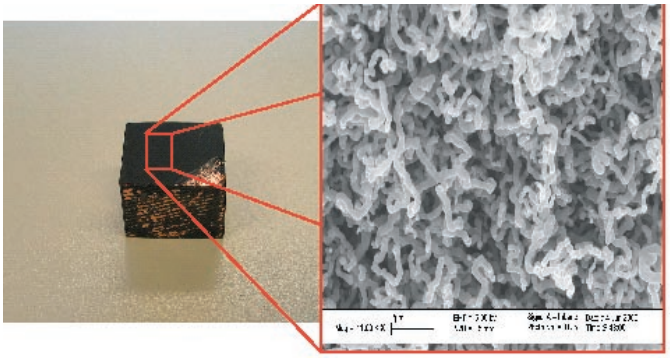

Figure 1. Growth of carbon nanotubes on a copper substrate (left) and a scanning electron microscope image showing the details of the growth (right).

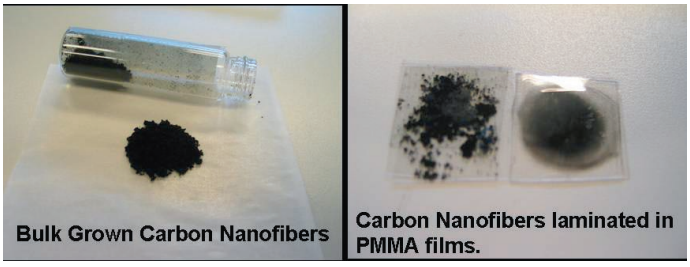

Figure 2. Growth of carbon nanofibers (left) which were laminated between sheets of PMMA to create a flexible heat spreader (right) integrated into a polymer substrate.

ACKNOWLEDGEMENTS

Research support is gratefully acknowledged from the National Science Foundation Center on Materials and Devices for Information Technology Research (CMDITR), DMR-0120967.

My name is Aaron Montgomery and I am currently a third year student at the University of Virginia. My current major is Mechanical Engineering with an Engineering and Business Minor. My expected graduate date is May 2007. My plan after obtaining my degree is to pursue graduate school.

1,1-Diphenyl-2,3,4,5-tetrakis(9,9-dimethylfluoren-2-yl)silole Properties in Organic Light-Emitting Diodes and Organic-Field Effect Transistors

Sarah Montgomery
Purdue University

Bernard Kippelen, Benoit Domercq
School of Electrical and Computer Engineering
Georgia Institute of Technology

Organic light-emitting diodes (OLED) and organic field-effect transistors (OFET) have been central to current research because displays and integrated circuits made with organic materials can be fabricated on plastic, making them flexible and lightweight and potentially reducing production costs. OLEDs and OFETs were fabricated out of a new family of materials based on silole derivatives, specifically 1,1-Diphenyl-2,3,4,5-tetrakis(9,9-dimethylfluoren-2-yl)silole (**XZ-III-20**), shown in Scheme 1, using vapor deposition techniques. These devices were then tested to determine their physical characteristics and properties using lab equipment and the software program LabView.

INTRODUCTION

The extent of research currently on OLEDs is extensive. One of the advantages of an OLED display to that of a liquid crystal display (LCD) is it does not require a backlight which can ultimately reduce its size, power consumption and production cost. OLEDs consist of subsequent organic layers sandwiched between electrodes that inject holes and electrons into the organic layers. The organic layers must transport holes, electrons and emit light. Holes are injected from the anode, a high work function metal while electrons are simultaneously injected from the cathode, a low work function metal. The differing electrodes call for different organic materials, a hole transport layer (HTL) that has a low ionization potential and an electron transport layer (ETL) that has a high electron affinity [1]. Holes are transported in the HTL while electrons travel in the opposite direction through the ETL; the charges will either find an energy barrier between the HTL and ETL or at the emission layer and will ultimately recombine, creating an exciton which emits a photon when it relaxes to the ground state.

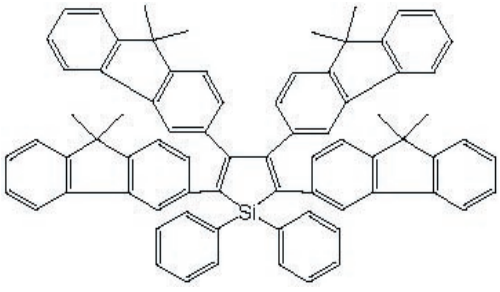

Scheme 1. 1,1-Diphenyl-2,3,4,5-tetrakis(9,9-dimethylfluoren-2-yl)silole (XZ-III-20).

Siloles have been found to have close to 100% photoluminescence efficiency, in turn allowing for a high external quantum efficiency of 8% [2]. This photoluminescence efficiency is over three times higher than that of tris-(8-hydroxyquinoline) aluminum (AlQ_3), one of the leading emitting electron transport layers used in OLEDs today. These silole materials are of interest because they are primarily singlet emitters but it has been proposed that there may be phosphorescent emissions as well [2]. XZ-III-20 has been the focus of this research. From its expected electron affinity and ionization potential which are comparable to *N-N'*-diphenyl-*N-N'*bis(3-methylphenyl)-[1-1'-biphen- yl]-4-4'-diamine (TPD) and $AlQ_{3;}$ it could be ambipolar or work effectively as both an ETL and a HTL. XZ-III-20 has four fluorene groups attached to the silole. These fluorene groups decrease the ionization potential of the silole material which could lead to favorable hole-transport properties.

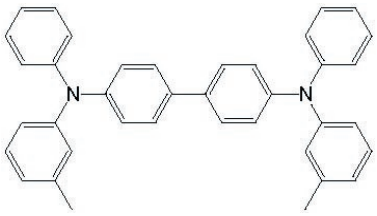

Scheme 2. Structure of a hole transport material: N-N'-diphenyl-N-N'bis(3-methylphenyl)-[1-1'-biphenyl]-4-4'-diamine (TPD).

OFETs can be used in integrated circuits as a switching device in technology such as computers and displays [3,4]. Like inorganic field-effect transistors, OFETs are three terminal devices consisting of a gate, drain and source. In an OFET the gate voltage controls the S-D current or I_D. OFETs are being used to determine the dominant charge carriers present in XZ-III-20 and

its charge carrier mobility, μ, which is the velocity of the charge carriers under a given electric field. This can be done by applying a voltage of the same polarity to both the gate and drain. If there is a small current present, then the charge carrier has a charge opposite of the applied voltage.

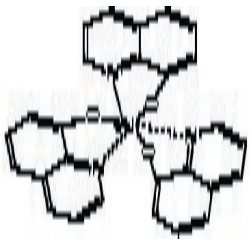

Scheme 3. Structure of an electron transport and emitting material: tris-(8-hydroxyquinoline) aluminum (AlQ3).

DEVICE FABRICATION AND TESTING

OLEDs were fabricated on glass substrates coated with indium tin oxide (ITO) as the anode. The subsequent organic layers were deposited using high vacuum thermal evaporation. The metal cathode is composed of a very thin layer of Lithium Fluoride and 300 nm of Aluminum. XZ-III-20 was tested by fabricating OLEDs using various device geometries: as an ETL **(1)** ITO/ TPD (40 nm)/ XZ-III-20 (40 nm)/ LiF (1nm)/ Al (300 nm), as a HTL **(2)** ITO/ XZ-III-20 (40 nm)/ AlQ_3 (40 nm)/ LiF (1nm)/ Al (300 nm), as an emission layer **(3)** ITO/ TPD (40 nm)/ XZ-III-20 (40 nm)/ AlQ_3 (40 nm)/ LiF (1nm)/ Al (300 nm) and as a single layer of varying thickness **(4)** ITO/ XZ-III-20/ LiF (1nm)/ Al (300 nm).

Each device structure was fabricated and tested in a nitrogen environment and current-forward light output measurements, as a function of the applied voltage, were acquired using a Keithley 2400 sourcemeter and a silicon photodiode interfaced using LabView software. The electroluminescent (EL) spectrum was taken for each device structure at different voltages to ensure that there was not a shift in the emission peak when increasing the applied voltage. The EL spectrum of each device geometry is shown, along with a device fabricated with AlQ_3, a widely used material in OLED (Figure 1). The geometry of the AlQ_3 device shown in Figure 1 is ITO/ TPD / AlQ_3 / LiF/ Al.

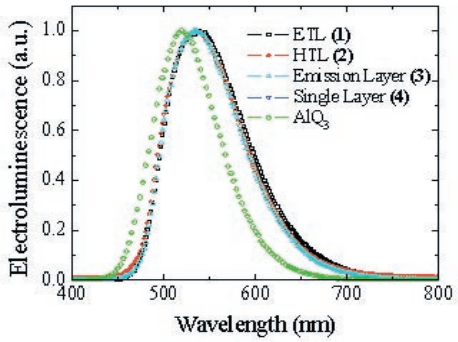

Figure 1. EL spectrum of devices fabricated with XZ-III-20 in various device geometries. EL spectrum of a device using AlQ_3 as an ETL.

OFETs were fabricated using a bottom contact geometry with the organic semiconductor, XZ-III-20 (40 nm), deposited on top of a heavily doped silicon wafer coated with a thermally grown oxide and gold electrodes defining the source and drain. The organic semiconductor, XZ-III-20, was deposited on top of the gate insulating layer and gate electrode. The use of gold electrodes favors a p-type response due to its work function. The device was tested as n-type and p-type, however only the p-type structure produced an output. For a channel width of 500 nm and length of 50 nm, a drain sweep was conducted from 0 to -80 V with gate voltages ranging from 0 to -80 V in step sizes of 10 V. The transfer curve was obtained by sweeping the gate holding V_D constant at - 80 V. As the channel length decreased and the width increased, the voltage sweep had to be increased to -100 V. The output characteristic and transfer curve are shown in Figure 2 and Figure 3 respectively.

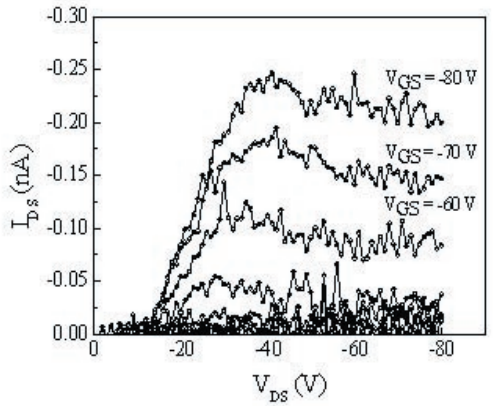

Figure 2 *I-V* characteristics at several values of the gate voltage (V_{GS}) for an OFET using XZ-III-20, having a channel width of 500 nm and length of 50 nm.

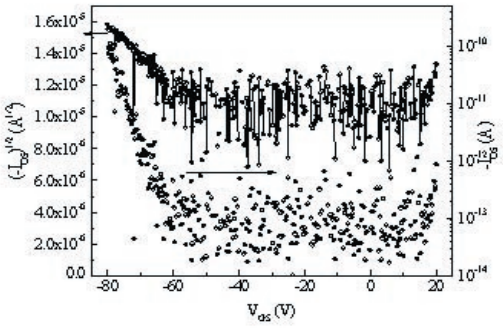

Figure 3. Transfer curve with V_D = -80 V for an OFET using XZ-III-20, having a channel width of 500 nm and length of 50 nm.

RESULTS AND DISCUSSION

From the OLED testing, current density (*J*), luminance and external quantum efficiency were calculated. Luminance takes into account photopic response (how the human eye responds to the light emitted), the sensitivity response of the photodetector and the physical geometry of the measurement set-up. External

quantum efficiency is the measurement of photons emitted from the device in the forward direction divided by the amount of electrons injected into the device [5]. Figure 4 (top) shows a comparison of current density for different device geometries **(1), (2),** and **(3)**, while Figure 4 (bottom) compares the luminance and external quantum efficiency. It is seen from the plot of current density, when XZ-III-20 acts as an ETL and HTL, the responses are comparable, however the luminance for the ETL structure is lower, leading to a lower external quantum efficiency. The current density for **(3)** is lower than that of **(1)** or **(2)** primarily because it is 40 nm thicker. The small jagged bumps in the *J-V* plot represent leakage current; there is current flowing through the device that is not producing photons. In device structure **(3)** the holes and electrons are transported by TPD and AlQ_3 respectively and trapped in the emission layer resulting in such high external quantum efficiency.

A standard LCD monitor has a luminance of about 300 cd/m^2. For XZ-III-20 as an ETL, it reaches a brightness of 300 cd/m^2 at 6.3 V with an external quantum efficiency of 0.55%. As an HTL it reaches the same brightness at 5.8 V with an external quantum efficiency of 0.6%. When XZ-III-20 acts as an emission layer it has a much higher external quantum efficiency value of 0.95% at 7.6 V when the luminance is 300 cd/m^2.

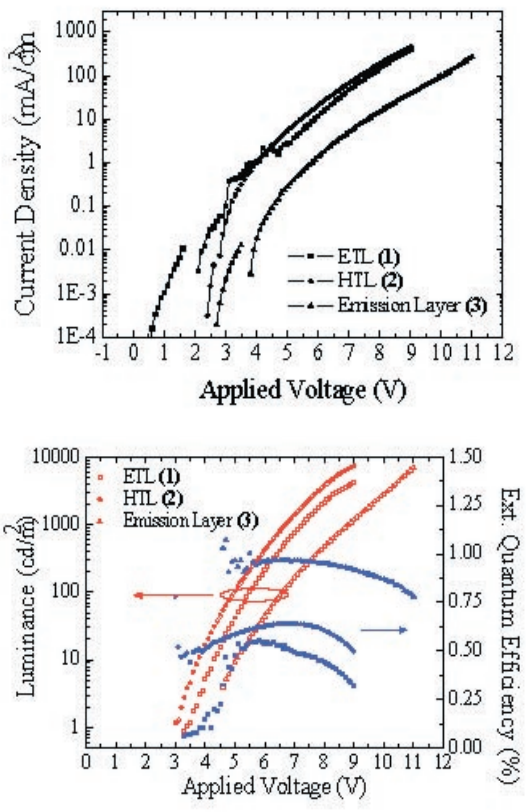

Figure 4. Current density (top), luminance and external quantum efficiency (bottom) as a function of the applied voltage of devices using XZ-III-20 as an ETL, HTL, and emission layer.

Single layer devices using XZ-III-20 were fabricated with varying thicknesses: 50 nm, 80 nm, 100 nm, 120 nm, and 150 nm. Figure 5 (top) and Figure 5 (bottom) show respectively the current density and luminance, external quantum efficiency as a function of the applied voltage for each of the thicknesses. It is seen that with increasing thickness, the current density decreases as expected. The luminance decreases while the external quantum efficiency increases, however the turn-on voltage is significantly increased from 3.6 V for 50 nm to 10.4 V for 150 nm, and to 11.6 V for 120 nm thick. With a thickness of 50 nm, a luminance of 300 cd/m^2 is reached at 6.5 V with an external quantum efficiency of 0.08%; while with a thickness of 150 nm, the same luminance is achieved at 16.9 V with an external quantum efficiency of 0.09%.

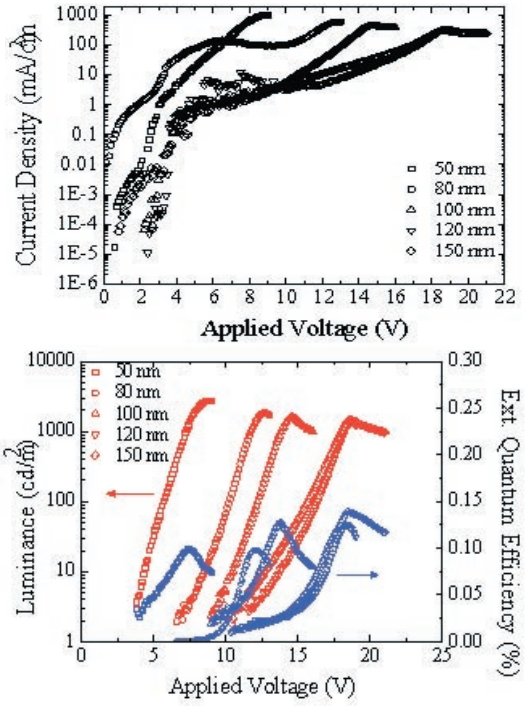

Figure 5. Current density (top) and luminance and external quantum efficiency (bottom) as a function of the applied voltage of devices using XZ-III-20 as a single layer of varying thickness.

From the OFET output characteristic, it is evident that there is a very small I_D current flowing, on the order of nA, and the signal is noisy. The on/off ratio, threshold voltage and mobility are extracted from the transfer curve. For a channel width of 500 nm and length of 50 nm, the mobility is 4.0 x 10^{-6} cm^2/Vs, The threshold voltage, the voltage required to switch the device on, is very high, -56 V. The on/off ratio, the ratio of the current flowing through the device when it is on, divided by the current flowing through the device when there is 0V applied at the gate, is 10. These values are very low compared to pentacene, a common organic hole-transport material used in OFETs, having a hole mobility of $\mu = 2.4$ cm^2/V-s and an on/off ratio of 10^8 [3].

CONCLUSION

From the information learned about XZ-III-20 in the OLED device structures of **(1)**, **(2)**, **(3)** and **(4)**, it can be concluded that XZ-III-20 works both as an ETL and/or a HTL; however it has the highest external quantum efficiency, 0.95%, at 300 cd/m^2, in the emission layer geometry. In the future, the thicknesses of TPD and AlQ_3 as injection layers should be optimized. As a single layer, there was a high current density that leaked producing low external quantum efficiency, as well as high turn-on voltages for the thicker devices. Lifetime measurements at constant current have been taken for most of the devices but need to be completed. For XZ-III-20 in the bottom contact, p-type OFET geometry, the mobility was very low with a high threshold voltage and small on/off ratio. In the future, a top contact OFET should be fabricated, using a different metal for electrodes that would promote n-type behavior to test if XZ-III-20 also has electrons as charge carriers.

ACKNOWLEDGEMENTS

This research was supported by MDITR, a Science and Technology Center of NSF under Agreement Number DMR-0120967. Special thanks go to Andreas Haldi, Joshua Haddock, Xiaowei Zhan, Benoit Domercq, Seth Marder, Bernard Kippelen and the Kippelen Research Group.

REFERENCES

[1] Dini, D. *Chem. Mater.* **2005**, *17,* 1933-1945.
[2] Chen, H. Y.; *et al*. *Appl. Phys. Lett*. **2002**, *81*, (4), 574-576.
[3] Dimitrakopoulos, C. D.; Malenfant, P. R. L. *Adv. Mater.* **2002**, *14,* (2), 99-117.
[4] Newman, C. R.; *et al*. *Chem. Mater.* **2004**, *16,* 4436-4451.
[5] Okamoto, S.; *et al*. *Jpn. J. Appl. Phys*. **2001**, *40*, (2), 783-784.

Sarah Montgomery is currently studying Electrical Engineering at Purdue University. She plans to pursue a Masters Degree after her graduation in May.

Effects of Surface Chemistry on Cadmium Selenide Nanocrystal Fluorescence

Marsha S. Ng
University of Hawaii

Andrea M. Munro and David S. Ginger
Department of Chemistry
University of Washington

INTRODUCTION

CdSe semiconductor nanocrystals (NCs) possess size-tunable optical and electronic properties that make them promising candidates for applications such as light emitting diodes, solar cells, and biological labels. To be useful in these applications, the NCs must be highly fluorescent. These potential uses have propelled many studies exploring various means of increasing the quantum yield (QY) of CdSe NCs. The NCs have a large surface to volume ratio, causing their surface chemistry to be a major factor in their fluorescence. Dangling bonds at the surface cause trap states that lower the chances for radiative recombination of an electron hole pair by creating non-radiative decay pathways. One solution to this problem is to grow an inorganic shell (e.g. CdS or ZnS), another method is to passivate the surface with organic ligands. The functionalization of the ligand bound to the NC surface is important (e.g. hydrophilic functional group will allow NC to be soluble in water) and the effects of the ligands on fluorescence are still controversial[1-6]. To gain a greater understanding of the effects of organic ligands on NC fluorescence, we study how the concentration of 1-octadecanethiol (ODT), 1-butanethiol (BT), 1-octadecylamine (ODA), and 1-butylamine (BA) alter the photoluminescence (PL) of CdSe nanoparticles in chloroform solution.

EXPERIMENTAL

We synthesize CdSe NCs by a derivative of the method of Peng et al.[7] The synthesis is conducted under nitrogen gas in minimal light conditions. A thermocouple and heating mantle are used to regulate reaction temperature. Cadmium stearate stock solution is formed by heating 0.514g cadmium oxide and 4.552g stearic acid at 220°C for about 2 hours. Tri-n-butylphosphine selenium (TBP=Se) solution is formed by mixing 1.421g selenium powder, 3.843g TBP, 12.33g octadecence (90%). In a 25-mL 3-neck flask, 0.539g cadmium stearate powder, 2.0g octadecene (95%), 1.0g trioctylphosphine oxide (90%), 3.0g octadecylamine (97%) are purged for 10 minutes and heated to an injection temperature of 270°C. At the injection temperature, 2.25g of the TBP=Se solution is swiftly injected and the temperature reset to 250°C for growth. When the NCs reach their desired size the reaction is stopped by removing the heat. When the solution reached 60°C, the NCs were precipitated with acetone and centrifuged. The synthesis yielded monodisperse ~4 nm diameter CdSe NCs with maximum absorbance of 586 nm, full width at half max at ~30 nm. NC size was determined using the absorbance peak[8], and the initial quantum yield (QY) was found to be 13%.

It was observed that NCs in different regions of the centrifuge tube had differing fluorescence intensities. The NCs on the top layer of the centrifuge tube were more fluorescent than the middle layer, and the middle layer more fluorescent than the bottom layer. To eliminate this source of variation, we mixed all nanocrystals thoroughly after centrifugation unless otherwise noted.

For the ligand exchange experiments, 7.6E-7 mmol of CdSe NCs were mixed with ligand to make 3 mL solutions. The BA was purged with nitrogen for six hours. ODA and ODT stock solutions were prepared by dissolving the ODA or ODT solid in chloroform. ODA stock solutions were prepared at ~0.10 M, its estimated saturation point in chloroform. ODT stock solution concentrations were generally prepared at ~1.8 M.

A Perkin Elmer LS-50B Fluorimeter was used to measure the emission intensity of the test solutions. The fluorimeter response was calibrated using an external light source with known light intensity and Rhodamine-101 (R101) with a 100% quantum efficiency was used as a fluorescence standard. During emission spectra runs, the emission spectrum of 1E-6 M R101 in HCl/EtOH solution was monitored at fixed intervals to allow the data to be corrected for fluctuations in lamp intensity.

To investigate if H-NMR can be used to determine the relative amount of free and bound ligand in solution, solution state ^{1}H-NMR data was taken on a 300 MHz Bruker AV300. All CdSe NCs used in the NMR experiments were washed two times with acetone and dried prior to use. Deuterated chloroform ($CDCl_3$) was used as the lock solvent. The free ODA test solution was prepared with 0.019g ODA in 0.6 mL $CDCl_3$. The free ODT test solution was made by adding 0.1g ODT to 0.6 mL. The CdSe-ODA test solution was prepared by adding 0.019g ODA to 1E-5 mmol CdSe in 0.6 mL $CDCl_3$. The CdSe-ODT test solution was prepared by adding 0.02g ODT to 1E-5 mmol CdSe in 0.6 mL $CDCl_3$.

RESULTS

Figures 1 and 2 show that addition of both ODT and BT quench the fluorescence of CdSe NCs. Figures 3 and 4 show that at low concentrations (below ~0.01 M) of ODA and BA, the NP fluorescence is enhanced. This quenching can be fit with a single component Langmuir isotherm. Due to solubility issues, solutions with ODA concentrations above ~0.12 M were not tested. Solutions with 0 M ligand concentrations are plotted as 1E-15 M for the log scale in figures below.

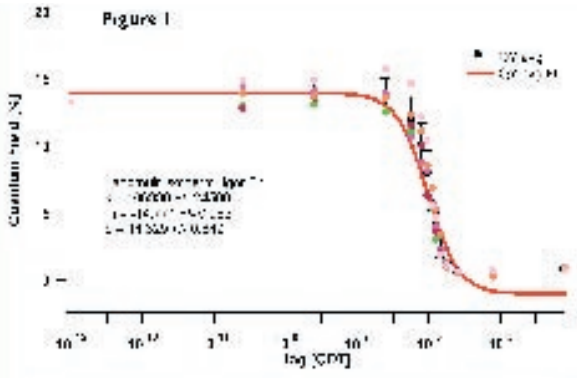

Figure 1. Quantum yeild vs 1-octadecanethiol concentration [M] for 4 nm diameter CdSe NCs in chloroform. (Core vials not mixed so absolute initial quantum yeild has err or).

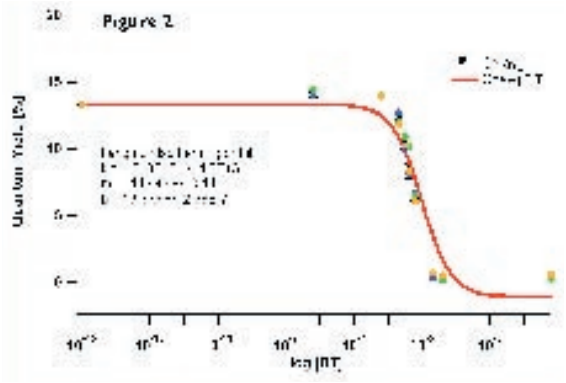

Figure 2. Quantum yeild vs 1-butanethiol concentration [M] for 4 nm diameter CdSe NCs in chloroform. (Core vials not mixed so absolute initial quantum yeild has error).

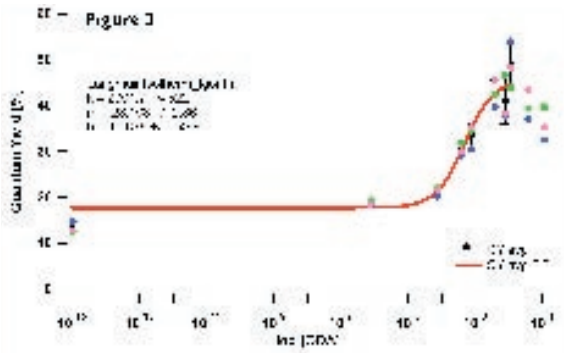

Figure 3. Quantum yeild vs 1-octadecylamine concentration [M] for 4 nm diameter CdSe NCs in chloroform.

Addition of degassed BA at low concentrations increased the QY, but quenching occurred at concentrations above 4E-3 M. Mixing BA and chloroform is exothermic, and the temperature rise for BA concentrations above ~0.6 M is noticeable. Figure 5 shows the blue-shift phenomena of the maximum absorbance peak at high BA concentrations.

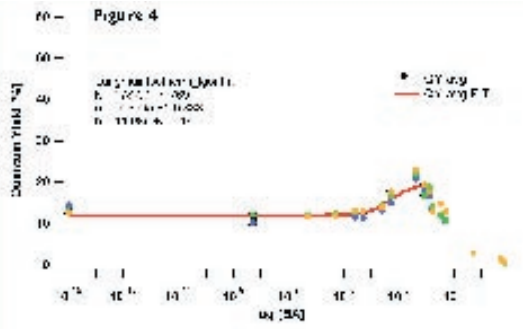

Figure 4. Quantum yield vs. 1-butylamine concentration [M] for 4 nm diameter CdSe NCs in chloroform.

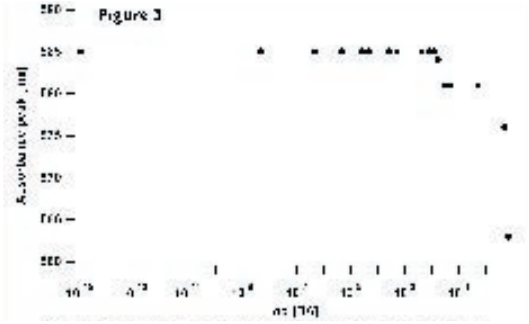

Figure 5. The maximum absorbance peak vs 1-butylamine concentrations [M].

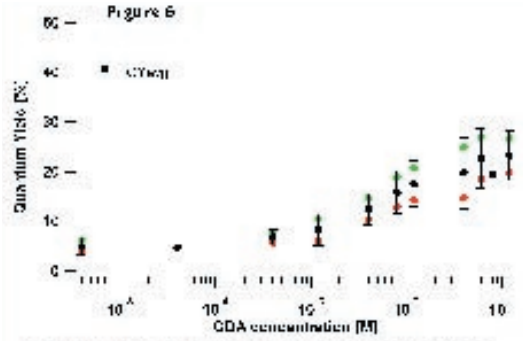

Figure 6. The quantum yield vs ODA concentration [M] with constant [ODT] = 1.2E-5 M present in solution.

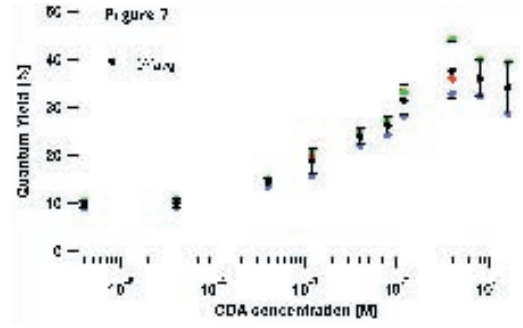

Figure 7. The quantum yield vs ODA concentration [M] with constant [ODT] = 6.2E-6 M present in solution.

The QY was enhanced more by the addition of ODA than BA.

To investigate the reversibility of ligand binding, ODA was added to CdSe NCs already partially exchanged with ODT. The QY of CdSe NCs in 1.2E-5 M ODT was ~6%. Figure 6 shows that upon addition of ~0.1M ODA, the QY was increased to ~21%. The QY of CdSe NCs in 6.2E-6 M ODT was ~10% and figure 7 shows that the addition of ~0.04 M ODA increased QY up to ~35%.

Figure 8, 9, and 10 show the H-NMR[9,10] spectra that was performed to attempt to determine the relative amounts of each ligand in solution that is free or bound to a CdSe NC. H-NMR spectra of 1E-5 mmol washed CdSe NCs, ODA, ODA bound to CdSe, ODT, and ODT bound to CdSe in deuterated chloroform were conducted.

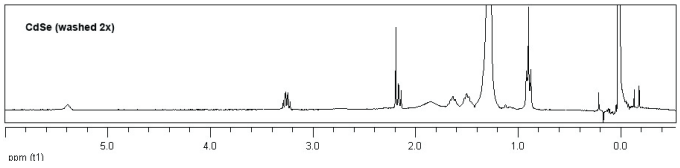

Figure 8. shows the 300 MHz solution state H-NMR spectra of 1E-5 mmol CdSe NCs in deuterated chloroform.

Figure 9. shows the structure of 1-octadecylamine (a) and corresponding peak assignments (b) on the colution state H-NMR spectra of ODA. Figure 9 (c) shows the H-NMR spectra when ODA is bound to IE-5 mmol CdSe deuterated chloroform.

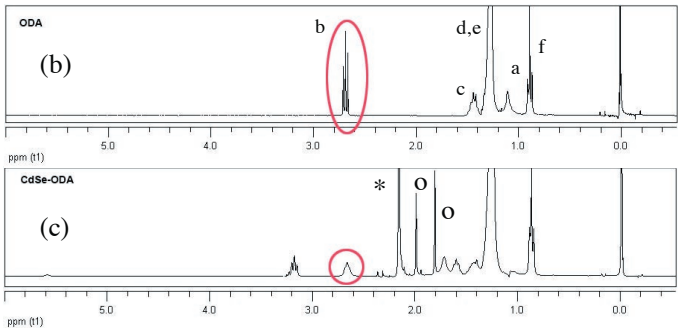

Figure 10. shows the structure of 1-octadecanethiol (a) and corresponding peak assignments (b) on the solution state H-NMR spectra of ODT. Figure 10 (c) shows the H-NMR spectra when ODT is bound to 1E-5 mmol CdSe in deuterated chloroform.

In the case of ODA binding to CdSe, the triplet peak (b) at ~2.66 ppm corresponding to the alpha-protons (circled in Figure 9) is broadened. The pentet at ~3.19 ppm leans towards the upfield peaks indicating that it is interacting with the ODA. *Acetone and stearic acid impurities. °Peaks are a result of amine bound to NC.

Figure 10 shows the structure of 1-octadecanethiol (a) and corresponding peak assignments (b) on the solution state H-NMR spectra of ODT. Figure 10 (c) shows the H-NMR spectra when ODT is bound to 1E-5 mmol CdSe in deuterated chloroform.

In ^{1}H-NMR studies of ODT, the proton on the sulfur atom (circled region in Figure 10) is presumed to have a chemical shift near the methylene peak at ~1.2 ppm making the peak difficult to resolve.

DISCUSSION

We hypothesized that the ligand binding could be described by a Langmuir isotherm (eqn 1). The Langmuir isotherm relates the fractional surface coverage, θ, of ligand on surface sites to the concentration of ligand in solution and can be derived from an equilibrium reaction given the equilibrium binding constant, K, and ligand concentration, [ligand].

$$(eqn\,1) \qquad \theta = \frac{K[ligand]}{1 + K[ligand]}$$

In order to use the isotherm, four assumptions were made: (1) the reaction is reversible, (2) only one monolayer can be formed, (3) binding of a ligand to a surface site does not affect the binding at any other sites, and (4) the QY is linearly dependent on the fractional surface coverage, θ. We also assumed that the NCs started with all empty surface sites, which is not true because there are stearic acid, TOPO, ODA bound to the surface.

A more accurate model would use a multiple component Langmuir isotherm in which the ligand already bound to the surface is taken into account. The fluorescence quenching that occurs at high amine concentrations does not agree with the assumption (4) that the QY increases linearly as the surface is passivated with more amine. For the amine curves the fits were made with data at amine concentrations below the solution saturation point of ODA (~0.01 M).

To improve the model, fits with the Hill equation (eqn 2) were performed. The Hill equation is widely used as an empirical fitting function when some degree of deviation from the Langmuir isotherm assumptions is expected.

$$(eqn\,2) \qquad \theta = \frac{K[ligand]^n}{1 + K[ligand]^n}$$

Table 1	Langmuir isotherm- K	Hill equation- K	Hill equation- n
CdSe + ODT	106980 +/- 24500	94877	2
CdSe + BT	101800+/- 4300	186470	2
CdSe + ODA	2001.7 +/- 522	4180	1
CdSe + BA	1787.3 +/- 769	2000	1

Table 1. shows the equilibrium binding constant (K) values found for least-squares fits of the Langmuir isotherm and Hill equations to the experimental data.

The similarity between the K-values of the amine and thiol pairs suggest that the alkyl chain effects are secondary to the effects of the head group. The larger K-values for the thiols shows that the sulfur binds better than nitrogen, which is consistent with the Hard-Soft Acid-Base Principal (HSAB). HSAB states that soft acids such as cadmium preferentially bind to soft bases such as sulfur; nitrogen is a borderline soft base and is less likely to coordinate to the cadmium.

Quenching occurs in the presence of thiol due to increased hole traps[11]. The thiol's sulfur atom is less electronegative than the amine's nitrogen and therefore would donate electrons more readily. When the sulfur atom binds to the cadmium, the cadmium atom becomes more negatively charged. The increased partial negative charge on the cadmium attracts holes in the semiconductor valence band resulting in "hole trapping." The trapping of holes hinders recombination of an electron-hole pair resulting in fewer radiative decay events and thus a lowered emission intensity.

The QY enhancement occurring at amine concentrations below ~0.01 M can be explained by an initial decrease in electron traps when the nitrogen binds to cadmium sites. After all the electron traps have been passivated, the amine will then bind creating hole trap sites and quenches the florescence. This could suggest that the amine preferentially binds to electron trap surface sites.

The quenching by amines could result from several possibilities: (1) impurities in BA, (2) etching of CdSe NCs at high amine concentrations, and (3) temperature changes. The molar ratio of CdSe NCs to water is ~10 in our test solutions. However, purging the BA with N_2 (g) did not appear to change the amount of quenching. The quenching and blue-shifting of the absorbance and PL peaks at high amine concentrations implies that the amine is etching the NC surface as demonstrated by Li et al.[12] Adding BA to chloroform caused the solution to heat up 10°C. This suggests that the heat released could be the heat of solvation of BA in chloroform solvent.

To check the reversibility of the BA quenching, the BA from a test solution with 6.75 M BA concentration was pumped off and chloroform was added back. Before pumping, the CdSe NCs had a maximum absorbance peak at 563 nm and quantum yield of 0.5%. After pumping off the BA, QY was 0.9% and the absorbance spectra appeared more broadened. However, the large blue shift of ~22 nm in the absorbance spectra was not reversible suggesting that indeed the nanoparticles were etched.

The restoration of the quantum yield upon addition of ODA to ODT-quenched CdSe NCs indicates that the ligand binding may be reversible at low concentrations. However, the initial 13% QY however was not achieved with the addition of ODA. At the high ODA concentrations, a drop in QY occurs. This drop is observed at the same ODA concentration as in the earlier tests of CdSe NCs and ODA.

CONCLUSION

Our studies have shown that thiols quench the fluorescence of 4 nm diameter CdSe NCs, whereas at low concentrations (below ~0.01 M) amines enhance PL and at high amine concentrations quench PL. At low concentrations, the thiol and amine can be reversibly exchanged. Reversibility tests indicate that the reaction with high concentrations of amine is not completely reversible due to surface etching. Fluorescence measurements can allow us to calculate the amount of ligand bound to the core if we assume that PL is proportional to surface coverage. In the future, H-NMR could be used to quantify surface coverage to complement fluorescence data.

ACKNOWLEDGEMENTS

Many thanks to my mentors, Andrea Munro and David Ginger, for their help and guidance. Thank you to the NSF Science & Technology Center for Materials and Devices for Information Technology Research for funding the Summer 2005 Hooked on Photonics REU program and allowing me to enrich my summer with research. Thanks to Loren Kruse and Rajan Paranji of the UW NMR facilities and Brenden Carlson and Kolby Allen of the Dalton Lab for their help in NMR spectroscopy. Also thanks to Yeechi Chen for her support and guidance.

REFERENCES

1. Dannhauser, T.; O'Neil, M.; Johansson, K.; Whitten, D.; McLendon, G. "Photophysics of Quantized Colloidal Semiconductors Dramatic Luminescence Enhancement by Binding of Simple Amines" *J. Phys. Chem* ***1986****, Vol 90, No. 23, 6074-6076.*

2. Landes, C.; Burda, C.; Braun, M.; El-Sayed, M. A. "Photoluminescence of CdSe Nanoparticles in the presence of a Hole-Acceptor: n-butylamine" *J. Phys. Chem. B* ***2001****, Vol 105, No 15, 2981-2986.*

3. Landes, C.; Braun, M.; El-Sayed, M. A.;"On the Nanoparticle to Molecular Size Transition: Fluorescence Quenching Studies" *J. Phys. Chem. B* ***2001****, Vol 105, No 43, 10554-10558.*

4. Hohng, S.; Ha, T. "Near-Complete Suppression of Quantum Dot Blinking in Ambient Conditions" *J. Am. Chem. Soc.* ***2004****, Vol 126, No 5, 1324-1325.*

5. Kalyuzhny, G.; Murray, R. "Ligand Effects on Optical Properties of CdSe nanocrystals." *J. Phys. Chem. B* ***2005****, Vol 109, No 15, 7012-7021.*

6. Jeong, S.; Achermann, M.; Nanda, J.; Ivanov, S.; Klimov, V.; Hollingsworth, J. "Effect of Thiol–Thiolate Equilibrium on the Photophysical Properties of Aqueous CdSe/ZnS Nanocrystal Quantum Dots" *J. Am. Chem. Soc.* ***2005****, Vol 127, No 29, 10126-10127.*

7. Peng, Z.; Peng, X. "Nearly Monodisperse and Shape-Controlled CdSe Nanocrystals via Alternative Route: Nucleation and Growth" *J. Am. Chem. Soc.* ***2002****, Vol 124, No 13, 3343-3353.*

8. Yu, W.; Qu, L.; Guo, W.; Peng, X. "Experimental Determination of the Extinction Coefficient of CdTe, CdSe, and CdS Nanocrystals." *Chem. Mater. 2003, Vol 15, No14, 2854-2860.*

9. Sachleben, J.; Wooten, E.; Emsley, L.; Pines, A.; Colvin, V.; Alivisatos, A. "NMR studies of the surface structure and dynamics of semiconductor nanocrystals" *Chem. Phys. Lett,* ***1992****, Vol 198, No 5, 431-436.*

10. Berrettini, M.; Braun, G.; Hu, J.; Strouse, G. "NMR Analysis of Surfaces and Interfaces in 2-nm CdSe" *J. Am. Chem. Soc.* ***2004****, Vol 126, No 22, 7063-7070.*

11. Wuister, S.; de Mello Donega, C.; Meijerink, A. "Influence of Thiol Capping on the Exciton Luminescence & Decay Kinetics of CdTe and CdSe Quantum Dots." *J. Phys. Chem. B* ***2004****, Vol 108, No 45, 17393-17397.*

12. Li, R.; Lee, J.; Yang, B.; Horspool, D.; Aindow, M.; Papadimitrakopoulos, F. "Amine-Assisted Facetted Etching of CdSe Nanocrystals." *J. Am. Chem. Soc.* ***2005****, Vol 127, No 8, 2524-2532.*

Synthesis of a Polyene EO Chromophore: Using a Diels-Alder Reaction to Form a Side-Chain Structure

Denis Nothern
Cornell University

Jingdong Luo, Alex K.-Y. Jen
University of Washington

INTRODUCTION

Nonlinear optical (NLO) polymers have drawn significant attention over the past decade for their growing potential to revolutionize the field of electro-optics (EO). These polymers combine comparatively simple and low cost processing with the advantages of high signal bandwidth and low operating voltages. Recent work has focused on improving the stability of the host-polymers via a cross-linking scheme based on a Diels-Alder reaction.[1] In this research, a similar concept has been applied to the bonding between the nonlinear chromophores and the host-polymer, to form a side-chain structure utilizing a Diels-Alder reaction.

The larger motivation behind this research is maximizing two key material characteristics: the poling efficiency and the thermal stability. The poling efficiency, while not the only factor associated with achieving a high electro-optic coefficient, is an important material property that indicates the polymer's ability to form a noncentrosymmetric system (a condition imposed by the second order nature of the electro-optic effect). To achieve a high poling efficiency the chromophores in the polymer must be free to rearrange their alignment when it is desired while avoiding chromophore-chromophore interactions that lead to close packing aggregation in the lower energy symmetric configuration. With chromophores freely embedded in the host-polymer (a guest-host system) they are able to easily align with the poling field, but will also be relatively free to return to the lowest energy state once the poling field is removed. Alternatively, the chromophores can be embedded into the host-polymer as side-chains that limit their ability to rearrange, thus avoiding aggregation but limiting the ability to align with the applied field. This leads to the examination of the thermal stability of the system.

The thermal stability of the material is crucial because of the demands on such a device. In use it will be exposed to a wide range of temperatures—sources both intrinsic to the operation of the device and sources extrinsic to the device present in the operating environment. For example, a device is not useful if it cannot be used for extended periods of time due to overheating as a result of its normal use, nor is it useful if it has only very limited implementation resulting from temperature constraints placed on the system around it. The polymer's thermal stability is primarily dependant on its glass transition temperature (T_g). As the material approaches its T_g it will typically experience thermal relaxation in which the polymer backbone becomes pliable enough for the chromophores that had previously been aligned noncentrosymmetrically to become free and return to the preferential centrosymmetric state. At high temperatures it is also common that the chromophores and the host-polymer experience phase separation due to unequal thermal characteristics, this is evidenced by high currents during poling. As discussed earlier, forming side-chains will help counter thermal relaxation and will also help maintain a homogeneous system, but at the same time will make poling more difficult. It is because of this trade-off between poling efficiency and thermal stability that this research explores a solution that maximizes them both. If one embeds the chromophores as guests in the host-polymer but also functionalizes the chromophores so that as the temperature is increased upon poling they undergo a reaction with the host-polymer and attach as side-chains aligned with the applied field, the poling efficiency and thermal stability can be balanced.

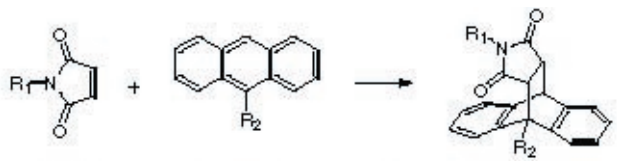

Scheme 1. Maleimide undergoes cycloaddition with anthracene in a Diels-Alder reaction.

The ability to attach the chromophores as side-chains *in situ* during poling is dependant on a Diels-Alder (DA) reaction between the chromophores and the host-polymer. DA reactions have been extensively explored and are based on the cyclo-addition of a diene with a dienophile to form a six-membered ring (scheme 1)[2]. The use of this type of reaction is promising in that it can be thermally controlled and produces no additional products beyond the desired cyclohexene (this gives it the name "Click Chemistry"). If additional products are present in the polymer system they could have adverse and fundamentally unpredictable effects on the operation of the device. Since the system must be heated close to its T_g in order to achieve maximum alignment during poling, a thermally controlled DA reaction with a very high

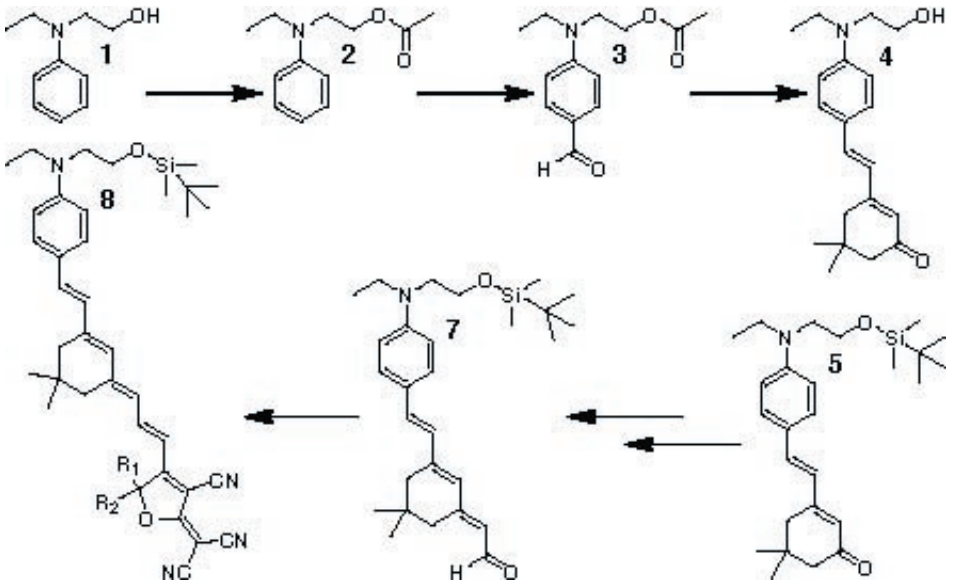

Scheme 2. Synthesis of polyene chromophore.

temperature required to reverse and an activation energy similar to the poling temperature is ideal so that complete linking of the chromophores to the polymer occurs once they have already been mostly aligned with the field. A DA reaction also exhibits essential characteristics when taking processability into account because the chromophore can be bound to the polymer cleanly and in a controlled manner without the need for solvents, catalysts or any other external chemical processes—this is particularly important for more efficient chromophores that are sensitive to their surroundings.

This concept has been shown to work with nonlinear chromophores already, but difficulty arises when it is applied to highly efficient nonlinear chromophores. More efficient chromophores, by nature, are highly polar and consequently they are quite sensitive to their chemical environment. This makes it exceedingly difficult to functionalize them without decomposing them completely.

With this in mind, the objective was to synthesize several polyene-type chromophores with a dienophile group at R_1 so that it may combine with a diene-functionalized host-polymer to form a side-chain system via a DA reaction (figure 1). Other structures are present at R_2 and R_3 to benefit from the advantages of further limiting the chromophore-chromophore interactions. Once synthesized, the materials properties were analyzed.

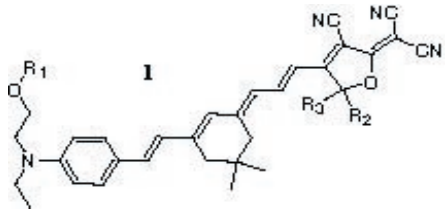

R_1=dienophile group
R_2=phenyl group

Figure 1. A polyene-type chromophore.

EXPERIMENTAL

Synthesis of the polyene chromophore was carried out with a fairly standard procedure (scheme 2).

The maleimide functional group to be used as the dienophile was synthesized as an acid chloride (scheme 3). Literature indicated that this reaction would only last a matter of hours however it was found to take significantly longer.[4] The first batch was only reacted for 3 hours and had a great deal of impurity, which greatly affected the functionalization results.

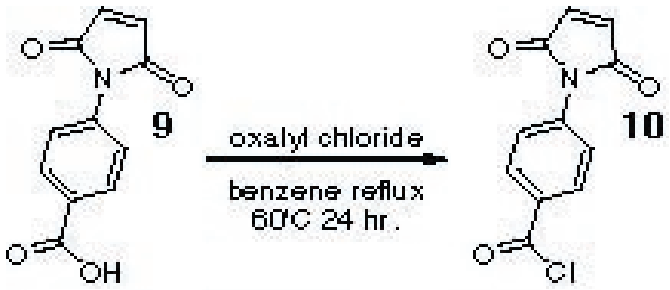

Scheme 3. Production of acid chloride.

The finished chromophore **8** was deprotected and the acid chloride **10** was added (scheme 4). The yield of this reaction was negligible due to the poor purity of the acid chloride. Despite extremely low yield, chromatography indicated that the reaction did occur as hoped for. To confirm the success of this reaction scheme, a sample of the AJC-139 chromophore was reacted for 24 hours with purer acid chloride (scheme 5).

This reaction was a success with 57% yield. A chromophore similar to the original was synthesized from an intermediate **16** and a slightly different acceptor group (scheme 6).

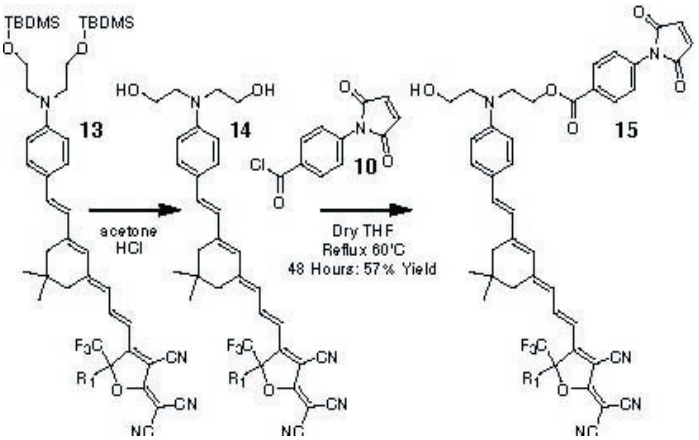

Scheme 4. Functionalization of polyene chromophore.

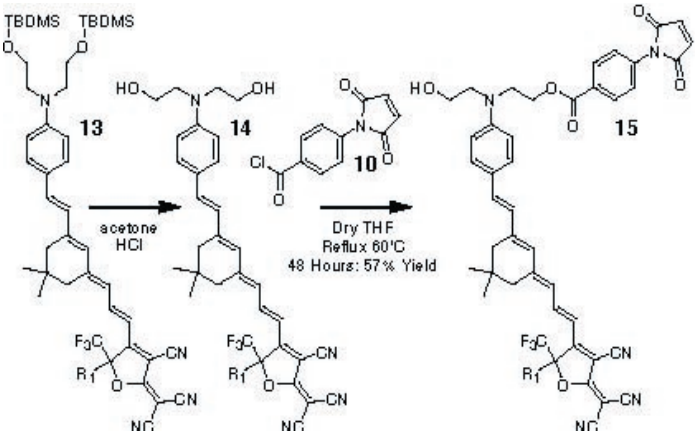

Scheme 5. Functionalization of AJC-139 chromophore

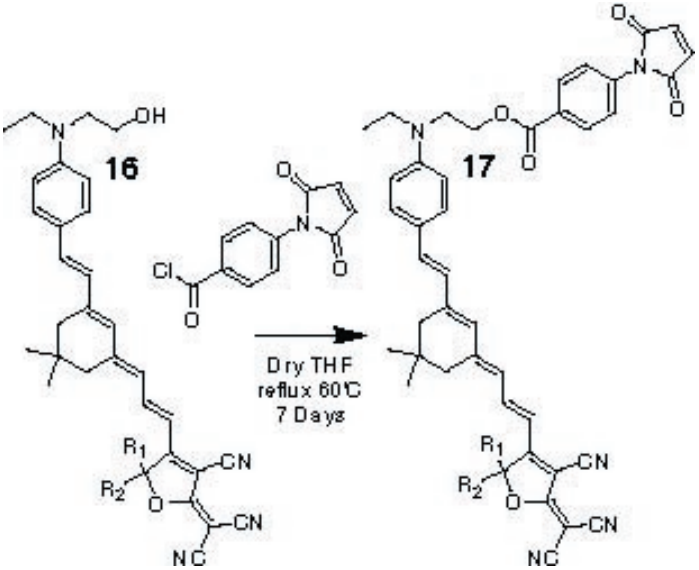

Scheme 6. Functionalization of 2nd polyene cromophore.

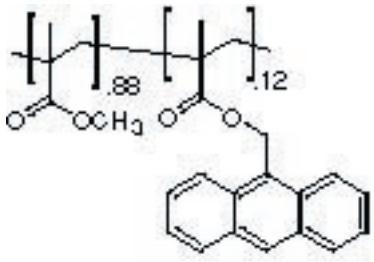

Figure 2. Polymer Host.

At this point synthesis was considered complete and chromophore **17** was embedded in an anthracene functionalized polymethyl-methacrylate (PMMA) host polymer with a 25 wt.% loading density (figure 2). It was spin-cast to form a .75um film on a glass substrate half coated with conducting indium-tin-oxide (ITO) (120nm) particularly designed to be optically transparent at telecommunications wavelengths (1.3um). Three samples were prepared by sputtering a gold electrode onto the top of the polymer film such that they were half over the ITO and half over the glass (figure 3). This allowed a voltage to be applied across the electrode and the ITO layer and pole the polymer. While the poling voltage was being applied, current passing through the polymer was carefully monitored for indications of damage to the film. During heating, the current was recorded overtime. Once poled, the r_{33} value was measured via the reflection technique[3]. The results can be seen in the following section.

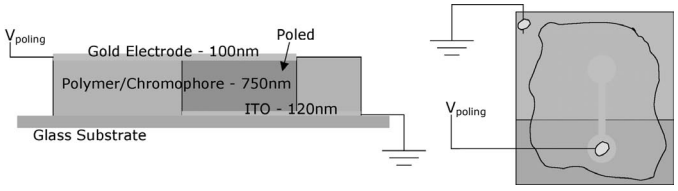

Figure 3. Poling setup.

All the samples were exposed to the poling voltage and then heated at a rate of 5°C/sec starting at 50°C. The current through the polymer layer varies over time as the sample is heated (figure 4). This gives an indication of when the T_g is being approached as the current reaches a local maxima (or a minima in the case of polymer breakdown and current is able to jump directly from the gold to the ITO).

With a 25 wt.% loading density, poling with 100V/um at 111°C the r_{33} value was found to be as high as 44pm/V (Table 1). This is nearly double the value for the less efficient chromophores previously implemented in such a side-chain scheme. The high poling temperature is an indication that the side-chains formed and that the thermal stability of the system will be good. Additionally, the very low current at such high temperatures (4.5 uA at 160°C) indicates that there is little phase separation between the polymer and the chromophores, which is in agreement with expectations for a side-chain structure.

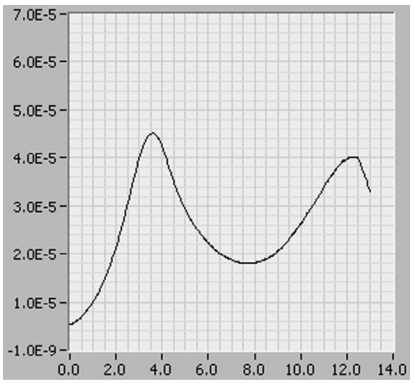

Table 4. Current vs. Time

Sample	Field (V/um)	Temp (‘C)	Current (uA)	r_{33} (pm/V)
#1	100.00	160	4.5	42
#2	100.00	110	58	35
#3	100.00	111	45	44

Table 1. r_{33} values.

CONCLUSION

It has been shown that a highly efficient polyene chromophore can be functionalized with a dienophile. A feat that was previously unachievable. Furthermore, the resulting compound can be incorporated into a side-chain polymer via Diels-Alder “Click Chemistry” and efficient poling has been achieved in this polymer system resulting in a reasonable r_{33} value.

Improvements in long-term stability compared to the guest-host structure are yet to be shown for such a system, but previous investigations of Diels-Alder based side-chain structures with other chromophores is promising.

ACKNOWLEDGEMENTS

Research support is gratefully acknowledged from the National Science Foundation Center on Materials and Devices for Information Technology Research (CMDITR), DMR-0120967.

REFERENCES

[1] J. Luo, M. Haller, H. Li, T.-D. Kim, A. K.-Y. Jen, *Adv. Mater.* **2003**, 15, No. 19.

[2] Francesco Fringuelli and Aldo Taticchi, *The Diels-Alder Reaction: Selected Practical Methods*. John Wiley & Sons: 2002.

[3] P. Gunter (Ed.), *Nonlinear Optical Effects and Materials*. Springer-Verlag: New York, 2000. (p. 197)

[4] Hoyt and Benicewicz. *Poly. Sci. Part A: Poly. Chem.* **1990**, v. 28, p. 3403.

Spectroscopic Investigations of Chromophores in Dyed Salt Crystals

Stacy A. Oliphant
Edmonds Community College

Kristin L. Wustholz, Bart Kahr and Philip J. Reid
Department of Chemistry
University of Washington

INTRODUCTION

The Science and Technology Center (STC) is committed to the development of next-generation electro-optic (EO) devices, typically based on dye-doped polymers. Polymer-based switches have demonstrated greater device efficiencies when compared to traditional inorganics. Since the EO effect relies on the nonlinear material response, the dye-doped polymers must be noncentrosymmetric. This is typically achieved via the application of a poling field. Ultimately, EO activity is given by:

$$|N\mu\beta\langle\cos 3\ \theta\rangle|$$

where the EO response is proportional to the number of dye molecules (N), the molecular dipole moment (μ), hyperpolarizability (β), and the ordering parameter ($\cos^3\theta$) that represents the extent of alignment afforded by poling. Understanding the factors that influence chromophore orientation has taken a backseat to the development of enhanced molecular properties (i.e. β). Yet, recent work suggests that poling is only partially effective in achieving molecular alignment[1] – making it quite clear that the poling procedure and ordering parameter are not well understood.

To experimentally test the efficacy of poling, and hence bulk EO device efficiency, it makes sense to begin with a system in which the chromophores are intrinsically aligned by the host. When grown in the presence of many organic dyes, aqueous solutions of potassium acid phthalate (KAP) and sodium potassium tartrate tetrahydrate (commonly known as Rochelle salt) frequently deposit "dyed crystals" wherein chromophores are oriented and overgrown by the host lattice. In these crystals, dyes selectively adsorb to particular sub-volumes within the lattice and bulk spectroscopic studies suggest that they are intrinsically aligned during the growth process. For example, Figure 1 shows that 4-(Dicyanomethylene)-2-methyl-6-(p-dimethylaminostyryl)-4H-pyran (DCM) adsorbs to the {11^{-}1} growth sector, while Violamine R (VR) adds to the {010} growth sector of the host crystal, KAP.

Here, a natural comparison presents itself in the study of the NLO properties of chromophore-polymer composites and dye-doped single crystals. We use single-molecule spectroscopy to measure the orientations and fluorescence spectra of embedded dye molecules. The focus of this work was to interrogate the alignment and photophysics of single chromphores in dye-doped crystal hosts using confocal microscopy. Furthermore, by comparing the orientations of dyes to their energetics, the environmental heterogeneity among individual dye molecules within the crystal can be studied.

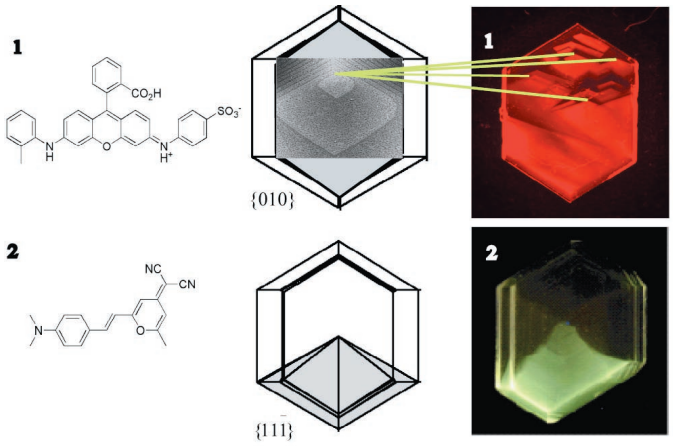

Figure 1. Dye-Doped KAP Crystals. Violamine R (1) and DCM (2) ad3sorb to different growth sectors of the KAP crystal host.

EXPERIMENTAL

Dyed crystals were grown by slow evaporation from aqueous solution, in a temperature controlled air chamber (30°C) with dye concentrations of 10^{-4} M to 10^{-8} M. The latter concentration was used to ensure single-molecule resolution.

Single-molecule experiments were performed using a confocal microscope with the following parameters: an inverted microscope (Nikon, TE2000). Excitation from a 532 nm solid-state laser (NovaLux) was filtered (Chroma) and the excitation polarization was manipulated using a half-waveplate. The laser was focused to a diffraction-limited spot with an objective (100x, Nikon, 1.3 NA). Cleaved crystal samples (~1 mm) were mounted on a closed loop x-y piezo scanning stage (Queensgate). Emission was spectrally filtered by a dichroic mirror and emission filters (Chroma) and spatially filtered with a confocal pinhole (ThorLabs: 50 μm). The fluorescence intensity was imaged onto a single-photon counting APD (PerkinElmer). Single-molecule fluorescence spectra were measured by adding a monochromator (Acton) attached to a liquid N_2 CCD camera (Princeton Instruments) to the confocal instrument.

RESULTS

The heavily-dyed crystals were grown and studied by absorbance and fluorescence. By using these techniques, ensemble-average properties of the dyes were measured. Figure 2 shows polarized absorption spectra of a heavily dyed VR/KAP crystal, demonstrating that chromophores are oriented ~42° from [100]. Bulk studies allow one to measure average orientation, but the extent of alignment (the orientational distribution) is concealed at high loading densities. To measure the extent of alignment and single-dye energetics, we chose to study dyed crystals on a molecular level. By using single-molecule excitation dichroism, the orientation of the dyes included in crystals can be measured. Figure 3 shows the fluorescence dichroism of a single-molecule VR dyed KAP crystal grown from a concentration of 10^{-8} M dye. The dichroism was measured using the equation $\theta = \tan^{-1}[\sqrt{I_a}/I_c]$ and the average orientation for 11 molecules is 39.6° from [100] which agrees with the bulk absorption measurement of ~42° from [100]. Our results showed agreement between single-molecule and bulk measurements; and to prior single-molecule measurements on this system.[2] Yet, to study the emission properties of single-dye molecules in this system we needed to modify the confocal instrument accordingly.

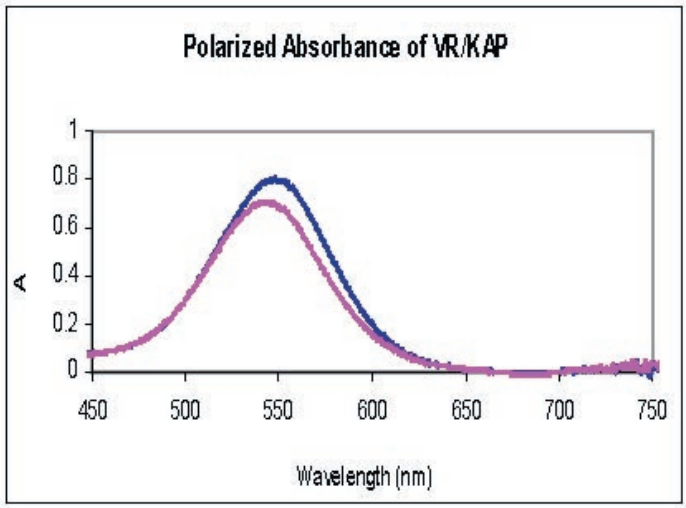

Figure 2. Polarized Absorption Spectra of 10^{-5} M VR/KAP Crystal. Dyes were measured to be oriented ~42° from [100] at an absorption maximum (λ_{max}) of ~545nm.

A monochromator/ Hamamatsu CCD camera assembly was added to the confocal microscope and used to measure fluorescence spectra of dyes in growth hillocks. Preliminary work on lightly-dyed (10^{-5} M dye) VR/KAP crystals using a Hamamatsu CCD camera suggested environmental heterogeneity between dyes located on or off growth hillocks (Figure x). The fluorescence intensities at 604 nm and 647 nm were monitored as a function of location on/off the hillock. Interestingly, dyes were less intense on the hillock, and exhibited stronger fluorescence at 647nm than 604 nm. Further work will be done to explore the properties of dyes on/off hillocks. Since we were unable to measure single-molecule spectra with this detector, a liquid N_2 cooled CCD camera and monochromator was coupled to the confocal microscope. The new setup was characterized using fluorescent beads (Molecular Probes) and heavily-dyed VR/KAP crystals. The procedure for obtained a single-molecule fluorescence spectrum was as follows: the crystal was first scanned using the unmodified confocal set-up to obtain the 10 x 10 μm^2 image with 100 ms integration time at a power of 5 μW. Then, the microscope stage was used to focus the excitation on a single molecule, and the power was intensified to 10 μW and the integration time was increased to 10 minutes. Figure 4 shows a fluorescence spectrum of a single dye molecule in VR/KAP. With single-molecule resolution demonstrated, future work will be done to optimize data collection and correlate the fluorescence spectra with orientation.

Another interesting system that was studied this summer is dyed Rochelle salt crystals. Rochelle salt (RS) is a ferroelectric crystal that undergoes a phase transition at certain temperatures called Curie points. Our goal was to grow dyed RS crystals and to use the embedded dyes to report on the ferroelectric phase transition. Unfortunately, most of the time was spent determining the optimal growth conditions for the RS crystals, and we were unable to study to begin single-molecule spectroscopic investigations. Yet, preliminary studies on sulforhodamine B (SB) and Chicago Sky Blue (CSB) dyed RS crystals were performed (Figure 5). We successfully reproduced prior work on CSB/RS crystals and demonstrated that the fluorescent dye SB incorporates in the {010} growth sector of RS, absorbs at 505 nm, and emits at 583 nm. Future work will be done to learn more about the ferroelectric properties of the crystal by monitoring SB dye orientation during a phase transition at the single-molecule level.

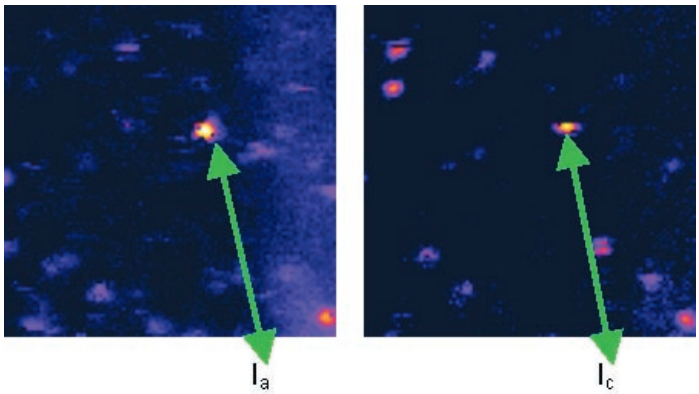

Figure 3. Single-Molecule Orientations in VR/KAP. The crystal was scanned on both the "a" and "c" directions to obtain a 10 x 10 μm2 area, over 100 ms integration time, at 100 nm step size at 5 μW power. Fluorescence Intensity (**Ia**): 506 – 29 / 100 ms, Fluorescence Intensity (**Ic**): 233 – 29 / 100 ms, θ_{avg} = 39.6° for 11 molecules using $\theta = \tan^{-1}[\sqrt{I_a}/I_c]$.

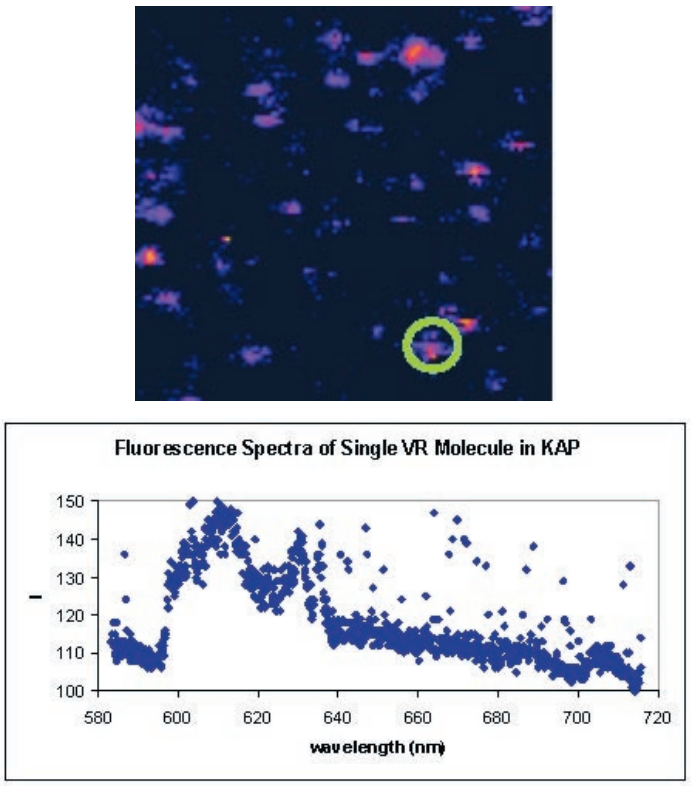

Figure 4. Intensity Map and Corresponding Single-Molecule Fluorescence Spectra in VR/KAP. The single-molecule fluorescence spectrum was obtained using 10 μW incident power and 10 min integration time.

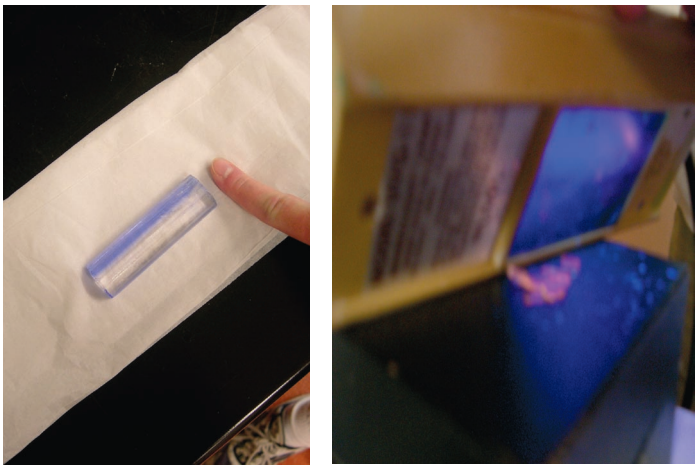

Figure 5. Rochelle Salt Dyed Crystals; Chicago Sky Blue (left) & Sulforhodamine B illuminated by a short wave ultra-violet lamp (254 nm) (right).

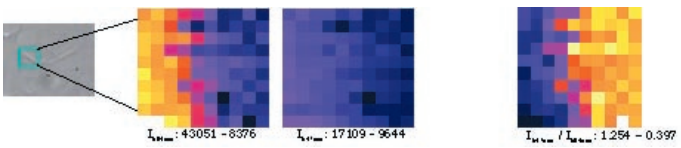

Figure 6. Fluorescence on Growth Hillocks in 10^{-5} M Dyed VR/KAP. A 5x5μm2 area (box in blue) was scanned, using a 500 nm step size and 18 sec. integration time. The intensity maps show environmental heterogeneity within the crystal. The third intensity map (I_{647} nm/I_{604} nm) shows change in relative intensity of these peaks on the hillock versus off the hillock.

SUMMARY

This summer, dyed crystals were grown and characterized using conventional and single-molecule spectroscopy. The average of single-molecule orientations in VR/KAP crystals agreed with the ensemble-average measurements, yet orientations outside the ensemble-average were observed. These results are in agreement with prior work on this system. [2] Preliminary work on lightly-dyed (10^{-5} M dye) VR/KAP crystals suggested environmental heterogeneity between dyes located on or off growth hillocks. By modifying the confocal microscope to include a monochromator and liquid N_2 cooled CCD camera, single-molecule fluorescence spectra were obtained. In demonstrating the single-molecule resolution of the monochromator/CCD camera setup, we have shown that this instrument can be used to further investigate the environmental heterogeneity among dyes within crystals and eventually, poled polymers.

Only limited studies, particularly bulk characterization of dyed Rochelle salt, were completed. Future work will be done on these crystals to study the ferroelectric properties of the host using single fluorescent reporters to monitor a phase transition.

ACKNOWLEDGEMENTS

The authors thank the National Science Foundation (NSF) and the Center on Materials and Devices for Information Technology Research (CMDITR) for support of this work. S.O. is supported by the CMDITR REU summer program.

REFERENCES

1. Robinson, B.H.; Dalton, L.R. *J. Phys. Chem. A.* **2000**, *2000*, 4785.

2. Wustholz, K.L; Kahr, B.; Reid, P.J. *J. Phys. Chem.* In press Sept. 2005

Characterization of the Molecular Parameters Determining Charge-Transport in a Series of Substituted Oligoacenes

Robert Snoeberger
University of Washington

Seth Marder
Georgia Institute of Technology

Organic semiconductors are currently receiving much research interest due to applications in devices such as field-effect transistors (FET), photovoltaic (PV) cells, and organic light-emitting diodes (OLED). These organic devices may be produced more cheaply and efficiently than inorganic counterparts, however, more efficient and stable materials need to be designed for organic devices to become feasible for production.

Currently, pentacene is commonly used as an organic semiconductor, in crystalline FET applications, due to the large hole mobility1. It has been seen however, that the mobility of pentacene based FETs decrease with exposure to air2,3. A remedy is the replacement of the terminal fused benzene rings with thiophene rings making anthradithiophene (ADT); ADT provides greater air stability with an acceptable drop in device mobility[4,5], with a measured mobility of 0.02 cm2/Vs at room temperature.

A further extension to this idea, explored by Takimiya et al[6], was the replacement of the sulfur atoms in the thiophene rings with larger chalcogen atoms. The intent is to increase the electron coupling between adjacent molecules. Takimiya reported the synthesis of diphenyl-benzodithiophene (DPh-BDS) along with the selenium and tellurium analogs. Device mobilites were measured for hole-transport for the molecules, DPh-BDS gave a mobility of $1.6\text{x}10^{-2}$ cm^2/Vs at room temperature compared to DPh-BDT which gave a mobility of $4.6\text{x}10^{-3}$ cm^2/Vs at room temperature[6].

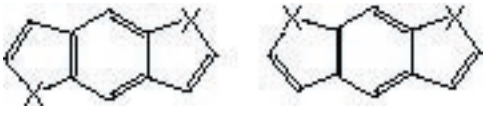

Anti (a) Syn

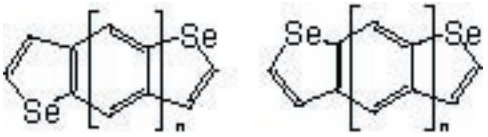

Anti (b) Syn

The goal of our summer work has been to characterize these systems using charge-transport theory. The theoretical effort was applied to the oligoacenes without phenyl substituents so that the effect of the chalcogen atom on the oligoacene may be isolated. A second type of systems which was characterized was based on chalcogen-substituted oligoacenes, where the number of fused benzene rings in the center of the molecule is increased. The molecules used in the study, system (a) and system (b), are displayed in figure 1.

Marcus theory may be used to characterize the charge-transfer properties of organic materials which will help the development of future systems. The mobility of a material may be described with equation 1,[4,7,8] at high temperature and assuming the transfer process is described by a series of uncorrelated hops.

$$\mu = \frac{ea^2}{k_B T} k_{ET}. \qquad (1)$$

Where e is the electronic charge, a is the distance between molecules, k_{ET} is the hopping rate, k_B is the Boltzmann constant, and T is the temperature in Kelvin. It is shown that the mobility is proportional to the hopping rate, which is expressed by equation 2,[4,7,8]

$$k_{ET} = \frac{4\pi^2}{h} \frac{1}{\sqrt{4\pi k_B T}} t^2 \exp\left(-\frac{\lambda}{4k_B T}\right) \qquad (2)$$

Here, λ is the reorganization energy, t is the transfer integral, and h is the Planck constant. The reorganization energy is composed of intermolecular (outer) and intramolecular (inner) contributions. The outer reorganization energy arises from the polarization and relaxation of the surrounding environment while the inner reorganization energy corresponds to the geometry relaxations occurring during the charge-transfer reaction. The charge-transfer reaction may be modeled as a simultaneous oxidation and reduction reactions. The oxidation and reduction reactions include associated vibrational relaxations, whose energy corresponds to the relaxation energy. The inner reorganization energy is composed of the sum of the two relaxation energies, one from the oxidation reaction and the other from the reduction reaction.

According to equation 2, the activation energy for the hopping rate is equal to one fourth of the reorganization energy. This relation makes the reorganization energy an important parameter to characterize for charge-transport systems, and is the dominant focus of the current work. The reorganization energy for the systems of interest were calculated using the Gaussian[9] 98 suite of programs with Density Functional Theory (DFT)[10] using Becke three-param-

eter Lee, Yang, Parr (B3LYP)[12] functional. The results of the reorganization energy calculations for system (a) are shown in chart 1 below. The LanL2dz basis set[13,14] was used during the calculations, unless otherwise specified, because the 6-31G** basis set[15] is not available for tellurium, but would be preferred. Therefore, chart 1 contains values calculated with the 6-31G** basis set for sulfur and selenium as a comparison with the LanL2dz basis set.

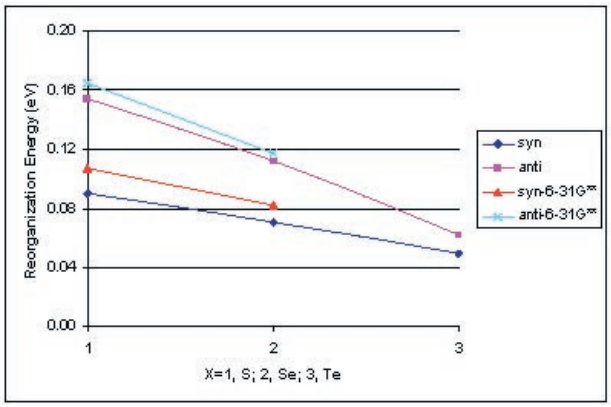

Chart 1. Reorganization Energy of System (a)
Calculated with B3LYP/LanL2dz
For Hole-transport

The results on chart 1 show as a general trend, for system (a), that the reorganization energy, for hole-transport, decreases moving along the system from the sulfur analog to the tellurium analog. This is attributed to a smaller geometry relaxation for the tellurium analog than that of the sulfur analog because the bond-length change of the carbon-carbon bonds becomes smaller moving toward the tellurium analog (0.10A to 0.068A) showing that larger portion of the positive charge in the cation state is being located on the chalcogen atom. A population analysis confirms that more of the cation charge is located on the larger chalcogen atoms (0.18 electron charge on S in BDT-syn compared to 0.28 electron charge on Te in BDTe-syn) but that the geometry change associated with the larger population is minimal (0.090A in BDT-syn compared to 0.084A in BDTe-syn).

Chart 1 also displays an isomer dependence in the system, where the syn isomer has a lower reorganization energy. This trend is also caused by the change in cationic character on the chalcogen atom in the syn isomer compared to the anti isomer. The bond-length change of the chalcogen-carbon bonds was larger in the syn isomer than that of the anti isomer (0.09A for the syn isomer and 0.08A for the anti isomer of BDT) while the bond length change of the carbon-carbon bonds was much larger in the anti isomer than the syn isomer (0.10A for the syn isomer and 0.15A for the anti isomer of BDT). A population analysis also confirms the correlation between reorganization energy and amount of charge of the chalcogen atoms (0.18 electron charge in BDT-syn compared to 0.17 electron charge in BDT-anti).

The results of the reorganization energy calculations for system (b) are shown in chart 2 below, calculated using the 6-31G** basis set.

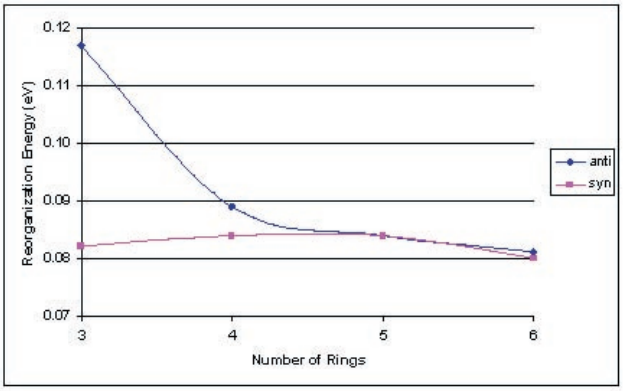

Chart 2. The Reorganization Energy for System (b)
Calculated with B3LYP/6-31G**
For Hole-transport

The results from chart 2 show that the isomer dependence becomes negligible at long molecular lengths. The reorganization energy for the syn isomer stays approximately constant along the series which is due to the overall change in geometry being the same. This may be attributed to more of the cation charge being localized on the chalcogen atom at small molecular lengths but becomes less of a factor at longer molecular lengths.

The transfer integral, which is the dominant constituent of the exponential prefactor in equation 2, may be approximated as half the electronic coupling between the donor and acceptor. However, a direct calculation of the transfer integral for a particular system is dependent on bulk order, which is difficult to determine. A general trend may be extracted by changing the dimer orientation during the electron splitting calculations, which is presented in chart 3 below, where the dimer distance is increased. The calculations were performed on Ampac[16] using the AM1[17] semi-empirical method.

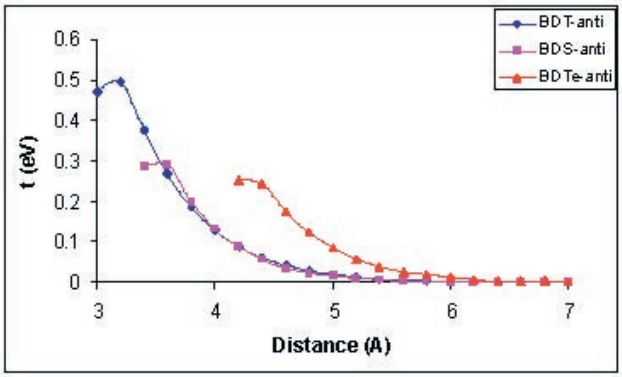

Chart 3. Transfer Integral for System (a)
Calculated with AM1
For Hole-transport

The roll-over in the plots in chart 3 occur at approximately twice the vanderwaals radius of the chalcogen atom, which is 3.7A for the sulfur analog, 4.0A for the selenium analog, and 4.4A for the tellurium analog. The results of chart 3 show that the tellurium analog has a larger transfer integral at larger dimer distances than that of the selenium and sulfur analogs, which is consistent with the idea that a larger atomic radii will result in a larger transfer integral. However, this is not seen between the sulfur and selenium analogs which suggests that the interaction between the carbon orbitals dominant the electron splitting.

The current work shows that including large chalcogen atoms in hole-transport materials results in desirably low reorganization energies and that the smaller molecules show an isomer dependence, which is more pronounced with the smaller chalcogen atoms. These systems are interesting for charge-transport and synthesis is recommended.

REFERENCES

1. O.D. Jurchescu, J. Baas, T.T.M. Palstra, Appl. Phys. Lett. 84. 3061-3063. (2004)
2. J.H. Schon, Appl. Phys. Lett. 79. 4163-4162. (2001).
3. M. Yamada, I. Ikemote, H. Kuroda, Bull. Chem. Soc Jpn.61. 1057. (1988).
4. O. Kwon, et. al. J. Chem. Phys. 120, 8186-8194. (2004).
5. J.G. Laquindanum, H.E. Katz, A.J. Lovinger, J. Am. Chem. Soc. 120. 664-672. (1998).
6. K.Takimiya, Y. Kunugi, Y, Konda, N. Niihara, T. Otsubo. J. Am. Chem. Soc. 126. 5084-5085. (2004).
7. V. Coropceanu, J.M. Andre, M. Malagoli, J.L. Bredas. Theor Chem Acc. 110. 59-69. (2003)
8. M. Malagoli, V. Coropceanu, D.A. da Silva Filho, J.L. Bredas. J. Chem. Phys. 120, 7490-7496. (2004).
9. M.J. Frisch, et al. Gaussian98, Revision A. 11, Gaussian, Incorporated: Wallingford, CT, 1998.
10. P. Hohenberg and W. Kohn, Physical Review 136, B864-B871 (1964).
11. R.G. Parr and W. Yang, Density-functional theory of atoms and molecules, Oxford Univ. Press: Oxford, (1989).
12. A.D. Becke, J. Chem. Phys. 98 5648 (1993).
13. T. H. Dunning, Jr. and P. J. Hay, in Modern Theoretical Chemistry, Ed. H. F. Schaefer, III, Plenum: New York, 1-28, (1976).
14. P.J. Hay and W.R. Wadt, J. Chem. Phys. 82, 270 (1985).
15. R. Ditchfield, W.J. Hehre and J.A. Pople, J. Chem. Phys. 54, 724 (1971).
16. AMPAC 8, © 1992-2004 Semichem, Inc. PO Box 1649, Shawnee, KS 66222.
17. M.J.S. Dewar, E.G. Zoebisch, E.F. Healy, J.J.P. Stewart. J. Am. Chem. Soc. 107. 3902-3909. (1985).

ACKNOWLEDGEMENTS

Research support is gratefully acknowledged from the National Science Foundation Center on Materials and Devices for Information Technology Research (CMDITR), DMR-0120967.

Optimization of Semiconductor Nanoparticle Synthesis and Integration into Sol-Gel Monoliths

Cindy Taylor
University of Arizona

Scott Saavedra and Neal Armstrong
Saavedra Lab, Department of Chemistry
The University of Arizona

INTRODUCTION

Energy sources today are becoming limited and therefore expensive. Gasoline prices are skyrocketing and our nonrenewable sources of energy such as fossil fuels are running low. Research has been done and continues on for a solution to this problem. One possible answer, hydrogen, has incredible possibilities.

Hydrogen fuel cells have been built that successfully convert hydrogen gas into usable energy forms such as electricity. Hydrogen atoms are electrochemically separated from protic solutions, such as water, and combined to form hydrogen gas. The hydrogen gas can then be put to work running a car or even heating a house.

These cells are not only attractive for what they do, but how they do it. They are clean, efficient, and renewable. With only water and heat as byproducts, hydrogen fuel cells are ecological as well as economical. The water can also be reseparated into hydrogen and oxygen, contributing to the self-sustaining process that makes fuel cells so efficient and appealing.

The research performed at the Center for Materials and Devices for Information Technology Research (CMDITR) is aimed at creating a hydrogen generating device. The arrangement produces hydrogen through photocatalytic reduction of water/protic solution using ligand-protected semiconductor nanoparticles (SC-NP) embedded in a sol-gel matrix and attached to conducting polymer chains (Figure 1).

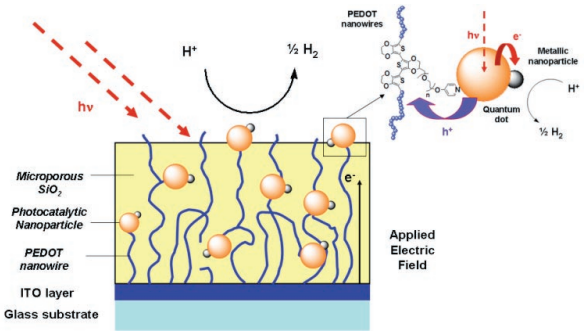

Figure 1. Proposed matrix for photocatalytic reduction of protons using SC-NP's and conducting polymers in a sol-gel matrix.

EXPERIMENTAL PROCEDURES

Two aspects of the proposed device, that of the synthesis and optimization of the SC-NP's and their inclusion in the sol-gel matrix, were the focus of recently conducted research.

Nanoparticle Synthesis

The procedure for synthesizing nanoparticles developed by Jiang[1] was used to create both cadmium sulfide (CdS) and cadmium selenide (CdSe) SC-NP's.

Cadmium myristate (CdMA, 1.134g, 2mmol) was placed in a 250 mL round bottom flask with toluene (50mL) and n-trioctylphosphine oxide (TOPO, 4.99g, 12.9mmol) or oleic acid (OA, 5mL) or a combination of the two. This solution was stirred vigorously at 100°C until all solid had dissolved. Following dissolution, an aqueous solution of thiourea (0.19g, 2.5mmol) in deionized water (50mL) was added. The reaction was performed under reflux at 100°C for six hours.

The formation of the nanoparticles occurred at the water/toluene interface (Figure 2). Here the decomposing thiourea combined with the cadmium to form CdS molecules that would then move into the organic phase. The excess TOPO or OA in this layer "capped" or attached to the surface of the CdS molecule creating a protective ligand layer. As the nanoparticles were stirred, they returned to the interface where more CdS molecules attached to the core, increasing the diameter of the nanoparticle.

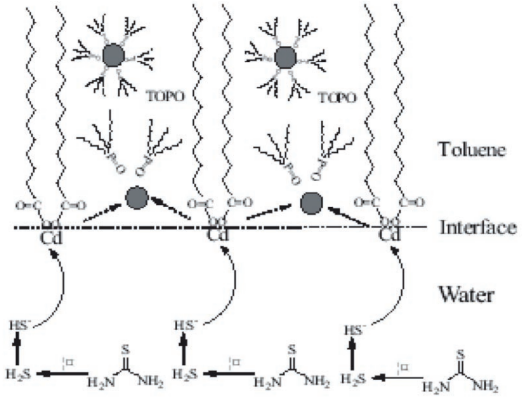

Figure 2. Reaction scheme for TOPO capped CdS semiconductor nanoparticles. (Ref. 1)

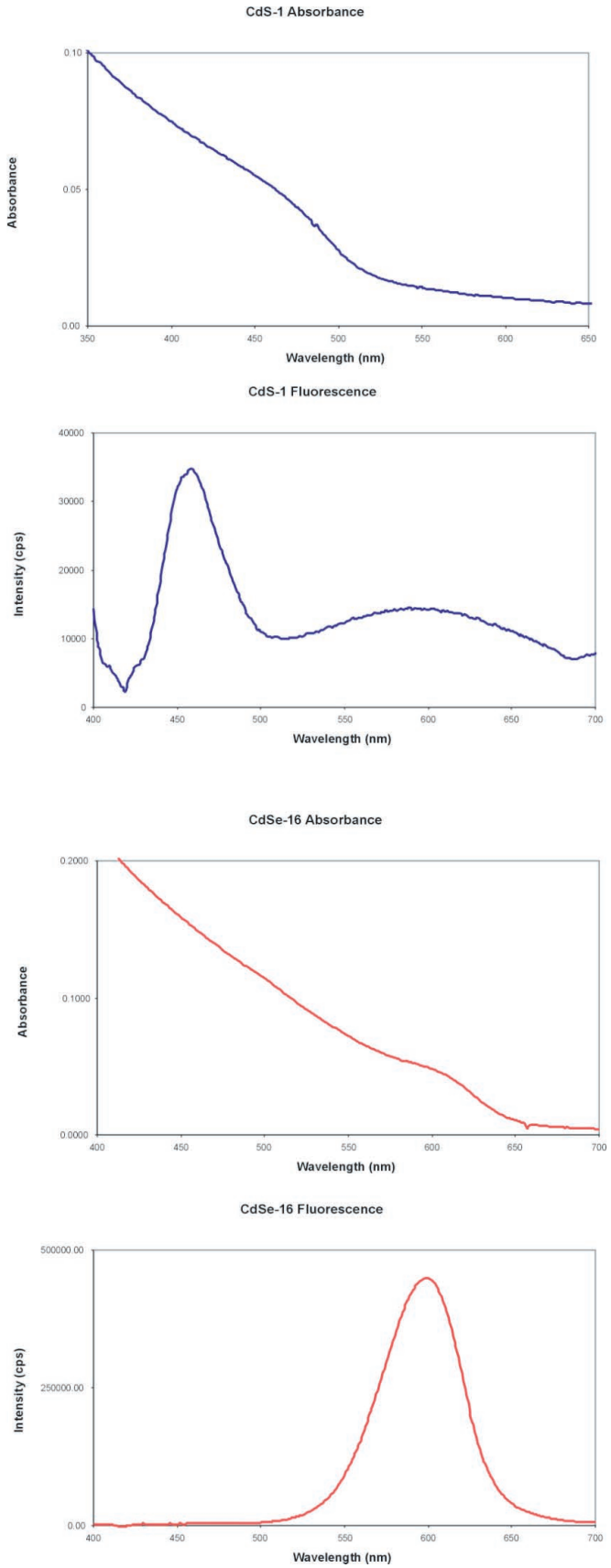

Figure 3. Absorbance and Fluorescence Spectra of CdS-1 and CdSe-16 (24 minutes), the nanoparticle samples used in sol-gel inclusion experiments.

Once the reaction was complete the mixture was separated using a separatory funnel and the aqueous phase discarded. The remaining organic layer was then washed with ethanol and centrifuged three times. The resulting solid was dispersed in dichloromethane and allowed to dry overnight yielding yellow to orange crystalline CdS nanoparticles. It was later noted that carrying out these washings resulted in a substantial loss of product and diminished the desired optical properties of the SC-NP's.

Cadmium selenide nanoparticles were synthesized using the same procedure as the cadmium sulfide NP's with slight differences. The molar quantities of the reagents were scaled down by a factor of five and selenourea (0.016g, 0.12mmol) replaced thiourea in the aqueous phase. In replacing the sulfur atom with selenium it became necessary to degas the aqueous phase with argon prior to the reaction. This prevented oxidation of the precursors. Only oleic acid was used as the capping ligand during CdSe formation. Also, the formation of CdSe was considerably quicker than that of CdS due to the faster decomposition rate of selenourea, resulting in a reaction time of only three minutes at 100°C. Because of this, the synthesis was also performed several times at 80°C, resulting in a required time of 16-20 minutes to reach the desired nanoparticle diameter. Due to the product loss that occurred during the ethanol washing/centrifuging process of the CdS nanoparticles, only an extraction was performed on the CdSe reaction mixture and the organic layer containing the nanoparticles was transferred directly to a storage vial.

The SC-NP's were characterized by UV-Vis absorbance and fluorescence spectra (Figure 3). SC-NP's typically have a high molar absorptivity, which was observed in the analyses taken of the samples. Due to the incredibly small size of the nanoparticles (5-7 nm for CdS & 2-3 nm for CdSe), the absorbance spectra were blue shifted relative to the bulk material.

The fluorescence spectra for the cadmium sulfide nanoparticles contained two peaks. The first high-energy peak was anticipated, proving the nanoparticles had the desired optical property of photoluminescence while the second was much smaller and red-shifted. This was due to unpassivated sites on the surface of the nanoparticles called "surface traps" that trapped photons and released them at higher wavelengths. This second low- energy peak increased in size as the size of the CdS nanoparticles increased. Surface traps were not a problem in the spectra for the cadmium selenide though, indicating that these NP's had more thoroughly passivated surfaces. The intensity of the CdSe particles was also much greater than that of CdS at the same concentration giving them greater efficiency.

Sol-Gel Formation

Sol-gels are formed by the hydrolysis of an alkoxide followed by condensation (Figure 4). Deionized water (0.214 mL, 12mmol) and hydrochloric acid (0.56 µmol) were added to tetramethyl orthosilicate (TMOS, 1 mL, 6.7mmol) in a small vial and stirred for 15 minutes to hydrolyze the methyl terminated ends of the alkoxide, yielding the precursor solution. Once completely hydrolyzed (evidenced by the evolution of the liquids to one phase) the precursor was added to a disposable acrylate cuvette containing phosphate buffer (20mM, pH 7, 2 mL) and deionized water in a 1:1 ratio with the volume of solvent containing nanoparticles.

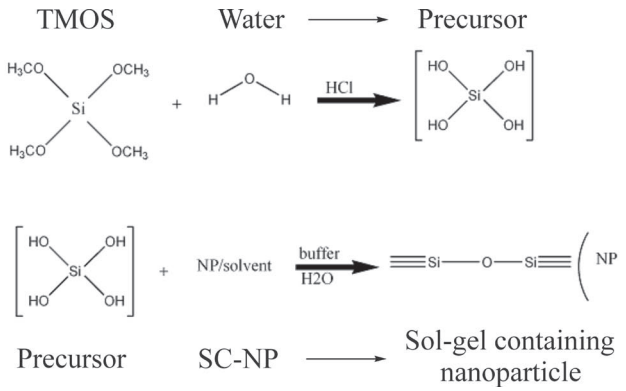

Figure 4. Schematic representation of hydrolysis and condensation occurring during sol-gel monolith formation.

The first variable optimized was the pH of the buffer solution used. The polymerization (solidifying) rate of the sol-gel increased in direct proportion with pH. This was initially a problem as the sol-gel would polymerize quickly, entrapping air bubbles and weakening the matrix. It was determined that a pH of 6.5 was ideal because the sol-gel solidified in a reasonable amount of time while allowing a majority of the air bubbles to escape.

The second factor to be modified was the solvent. The desired characteristics were a solvent the nanoparticles would be soluble in, water miscible, and one that would not quench the luminescence of the nanoparticles. This luminescence quenching effect was determined to be a problem with the first solvents used, methanol and ethanol. These solvents, as well as tetrahydrofuran (THF) and dimethylformamide (DMF), acted as electron donors, filling in the exciton hole left by excited electrons in the SC-NP. This resulted in a lack of emission by the nanoparticles and consequently no peaks in the spectrum.

A peak was finally found in the fluorescence spectra of CdSe-16 when p-dioxane was used as the solvent (Figure 5). The peak indicated that this solvent did not have the same problem as its predecessors. p-Dioxane also has intermediate polarity so the SC-NP was able to be dispersed while the solution remained water miscible giving this solvent all the necessary characteristics.

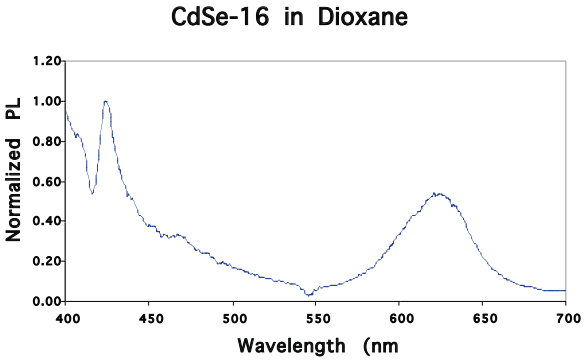

Figure 5. Fluorescence spectrum of CdSe-16.24 in p-dioxane solvent.

Two additional factors altered from the printed procedure were temperature and the time of nanoparticle addition. Sol-Gels are very sensitive to temperature and humidity. As time passed, the humidity in the air increased due to seasonal changes (monsoons), affecting the formation of the sol-gels. To counteract this effect, the temperature at which the precursor was hydrolyzed was lowered to 10°C. Also, to minimize the effects of precursor addition on the nanoparticles, the SC-NP's were introduced at the beginning of the hydrolysis step rather than in the buffer solution. By including these small changes in the experimental procedure, transparent sol-gels with known inclusion of CdSe nanoparticles were created (Figure 6).

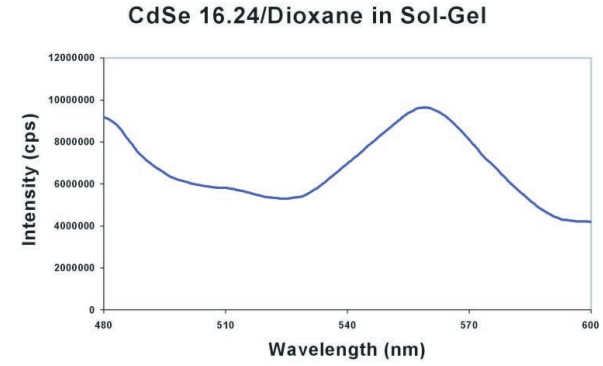

b)

Figure 6. a) Fluorescence spectrum of a CdSe loaded sol-gel monolith, b) A picture of a sol-gel containing nanoparticles.

CONCLUSIONS

The research conducted thus far supports the idea that the goal of a hydrogen generating device is a possibility. The cadmium selenide semiconducting nanoparticles created had the desired optical properties theoretically necessary for the proposed arrangement in quantitative amounts for excellent efficiency. Also by modifying the buffer medium pH, reaction temperature, and solvent used in the accepted sol-gel monolith procedure, the successful formation of a nanoparticle loaded sol-gel matrix pushes the dream of the device closer to becoming a reality.

REFERENCES

[1] Jiang, S., L. An, D. Pan and B. Jiang. 2004. Controllable Synthesis of Highly Luminescent and Monodisperse CdS Nanocrystals by a Two-Phase Approach under Mild Conditions. Advanced Materials. 16:982-985

ACKNOWLEDGEMENTS

Clayton Shallcross, Graduate Student, Chemistry, University of Arizona
Dr. Neal Armstrong, Professor, Chemistry, University of Arizona
Dr. Scott Saavedra, Professor, Chemistry, University of Arizona
Zhijie Sui, Post Doctorate, Chemistry, University of Arizona
Sam Phimphivong, Graduate Student, Chemistry, University of Arizona
Muditha Senarathyapa, Graduate Student, Chemistry, University of Arizona

Funding provided by the Center on Materials and Devices for Information Technology Research (CMDITR), an NSF Science and Technology Center No. DMR 0120967

Cindy Taylor will complete her studies at the University of Arizona in May 2006 and plans on pursuing a doctoral degree in Analytical Chemistry in the fall of the same year.

Characterization of the Photodecomposition of the CF3-FTC Chromophore

Jillian Thayer
Olympic College

Jason Benedict, Dawn Cohen and Dr. Bart Kahr
University of Washington

INTRODUCTION

Demands for improved electro-optic devices support ongoing research in photonics. Non-linear optical (NLO) materials have so far been the focus of meeting such demands, as they show significant optical effects when an electrical field is applied. Newer NLO materials are organic chromophores, light absorbing molecules which consist of an electron donor, pi system conjugation bridge, and an electron acceptor. Chromophores are often studied while suspended in a polymer, which is spin coated and hardened on a glass slide. They have increasingly complex structures and proportionally increased susceptibility to decomposition. For instance, many bonds can be broken in an organic molecule with a molecular weight of about 850 atomic mass units. Among the ten characteristics of ideal NLO materials are concerns over strength, stability, and laser damage thresholds[1]. These areas of interest prove to be a problem for NLO chromophores, and there developed the idea of a non-linearity/stability tradeoff. For chromophores, inherently sensitive to light, photodecomposition is of particular concern.

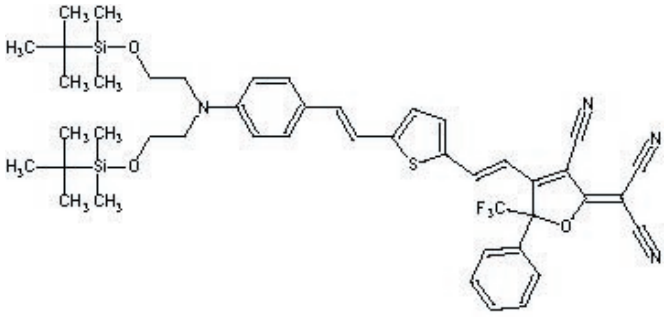

Figure 1.1. A new NLO chromophore, CF3-FTC

Understanding the mechanisms of photodecomposition is imperative if improvement of chromophores and the lengthening of electro-optic device lifetime are expected. Photodecomposition occurs when light energy absorbed by a chromophore is sufficient to break molecular bonds, or allow high energy reactions with their environment to occur. Controlled experiments are required to research photodecomposition. In this project linearly polarized light was directed at a sample of chromophores doped into a polymer. In the polymer matrix, molecules are randomly dispersed. Only those molecules whose dipole moment is approximately parallel to the direction of polarization should be destroyed. This will result in a sample having differential absorption for mutually orthogonal input polarization, known as linear dichroism or absorption anisotropy.

Previous experiments conducted in the Kahr lab with polarized light however, resulted in isotropic decay of the chromophore, and no dichroism. This unexpected behavior implied the presence of interactions amongst the chromophores. One hypothesis proposed a transfer of energy from molecules excited by the polarized light to molecules out of the plane of polarization, unable to be excited by the polarized light directly. Polarized light absorption spectrophotometry was the primary tool in assessing decay of chromophores, while various forms of spectroscopy were used to examine resulting photodecomposition products.

METHODS AND MATERIALS

Methods of analysis involved using slides spin coated with a thin film of varying concentrations of dye-doped polymer. Electrodes attached to conductors on both sides of the film subject a region of the chromophores to electric field poling and partial reorientation parallel to the plane of the applied electric field. The poled region should then be anisotropic relative to the unpoled region.

For analysis of photodecomposition products, previously poled films of AJL-8 (chromophore) were used and subjected to various forms of spectroscopy. In order to look for clues as to the structure of photodecomposition products, clean spectra and convenient use with the thin films were important requirements. Flakes of polymer doped with chromophore were scraped from poled slides, separated by poled and unpoled regions, and mixed with KBr to form pellets. The pellet was used with an infrared (IR) spectrometer, and a spectrum was obtained for both the poled and unpoled regions. Next, poled slides were left intact, and IR spectra were obtained for both poled and unpoled regions on an attenuated total reflectance spectrometer. Finally, intact poled slides were viewed under a Raman microscope coupled to a Raman spectrometer, and Raman spectra were taken again for both the poled and unpoled regions.

The next group of experiments also used thin films dye doped polymer, specifically containing the chromophore CF3-FTC, designed and synthesized by the University of Washington's Dalton

Lab. No electric poling was applied to these slides, and concentrations of 5%, 10%, 15%, and 25% chromophore in amorphous polycarbonate (APC) were made to illustrate the behavior of decay as chromophore interactions change directly with concentration. A slide was placed at a precise location on the stage of a polarizing microscope, and at a precise angle, denoted as 0 degrees. The microscope light source was a tungsten bulb, set at a constant intensity setting. Other light sources considered and tested were the differential interference contrast (DIC) microscope and a xenon arc lamp. A beam of light was focused onto the thin film of CF3-FTC/APC and a spectrum was taken by the charge coupled device (CCD) absorbance spectrophotometer. The rotating stage was then turned 90 degrees counterclockwise, and a second spectrum was taken. This set of absorbance measurements at 0 and 90 degrees were repeated to improve statistical error, and the stage was left at the angle of 90 degrees. A comparison of the orthogonal measurements will assay the degree of dichroism in the photolyzed region of the films. For the next 24 hours, this setup was left undisturbed, while a timed acquisition program gathered spectra every hour. At the conclusion of 24 hours, four more spectra were taken at 0, 90, 0 and 90 degrees. This was repeated for samples of all concentrations. A few samples were also tested in 3.5 hour experiments using the polarizing microscope's condensing lens.

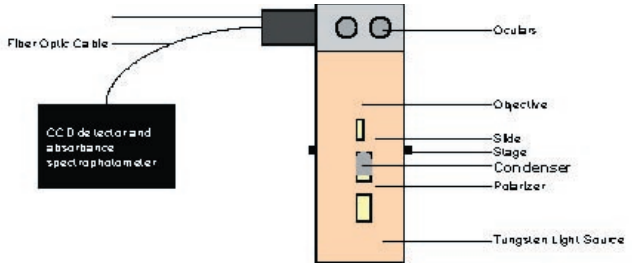

Figure 1.2. Experimental Design

RESULTS AND DISCUSSION

Knowledge of decomposition product structure will guide other photodecomposition research. The spectroscopic studies used in this research held potential for being convenient to use with the poled or unpoled films of dye doped polymer. In actuality, practical limitations kept these three forms from providing useful information. All three sets of spectra yielded from these techniques were indecipherable. The infrared spectrometer produced a very weak spectrum due to both moisture in the KBr pellet and heterogeneous dispersion of the polymer film. The ATR spectrometer also gave very weak spectra because of poor contact between the internal reflectance element and the film of chromophore doped polymer. Lastly, the Raman microscope and spectrometer gave very weak spectra, caused by fluorescence of the chromophore. Raman spectrometers are very susceptible to interference by fluorescence.

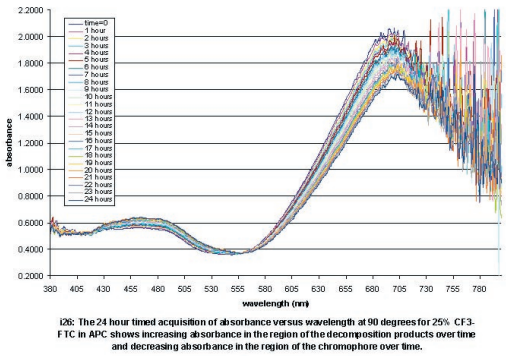

Figure 1.3. The changes in absorbance of CF3-FTC in 24 hours is shown at approximately 660 nanometers.

The timed acquisitions of absorbance by the chromophore did provide some interesting data. It can be concluded that no anisotropy is induced by spin coating the films. Measurements of absorption at 0 and 90 degrees before photolysis show statistically insignificant differences; no dichroism is observed. As time progressed in the experiments the absorbance at 660 nanometers (indicative of CF3-FTC) decreased steadily while the absorbance in the region of the decomposition products (around 440 nm) increased. Most trials exhibited predictable exponential decay of the chromophore, but many trials showed a poor fit to an exponential growth model for the decomposition products. Measurements of absorption at 0 and 90 degrees after photolysis showed no signs of induced anisotropy. As there should be induced dichroism, the fact that there is none at all is curious and raises questions.

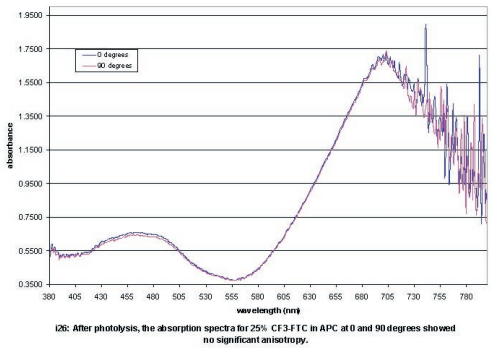

Figure 1.4. No anisotropy is shown after 24 hours of polarized photolysis.

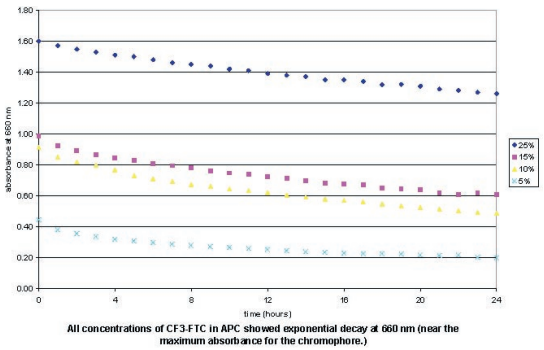

Figure 1.5. All concentrations of chromophore decay exponentially.

CONCLUSIONS

Several conclusions may be drawn from this research. Limitations on spectroscopic techniques used with poled films are significant and these methods need revision before further testing. Specifically, a laser of a different wavelength could minimize fluorescence of chromophores when using a Raman microscope. No statistically significant anisotropy is induced by the process of spin coating, before poling has occurred. Additionally, after photolysis using the setup followed in this research, no significant anisotropy is induced. To pursue the hypothesis of energy transfer among the chromophores, the current experiment of photolysis should be altered. Taking measures to cool the experiment or using lasers as a light source would inhibit sample heating that may be allowing chromophore mobility. Nuclear magnetic resonance (NMR) spectra will be taken at stages of photolysis to look for decomposition products. Experiments of photolysis will also be conducted under vacuum to test the possibility of reaction between the chromophores and oxygen.

The underlying principles surrounding the photodecomposition of organic chromophores overlap with that of dendrimers and dendronized polymers. Research in this area will therefore be continued, to contribute knowledge to these systems as well.

ACKNOWLEDGMENTS

- Thank you to Thank you to members of the Kahr research group; special thanks to mentors Jason Benedict, Dawn Cohen, and Dr. Bart Kahr for their guidance and knowledge.
- Thank you to the Dalton lab, for providing supplies of CF3-FTC and APC; special thanks to Phil Sullivan for spin coating.
- Thank you to the University of Washington Department of Chemistry, the National Science Foundation, and the Materials and Devices for Information Technology Research-Science and Technology Center.
- Special thanks to the organizers and supporters of the 2005 Hooked on Photonics Undergraduate Research Program, specifically Kristin Wustholz, Dr. Sara Selfe, and Dr. Phil Reid

REFERENCE

[1]Ewy, T. R. Design and Synthesis of High Performance Nonlinear Optical Chromophores. University of Washington, Seattle, WA, 1996.

Electroluminescent Properties of Organic Light-Emitting Diodes (OLEDs) with 2,5-Bis(9,9-dimethylfluoren-2-yl)-1,1,3,4-tetraphenylsilole

Evans Thompson
Georgia Institute of Technology

Benoit Domercq and Bernard Kippelen
School of Electrical and Computer Engineering
Georgia Institute of Technology

A new organic compound, 2,5-Bis(9,9-dimethylfluoren-2-yl)-1,1,3,4-tetraphenylsilole (DTS), derived from the silole family has been electroluminescently characterized. Functional organic light-emitting diode (OLED) devices were fabricated using DTS as electron-transport layer (ETL), hole-transport layer (HTL), emission layer (EML), and single layer (SIL). DTS was found to be a bright green emitter with a peak wavelength of 535 nm and a maximum half life of 4000 s.

Background of OLEDs in high resolution displays

The demand for high resolution large area flat panel displays is large. Liquid Crystal Displays (LCDs), the leading flat panel display technology, hold that title because of their long life of operation, light weight, low operation costs and brightness. However, LCDs are not without their disadvantages. LCDs require a backlight, causing low contrast ratios due to an inability to produce a true black image. Additionally, LCDs are expensive, especially for displays exceeding 30 inches, and have low viewing angles.

A new display technology using OLEDs, has the potential to supplant LCDs as the leading display technology. OLEDs convert electricity directly into light. By creating their own light these devices will require no backlighting, reducing the operating power requirements. They will be very efficient and have low operating costs. The organic materials are inexpensive and the actual fabrication of large displays will be cheaper than large LCDs. In addition, flexible displays can be made with OLEDs since they do not require a rigid substrate.

Currently OLED displays still have a few hurdles to overcome before they make their way to the living room. The efficiency and lifetime of the organic compounds are still too low, and fabrication is still too expensive. Researchers have been working to find new compounds with high efficiencies and longer lifetimes as well as new OLED fabrication techniques.

Background of siloles Siloles, or silacyclopentadienes, are Si-containing five-membered cyclic dienes with conjugate rings having different structures attached.[1,2] The highest external quantum efficiency (EQE) for a singlet emitting OLED is between 1.1 and 1.5% for a TPD-Alq_3 OLED device. While for a silole the maximum EQE is roughly three times that of TPD-Alq_3 OLEDs, due to its 100% photoluminescent efficiency [3]. Siloles also have a low electron affinity (EA) comparable to that of Alq_3, a widely used electron transport material. DTS, in particular, has an Ionization potential comparable to that of TPD, an organic compound used for hole-transport. Figure 1 shows the chemical structure of DTS.

Figure 1. Chemical structure of 2,5-Bis(9,9-dimethylfluoren-2-yl)-1,1,3,4-tetraphenylsilole (DTS).

Device Structure

The devices consist of multiple layers of organic and inorganic compounds. The layers are deposited on an Indium Tin Oxide (ITO) coated glass slide using high vacuum physical vapor deposition (PVD). PVD is a deposition technique where the material is vaporized by heating to condense on a substrate forming a uniform thin film.

The glass slides went through 4 stages of ultra sonic cleaning in which they were submerged in soap water, deionized water, acetone and ethanol. The slides were then baked in a vacuum oven to remove any left over ethanol. Silicon oxide was then deposited on the slides and again ultrasonically

cleaned with acetone and ethanol. The silicon oxide slides were then placed in a microwave vacuum chamber where they were oxygen-plasma treated. The silicon oxide served as an insulation layer to limit area of emission of each OLED device.

The order of deposition on the silicon oxide slides was organic layers, lithium fluoride (LiF), and aluminum. The organic and inorganic layers and their thicknesses are listed as follows: TPD (40 nm), Alq_3 (40 nm), LiF (1 nm), and Al (300 nm). The thickness of DTS varied. The LiF was used to help the injection of electrons by the aluminum cathode. Four combinations of deposition of the organic layers were made corresponding to the four different types of devices: ETL, HTL, EML and single layer (SIL). ETL, HTL EML devices had a DTS thickness of 40 nm. SIL device had a DTS thickness of 120 nm.

Tests An Ocean Optics fiber spectrometer was used to measure the electroluminescent (EL) spectra of each device [4]. Figure 2 shows the normalized EL spectra of each type of device. To measure the EL characteristics of the devices each device was placed in an electrical contact box fixated directly in front of a photodetector. The electrical contact box and photodetector where then covered with a black box to block outside light. The applied voltage was varied using a Keithley 2400 sourcemeter. The current through each device and the light emitted by the device was measured. All tests were automated using Labview software. The luminance and the external quantum efficiency (EQE) was then calculated by normalizing the measurement of the photodiode to the photopic response of the human eye and the sensitivity response of the photodiode. Figures 3 through 6 show the mean luminescence, EQE, and current density curves for each device structure as a function of applied voltage [5].

The luminescent lifetime of each device was measured at a constant current density of 50 mA/cm^2. The voltage needed to keep that current was automatically adjusted by the source meter. Figures 7 and 8 show the lifetime measurements of the HTL, EML, and SIL devices.

RESULTS

All devices emit bright green light. The ETL, HTL, and EML devices emit light at a wavelength of 535 nm, while the SIL device emits light at a wavelength of 540 nm.

Table 1 shows the applied voltage, luminance, EQE, and current density and their respective errors at the maximum EQE.

For a constant current density of 50 mA/cm^2 the HTL, EML, and SIL had half lives of 840, 1100, and 4000 s, respectively. Lifetime measurements of the ETL devices could not be obtained due to a significant amount of leakage as can be seen in figure 4.

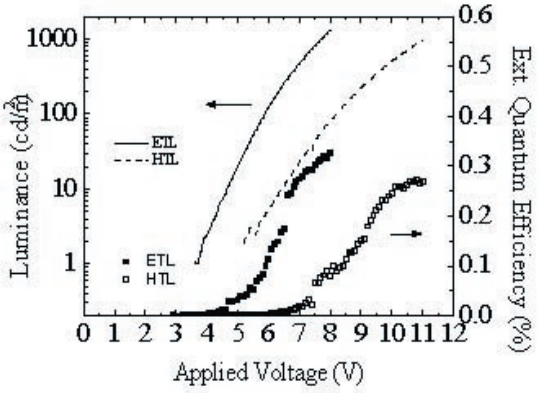

Figure 2. Normalized EL spectra of ETL, HTL, EML, and SIL devices.

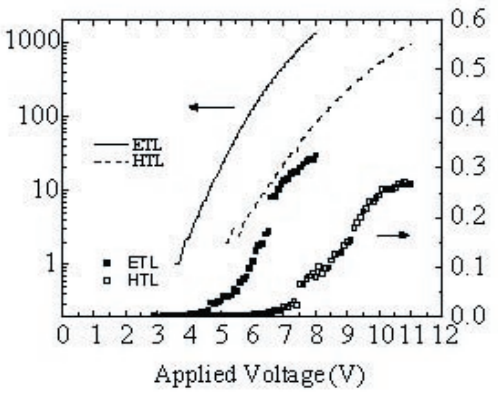

Figure 3. Averaged luminance and EQE of ETL and HTL devices as a function of applied voltage.

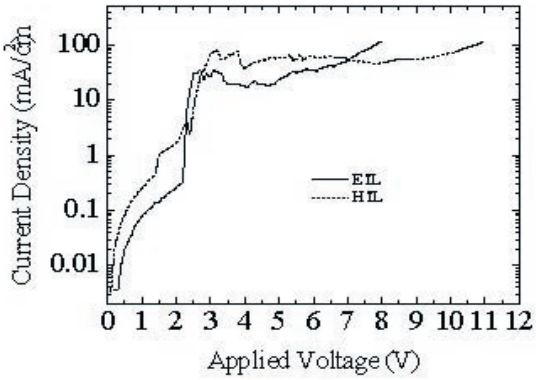

Figure 4. Averaged current density of ETL and HTL devices as a function of applied voltage.

Device	Vappl.	Luminance (±Er)	EQE(±Er)	Current Density(±Er)
	(V)	(cd/m^2)	(%)	(mA/cm^2)
ETL	8.0	1300(±100)	0.3(±0.2)	115(±5)
HTL	10.8	850(±150)	0.3(±0.1)	100(±50)
EML	9.4	1550(±150)	1.0(±0.1)	45(±5)
SIL	13.1	800(±200)	0.3(±0.1)	85(±5)

Table 1. Maximum EQE results.

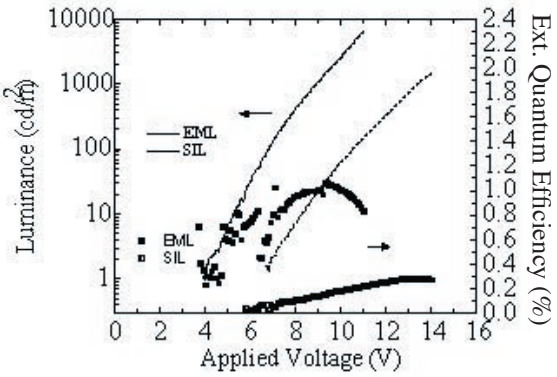

Figure 5. Averaged luminance and EQE of EML and SIL devices as a function of applied voltage.

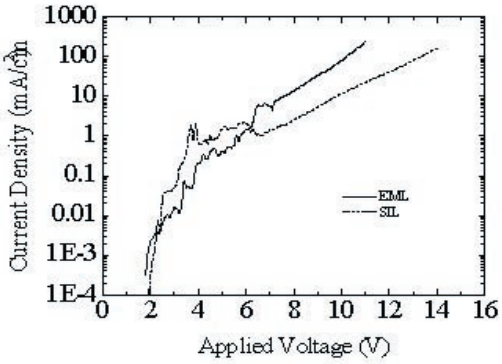

Figure 6. Averaged current density of EML and SIL devices as a function of applied voltage.

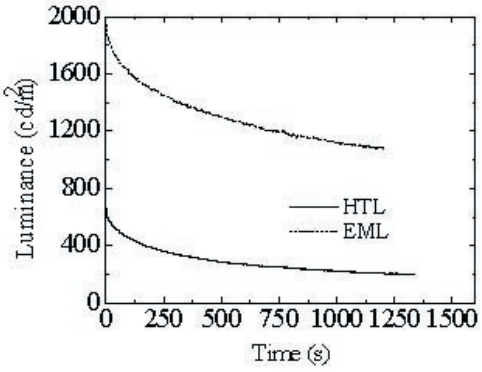

Figure 7. Luminance of HTL and EML devices as a function of time.

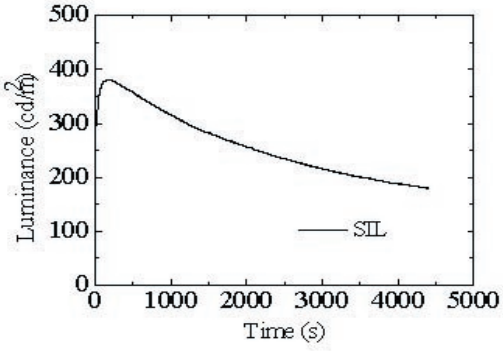

Figure 8. Luminance of SIL device as a function of time.

CONCLUSION

The ETL devices do not appear to operate significantly better than the HTL devices. The ETL devices do have a lower turn on voltage but the current densities are very similar. The nearly horizontal shape of the current density plot shows there is current leakage. DTS appears to be ambipolar meaning it can be used to transport both holes and electrons.

ACKNOWLEDGEMENTS

This work was supported by the MDITR, a Science and Technology Center of the National Science Foundation (NSF) under Agreement Number DMR-0120967.

REFERENCES

[] Chen, H. Y.; Lam, W. Y.; Luo, J. D.; Tang, B. Z.; Zhu, D. B.; Wong, A.; Kwok, H. S. *App. Phys. Let.* 2002, 81, 574-576.

[2] Lee, J.; Liu, Q.; Bai, D.; Kang, Y.; T, Y.; W, S. *Organometallics*. 2004, 23, 6205-6208.

[3] Murata, H.; Kafafi, Z. H.; Uchida, M. *App. Phys. Let.* 2002, 80, 189-191.

[4] Dini, D. *Chem. Mater.* 2005, 17, 1933-1944.

[5] Forrest, S. R.; Bradley, D. D. C.; Thompson, M. E. *Adv. Mater.* 2003, 13, 1043-1048.

Evans Thompson is currently studying mechanical engineering at Georgia Institute of Technology. Evans intends to obtain a master's degree in mechanical engineering upon graduating from Georgia Tech.

Determination of Molecular Orientation of Self-Organized Aggregates of New Liquid-Crystal Perylene Dye

Natalie Thompson
Georgia Institute of Technology

Neal R. Armstrong, P. Alex Veneman,
Armstrong Lab, Department of Chemistry
The University of Arizona

INTRODUCTION

Organic compounds with π-conjugated systems which often exhibit high charge mobilities have a growing interest within the scientific community because of the possibility of creating organic films that can act as conducting materials. These compounds are expected to be used to create cheaper electronics through all-plastic circuits [(1)]. Also, these materials could be used in other organic electronic applications, such as organic light emitting diodes, organic photovoltaics, and organic field effect transistors. Liquid-crystalline organic materials are of interest due to their ability to self-aggregate into columns. It is thought that the charge mobilities of the aggregates are related to the cofacial overlap of the conjugated system. Brédas, et al. reported that the largest splitting between the highest occupied molecular orbital (HOMO) and the lowest unoccupied molecular orbital (LUMO) correlates with the cofacial overlap and then influences the hole (electron) transport of the aggregate. [(1)] Donley, et al. reported that cofacial overlap results in low activation energies for charge migration. However, this migration, or hopping, prefers to move along a certain axis of the aggregate. [(2)] Flora, et al. reported a much higher charge mobility along the axis that is parallel to the columnar axis, as opposed to perpendicular to it. [(3)] It has been reported that discotic mesophase materials, such as phthalocyanines, triphenylenes, and hexabenzocoronenes, organize into columnar aggregates within films which are then stiff enough to transfer via horizontal transfer on a Langmuir-Blodgett trough. [(4)] Often these π-conjugated cores have surrounding side chains which are used to help control the self-organization process. It is also thought that the side chains may help prevent electrical cross-talk between columnar aggregates due to their insulating nature. [(5)]

OBJECTIVES / THESIS

This summer's research focused on the characterization of a relatively new perylene-dianhydride-bisimide. Scheme 1

The Derivatives of perylene-dianhydride-bisimide are of interest because of their high electron mobility, which would aid in the efficient transport of electrons in a thin film comprised of this molecule. Also, these derivatives have an electron affinity that is high enough that the reaction with oxygen in the electron transport is not significant, as compared with hole transport materials, indicating an ability to use organic electronics in air. The perylene-dianhydride-bisimide was made into thin films using Langmuir-Blodgett methods and was then characterized by atomic force microscopy (AFM), UV-Vis transmission, Fourier Tranform Infrared (FTIR), reflective-absorptive infrared spectroscopy (RAIRS), and X-ray reflectivity (XRR).

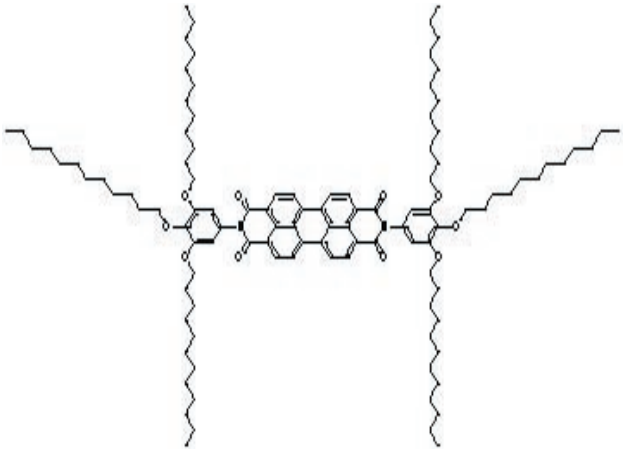

Scheme 1

EXPERIMENTAL

Langmuir-Blodgett film preparation

The substrates for Langmuir-Blodgett thin films were silicon wafers, highly ordered pyrolytic graphite (HOPG), glass, and commercial gold. The silicon wafers and glass slides were modified via sonication for thirty minutes in a solution of 1,1,1,3,3,3-hexamethyldisilazane (HMDS) and 1,3-diphenyl-1,1,3,3-tetramethyldisilazane (DPTMDS) in chloroform (5 : 5 : 90 :: HMDS : DPTMDS : $CHCl_3$). After sonication, the substrates remained in solution until LB deposition. The preparation of the HOPG involved cleaving the substrate to obtain a flat clean surface. The gold surface was rendered hydrophobic by sitting in a solution of benzyloxyethanethiol in ethanol overnight.

Monolayer and multilayer films of N,N'-1,2,3-tridodecoxyphenyl-3,4,9,10-perylenetetracarboxylicdiimide (PTCDI) were prepared on a Nima model 611D LB trough using chloroform as

the spreading solvent. The PTCDI solution (1 mM, 250 μL) was spread onto the surface of a deionized water subphase at room temperature and pressure. The solvent was given about 45 minutes to evaporate completely. Once, evaporated, any aggregates that formed in the spreading of the compound were removed from the water surface via suction. Compression was performed at a rate of 45 mm/s until a condensed phase monolayer or multilayer was formed. This phase was observed by the presence of one or multiple shoulders exhibited on a pressure-area (π-A) isotherm.

The LB thin films were deposited onto the modified surfaces via horizontal deposition in which the surface of the substrate is parallel to the surface of the trough. After each deposition, the sample was dried with compressed N_2. Annealed films were held at 120°C for 4 hours and then cooled to room temperature over 6 hours. The samples were then stored in a sealed container in air until analysis.

Spectroscopic Measurements

UV-Vis spectra were obtained at room temperature and pressure. The sample was such that the visible columns were vertical with respect to the sample holder. The sample was placed either perpendicular or at 45° with respect to the incident beam. A polarizer was used to obtain TM and TE polarizations.

Transmission IR was obtained with the sample perpendicular to the IR beam. A polarizer was used to obtain TM and TE. For RAIRS, the sample was placed such that the columns were running along the length of the sampling area.

X-ray reflectivity (XRR) was performed on a sample that was composed of five bilayers deposited on modified silicon.

Atomic Force Microscopy

The topography of LB thin films on silicon wafers and HOPG was examined using atomic force microscopy (AFM) performed in tapping mode, *ex situ*. The minimum force required to acquire optimal resolution was used in order to minimize distortion of the sample. The driving amplitude applied was determined by the instrument and in between 100 and 400 mV. Once the tip was engaged, imaging began. The setpoint value was increased until sinusoidal waves were observed indicating no contact with the surface. It was then decreased until contact with the surface was optimized, as monitored by the trace-minus-retrace (TMR) values. Optimal TMR was considered to be under 0.2 nm.

RESULTS AND DISCUSSION

Analysis of the π-A isotherm showed that PTCDI forms coherent monolayer and multilayer thin films, though the steps were not as distinct as those exhibited by phthalocyanine derivatives (Figure 1). This behavior exhibited on the π-A isotherm leads to the conclusion that PTCDI does not behave as a true amphiphile with distinct isolated polar (hydrophilic) and apolar (hydrophobic) regions. This behavior was expected due to the small aromatic region in the side chains. Also, the compression of the LB thin films showed that PTCDI forms stiff films which can be deposited via horizontal transfer. The horizontal transfer could prove to be useful in easing the process for the creation of organic electronic devices.

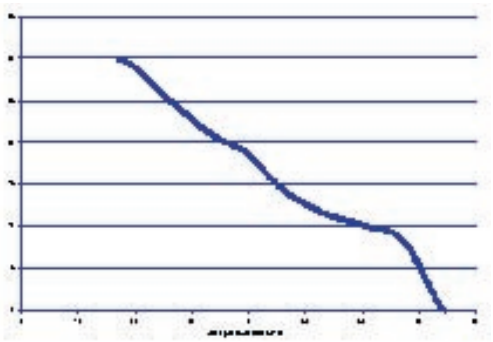

Figure 1. The π-A isotherm exhibits the formation of a trilayer. This was determined by observation of the shoulders in the isotherm. This isotherm showed that PTCDI does not have linear regions in between the formation of the layers. This is indicative that PTCDI is not a true amphiphile.

Analysis of the AFM images proved that the horizontal transfer was successful and that PTCDI does self-organize. AFM also displayed the nature of the aggregates. With a sole deposition, PTCDI forms islands of aggregates on the surface of the silicon (Figure 2). This is expected to be a result of the dewetting process in the transfer. Further studies showed that multiple depositions results in a more solid and organized thin film (Figure 3). AFM analysis of annealed films showed that the annealing process raises the sample temperature to a point where the sample behaves more like a liquid and is able to reorganize the aggregates. It also showed that the self-organization of the liquid-like sample has a tendency to aggregate into a linear fashion, the like of which can extend for at least 2 μm (Figure 4). The presence of linear aggregates hints at the idea that PTCDI forms columns which can extend significant distances. These columns with cofacial overlap of the π-conjugated systems can be used in organic electronic devices. In particular, PTCDI could be used as an electron transfer material due to its high electron affinity and mobility.

Analysis of the UV-Vis data showed little evidence of dichroism in the plane that was analyzed (Figure 5). Though no organization of the molecular transition dipole moment is evident, the data does not lead to the conclusion that there is no organization. Other possibilities include: that there is organization in other planes; that there are islands that are coherent in themselves, but not with other islands; or that the organizational structure does not have aligned molecular transition dipole moments, for example if PTCDI forms a helical column where each molecule is slightly tilted with respect to the surrounding molecules (Figure 6).

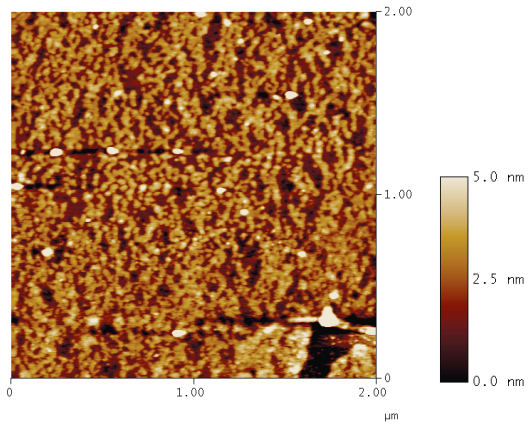

Figure 2. AFM image of one deposited bilayer, unannealed. The sample is NJT-I-53A

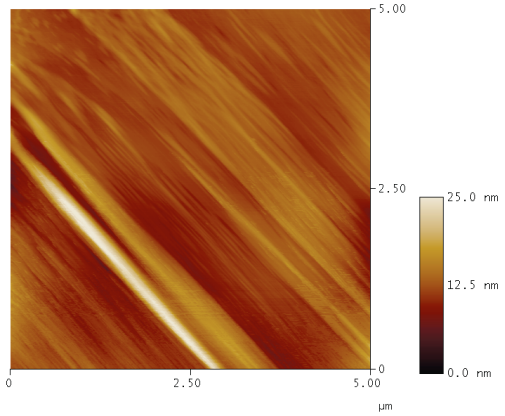

Figure 3. AFM image of 2 bilayers, unannealed. The sample is NJT-I-52B

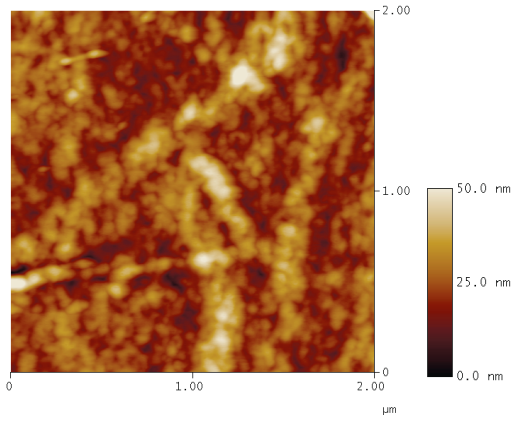

Figure 4. AFM image of 2 bilayers, annealed. The sample is NJT-I-52B

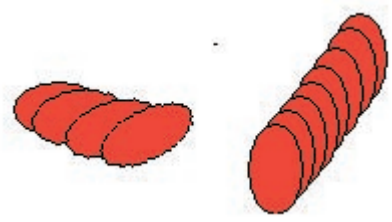

helical out of plane

Figure 6. Possible arrangements for PTCDI that would not show dichroism.

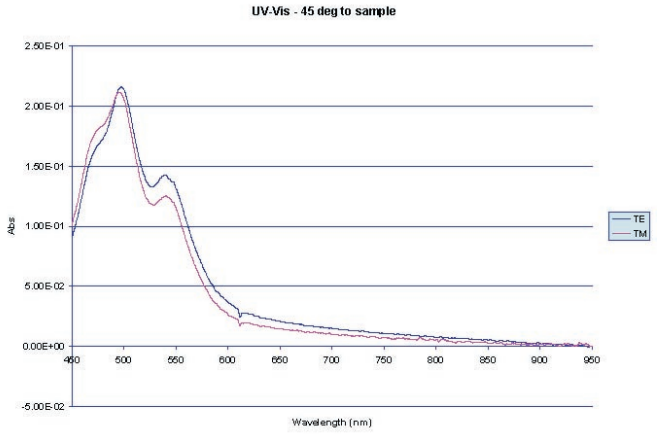

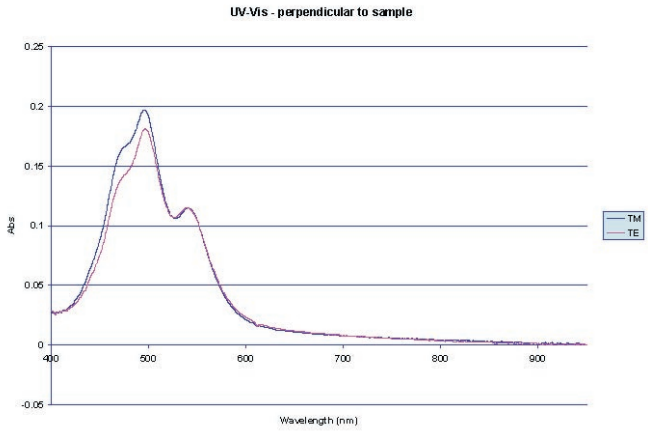

Figure 5. UV-Vis spectra of 8 deposited bilayers, unannealed.

The transmission IR data and the reflective absorptive IR (RAIRS) data came to no precise conclusions. Though some dichroism is evident between the spectra, there is not enough information to determine the exact vector orientation of PTCDI (Figure 7).

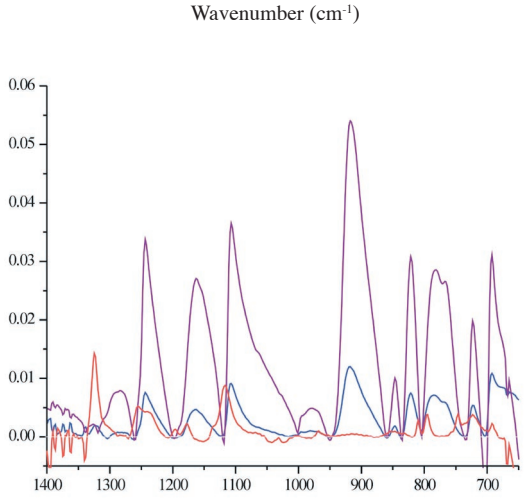

Figure 7. FTIR and RAIRS data. The red is RAIRS. The blue is transmission IR parallel to the columns. The purple is transmission IR perpendicular to the columns.

The X-ray reflectivity (XRR) data came to no conclusions. It was decided that the concentration of the sample was too dilute to obtain accurate information on the thickness, density, and roughness of the thin film (Figure 8).

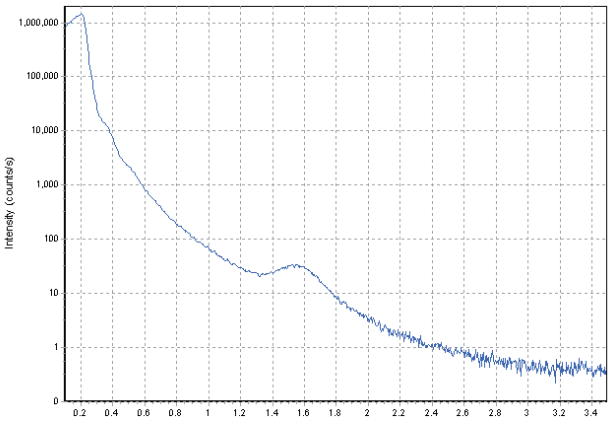

Figure 8. XRR graph

CONCLUSIONS

LB formation of thin films of PTCDI results in a stiff film that can be transferred to a silanized surface using horizontal transfer. These thin films form islands with only one deposition, but multiple depositions results in linearity of the thin film. Also, annealing of the sample allows the molecules to reorganize into linear aggregates. Spectroscopic measurements led to no solid conclusions about the orientation of the molecules within the thin film, but hinted that the molecules might be organized outside of the sample plane (parallel to the substrate).

REFERENCES

[1] Brédas, J. L., Calbert, J. P. da Silva Filho, D. A., Cornil, J. *Proceedings of the National Academy of Sciences*. **2002,** *99*, 5804.
[2] Donley, Carrie L., Xia, Wei, Minch, Britt A., Zangmeister, Rebecca A. P., Drager, Anthony S., Nebesny, Ken, O'Brien, David F., Armstrong, Neal R. *Langmuir*. **2003,** *19,* 6512.
[3] Flora, Ware, H., Mendes, Sergio B., Doherty, III, Walter J., Saavedra, S. Scott, Armstrong, Neal R. *Langmuir*. **2005**, *21*, 360.
[4] Xia, Wei, Minch, Britt A., Carducci, Michael D., Armstrong, Neal R. *Langmuir*. **2004,** *20,* 7998.
[5] Donley, Carrie L., et al. *J. Mater. Res*. **2004,** *19,* 2087
[6] Doherty, III, Walter J., Simmonds, Adam G., Mendes, Sergio B., Armstrong, Neal R., Saavedra, S. Scott. *In press*.

ACKNOWLEDGEMENTS

-**Dr. Neal R. Armstrong**, Professor of Chemistry and Optical Sciences, University of Arizona
-**Armstrong Research Group**

Funding provided by the Center on Materials and Devices for Information Technology Research (CMDITR), an NSF Science and Technology Center No. DMR 0120967

Natalie Thompson is finishing her senior year at Georgia Tech and plans to graduate in Spring 2006. She would like to thank Dr. Neal Armstrong, Alex Veneman, and Nira Kumaran for their support and friendship.

Hydrogel Materials for Two-Photon Microfabrication

Mayen Udoetuk
Norfolk State University

Dr. Joe Perry and Vincent Chen
Georgia Institute of Technology

OBJECTIVE

The purpose of the research is to develop a hydrogel material system for two-photon microfabrication. Problems that were addressed in this research project are:

1) For what composition can sufficient crosslinking be achieved by ultra-violet (UV) exposure such that the patterned structure will not wash away upon development?

2) Can hydrophilic monomers be crosslinked using current two-photon absorbing dyes?

3) What are the requirements of the material and the structure to ensure that pores and other desired features within the structure are maintained after swelling?

Potential practical applications of these materials are, for example, microstructures to be used for cell adhesion, which can find applications in tissue engineering, and structures that respond to the solvent environment for sensors or microfluidics. Most research in microfabrication to date has been carried out with acrylate and epoxy type polymers.[1] However, in applications that involve biological molecules or require the adhesion of cells onto polymeric structures, biocompatible materials need to be used. Hydrogel systems have hydrophilic surfaces and are of particular interest due to their ability to swell and de-swell, depending on their environment.

RESEARCH METHODS

The research problems were approached by testing resins based on hydrophilic monomers and two-photon absorbing dyes or UV initiators. Photolithography is a process of transferring spatial patterns onto a surface of a material by exposure to light with a mask. Steps usually involved in this process include substrate cleaning, adhesion layer formation, photoresist application, soft baking, mask alignment, exposure, development, and hard-baking.

The hydrophilic monomers and crosslinker that were used include N-vinylpyrrolidone (VP), hydroxyethylmethacrylate (HEMA), and ethyleneglycol-bis-methacrylate (EGMA). Resins containing various amounts of these compounds were prepared. The initiator used for UV exposure was 1-[4-(methylthio)phenyl]-2-methyl-2-morpholinopropan-1-one, (UV initiator #7).

The amounts of initiator used were 0.1, 0.2, and 0.5 wt%, see table 1.1). To ensure that the structures remained attached to the substrate, the surface of the substrate was modified with an adhesion promoter (95% methanol and 5% 3-(trimethoxysilyl)propyl methacrylate). The adhesion promoter solution was spin-coated onto microscope slides and cover slips, and baked on a hotplate at 90°C for 2 minutes.

Five drops of the hydrophilic resin were placed on surface treated microscope slides and cover slips, and were exposed to UV light from a mercury UV lamp (254nm) for various times. Solubility tests were done in order to find a solvent that would wash away any resin left after exposure, while leaving the polymerized structure intact. All of the following were found to perform well as development solvents: dichloromethane, toluene, ethanol, dioxane, cyclohexane, dimethyl formamide, and 4-methyl-2-pentanone. 4-Methyl-2-pentanone was chosen for use in the experiments.

Several sample geometries were tested but some gave an inadequate amount of crosslinking. The initial setup included the resin on top of a microscope slide modified with adhesion promoter, with the UV light shining down on it. Due to the thickness of the resin, the UV light did not penetrate to the resin-substrate interface in order to yield sufficient crosslinking. Two geometries that were found to provide sufficient exposure and crosslinking at the interface are shown in diagram 1.1.

Experiments were conducted to determine the swelling properties of the crosslinked materials. The dimensions of the lines were measured before and after swelling with water at room temperature. The feature dimensions were measured using optical microscopy.

Bulk materials of the hydrogels were prepared using setup 1 in order to better visualize the swelling. Fluorescence and transmission imaging were used to characterize and document the fabricated structures. A laser was used for 3D microfabrication of structures[3]. A test structure consisting of a vertical stack of crossing lines was designed and fabricated using two-photon microfabrication.

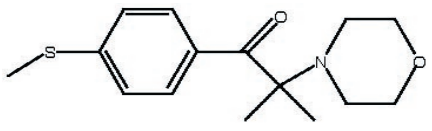

1-[4-(methylthiophenyl]-2-methyl-2-morpholinopropane-1-one (UV #7) was varied in the compositions. 0.1, 0.2, and 0.5 wt% were used.

Solution	Ethylene glycol dimethacrylate 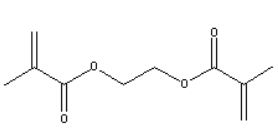	1-vinyl-2-pyrrolidinone 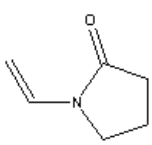	2-Hydroxyethyl methacrylate 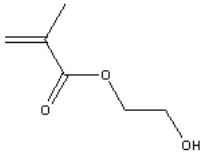
A	1	1	1
B	2	1	1
C	1	2	1
D	1	1	2

Table 1.1. Hydrogel Compositions

RESULTS

It was found that setup 1 allowed the UV light to penetrate the resin-substrate interface in order to yield sufficient crosslinking. Sample A with a 1:1:1 ratio of EGMA, VP, and HEMA, and C with a 1:2:1 ratio of EGMA, VP, and HEMA gave the most crosslinking in the least amount of time. Composition C crosslinked in 3 minutes, whereas composition A required 7 minutes, and compositions B and D could not be crosslinked. This was determined by observing how much of the sample became solid after UV exposure. Only the part of the sample behind the opening in the mask should crosslink. Samples that did not yield sufficient crosslinking remained in the liquid state after UV exposure. Composition C was also used in the UV mask experiments due to its ability to yield higher crosslinking than composition A. Table 1.2 contains data on swelling ratios in the bulk material after exposure to UV light at various times. The diameter and the thickness of the samples were measured before and after swelling in water overnight. Setup 1 was used with composition C, with exposure times of 5, 10, 15, 20, and 25 minutes. The results indicate that the bulk materials of composition C swell 4-5 times its original size. Most of the swelling was observed to be in the vertical direction. Setup 2, which includes a mask, was used with composition C for 3 minutes. Picture 1.1 shows an example of structures obtained by photo-patterning of composition C through a mask. The width of the features was measured before and after swelling in water overnight. No change in width was observed (see Table1.3).

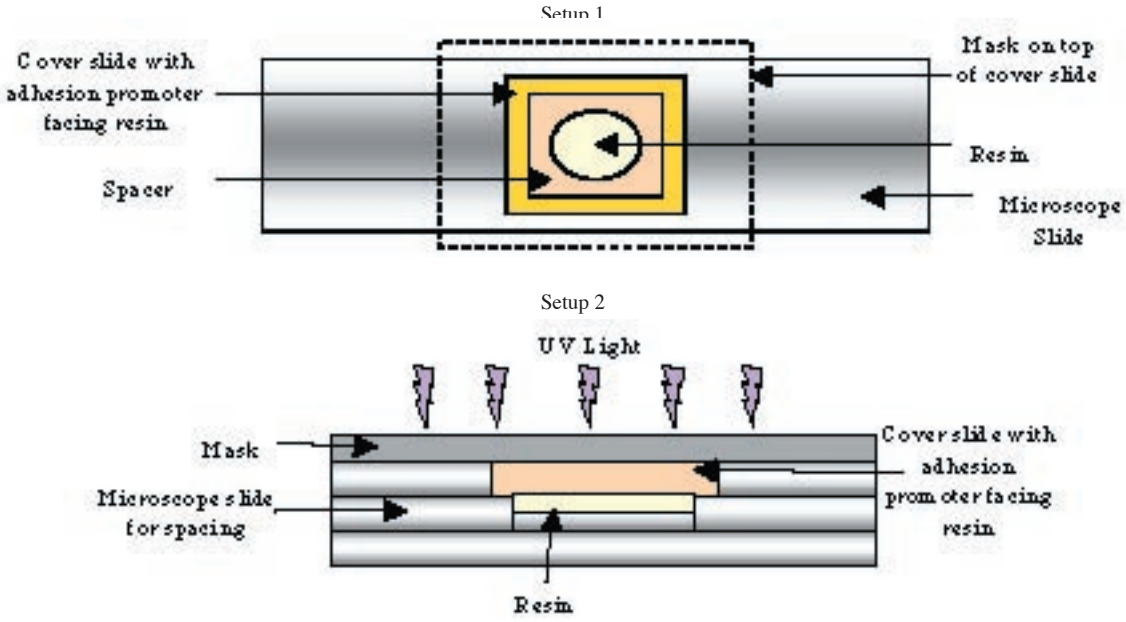

Diagram 1.1. Experimental Setups for UV Experiments

Exposure Time (minutes)	Diameter (dry) (inches)	Thickness (dry) (inches)	Diameter (wet) (inches)	Thickness (wet) (inches)	Volume Ratios (wet/dry)	Thickness Ratios (wet/dry)
5	0.350	0.030	0.358	0.136	3.7	3.5
10	0.340	0.026	0.360	0.138	5.0	4.3
15	0.349	0.032	0.365	0.135	3.6	3.2
20	0.344	0.027	0.361	0.135	4.5	4.0
25	0.343	0.028	0.365	0.131	4.3	3.7

Table 1.2. Results for bulk materials

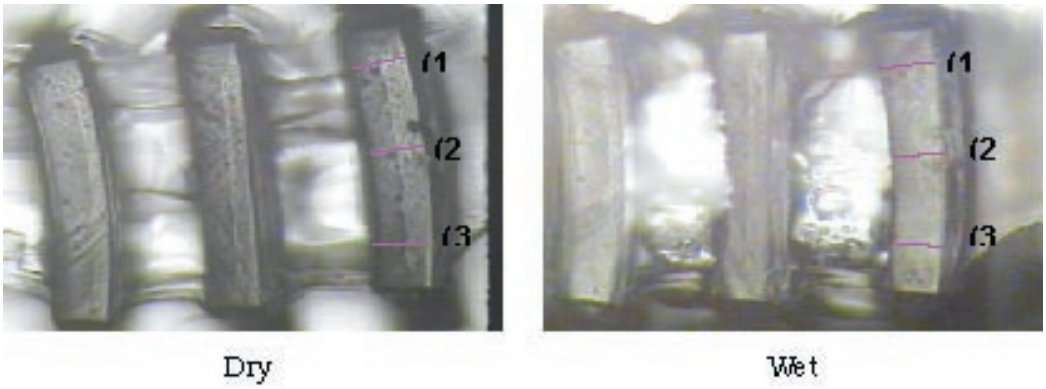

Picture 1.1 Optical images of structure obtained by UV illumination of resin C through a mask

Condition	Width (1)	Width (2)	Width (3)	Average
Dry	0.34	0.35	0.36	0.35
Wet	0.36	0.34	0.33	0.34
%Change	5.8%	-2.9%	-8.3%	

Table 1.3. Results from UV Mask (widths are in arbitrary units).
Widths (1), (2), and (3) refer to the lines on the wet and dry images. They represent the width before and after swelling the samples with water.

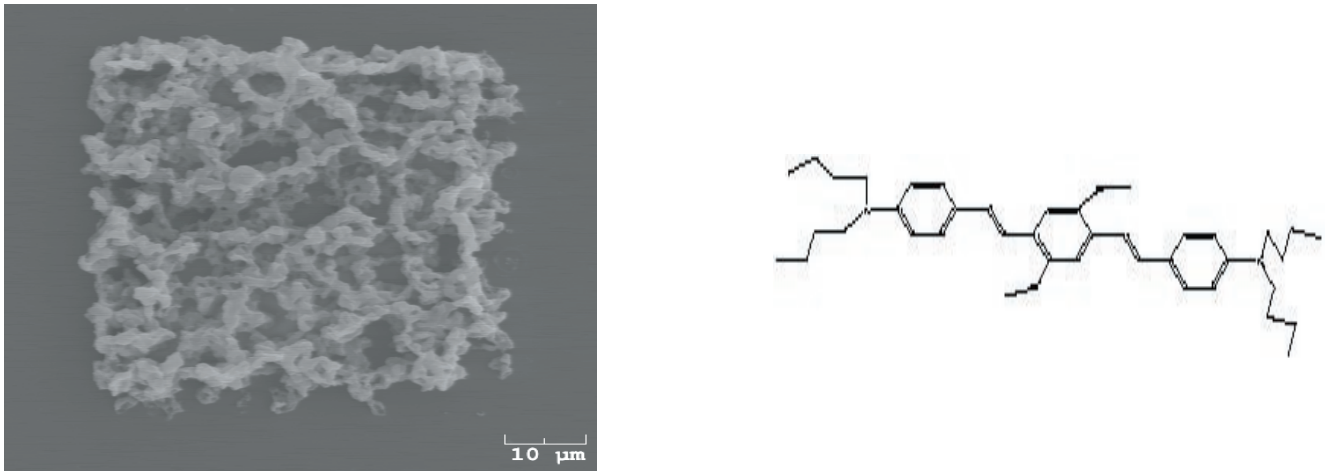

Picture 1.2. (left) SEM Image of Stack of Log Microstructure Obtained by two-photon microfabrication in resin C. (right) Dye #41.

The SEM image was obtained by using two-photon microfabrication. The following parameters were used: laser scan speed: 20 μm/s; 60 mW; λ= 730nm; 1 %wt of dye #41, composition C. A porous 3D grid (stack of logs) was intended. Dye #41 was used because it has large photon cross sections, and has been observed to polymerize acrylate systems. The fabricated structure appears highly deformed, which could be due to inadequate crosslinking or laser induced deformations.

CONCLUSION

Sufficient crosslinking can be achieved by UV exposure. It was found that setup 1 was the most effective in the UV exposure experiments. From the different compositions that were tested, composition C (1:2:1 ratio of EGMA:VP:HEMA) gave the most crosslinking per exposure. In later experiments using the UV mask, composition C with a 1wt% of UV #7 was used. No change in width was observed. This may have been due to a large amount of crosslinking within the structure. At high crosslinking, the swelling of a structure in the presence of water may be limited. In the bulk specimen, the thickness of the samples showed a large change relative to the diameter. The small change may result in the lack of the sample's ability to expand, as a large area adheres strongly to the substrate. This may also explain the lack of change in width for the features produced lithographically. It will be useful explore a method that allows measurement of the height of the fabricated features. This work shows that hydrophilic monomers can be crosslinked using UV initiators and current two-photon absorbing dyes (#41). However, other dyes should be investigated for higher efficiency. Future work will involve investigating more efficient two-photon absorbing dyes, find other biocompatible materials, write functional microstructures, and characterize the swelling ratios in more detail.

REFERENCES

(1) Zhou, W.; Kuebler, S.M.; Braun, K.L.; Yu, T.; Cammack, J.K.; Ober, C.K.; Perry, J.W.; Marder, S.R. *Science*, 2002, 296, 1106-1109

(2) Watanabe, T; Akiyama, M.; Totani, K.; Kuebler, S.M.; Stellacci, F.; Wenseleers, W.; Braun, K.; Marder, S.R.; Perry, J.W. *Adv. Funct. Mater.*, 2002, 12, 611-614

(3) Cumpston, B; Sundaravel, A.P; Barlow, S; Dyer, D.; Ehrlich, J.; Erskine, L.L; Heikal, A.; Kuebler, S.; Lee, S.; McCord-Maughon, D.; Qin, J.; Röckel, H.; Rumi, M.; Wu, X.; Marder, S.; Perry, J. *Nature*, 1999, 398, 51-54

ACKNOWLEDGEMENTS

Dept. of Chemistry and Biochemistry at the Georgia Institute of Technology
MDITR REU
National Science Foundation
Dr. Joe Perry
Dr. Mariacristina Rumi
Vincent Chen
Wojtek Haske
Kelly Perry
Perry Group
Dr. Keith Oden
Ms. Olanda Bryant
Beverly Scheerer

For me, understanding the physical forces in life mean understanding science. Norfolk State University and Georgia Institute of Technology have afforded me many opportunities to do so.

The Design of a Fluid Delivery System for Micro-Core Optical Fiber

Greg Winchell
Everett Community College

Ann Mescher
Mechanical Engineering, University of Washington

INTRODUCTION TO POLYMER FIBER DRAW

The objective of this research has been to develop a method for drawing a single-hole polymer optical fiber from a pre-drilled acrylic preform, with accurate control (+/- 2 microns) of the fiber outer diameter and internal channel diameter. Polymer fiber offers superior design capabilities compared to currently manufactured glass fiber, along with potential savings in energy and manufacturing cost. The most significant advantages of polymer fiber are: 1) the ability to incorporate unique organic optical materials, and 2) much greater flexibility in designing and processing polymer materials as opposed to glass into photonic bandgap structures. The next paragraph will discuss how polymer fiber is made.

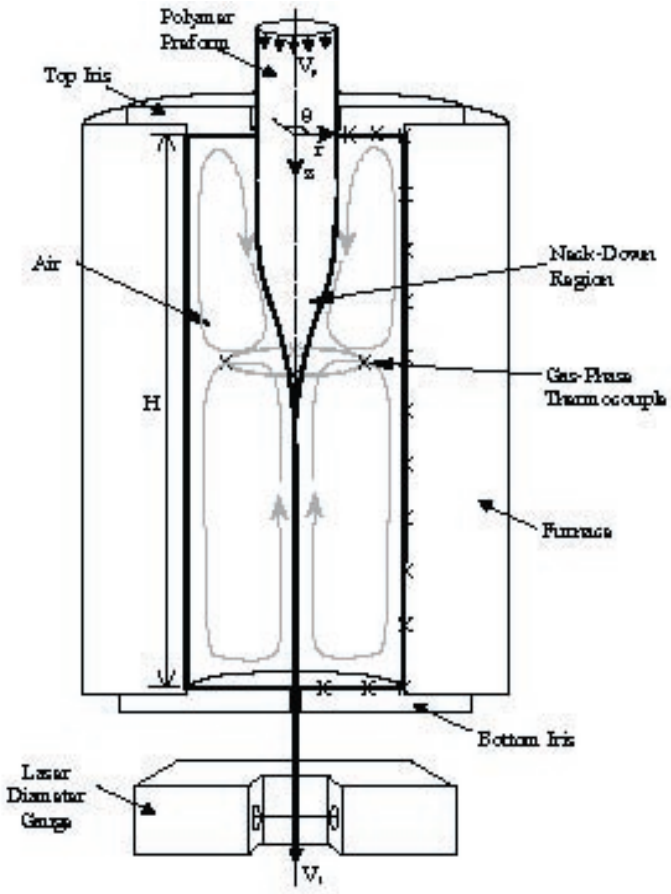

Figure 1. The Polymer Fiber Draw Process

The basic approach to making polymer fiber is to first trim and machine the polymer preform (which is an acrylic rod) to specifications inherent to the fiber making procedure. Then the preform is attached via cross pin to the draw mechanism and is slowly fed downward into the furnace as shown in Figure 1. The furnace heats the preform (with wall temperatures peaking at approximately 184°C) such that polymer fiber can be drawn mechanically by the Draw Tower spindle and spooled. While the fiber is drawn a Laser Diameter Gauge measures the outer diameter of the fiber produced by the process. This is the basic process for producing polymer fiber.

If we take a polymer preform and drill a hole in the radial center along the axis of the preform (thus forming a "thick-walled tube"), and we then heat this preform, the resultant fiber will have the same aspect ratio (i.e. the inner hole diameter divided by the outer diameter of the fiber) as the original drilled preform before heating. Now if we take another polymer preform and drill a hole in the radial center and this time place fluid in the hole, the aspect ratio of the resultant fiber will not be the same as the preform aspect ratio before heating. Why is this happening?

Fluid Core and the Effect Of Fluid Pressure

When the preform with a hole (but no fluid inside the hole) is heated, the experimental evidence consistently shows that the aspect ratio of the fiber produced does not differ from that of the unheated preform. This suggests that mere atmospheric pressure inside the drilled hole is not enough to alter the aspect ratio. However when fluid is added to the drilled hole, this is enough to change the aspect ratio of the fiber indicating that atmospheric pressure in combination with fluid pressure will alter the aspect ratio of the resultant fiber compared to the aspect ratio of the unheated preform. Fluid Pressure is equal to the density of the fluid multiplied by gravitational acceleration multiplied by height of the fluid column (Fluid Pressure=ρgh). The illustration below (Figure 2) shows that the fluid pressure is highest in the region where the polymer radius is rapidly changing. As the fiber is created below the fluid column, the aspect ratio increases and therefore fluid is gradually removed from the preform. This results in a continuous drop in the fluid column height which means that the fluid pressure itself will also begin to decline.

Since there is a decline in the fluid pressure, the pressure exerted against the inner diameter hole decreases. The decrease in pressure will reduce the aspect ratio over time unless the fluid is replaced as needed. This engenders the need for a reliable fluid delivery system to control the aspect ratio as needed.

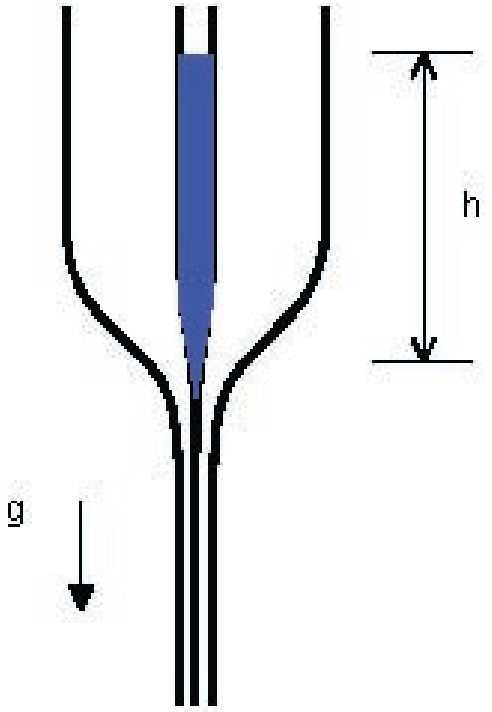

Figure 2. Fluid Pressure in Preform due to Fluid Column

Fluid Delivery Apparatus

The fluid delivery system considered first was a type of automated syringe pump known as the NE-1000 Programmable Syringe Pump retailed by the New Era Pump Systems, Inc. The NE-1000 Programmable Syringe Pump retails for $995 US Dollars and has the following features [1]:

1. The infusion rates are from 0.73 µl/hr (1 cc syringe) to 2100 ml/hr (60 cc syringe).
2. Stand-alone operation or computer-controlled operation are available.
3. Infusion and withdrawal of fluid is performed as needed.
4. The operator can program up to 41 pumping phases that change pumping rates, set dispensing volumes, insert pauses, control and respond to external signals.
5. Motor stall detection is included.
6. Dispensing accuracy of the device is +/- 1%
7. Unlimited lifetime technical support is available.
8. It has a two-year warranty.

The second fluid delivery system that was considered was a gravity feed design that was developed and tested in the Polymer Optics and Processing Laboratory at the University of Washington. Below is the drawing of the Gravity Feed Apparatus (Figure 3):

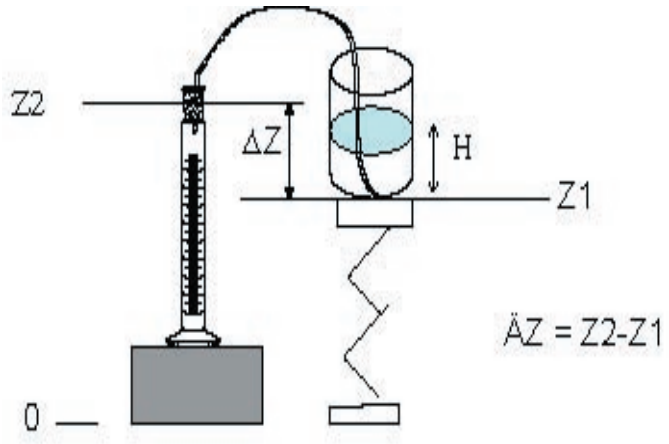

Figure 3. The Gravity Feed Apparatus

The Gravity Feed Apparatus was essentially a siphon arrangement composed of an adjustable lab jack, a plastic flow tube, a 2000ml beaker, a 1ml capacity graduated cylinder, a top-mounted fluid feed ramp, and a graduated cylinder stand. This device demonstrated excellent flow control. Under laboratory conditions the single most important factor affecting the flow rate of the fluid with this device (i.e. the volumetric flow rate) was the difference in the height of the collection container (Z2) minus the height of the reservoir (Z1) otherwise known as ΔZ (ΔZ= Z2-Z1). However to properly predict volumetric flow rates from this device requires math models from Fluid Mechanics [3], combined with an understanding of the components of fluid flow. Thus we need to understand and utilize the following equations:

$$V = [D2\ g / (32\ \nu\ L)] * (h + \Delta Z)$$

equation 1

$$Q = V\ \pi\ D^2 / 4 = [\pi\ D^4\ g / (128\ \nu\ L)] * (h + \Delta Z)$$

equation 2

Equation 1 refers to the average velocity (V) in the flow tube. Average velocity is dependent upon the following parameters:

1. D is the internal diameter of the flow tube.
2. g is the gravitational acceleration.
3. ν is the kinematic viscosity of the fluid.
4. L is the length of the flow tube.
5. h is the height of the fluid column in the reservoir.
6. ΔZ is the difference between Z2-Z1 (see Figure 3)

Now that we have noted the important parameters for the average velocity V, we can use equation 2 to find the volumetric flow rate $Q = V\ \pi\ D^2 / 4$, where $\pi\ D^2 / 4$ is the internal cross-sectional area of the flow tube.

RESULTS

Flow Rate vs. ΔZ

All of the variables to find the volumetric flow rate for the purposes of the lab research were kept constant except for ΔZ. There is a visual representation of data in Figure 4 that illustrates the direct proportionality between ΔZ and the volumetric flow rate Q. Both the math model and the experimental results of volumetric flow rate Q vs. ΔZ show linearity.

It is important to note that in some cases, there were several different values of Q for the same value of ΔZ. This is because the experiments were carried out on more than one day when the lab air temperature (and thus the fluid temperature during fluid flow) was different for each experiment. This resulted in different kinematic viscosities of the fluid from one experiment to another. The different viscosity then results in a different volumetric flow rate for a given ΔZ, if all other factors are held essentially constant.

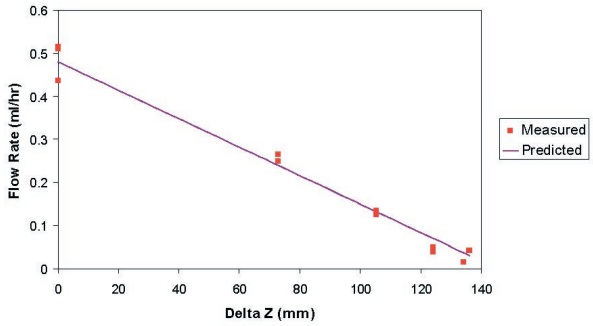

Figure 4. Flow Rate vs. ΔZ

The Aspect Ratio vs. Distance.

When a polymer preform is drilled with a hole as shown in Figure 2, and the hole is filled with a finite amount of fluid, the aspect ratio of the drawn fiber will show an eventual decline with increased distance along the length of drawn fiber. This is the result of decreasing fluid pressure exerted against the internal walls of the inner hole due to the reduction of the fluid column height as the fiber is being drawn. Figure 5 clearly shows the experimental results of this phenomenon:

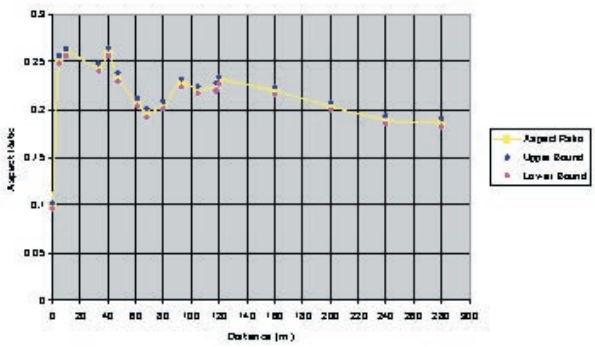

Figure 5. Aspect Ratio vs. Distance

The origin of the inner hole has been measured and is listed at "0" meters on the chart with an initial aspect ratio of about 0.1. Other than a few aberrations in the aspect ratio between approximately 30 meters and 120 meters the aspect ratio shows a gradual decline, which is very apparent after 120 meters. How do we explain the aberrations? First, there is a sharp rise in the aspect ratio between 0 and approximately 10 meters: this is the effect of the tip of the drill bit. Second, in the range of 10 to 120 meters there are several sharp spikes in the aspect ratio. These are most likely caused by trapped air bubbles and/or preform drill shavings that were not removed before the fluid was added, thus creating multiple "plugs" which in turn created abnormal spikes in the aspect ratio. It is clear that along the length of approximately 280 meters of drawn fiber, the aspect ratio generally decreases from a value over 0.25 to a value below 0.20.

FUTURE RESEARCH

There are several items of future research that are relevant to this investigation. First, it would be useful to develop a real-time optical scanner for determining the inner diameter of fiber as it is produced. Dr. Kaminsky of the University of Washington Chemistry Department will be assisting personnel in the Polymer Optics and Processing Laboratory to develop such a system. Second, it will be imperative to develop a method to eliminate trapped air bubbles and/or debris in the fluid as it is infused into the polymer preform during fiber production. Third, the method by which the Gravity Feed Apparatus is connected to the polymer fiber production system will pose challenges that need to be addressed. Fourth, the means by which chromophores align in the inner channel of the fiber will need to be researched; chromophore alignment is needed for optimum optical activity in polymer optical fiber. These areas of research plus potentially many others lie ahead for researchers.

CONCLUSION

Polymer optical fiber offers potential advantages over traditional glass optical fiber. First, it is easier from an energy transfer standpoint to produce than glass fiber (glass fiber requires ≈ 2000°C to produce vs. ≈ 184°C for polymer fiber). Second, it is possible to make 1-2 micron diameter holes in the fiber (or even smaller) and possibly align chromophores within the holes to achieve optimum optical activity for use in amplifiers and such. Third, since polymer is composed of organic molecules, the potential polymer combinations available for fiber experimentation are numerous compared to combinations with glass fiber. These three aspects (plus potentially others) illustrate the need for additional polymer fiber research.

APPENDIX

Distance	Internal Diameter	Outer Diameter	Aspect Ratio	Upper bound	Lower bound
0	58	584	0.09931507	0.10273973	0.095890411
5	127	503	0.25248509	0.25646123	0.248508946
10	130	500	0.26	0.264	0.256
33	118	483	0.24430642	0.2484472	0.240165631
40	124	476	0.2605042	0.26470588	0.256302521
47	112	479	0.23382046	0.23799582	0.229645094
61	98	472	0.20762712	0.21186441	0.203389831
68	95	484	0.19628099	0.20041322	0.19214876
80	100	488	0.20491803	0.20901639	0.200819672
93	118	518	0.22779923	0.23166023	0.223938224
104.5	116	526	0.22053232	0.2243346	0.216730038
118	115	514	0.22373541	0.22762646	0.219844358
120	116	503	0.2306163	0.23459245	0.226640159
160	108	491	0.21995927	0.22403259	0.215885947
200	106	520	0.20384615	0.20769231	0.2
240	91	480	0.18958333	0.19375	0.185416667
280	100	536	0.18656716	0.19029851	0.182835821

Excel Table of Values (used to create figure 5)

REFERENCES

[1] http://www.syringepump.com/NE-1000.htm
[2] Heat Transfer with Applications, Kirk D. Hagen, p. 639.
[3] Fundamentals Of Fluid Mechanics, Bruce R. Munson, Donald F. Young, Theodore H. Okiishi, p. 830, Appendix B

ACKNOWLEDGEMENTS

Research support is gratefully acknowledged from the National Science Foundation Center on Materials and Devices for Information Technology Research (CMDITR), DMR-0120967.